

Copyright  
by  
William Joseph McDoniel  
2015

The Dissertation Committee for William Joseph McDoniel  
certifies that this is the approved version of the following dissertation:

**Realistic Simulation of Io's Pele Plume and its Effects on Io's  
Atmosphere**

Committee:

---

David Goldstein, Supervisor

---

Philip Varghese, Co-Supervisor

---

Laurence Trafton

---

Laxminarayan Raja

---

John Spencer

**Realistic Simulation of Io's Pele Plume and its Effects on Io's  
Atmosphere**

**by**

**William Joseph McDoniel, B.S.M.E.; B.A.**

**DISSERTATION**

Presented to the Faculty of the Graduate School of  
The University of Texas at Austin  
in Partial Fulfillment  
of the Requirements  
for the Degree of

**DOCTOR OF PHILOSOPHY**

THE UNIVERSITY OF TEXAS AT AUSTIN

December 2015

Dedicated to my parents, Julie and Bill.



# Acknowledgments

First, I would like to thank my advisors, Dr. David Goldstein and Dr. Philip Varghese, for their guidance and support during the long course of this work. I also thank Dr. Laurence Trafton, who provided insight at our weekly meetings.

I relied extensively on the work of Dr. Ju Zhang, who I never actually met, to first get a handle on Io's plumes. Dr. Bénédicte Stewart introduced me to the UT DSMC code and taught me how to use it. Drs. Chris Moore, James Strand, Aaron Morris, and Andrew Walker were (before they graduated) excellent colleagues and are great friends. I worked through many of my early classes with the help of Jeff Chu and Nathan Wu. I am grateful for many other past and present colleagues and friends I've had here: Dr. Kelly Stefani, Dr. Seng Yeoh, Parvathy Prem, Will Hoey, Peter Clark, and Kyle Higdon.

Finally, I would like to thank the Texas Advanced Computing Center (TACC) for the use of their supercomputers Lonestar and Stampede. Funding for this work has been provided by several NASA programs including Planetary Atmospheres and the NASA Earth and Space Science Fellowship program.

# Realistic Simulation of Io's Pele Plume and its Effects on Io's Atmosphere

Publication No. \_\_\_\_\_

William Joseph McDoniel, Ph.D.  
The University of Texas at Austin, 2015

Supervisor: David Goldstein  
Co-Supervisor: Philip Varghese

The direct simulation Monte Carlo (DSMC) method is used to investigate gas and dust in Io's giant Pele plume as well as the interaction of giant plumes with other plumes, with Jupiter's plasma torus, and with Io's sublimation atmosphere. Three-dimensional simulations of time-varying systems are performed on up to 2002 processors. Methods for the efficient simulation of interactions between neutral gas and dust particles and between neutral gas and ions (including chemistry) are developed. Simulations are load-balanced dynamically and the grid structure adapts to resolve (potentially moving) regions of high density.

Three-dimensional simulations of the Pele plume show how gas erupting from cracks and holes in a lava lake produces the observed plume and deposition pattern. Small-scale features of the lava lake are found to explain the asymmetric shape of the giant deposition ring. Dust particles are included in the simulations and the computed deposition patterns of different sizes of dust are compared with observations in order

to obtain a best-fit size distribution for particles in the plume. The interaction of Pele and Pillan is investigated by the simultaneous simulation of both plumes.

Giant plumes on Io's equator and north pole are simulated alongside ions which move with Jupiter's magnetic field, and a chemistry model allows for high-energy collisions to produce daughter species. The effect of plasma bombardment on plumes is found to depend on the location of the plumes, and it gives rise to a large, diffuse cloud of neutrals surrounding the plumes. The dense gas in plume canopies also influences the trajectories of ions in the plasma torus, causing ion slip and further asymmetry in the plumes.

Dynamic simulations of plumes on Io's equator and at 30° north latitude over an Io day show how plumes interact with Io's sublimation atmosphere. Plume material becomes suspended in the atmosphere, displacing many times the night-side mass of the plume in sublimated material. The total mass of the atmosphere, however, increases by only a fraction of the plume's night-side mass as the surface frost effectively maintains vapor pressure equilibrium.

# Table of Contents

<b>Acknowledgments</b>	<b>v</b>
<b>Abstract</b>	<b>vi</b>
<b>List of Figures</b>	<b>xi</b>
<b>Chapter 1. Introduction</b>	<b>1</b>
1.1 Motivation . . . . .	1
1.2 Objectives . . . . .	2
1.3 Overview . . . . .	3
<b>Chapter 2. Literature Review</b>	<b>5</b>
2.1 Plume Observations . . . . .	5
2.2 Atmosphere Observations . . . . .	8
2.3 Plasma Observations . . . . .	11
2.4 Simulation and Modeling . . . . .	12
2.4.1 Atmosphere Simulations . . . . .	12
2.4.2 Effect of Io on the Plasma Torus . . . . .	14
2.4.3 Plume Simulations . . . . .	16
<b>Chapter 3. Method</b>	<b>18</b>
3.1 Overview . . . . .	18
3.1.1 Direct Simulation Monte Carlo Method . . . . .	20
3.2 Computational Method for Plume-only Simulations . . . . .	21
3.2.1 Source and Staging through Multiple Domains . . . . .	21
3.2.2 Gas and Dust Deposition Comparisons . . . . .	25
3.2.3 Time Integration of Dust Motion . . . . .	31
3.2.4 Computational Grid and Load-Balancing . . . . .	37
3.3 Computational Method for Plume-on-Planet Simulations . . . . .	40
3.3.1 Patching Plumes on to the Planet . . . . .	40
3.3.2 Vertical Grid Structure . . . . .	44

3.3.3	Ion Weighting . . . . .	50
3.3.4	Fast Plasma Simulation . . . . .	54
3.3.5	Tracer Particles . . . . .	55
<b>Chapter 4.</b>	<b>SO<sub>2</sub> in the Night-side Pele Plume</b>	<b>59</b>
4.1	Overview . . . . .	59
4.2	Below the Virtual Vent . . . . .	60
4.3	Near-Vent Flow . . . . .	67
4.4	Gas Canopy and Column Density . . . . .	73
4.5	Gas Deposition . . . . .	76
4.6	Explaining Other Observations . . . . .	79
<b>Chapter 5.</b>	<b>Dust Grains in the Night-side Pele Plume</b>	<b>83</b>
5.1	Overview . . . . .	83
5.2	Dust Inflow Conditions . . . . .	83
5.3	Dust Flow by Size . . . . .	88
5.4	Dust Deposition by Size . . . . .	91
5.5	Best-Fit Dust Size Distribution . . . . .	93
5.6	Dust Column Densities . . . . .	99
5.7	Non-Uniform Vent Conditions . . . . .	103
5.8	Overlaying of Dust by Gas . . . . .	105
5.9	Multiple Types of Particles . . . . .	108
<b>Chapter 6.</b>	<b>Night-side Plumes on Io</b>	<b>111</b>
6.1	Overview . . . . .	111
6.2	Plume/Plasma Physics . . . . .	112
6.3	Location-Dependent Plasma Interaction . . . . .	117
6.3.1	Sub-Plasma Plume . . . . .	118
6.3.2	Polar Plume . . . . .	120
6.4	Chemistry and Column Density . . . . .	122
6.5	Shielding and Deposition . . . . .	126
6.6	Plasma at Pele . . . . .	130
6.7	Pele and Pillan . . . . .	131
6.7.1	Canopy Interaction . . . . .	133
6.7.2	Gas Deposition . . . . .	136

<b>Chapter 7. Plumes and Io's Atmosphere</b>	<b>138</b>
7.1 Overview . . . . .	138
7.2 Axisymmetric Plume/Atmosphere Models . . . . .	138
7.3 A Simple Model for Total Column Density . . . . .	143
7.4 Equatorial Plume over an Io Day . . . . .	151
7.5 Equatorial Plume at Noon . . . . .	156
7.6 Mid-Latitude Plume at Noon . . . . .	165
<b>Chapter 8. Conclusions and Future Work</b>	<b>173</b>
8.1 Conclusions . . . . .	173
8.2 Future Work . . . . .	176
<b>Appendices</b>	<b>178</b>
<b>Appendix A. Effects of Source Geometry on Plumes</b>	<b>179</b>
<b>Appendix B. An Analytic Model for Plume Height</b>	<b>184</b>
<b>Appendix C. Comments on Simulating Complex Flows on Supercomputers</b>	<b>190</b>
C.1 Common Problems with Gridding and Load-balancing . . . . .	191
C.2 Weighting . . . . .	195
C.3 Communication . . . . .	195
C.4 GPU/MIC Acceleration . . . . .	197

# List of Figures

2.1	Changes to Pele over the course of the Galileo mission. Multiple flybys over the course of several months show the large gas deposition ring and the smaller dust fans fading out and reappearing in tandem. Pillan erupts and overlays Pele’s ring in the northeast before being covered over. From Geissler et al. (2004). . . . .	6
2.2	(left) Simulated (Walker et al., 2012) and (right) observationally inferred (Feaga et al., 2009) “average dayside” SO <sub>2</sub> column densities. Note the anti-Jovian hemisphere has the higher average column density. In the simulation this was largely due to eclipse. . . . .	14
3.1	(a) Galileo SSI image of Pele’s caldera. (b) Processed composite image from Voyager in-sunlight clear-filter observation, Galileo I32 thermal observation in red, and SSI image from (a) in green, from Howell and Lopes (2011). (c) The vent geometry used for the DSMC simulations, obtained by taking all regions of (b) with a grayscale pixel value >200 out of 255 (image processed with built-in Matlab functions). . . . .	22
3.2	(left) DSMC virtual vent with seven independent source regions circled and labeled following the convention in Howell and Lopes (2011), although note that my Source A1 includes the area where Howell and Lopes identify two more regions A4 and A5, and I identify a new area A6. Sources E, C, and A1 are simulated in 3D, with 40 m resolution of the source geometry. Sources A2, A3, A6, and B1 are treated as small axisymmetric plumes with source radii of 200 m. The center and right images show the full 1600 km diameter far-field domain in wire frame, curving over the surface of Io. In the center image the first domain (up to 20 km altitude) integrating all seven source regions is visible within a wire frame of the second domain. In the right image the second domain (up to 60 km altitude) is visible. . . . .	23
3.3	(a) Galileo image of Pele’s multicolored deposition pattern on Io’s surface. (b) A region around the plume source where I believe coloration of the surface is strongly influenced by plume activity and from which target regions for comparison will be chosen. (c) The primary target region used to compare dust deposition to simulations is colored black. (d) Close-up of the grayscale surface inside the two fans of the target only; I fit my dust deposition model to each of the 3,194 gray pixels shown. . . . .	25

3.4	(a) Sample overlapping basis functions which might be used to try to construct a best-fit size distribution are fed (b) one-by-one into the large plume simulation which yields (c) a simulated deposition pattern corresponding to each (the pattern shown corresponds to the red basis function in (a)). I then seek to find a fitting coefficient $\alpha_k$ for this kth basis function which minimizes the sum-of-squares error on a pixel-by-pixel (for all j) basis between the simulated pattern and the observed pattern (d). . . . .	28
3.5	Comparison of linearized drag calculation method (red lines) to the method of Burt and Boyd (2004) (black lines) for different time step sizes. . . . .	35
3.6	(a) Number density contours for flow in a constant-altitude slice 1 km above Source A1, with black processor boundaries visible. (b) A close-up of the polar cap processor and the innermost ring. Processor boundaries are in red and cell boundaries are in black. . . . .	38
3.7	Axisymmetric number density simulations for a Pele-type plume stem and 118 K sublimation atmosphere. (a) shows a plume stem with atmosphere. (b) shows a plume stem without atmosphere. (c) shows an atmosphere alone (with no sublimation where the plume vent was). Streamtraces show the motion of the gas. . . . .	43
3.8	Demonstration of dynamic load-balancing and adjustment of the vertical grid structure using the new linear segments implementation. An axisymmetric Prometheus-type plume with a sublimation atmosphere is simulated on 12 processors. Snapshots of number density are shown at 250 s, 750 s, and 1500 s, from left to right. Thick black lines are processor boundaries and thin black lines are cell boundaries. . . . .	50
4.1	Erta Ale lava lake in Ethiopia, 80 m across and (right) Nyiragongo lava lake in the Democratic Republic of the Congo, several hundred meters across (varies). Both exhibit cracks and lava fountains. These lakes are much smaller than the lava lake at Pele, but I assume that the surface features are similar and have similar length scales. . . . .	61
4.2	(left) Drawing of large, irregular feature modeled after Source A1 from Fig. 3.2, covered with uniformly spaced circular sources (not to scale). The inset shows the two relevant lengths in the uniform circular source field model – the hole diameter and the hole spacing. The dark border of the lava lake is $\sim 250$ m thick on this scale. (right) Schematic of flow emerging from an infinite plane of circular sources, seen from the side. . . . .	62
4.3	(a) Density contours for $\text{SO}_2$ gas emerging into a vacuum from an infinite plane of circular sources at Mach 1, expanding supersonically upwards. Four sources are pictured, with contours drawn on two of the domain's symmetry boundaries. Shocks and expansions in the gas flow strongly resemble shock diamonds typically seen in under-expanded supersonic jets in the atmosphere such as in (b) and (c). (b) Shock diamonds behind the engines of an SR-71B. (c) Shock diamonds in a jet at the Swiss Propulsion Laboratory. . . . .	63



4.4	(a) Number density contours for a uniform flow of SO <sub>2</sub> rising from an infinite plane of circular sources at approximately Mach 1 ( $2.73 \times 10^{-5}$ kg/m <sup>3</sup> , 1333 K, 465 m/s), which quickly expands to around Mach 3. The shocks are initially strong, but viscosity has driven the flow nearly uniform by 750 m above the vent. (b) Mach number contours for the same flow. Mach waves for Mach 2 and 3 flow are drawn from one edge of the simulation to qualitatively show the possible influence of the edge of the lava lake on the actual flow below the virtual vent. . .	64
4.5	Number density contours for SO <sub>2</sub> in the immediate vicinity of Source E. (a) A slice of the plume flow seen from the side, along the dashed red line in (c), with gas rising from each of the four collinear vent regions (each is labeled to aid discussion). (b) A constant altitude slice at the top of the domain (3 km altitude). (c) The labeled vent regions, in black, on the same scale as in (b), with a dashed line indicating the orientation of (a). . . . .	68
4.6	Number density and translational temperature contours for the first large domain. (a) Number density contours on a slice through the middle of the plume, along the red dashed line shown in (c). (c) The source regions used as the virtual vent, in black, except for Source B1. (b) Temperature contours on the same slice as in (a). (d) Number density contours on a constant-altitude slice at the top of the domain (20 km). (e) Temperature contours on the same constant-altitude slice as in (d). The virtual vent is superimposed (Source B1 is not pictured but is labeled). . . . .	70
4.7	SO <sub>2</sub> number density contours for the first and second large domains, 200 km in diameter and 60 km tall. (a) Contours for an east/west slice through the plume oriented in the same way as the slice in Fig. 4.6a. (b) Contours for a north/south slice oriented at 90 degrees to the slice in (a). (c) Contours on a constant-altitude slice at the top of the domain (60 km altitude). . . . .	72
4.8	SO <sub>2</sub> number density and temperature contours for all three large domains, 1,600 km in diameter along the surface of Io and 440 km tall. (a) Number density contours on an east/west slice showing the continued expansion of the smooth flow in Fig. 4.7. (b) Translational temperature contours for the slice in (a). (c) Number density contours on a north/south slice. (d) Translational temperature contours for the slice in (c). . . . .	74
4.9	SO <sub>2</sub> line-of-sight integrated column densities. (a) Column density seen from due south. (b) Column density seen from due west. . . . .	76
4.10	Gas deposition patterns. (a) Contours of the deposition rate of SO <sub>2</sub> on the surface (in kg / m <sup>2</sup> s) for the plume simulations. (b) Contours of the deposition rate of SO <sub>2</sub> when fictitious forces are implemented to account for the non-inertial reference frame. The plume shown here was simulated at the equator of Io. (c) Pele's ring on Io's surface, as seen from the same head-on perspective used for the simulations, drawn from Williams et al. (2011). Lines of maximum diameter are drawn on all images. . . . .	77

4.11	(a) Recolored gas deposition pattern from Fig. 4.10a. (b) Number density contours for a constant-altitude slice of the plume $\sim 500$ m above the surface. (c) Galileo image of Pele. . . . .	80
4.12	Gas deposition rates for four nominally identical plume simulations. All plumes are run in the largest domain for 6,000 seconds before sampling the deposition rate over 500 seconds. . . . .	81
5.1	Dust velocity as a function of particle size at the virtual vent for a variety of possible models. (a) Comparison of vertical velocity at the virtual vent for three “equilibrium” models. The black line shows the gas velocity of 850 m/s at the virtual vent. The red line shows the terminal velocity of dust in the gas at the virtual vent (calculated using an expression for the drag coefficient from Bird, 1994). The blue line shows the average vertical velocity at the virtual vent altitude dust when particles are created at the lava lake surface with 450 m/s vertical velocity and allowed to rise. (b) The 2D velocity distributions at the virtual vent altitude for three sizes of dust when dust is created at 450 m/s oriented in a random direction. The initial velocities of all dust particles lie along the solid black line. (c) The 2D velocity distributions for three sizes of dust when dust is created at 100 m/s oriented in a random direction. . . . .	86
5.2	Number density contours for several narrow size distributions of dust grains, with superimposed line contours of the gas slices from Fig. 4.8. (a), (b), and (c) show slices for three distributions seen looking north, while (d), (e), and (f) show slices for the same size distributions seen looking east. Only flow in the final simulation domain is shown and the absolute value of the number density is arbitrary due to my low mass loading assumption, but relative magnitudes are valid. . . . .	89
5.3	Simulated deposition patterns for various sizes of dust grains, with the gas deposition ring for scale in (a). Pixel darkness is proportional to deposition rate and is normalized by the total number of simulated particles of each diameter. The target region and observation are shown on (b) and the target region is outlined on the other simulated dust deposition patterns. . . . .	92
5.4	(a) Set of uniform basis function size distributions. (b) Set of Gaussian basis function size distributions. Basis functions are normalized such that the sum of the values a basis function takes at all integer nanometer diameters between 20 nm and $10\mu\text{m}$ is 1. (c) Best-fit size distributions obtained using the basis functions in (a) and (b). (d) Best-fit deposition pattern in target region obtained from the basis functions in (a), which is produced by the best-fit distribution in red in (c). (e) Best-fit deposition pattern in target region obtained from the basis functions in (b), which is produced by the best-fit distribution in blue in (c). (f) Target region from observation. Note the log scales on (a), (b), and (c), and in all cases “Fraction” represents the number fraction of particles in a distribution at each integer nanometer diameter. . . . .	94

5.5	(a) Comparison of the best-fit size distribution obtained earlier (Both) to those obtained when each butterfly wing is fit independently (Left and Right). (b) The composite best-fit deposition pattern produced when fitting each wing independently. The uniform basis functions from Fig. 5.4a were used. . . . .	97
5.6	(a) The target region used earlier. (b) A more generous target region which tries to capture nearly everything that could plausibly be due almost solely to dust deposition. (c) A circular target region extending out to the inner edge of Pele's red ring. (d) A comparison of best-fit size distributions obtained for different choices of target region. . . . .	98
5.7	Normalized line-of-sight integrated column densities for several size distributions of dust. (a), (b), (c), and (d) are uniform size distributions similar to those used in previous figures. (e) shows column density for the largest Gaussian basis function from Fig. 5.4b, where the dust is created at the virtual vent with a velocity of 450 m/s directly upwards, and no velocity parallel to Io's surface. All images are shown looking east, are drawn to the same length scale, and utilize the same color bar.	100
5.8	(a) Voyager 1 observation of Pele through its UV filter. Image from PDS C1636850, stretched and saturated to better show the plume. (b) Contour levels for the observation in (a) from Strom et al., 1981. . . .	101
5.9	(a) Sources E, C, and A1, with their individual areas labeled below. Above are the areas assumed to be contributing to dust deposition in the west (11 km <sup>2</sup> ) and in the east (8.45 km <sup>2</sup> ). (b) The best-fit deposition pattern obtained after scaling western dust deposition by 0.7. (c) The best-fit deposition pattern obtained after scaling the western deposition of only dust smaller than 1,384 nm in diameter. . . . .	105
5.10	(a) Comparison of best-fit size distributions to a single log-normal distribution, where $\mu$ is -7.51 and $\sigma$ is 2.81. (b) Comparison of best-fit size distributions to the weighted sum of two log-normal distributions. As with earlier plots of size distributions, 'Fraction' represents the fraction of particles with each integer nanometer diameter. . . . .	109
6.1	Illustration of Io's plasma environment in the simulation. (a) Contours of magnetic field strength with field lines drawn. (b) Contours of bulk plasma speed with streamtraces drawn. The velocity is due to the combined effect of the B field and an E field which is due to the motion of the Io-fixed reference frame relative to Jupiter's magnetic field. The viewer is above Io's equator looking towards Jupiter. Io and the plasma torus orbit to the right, with the faster moving plasma overtaking Io in its orbit. Magnetic field and bulk plasma velocity are from Combi et al. (1998). . . . .	112
6.2	Plots of an example ion's trajectory in 2D (a) velocity and (b) physical space. The trajectories are colored such that each part of the trajectory in velocity space corresponds to the same-colored regions of the physical trajectory. . . . .	113

6.3	Example axisymmetric simulations of plasma interacting with a plume. Tracer particles are shown for SO <sub>2</sub> (orange) plumes with O <sup>+</sup> and S <sup>+</sup> ions (teal). The central axis of the plume is an axis of symmetry. (a) Ions rain down from above on to a plume, as would happen at the sub-plasma point on Io. (b) When ions collide with dense gas in the plume canopy, they deflect in the direction of the E field. (c) Ions stream in from the side towards a plume, as would happen at the anti-Jupiter point on Io. (d) Ions that encounter the plume's dense upper canopy are deflected in the direction of the E field, away from Io's surface. Because these simulations are axisymmetric the fields behave oddly close to the axis, but away from the axis the plume/plasma interaction is nearly the same as it would be for truly uniform fields. . . . .	116
6.4	(a-f) Number density (left) and temperature (right) contours for slices through a plume at the sub-plasma point. (a) and (b) are viewed from the north, with Jupiter to the right. (c) and (d) are viewed from the east, looking towards Jupiter. (e) and (f) are of an axisymmetric plume without plasma. (g) and (h) show mean free path contours for the slices in (a) and (e) respectively, computed as $(\sqrt{2}n\sigma_{SO_2})^{-1}$ , where $n$ is SO <sub>2</sub> number density and $\sigma_{SO_2} = 1.61 \times 10^{-18} \text{ m}^2$ is the collision cross-section for SO <sub>2</sub> -SO <sub>2</sub> collisions. . . . .	119
6.5	(a-d) Number density (left) and temperature (right) contours for slices through a plume at the north pole. (a) and (b) are viewed with plasma streaming in from the right, with Jupiter behind the viewer. (c) and (d) are viewed with plasma streaming out of the page and Jupiter to the right. (e) and (f) repeat the two equatorial plume slices in Fig. 6.4c and d for ease of comparison. . . . .	121
6.6	Number density contours on slices for SO and SO <sub>2</sub> in the polar plume model with plasma. (a) and (b) show SO slices from the same perspectives as Fig. 6.5a and c. (c) is the same slice as (a), zoomed out and rescaled to show SO over all of Io. (d) is the same as (c) except it shows SO <sub>2</sub> . Slices here were time-averaged over 1000 time steps. . . .	123
6.7	Column densities for (a) SO <sub>2</sub> , (b) SO, and (c) O on Io's northern hemisphere around a polar plume with plasma, looking down at the north pole. Plasma streams in from the +Y direction and Jupiter is in the +X direction. . . . .	125
6.8	Mass flux of O <sup>+</sup> into hemispheres on Io's surface for (a) a polar plume and (b) a plume at the sub-plasma point. Plasma streams in from the +Y direction (streams into the page in (b)), Jupiter is in the +X direction, and the Z axis aligns with Io's polar axis. . . . .	127
6.9	Mass flux of SO <sub>2</sub> into hemispheres on Io's surface for a polar round hole plume. (a) and (c) have plasma while (b) and (d) do not. (a) and (c) differ from each other only in the choice of contour levels. Likewise (b) and (d). . . . .	129

6.10	(a) Deposition rate of the Pele plume from Chapter 4. (b) Deposition rate of the earlier Pele plume model simulated at $18.7^\circ$ south latitude $104.7^\circ$ east longitude, with plasma. (c) Galileo image of Pele on Io for comparison. Note that the color bar here is linear unlike for other presentations of gas deposition in this work. . . . .	130
6.11	Tracer particles for the Pele and Pillan at various times in the plume/plume system's development. Both plumes erupt in (a). The smaller Pillan plume forms a canopy first in (b). Pele's canopy begins to form in (c) and sweeps over Pillan, deforming it on the way. The plumes begin to go steady in (d), although the interaction region between the two is still sorting itself out. In (e) the system is essentially steady. (f) is a view from overhead at steady-state where the interaction region is clearly visible in column. . . . .	134
6.12	(a) Number density with streamlines, (b) temperature contours, and (c) mean free path contours for a slice through the Pele/Pillan system. The slice cuts through the centers of both plumes. The sharp spike at the center of the rising Pillan plume is a grid artifact. The low-density region under Pillan corresponds to where the separately-simulated inner domain is patched in, as with previous plume simulations. . . . .	135
6.13	(a) $\text{SO}_2$ deposition for the Pele/Pillan system. (b) Deposition for Pele in the absence of Pillan for comparison. (c) Galileo image of Pele on Io's surface some time after Pillan's eruption. . . . .	136
7.1	Axisymmetric plumes simulated with a sublimation atmosphere produced by $\text{SO}_2$ frost at several surface temperatures. Gas falling back to Io's surface in the plume canopy depresses the sublimation atmosphere locally. For higher surface temperatures there is a larger underlying atmosphere which is shielded from the plume by sublimated gas at higher altitudes. In (d), the 116 K case was simulated with a plume one tenth as dense as in the other simulations. This low density plume causes much less of a disturbance in the sublimation atmosphere. In all cases the plume gas "bounces" off the sublimation atmosphere to some extent, producing a region of enhanced density at high altitudes further to the right. In the low-density case (d), the falling plume has little effect on the atmosphere below about 20 km. . . . .	140
7.2	Column densities as a function of radius from the symmetry axis of the domain for a variety of cases. Red lines are for a sublimation atmosphere with no plume. These dip slightly at the axis because of the sink where the plume would otherwise be and dip significantly at the right side because of the vacuum boundary condition there. Green lines are for plumes like those in Fig. 7.1 simulated without any sublimation atmosphere. Blue lines are for the 110 K and 116 K simulations from Fig. 7.1, with an interacting plume and atmosphere. Note that the Y-axis is different between the figures because the atmosphere changes by an order of magnitude – the green plume line is the same in both. . . . .	141

7.3	Illustration of the model for total column density. (a) A plume of height $h$ simulated with no sublimation atmosphere, consisting of a rising section and a falling section. (b) A sublimation atmosphere simulated with no plume, which is collisional up to its exobase at an altitude $z$ . (c) The superposition of the rising plume, the sublimation atmosphere, and the falling plume above the exobase. . . . .	145
7.4	Comparison of Tsang et al.'s (2012) model with and without a temperature-dependent volcanic component. (a) and (b) are from Fig. 17 in Tsang et al. For the indicated thermal inertias and albedos, their model produces a sublimation component shown by the dotted line. The solid red line is a constant volcanic component. The dashed line is the sum of these two components, taken to be the total atmosphere. The gray symbols are observational data to which they are attempting to fit. (c) is my attempt to reproduce (a), where the blue line is the sublimation component, the red line is the constant volcanic component, and the black line is the total atmosphere. (d) is the model in (c) with the substitution of a temperature-dependent volcanic component which is proportional to $f$ and scaled to a minimum value of $4 \times 10^{16} \text{ cm}^{-2}$ , where $f = 0.5(1 + \sqrt{1 - z/h})$ , $z$ is the exobase altitude, and $h = 50$ km. The dashed line is the total atmosphere from (c) for comparison. . . . .	149
7.5	Images of tracer particles for a simulation of an equatorial plume over half of a 40-hour day. Red particles are $\text{SO}_2$ from a patched plume and blue particles are sublimated $\text{SO}_2$ . Plume particle are over-represented by a factor of 25 relative to sublimated particles (to better visualize the plume). Time stamps give minutes since dawn (noon is 600 minutes after dawn) and local time at the plume source. The viewer is above the south pole. . . . .	153
7.6	Images of tracer particles for a simulation of an equatorial plume over half of a 40-hour day. Red particles are $\text{SO}_2$ from a patched plume and blue particles are sublimated $\text{SO}_2$ . Plume particle are over-represented by a factor of 25 relative to sublimated particles. Time stamps give minutes since dawn (noon is 600 minutes after dawn) and local time at the plume source. The viewer is directly above the plume. . . . .	154
7.7	Slices of an equatorial Pele-type plume at noon, where the peak day-side frost temperature is 118 K. (a) Number density contours of $\text{SO}_2$ . (b) Temperature contours. (c) Temperature contours on an expanded color bar. For (b) and (c), regions with number density $\leq 2 \times 10^{13} \text{ m}^{-3}$ and cells with vertical resolution coarser than 70 km are blanked. . . . .	156
7.8	Slices of an equatorial Pele-type plume at noon, where the peak day-side frost temperature is 118 K. (a) Contours of mean free path. (b) Contours of the fraction of particles which originated from the plume source. (c) blown-up view of (b) with an adjusted color bar. Regions with number density $\leq 2 \times 10^{13} \text{ m}^{-3}$ and cells with vertical resolution coarser than 70 km are blanked. . . . .	157

7.9	Slices of an equatorial Pele-type plume at noon, where the peak day-side frost temperature is 118 K. (a) Number density contours of SO <sub>2</sub> with contours of total (combined plume and sublimation atmosphere) SO <sub>2</sub> column density over Io's surface. (b) Contours of the fraction of particles which originated from the plume source with contours of the deposition rate of plume material into Io's surface. Select lines of latitude are shown. Regions with number density $\leq 2 \times 10^{13} \text{ m}^{-3}$ and cells with vertical resolution coarser than 70 km are blanked. . . . .	160
7.10	Contours of column density and related properties for Io's day-side with an equatorial plume at noon, where the peak frost temperature is 118 K. (a) Column density for SO <sub>2</sub> which sublimated directly from surface frost. (b) Column density for SO <sub>2</sub> which erupted from the plume source. (c) Fraction of the local total column density due to sublimated material ((a) divided by (a) plus (b)). (d) Total column density. (e) Total or sublimated column density for a simulation of only the sublimation atmosphere, without a plume. (f) The relative difference in total column density between the plume/atmosphere simulation and the atmosphere-only simulation ((d) minus (e) divided by (e)), obtained by interpolating both onto a grid with half-degree resolution. These results do not include the plume inner domain below 60 km altitude, but this is almost entirely within regions where the figures are saturated already. . . . .	162
7.11	Slices of a Pele-type plume at 30° north latitude, where the peak day-side frost temperature is 118 K. (a) Number density contours of SO <sub>2</sub> . (b) Contours of the fraction of particles which originated from the plume source. (c) Temperature contours. (d) Temperature contours on an expanded color bar. For (b), (c), and (d), regions with number density $\leq 2 \times 10^{13} \text{ m}^{-3}$ and cells with vertical resolution coarser than 70 km are blanked. . . . .	166
7.12	Slices of a Pele-type plume at 30° north latitude, where the peak day-side frost temperature is 118 K. (a) Number density contours of SO <sub>2</sub> with contours of total (combined plume and sublimation atmosphere) SO <sub>2</sub> column density over Io's surface. (b) Contours of the fraction of particles which originated from the plume source with contours of the deposition rate of plume material into Io's surface. Regions with number density $\leq 2 \times 10^{13} \text{ m}^{-3}$ and cells with vertical resolution coarser than 70 km are blanked. . . . .	168

7.13	Contours of column density and related properties for Io's day-side with a 30° north latitude plume at noon, where the peak frost temperature is 118 K. (a) Column density for SO <sub>2</sub> which sublimated directly from surface frost. (b) Column density for SO <sub>2</sub> which erupted from the plume source. (c) Fraction of the local total column density due to sublimated material ((a) divided by (a) plus (b)). (d) Total column density. (e) Total or sublimated column density for a simulation of only the sublimation atmosphere, without a plume. (f) The relative difference in total column density between the plume/atmosphere simulation and the atmosphere-only simulation ((d) minus (e) divided by (e)), obtained by interpolating both onto a grid with half-degree resolution. These results do not include the plume inner domain below 60 km altitude. As with Fig. 7.10, the lobe features far from the plume source and near the pole are likely artifacts. . . . .	169
7.14	Contours of total column density with streamtraces for (a) the atmosphere-only simulation and (b,c) the 30° north latitude plume with atmosphere simulation. Streamtraces in (b) represent the velocity of only the sublimated material, while in (c) they represent the velocity of both sublimated and plume material. . . . .	171
A.1	Number density contours for a plume erupting from a 20 km by 2 km rectangle. (a) A slice through the source's minor axis. (b) a constant-altitude slice at surface-level, where number density is a proxy for deposition intensity. . . . .	179
A.2	Number density contours for a plume erupting from a half-annulus 1 km wide with an inner radius of 7 km. (a) Ground-level contours with streamtraces in the immediate vicinity of the source (symmetry axis at the top). (b) A slice through the symmetry plane with streamtraces in the immediate vicinity of the source. (c) Surface-level contours for half of the entire plume. . . . .	180
A.3	Number density contours for a plume erupting from a curved line source modeled after a 1999 Galileo SSI IR observation of Pele's caldera. (a) Ground-level contours in the immediate vicinity of the source. Unlike other results in this chapter, this was simulated at Pele's vent conditions on 64 processors. Galileo observation is inset. (b) Surface-level contours of the cold case for the entire plume, rotated by 90° to better compare with inset of Galileo observation of Pele. . . . .	182
A.4	Number density contours for a plume erupting from a source modeled after the entire black lava lake seen by Galileo, shown in the inset in (a). (a) Near-surface contours for the whole plume, showing expansion along the vent's minor axis with two jets emerging from each side of the source, corresponding to highly concave parts of the source geometry. (b) A north/south slice roughly along the vent's minor axis, showing a full plume with a canopy that remains dense all the way to the ground. (c) An east/west slice roughly along the vent's major axis, showing a much more confined rising plume and a canopy which rapidly becomes less dense as it approaches the surface. . . . .	183



B.1	(a) Schematic of a plume erupting from a source at $V$ , rapidly expanding to 1 at low altitude, then rising while decelerating due to gravity to conditions at 2. At a height $h$ the rising gas shocks, forming a canopy at conditions 3. (b) Idealized model of a plume which expands in a cone with half-angle $\theta$ from a point source. The rising gas produces a flat disc canopy with thickness $\Delta z$ and diameter $2h \tan \theta$ . Mass flux into the disc from below must equal mass flux out of the sides of the disc. . . . .	185
B.2	(a) Contours of constant canopy height for an axisymmetric plume erupting from an 8 km radius round hole as a function of vent velocity and vent temperature, from Zhang (2004). (b) Contours of constant plume height computed according to equation B.4 using half of the maximum turning angle for $\theta$ , $C_p = 520$ J/K, and $\gamma = 4/3$ . (c) Contours of constant ring diameter from Zhang (2004). Actual conditions simulated are marked with large squares; these were also the simulations used to construct (a). (d) Zhang's canopy height contours from (a) with the computed heights from (b) super-imposed as dashed red lines. . . . .	188

# Chapter 1

## Introduction

### 1.1 Motivation

Io's colorful surface, its atmosphere, and Jupiter's plasma torus are all ultimately due to Io's volcanism. It is the most volcanically active body in the solar system and its giant plumes rise hundreds of kilometers, above the atmosphere, before falling back to the surface. The deposited material gives rise to large red rings, black fans and splotches, and white frost-covered regions among other features.  $SO_2$  in the plumes becomes surface frost, which when warmed by the Sun produces a sublimation atmosphere. Material in the plumes or atmosphere can be ionized or dissociated by sunlight or by interactions with other particles, and ions and electrons produced at Io are swept up by Jupiter's strong magnetic field, supplying the plasma torus around Jupiter.

Many of the details of this story are currently unknown. Io's surface is not colored evenly or at random. The giant red rings appear around the sources of giant plumes, but these rings are asymmetric, with sharp features, and change over time. At the Pele plume, gas rising out of a large lava lake is somehow responsible for an egg-shaped red ring around 1000 km in diameter, but it is unclear why it takes this shape. Inside of Pele's large red ring are fans of black material extending to the east and west, although not to the north and south where sprays of red, similar to the large ring, are observed. This black material resembles the large black spot that

appeared on top of Pele’s red ring when the Pillan plume erupted. Simulations of the Pele plume can account for the appearance of its deposition ring and can provide explanations for features like the black fans. Simulations can also determine the extent to which interactions between the plume and the sublimation atmosphere or plasma are necessary to explain observations of Io’s surface.

The extent to which sublimated material dominates the atmosphere is another mystery. While Io clearly has an atmosphere, of which the volcanoes are the ultimate source, many observations seem to indicate that the atmosphere is primarily supported by sublimation. However, others show an insensitivity to insolation that suggests a large volcanic component of the day-to-day atmosphere. This has been difficult to address in part because little work has been done on the interaction between plumes and sublimated gas. When material directly erupting from a plume source is comparable in mass to material sublimating from surface frost, the interaction between these atmospheric sources may be complicated, and simulations can shed light on this interaction.

In part because the structure of the atmosphere is not well-constrained, the interaction between the atmosphere and Jupiter’s plasma torus is also not well understood. Plumes increase the cross-section Io presents to incoming ions and may shield the atmosphere beneath them. Simulations of the entire coupled plume/atmosphere/plasma system are necessary for teasing out the effects of all of the physics at work.

## 1.2 Objectives

In this work I develop a three-dimensional, physically-realistic model of the Pele plume, following the plume gas from where it erupts at the surface of a lava lake,

up into the plume’s umbrella-shaped canopy, and back down on to the surface. I use this model to explain features of the deposition pattern around Pele and to constrain particle sizes in the plume. Starting from a gas-only model of an isolated plume, I add dust grains which are one-way coupled to the gas. I then integrate the plume model into a simulation of other physics on Io. The effects of the plasma torus on plumes are investigated by linking plume simulations to a sub-stepped simulation of ions which interact with the gas according to a previously-developed chemistry model. I also link the plume simulations to simulations of the sublimation atmosphere in order to help explain apparent inconsistencies in observations of Io’s atmosphere and to investigate the structure of Io’s atmosphere.

In the course of this work I encountered a variety of challenges, ranging from the determination of input conditions for dust grains in the plume to needing to efficiently simulate a three-dimensional and time-evolving flow on a very large number of processors. This led to the development of additional models (e.g., a model of the flow in the immediate vicinity of Pele’s lava lake) or of computational methods for simulating or visualizing complex flows. This additional work is described in Chapter 3.

### **1.3 Overview**

Chapter 2 is a review of previous work relevant to this topic. It covers observations of Io’s plumes, Io’s atmosphere, and Jupiter’s plasma torus along with Io’s interaction with it, as well as prior simulations. Chapter 3 describes the basic DSMC method used for the simulations presented here, additions and modifications to that method made for this project, and the physical models used in determining inputs or

interpreting outputs. Chapter 4 presents simulations of gas in the Pele plume without interference from a sublimation atmosphere or plasma. I show the importance of the lava lake's geometry for determining the structure of the plume and explaining the shape of Pele's red ring. Chapter 5 adds dust grains to the gas plume simulations, shows how the motion of dust particles depends on the size of the particles, and constrains grain sizes in the Pele plume by comparing simulated dust deposition to the observed black fans inside of Pele's ring. Chapter 6 considers plume/plume and plume/plasma interactions. Pele's interaction with the plasma is simulated alongside an equatorial axisymmetric plume and a polar axisymmetric plume. A simple model of Pillan is simulated simultaneously with the earlier Pele model. Chapter 7 examines the interaction between plumes and the sublimation atmosphere. Guided by simulation results, a simple model is developed for the total column density produced by plumes and sublimating frost. Three-dimensional, time-varying simulations of a sublimation atmosphere and round-hole plumes on the equator and at  $30^\circ\text{N}$  latitude are presented and discussed. Chapter 8 lists the primary conclusions of this work and gives suggestions for future work.

There are three appendices. Appendix A presents some early simulations that shed light on the effect of source geometry on plumes and ultimately led to the choice of source geometry used for Pele in the rest of this work. Appendix B develops an analytic model for the height of a plume as a function of conditions at its vent and compares this model to simulation results. Appendix C contains comments on problems encountered in performing simulations like the ones presented here on supercomputers. It is intended to help others build on this work using the UT DSMC code.

# Chapter 2

## Literature Review

### 2.1 Plume Observations

Large SO<sub>2</sub> plumes on Io were first observed by Voyager (Smith et al., 1979). They are distributed over Io's surface and many extend well above its atmosphere. Strom and Schneider (1982) first suggested that the plumes' umbrella-like structure was a result of a large, curved canopy shock. McEwen and Soderblom (1983) distinguished giant Pele-type plumes and smaller Prometheus-type plumes, and noted that the Pele-types erupt over days and leave behind red rings on the surface while the Prometheus-type remain active for very long periods of time (years) and produce white rings on the surface. They suggested that Pele-type plumes are produced by the eruptions of sulfurous gas from below the surface while the gas in Prometheus-type plumes is the result of lava flows impinging on surface frost.

Spencer et al. (2000) and later Jessup et al. (2007) strongly supported this mechanism by showing that S<sub>2</sub> was present in small amounts in at least some Pele-type plumes, and it is thought that the redness of Pele-type deposition rings is due to the presence of S<sub>3</sub> or S<sub>4</sub> produced in the plume (McEwen and Soderblom, 1983) or perhaps on the surface. Many plumes also produce smaller, black deposition patterns (in round spots around their source). Geissler et al. (1999) suggests that this is silicate ash. These deposition patterns, of all colors, are not constant over time – implying unsteadiness in the plumes. Geissler et al. (2004) discusses many of these

changes over the course of the Galileo mission, including the eruption of Pillan on the east side of Pele's ring, overlaying Pele's red ring with a black circle of ash that was then covered over in turn. Williams et al. (2011) categorize the various sorts of surface materials seen on Io and summarize the literature on the silicate nature of black deposits and the contribution of  $S_2$  or sulfur-bearing chlorides to the red color of Pele's ring.

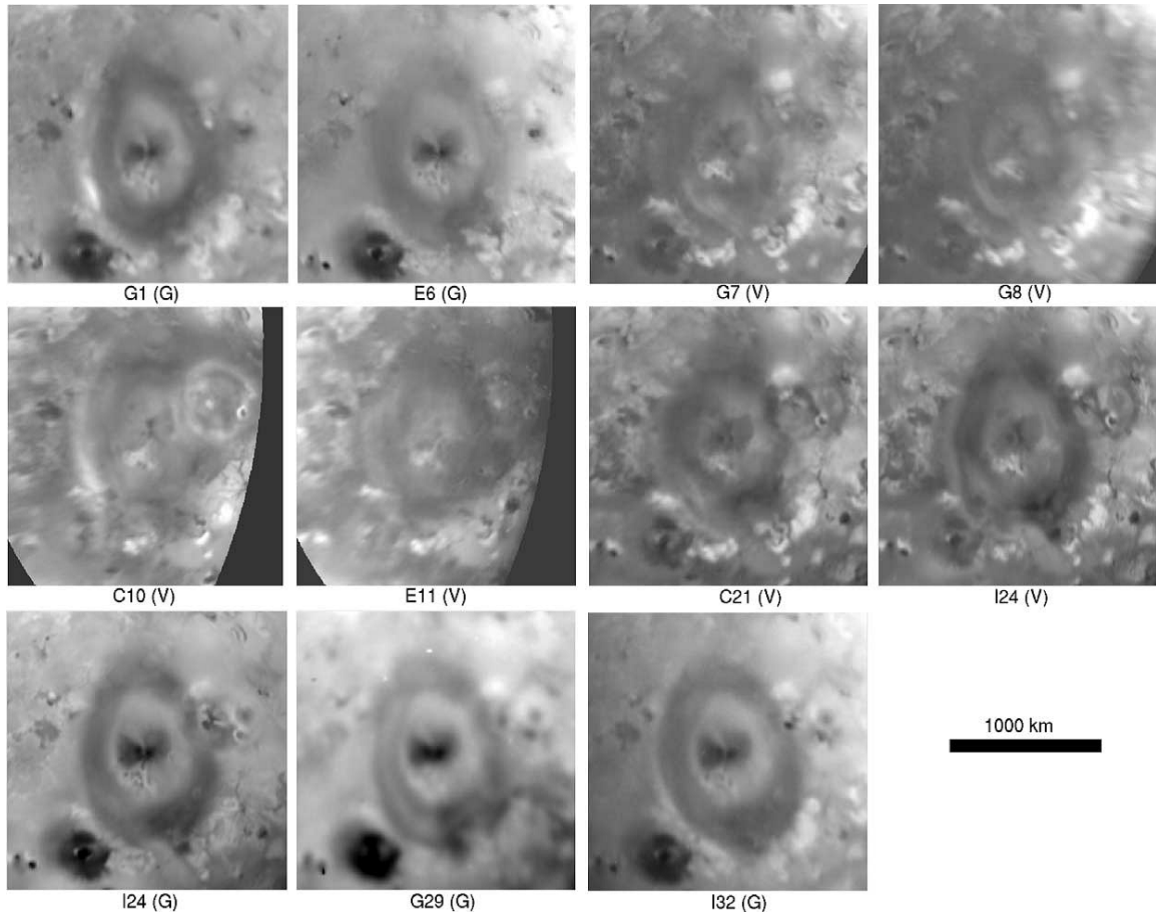


Fig. 2.1: Changes to Pele over the course of the Galileo mission. Multiple flybys over the course of several months show the large gas deposition ring and the smaller dust fans fading out and reappearing in tandem. Pillan erupts and overlays Pele's ring in the northeast before being covered over. From Geissler et al. (2004).

Observations of the plume sources shed light on the mechanisms giving rise to the plumes and are an important input to this work. Tvashtar’s fire fountain likely erupts from a thin fissure (Milazzo et al. 2005). Prometheus is probably formed by slowly creeping lava subliming surface frost (Davies et al. 2006). This work focuses on Pele, and Voyager, Galileo, and Cassini have yielded excellent observations of its patera. Of special interest are the hot regions indicating volcanic activity. McEwen et al. (2000) suggested that a bright curved line seen during the Galileo I24 orbit was the edge of a lava lake, where the crust met the patera wall and exposed liquid lava, and this interpretation has held up through later observation and analysis (Davies et al. 2001, Radebaugh et al. 2004).

Radebaugh et al. (2004) looked at Galileo I32 (this orbit was much closer to the surface) and Cassini observations and identified a much larger region of high temperature which seems to be persistent over time. They also found that the image intensity dropped with viewing angle much more strongly than expected for a flat, uniform surface. Howell et al. (2011) used similar data to project a temperature map of the lava lake at Pele onto Io’s surface, which was taken as a boundary condition for parts of this work.

Particle sizes and distributions in plumes have been constrained by observations of scattered or absorbed light. Geissler and McMillan (2008) used Galileo observations to find that small Prometheus-type plumes contain about  $10^6$  kg of  $\sim 100$  nm particles, but that Pele-type plumes do not contain high densities of such particles. They noted that Voyager observations in the ultraviolet produced clear images of Pele, indicating that the particles in these plumes are much smaller than the particles in Prometheus-type plumes. However, Jessup and Spencer (2012) used Hubble



observations and, assuming a normal distribution of particle sizes to estimate gas and dust column densities, argued that Pele had a mean particle size between 50 nm and 110 nm in 1995 and between 50 nm and 80 nm in 1999. Jessup and Spencer also found that the SO<sub>2</sub> content of the Pillan plume could be explained by the amount of SO<sub>2</sub> frost present at Pillan before an eruption, suggesting that, unlike Pele, the erupting material does not contain much SO<sub>2</sub>.

## 2.2 Atmosphere Observations

Voyager observations show that Io's atmosphere consists mostly of SO<sub>2</sub> (Pearl et al., 1979), the ultimate source of which is thought to be the volcanic plumes. However, much of Io's surface is coated with SO<sub>2</sub> frost (Fanale et al., 1979; Smythe et al., 1979), which sublimates in sunlight and could produce an atmosphere by itself. Differences in day/night surface temperatures cause the condensation of SO<sub>2</sub> gas on the night-side surface and lead to a much thinner atmosphere there. Io is tidally locked, and the sub-Jovian side periodically enters eclipse, possibly leading to a similar collapse, and resulting in the sub-Jovian hemisphere receiving less total solar energy than the anti-Jovian hemisphere over the course of a day. Surface sputtering from ion impacts can also free gas from the surface, but only until the atmosphere becomes thick enough to prevent further impacts (sputtering is reviewed in Cheng and Johnson, 1989).

It is not clear to what extent Io's atmosphere is supported by sublimation or to what extent the polar and night-side atmosphere is dominated by sputtering, and there is evidence supporting both sublimation-driven and plume-driven models. Some early observations (some are reviewed in Cruikshank and Murphy, 1973) found post-

eclipse brightening, thought to be due to the condensation of the atmosphere into high-albedo frost during eclipse. However, more recent observations have tended not to find post-eclipse brightening (many are reviewed in Bellucci et al., 2004, although those authors did see post-eclipse brightening in the infrared).

Other studies have sought to determine the distribution of Io's atmosphere over its surface. For example, Lellouch et al. (1992) used millimeter-wave observations of  $\text{SO}_2$  to argue that Io's atmosphere was very hot (500 – 600 K at 40 km) and localized, with  $10^{17} - 10^{18} \text{ m}^{-3}$  number densities over only 5–20% of the surface. But Ballester et al. (1990) viewed Io in the near-ultraviolet and argued for a much cooler ( $\sim 105$  K) and more uniform atmosphere at similar densities, although they did see small regions with an order of magnitude more  $\text{SO}_2$ . Trafton et al. (1996) made a similar observation and found disk-averaged column densities of  $5 \times 10^{19} \text{ m}^{-2}$  over Io's leading hemisphere and  $7 \times 10^{19} \text{ m}^{-2}$  over Io's trailing hemisphere, which is interesting because the  $\text{SO}_2$  frost is concentrated on the trailing hemisphere. Jessup et al. (2004) performed a spatially-resolved observation of the anti-Jovian hemisphere using Hubble's STIS and reported a sublimation-like atmosphere with a column density of  $1.25 \times 10^{21} \text{ m}^{-2}$  on the equator, which was enhanced over the Prometheus plume. Between  $30^\circ$  south and  $30^\circ$  north latitude, they saw an atmosphere which appeared to be in vapor pressure equilibrium with surface frost that cools with distance from the subsolar point. Feaga et al. (2009) used the same instrument to observe Lyman-alpha and found a fairly uniform atmosphere (at low latitudes) which changed little over five years, denser on the anti-Jovian hemisphere by a factor of 2 – 3 (column density of  $5 \times 10^{20} \text{ m}^{-2}$  at the anti-Jovian point). Spencer et al. (2005) observed Io in the infrared and obtained an anti-Jovian column density of  $1.5 \times 10^{21} \text{ m}^{-2}$  and a sub-Jovian column density of  $1.5 \times 10^{20} \text{ m}^{-2}$ , found temperatures between 150 and 200 K, and do not see a decrease

in density as Jupiter moved away from the Sun over three (Earth) years.

Continuing to observe Io over the course of almost a whole Jupiter year, seasonal variations in Io's atmosphere were seen (Tsang et al. 2012), strongly suggesting that the atmosphere depends on insolation. Tsang et al. find that sub-solar SO<sub>2</sub> column density on the anti-Jovian hemisphere varies from  $0.61 \times 10^{21} \text{ m}^{-2}$  to  $1.51 \times 10^{21} \text{ m}^{-2}$  as Jupiter and Io move closer to the Sun. Some exceptions to the majority of recent observations that seem to show a broad, asymmetric, and insolation-dependent atmosphere are the observations of Tsang et al. (2015) of Io emerging from eclipse; they saw little change in atmospheric SO<sub>2</sub> from almost immediately after re-emergence, suggesting that there was never a collapse of the atmosphere into the surface during eclipse. Importantly, this observation was of infrared emission from SO<sub>2</sub> in the atmosphere directly, whereas other studies that have concluded that collapse does occur were based on emission associated with other species produced by plasma interaction with SO<sub>2</sub> or by photo-dissociation of SO<sub>2</sub> (e.g. Saur and Strobel, 2004). Jessup and Spencer (2015) used HST/STIS to observe several longitudes at different times during Io's day and found almost no time-of-day dependence of Io's atmosphere. The models used by Tsang et al. (2015) and Jessup and Spencer (2015) yield best-fit thermal inertias for Io's surface frost which are high compared to some other estimates ( $> 300 \text{ Wm}^{-2}\text{s}^{-1/2}\text{K}^{-1}$  for the first and  $> 2000 \text{ Wm}^{-2}\text{s}^{-1/2}\text{K}^{-1}$  for the second), assuming that the atmosphere is in vapor pressure equilibrium with the frost at the surface and that the column density is proportional to the surface pressure.

## 2.3 Plasma Observations

Jupiter's extremely strong magnetic field and Io's volcanism give rise to a large plasma torus, which Io orbits through and supplies. Io is constantly bombarded by the energetic ions (mostly  $O^+$  and  $S^+$ ) and electrons which comprise the torus. The plasma overtakes Io in its orbit at a relative velocity of about 57 km/s, and these high-speed particles heat and ionize Io's atmosphere and can cause sputtering from the surface. Io's interaction with the plasma torus is asymmetric in two respects: (1) Jupiter's magnetic field is  $10^\circ$  off the plane of Io's orbit and (2) being tidally locked, Io always presents the same side ( $\pm 10^\circ$  latitude) to the oncoming plasma (which moves with Jupiter's rotating magnetosphere). For a detailed review of Io's interaction with Jupiter's plasma torus, see Saur et al. (2004 book).

Before probes examined the system, Bigg (1964) determined that Io influenced the strength of Jupiter's decametric radio emission. Later radio occultation measurements by Pioneer 10 detected an ionosphere around Io with a peak dayside electron number density of about  $6 \times 10^{10} \text{ m}^{-3}$  at 100 km altitude (Kliore et al., 1975). Voyager 1 and 2 flybys discovered the cold, co-rotating plasma torus itself (see e.g. Bridge et al., 1979), where ion densities increase by six orders of magnitude between  $\sim 47$  and  $\sim 5$  Jupiter radii. Galileo probed Io's interaction with the plasma over the course of seven close flybys with a closest approach of 200 km. Io was found to significantly disturb the plasma torus and Jupiter's magnetic field within Io's ionosphere. The plasma becomes much denser and slows almost to a halt in Io's wake and on its flanks, although farther away from Io's flanks the plasma velocity is nearly double that of ions in the undisturbed torus (Frank et al., 1996).

## 2.4 Simulation and Modeling

### 2.4.1 Atmosphere Simulations

Early modeling of Io's atmosphere was performed by Ingersoll et al. (1985) and Moreno et al. (1991). Ingersoll et al. solved vertically-integrated conservation equations to produce a one-dimensional model of Io's atmosphere as a function of distance from the sub-solar point. Surface frost temperature varies with insolation, and the frost emits and absorbs  $SO_2$ . The pressure gradient produced by the surface temperature gradient drives supersonic flow away from the subsolar point. Frost within about  $35^\circ$  of the subsolar point is a net producer of  $SO_2$ , but farther away the flow of  $SO_2$  away from the subsolar point produces pressures above vapor pressure equilibrium and so the surface becomes a net sink. Moreno et al. performed two-dimensional axisymmetric simulations and obtained similar results. Both used equations appropriate for continuum flow rather than the extremely rarefied flow high in Io's atmosphere or on its night-side, and neither included the effect of plasma or various other physics (although Moreno et al. implemented a crude model for radiative heat exchange between the atmosphere and the surface).

Direct simulation Monte Carlo (DSMC) modeling of Io's rarefied atmosphere and plumes began with Austin and Goldstein (1996), who examined the shocks in volcanic plumes and the effect of background non-condensibles (also considered by Moreno et al., 1991) using an early version of the code used in this work. Austin and Goldstein (2000) applied this model to the case of supersonic flow away from the subsolar point and argued that rarefaction effects are significant except very near the subsolar point. They also attempted to model plasma bombardment as an energy flux to particles (divided among translational and rotational modes) and found that

plasma heating dramatically inflates the atmosphere. This agreed with the work of Wong and Johnson (1995), who performed simulations like those of Moreno et al. (1991) with the addition of plasma heating. In this and Wong and Johnson (1996), the authors found that plasma heating enhances column density and controls the temperature at the exobase.

DSMC simulations of Io’s atmosphere continued to improve with the work of Moore et al. (2009), who simulated a one-dimensional atmosphere through eclipse, finding that the presence of even small amounts of non-condensable species such as O<sub>2</sub> or SO could significantly impede the collapse of the SO<sub>2</sub> atmosphere into the surface frost. Walker et al. (2010) performed three-dimensional simulations of Io’s rarefied atmosphere incorporating the frost map of Douté et al. (2001) and a rotating surface temperature distribution. As with earlier simulations they see supersonic flow away from the subsolar point, and they achieve the best match to observations such as the column densities from Feaga et al. (2009) with a high frost thermal inertia that causes the peak frost temperature to lag the subsolar point by  $\sim 32^\circ$ . However, they did not see the fall-off in column density beyond  $45^\circ$  latitude, and suggest that this may be due to plasma impacting the surface at high latitudes where the atmosphere is thin. Walker et al. (2012) add a surface temperature model that solves the one-dimensional heat conduction equation in depth, include the effects of eclipse, and fit thermophysical parameters for Io’s surface, finding a best-fit frost albedo of 0.55 and a frost thermal inertia of  $200 \text{ Wm}^{-2}\text{s}^{-1/2}\text{K}^{-1}$ . These parameters were then used to find an albedo of 0.49 and thermal inertia of  $20 \text{ Wm}^{-2}\text{s}^{-1/2}\text{K}^{-1}$  for the “non-frost” surface. A particle-based plasma model was also developed for the UT group’s DSMC code (Moore, 2011; Walker, 2012; and Moore et al., 2012), although some errors in implementation make the modeling results questionable.

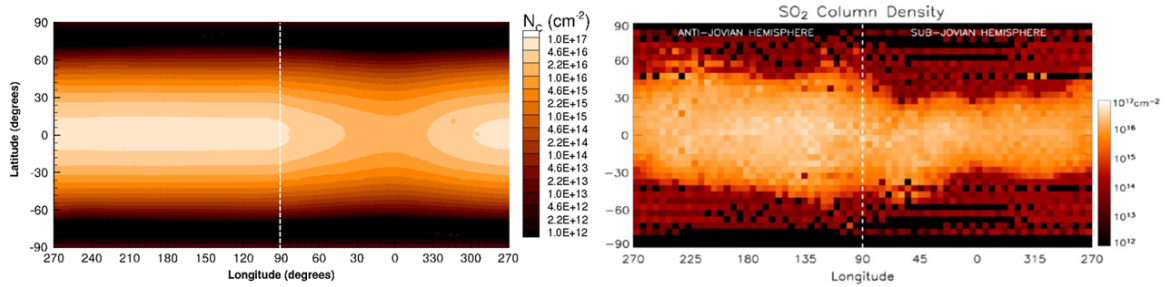


Fig. 2.2: (left) Simulated (Walker et al., 2012) and (right) observationally inferred (Feaga et al., 2009) “average dayside”  $\text{SO}_2$  column densities. Note the anti-Jovian hemisphere has the higher average column density. In the simulation this was largely due to eclipse.

More sophisticated continuum simulations of the Io/plasma interaction were performed by Smyth and Wong (2000, 2004), which improved the earlier Wong and Johnson model by introducing photochemistry and electron chemistry (in 2004) and by allowing ions to reaccelerate to the torus’ co-rotational velocity between collisions. They found that the exobase altitude could be as high as 465 km and as hot as 2800 K. Ions impinging on the dayside atmosphere heat it, inflate it, and increase total column density (although momentum transfer from the plasma is neglected). Electron chemistry greatly enhances the abundance of O, SO, S, and  $\text{O}_2$  at high altitudes relative to  $\text{SO}_2$ .

#### 2.4.2 Effect of Io on the Plasma Torus

Other work has attempted to determine or reproduce Io’s effect on the plasma torus, typically simulating the interaction between a fixed Io (perhaps with atmosphere) and the incoming plasma. Linker et al. (1988, 1991, 1998) treated Io as either a conducting or magnetized sphere surrounded by a large, diffuse neutral cloud and solve the magnetohydrodynamic (MHD) equations for the plasma flowing past

it. The 1998 work can explain many features of Galileo observations such as the high plasma density around Io and the depression in the magnetic field in Io’s wake. However, the authors could not explain the “double dip” in the magnetic field strength as the plasma moved past Io. Further they find that either model of Io (conducting or magnetized) can explain why Io disturbs the magnetic field as if it is larger than its actual diameter, as this could be due either to magnetization or to a conducting atmosphere. However, while this was a controversial issue for some time, note that a later Galileo observation is thought to have clearly shown Io to lack a strong magnetic field (Kivelson et al., 2001). Combi et al. (1998) performed similar MHD simulations and produced broadly similar results. Their model was improved in Kabin et al. (2001) which included day/night asymmetry and which was able to produce a “double dip” in the field (albeit somewhat misaligned). Lipatov and Combi (2006) model the ions as particles while still using the MHD equations for electrons, and they fit atmospheric parameters to reproduce the double peak in the magnetic field seen by Galileo.

Saur et al. (1999) take a different approach to modeling the Io/plasma interaction. They assume a fixed, unperturbed Jovian magnetic field and a spherically symmetric Ionian atmosphere and compute the electric field around Io as well as density, velocity, and temperature for electrons and one ion species. They find that electron impact ionization of an  $SO_2$  atmosphere with a scale height of 100 km and a column density of  $6 \times 10^{20} \text{ m}^{-2}$  best fits observations of the plasma. They also find that the Hall effect twists the electric field at Io substantially, producing large asymmetries in the electron flow past Io. Saur et al. (2000, 2002) continued to improve this model and eventually could use it to explain Galileo observations such as the double peak.



### 2.4.3 Plume Simulations

After Austin and Goldstein (2000), Zhang et al. (2003, 2004) performed axisymmetric simulations of Prometheus and Pele using the UT group’s DSMC code. They constrained vent conditions by canopy heights, ring radii, and UV brightness data from Voyager data via Strom and Schneider (1982). They were able to demonstrate canopy shock formation, “bounces” of the falling gas leading to a multiple ring structure when a sublimation atmosphere is present, and the importance of non-LTE rotational cooling. Their simulations demonstrate a symmetric circular source giving rise to a symmetric plume, and show how the gas expands upwards until it reaches an umbrella-shaped canopy shock. This canopy shock forms during start-up when plume material falling back to the ground under the influence of gravity meets rising gas, and gas in the canopy falls away to the sides of the plume in a ring.

Relatively little work has been done on the interaction between the plumes and the atmosphere. Many authors, in interpreting observations of Io’s atmosphere like those mentioned above, understand the plumes to cause local increases in density, often with no explicit model. Explicit models are often very simple, as in Tsang et al. (2012) where a constant volcanic component was added to a time-varying “sublimation component” (in vapor pressure equilibrium with the surface frost) to fit to column density observations. Similarly, Walker (2012) and Moore et al. (2010) super-imposed separately-computed volcanic plumes on their simulations of Io’s atmosphere, although Walker et al. (2011) did simulate flow over a hot spot at Loki (the surface did not emit material, however). Ingersoll (1989) worked out a simple model for the plume/atmosphere interaction where plumes were treated as sources of constant mass flux. Because frost on the surface attempts to maintain vapor pressure

equilibrium, Ingersoll finds that a volcanic source increases surface pressure not by a constant amount but by an amount proportional to surface temperature and inversely proportional to the sticking coefficient (where there is frost and a significant sublimation atmosphere). Moreno et al. (1991) also simulated plumes using the same model used for their atmospheric simulations discussed above. Using their continuum model, they found that even a cold (100 K) night-side plume could produce an atmosphere extending hundreds of kilometers from the plume source, but this is contradicted by the findings from Zhang et al.'s rarefied model.

## Chapter 3

### Method

#### 3.1 Overview

In this work, the motion of and collisions between particles around Io are computed using an enhanced version of the direct simulation Monte Carlo (DSMC) method (Bird, 1994). This is necessary because the flows of interest range from continuum or nearly-continuum to free-molecular. High-density gas emerges from narrow cracks in a lava lake at a plume’s source, but then expands upwards for hundreds of kilometers. Along the way collisions all but cease. Eventually the gas reaches an umbrella-shaped canopy shock (which formed initially when falling gas met rising gas) and slows to a halt, creating a thin, dense, and collisional canopy supported by the rising gas. In the absence of an atmosphere or plasma, gas in the canopy slides around the sides of the plume, eventually reaching the ground. Any sublimation-supported atmosphere falls off hydrostatically with altitude (at low altitudes), but is very collisional near the surface for peak daytime frost temperatures ( $\sim 120$  K) at low latitudes. The atmosphere fades away to almost nothing at the altitude of Pele’s canopy (the canopy is at  $\sim 350$  km and the day-side atmospheric scale height is at most about 10 km), so falling plume gas encounters a huge range of atmospheric densities.

I used and improved an existing DSMC code which had already been modified substantially from Bird’s original implementation (Zhang et al., 2003; Stewart et al.,

2009; Moore et al., 2009, 2011, 2012; Morris et al., 2012; Walker et al., 2010, 2011, 2012). For the night-side Pele plume (Chapters 4 and 5), the code I used most directly descends from Ju Zhang’s work performing single-processor axisymmetric simulations of SO<sub>2</sub> and grains in the Prometheus and Pele plumes. The code was subsequently made 3-D and parallel by Benedicte Stewart as part of her work simulating comet impacts on the Moon. Aaron Morris implemented a superior method for computing the coupled motion of dust grains in the gas flow from Burt and Boyd (2004). Chris Moore implemented a vacuum buffer cell, which adds a large, collision-less cell to the top of the simulation domain (allowing cheaper free-molecular simulation of high-altitude particles). For the interaction between the plumes and the plasma torus (Chapter 6), I made use of a particle description of the plasma as ions which move along pre-computed field lines (field lines from Combi et al., 1998) implemented by Chris Moore. The model for chemical reactions between ions and neutrals was implemented by Chris Moore and Andrew Walker, later updated by William Hoey, using MDQCT data from Parsons et al. (2012). For the simulations which include a sublimation atmosphere (Chapter 7), I relied on a photo-chemistry model from Benedicte Stewart and Chris Moore and many of Andrew Walker’s improvements and methods; see his work for a comprehensive explanation of how the UT DSMC code can model Io’s sublimation atmosphere. Chris Moore also developed a method for adapting the vertical grid structure to the gas flow, which I modified substantially for my own simulations involving a sublimation atmosphere.

In the rest of this chapter, I briefly describe the DSMC method, I explain the basic strategy used to simulate plumes, I detail many of my own improvements to the code, and I give the model used for comparing simulated dust deposition to observations (for Chapter 5 simulations). This chapter is split into two sections.

The first covers methods for the simulation of plumes alone, with no sublimation atmosphere or plasma (for Chapters 4 and 5). After developing this model for Pele by itself, I linked it to the previously-developed plasma, atmosphere, and chemistry models. The second section explains how plumes are initially simulated alone before being patched on to the planet and describes modifications I made to Chris Moore’s adaptive vertical grid and to the simulation of the plasma, as well as a useful method for visualizing complex flows.

### **3.1.1 Direct Simulation Monte Carlo Method**

All simulations in the present work were performed using a direct simulation Monte Carlo method (Bird, 1994). DSMC is a stochastic, particle-based method suitable for rarefied flows where collisions between gas molecules are still important. Degree of rarefaction can be gauged by the Knudsen number, which is the ratio of the mean free path of the gas to a length scale. For very small Knudsen numbers a continuum method is often suitable, while for very large Knudsen numbers the flow is free-molecular and computing collisions between individual particles is unnecessary. Mean free paths on Io can range from less than a meter near plume sources to meters at low altitudes in the dayside atmosphere to tens or even hundreds of kilometers below plume canopies and at high altitudes (at sufficiently high altitudes the gas is free-molecular and the mean free path goes to infinity). Some length scales relevant to flows on Io are vent diameters (potentially sub-meter), the diameter of lava lakes (tens of meters to kilometers), the atmospheric scale height (kilometers), and the height of plumes (tens to hundreds of kilometers). In many cases the mean free path and the relevant physical length scale will be of the same order such that collisions are important but the flow is too rarefied to simulate with a continuum method.

DSMC methods simulate rarefied flows by computing the motion of representative particles, where each computational molecule represents a very large number (around  $10^{20}$  in many of the simulations here) of real particles. These particles are moved as if real, and collide with other nearby particles (those in the same cell) at random, with the likelihood of a collision based on the relative velocity of the particles and the local number density. The results of collisions are also random, but conserve momentum and energy. On average and with a sufficient number of simulated particles, the DSMC solution is physically accurate for rarefied and continuum flows, although for dense flows the method becomes computationally expensive. DSMC is well-suited to large, parallel simulations because the particle interactions are local, and Io’s low densities and DSMC’s ready parallelism allow the physically accurate simulation of planet-scale flows.

## **3.2 Computational Method for Plume-only Simulations**

### **3.2.1 Source and Staging through Multiple Domains**

The night-side Pele plume is modeled as a jet of  $\text{SO}_2$  expanding into a vacuum from a defined source geometry (termed the “virtual vent”) on the surface of a sphere. The background atmosphere is taken to be negligible due to cold night-side surface temperatures. The gas density, temperature, and velocity are taken to be uniform across the entire vent. The total mass flux is taken directly from Zhang et al. (2003), and is fixed by choosing a vent density based on the area of the simulated virtual vent. The gas temperature and velocity are chosen so as to provide a good match to the observed average deposition ring radius and canopy height, and are generally consistent with the conditions found to be suitable by Zhang et al. (2003). Notably, the flow enters the simulation domain at about Mach 3; continuum flow near the

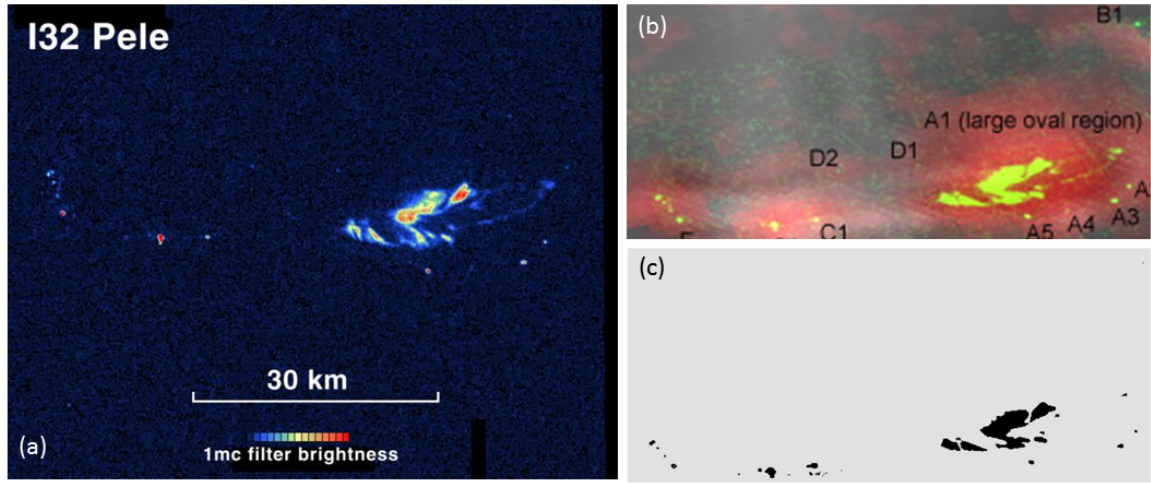


Fig. 3.1: (a) Galileo SSI image of Pele’s caldera. (b) Processed composite image from Voyager in-sunlight clear-filter observation, Galileo I32 thermal observation in red, and SSI image from (a) in green, from Howell and Lopes (2011). (c) The vent geometry used for the DSMC simulations, obtained by taking all regions of (b) with a grayscale pixel value  $>200$  out of 255 (image processed with built-in Matlab functions).

surface of the lava lake is not included in the giant plume simulations (near-surface flow is discussed in Section 4.2). This supersonic, uniform “virtual vent” region is discussed by Zhang et al. (2003) and is intended to reduce the computational expense of simulations by assuming isentropic expansion from some true vent conditions over a small distance, as if the flow is expanding in a quasi-1D fashion in a diverging nozzle. The flow can also be uniformly seeded with spherical dust grains drawn from a chosen size distribution as described in Section 5.2.

The particular geometry used as the source of the plume for the DSMC simulation is drawn from Howell and Lopes 2011 (Fig. 3.1). Matlab was used to convert the  $\sim 80$  m resolution color image to grayscale, and  $\sim 2700$  bright pixels above a cutoff brightness were taken as the source. Uniform-property  $\text{SO}_2$  flow (850 m/s, 500 K,

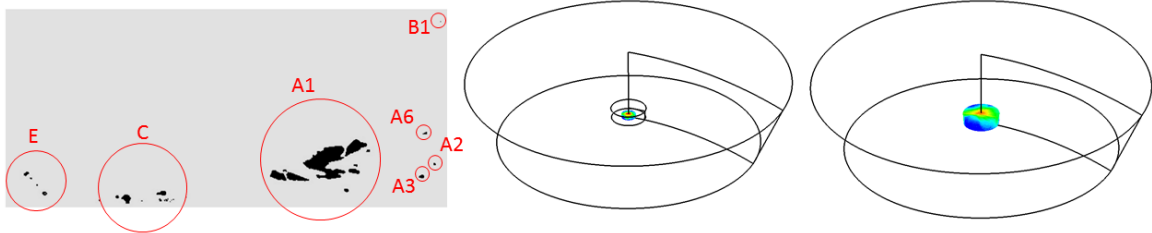


Fig. 3.2: (left) DSMC virtual vent with seven independent source regions circled and labeled following the convention in Howell and Lopes (2011), although note that my Source A1 includes the area where Howell and Lopes identify two more regions A4 and A5, and I identify a new area A6. Sources E, C, and A1 are simulated in 3D, with 40 m resolution of the source geometry. Sources A2, A3, A6, and B1 are treated as small axisymmetric plumes with source radii of 200 m. The center and right images show the full 1600 km diameter far-field domain in wire frame, curving over the surface of Io. In the center image the first domain (up to 20 km altitude) integrating all seven source regions is visible within a wire frame of the second domain. In the right image the second domain (up to 60 km altitude) is visible.

$6.426 \times 10^{-7} \text{ kg/m}^3$ ) is assumed for simplicity. This is reasonable to the extent that the actual plume emits from uniform-property lava by way of small holes or fissures which are approximately uniformly distributed across the simulated area (see section 4.2).

Inflow is created from a collection of uniform-property subsurface buffer cells (Stewart et al., 2009). At each time-step, gas molecules are created in each subsurface cell according to a Maxwellian velocity distribution and are allowed to move freely. Dust particles are also created in the subsurface cells and are given initial velocities from a prescribed distribution (see Section 5.2). Those gas molecules and dust particles that escape the subsurface cells into the computational domain are preserved for later time steps, and those remaining behind are removed from the calculation. Molecules exiting the top or sides of a domain are removed from the simulation and



recorded for use in outer domains (I record outflow over many time steps and then sample from this distribution of fluxing molecules to create inflow in the subsequent domain). The outermost domain features a large buffer cell extending to a very high altitude where collisions are not simulated. This enables cheap simulation of free-molecular high-altitude flow early in simulations before the canopy shock forms. Molecules in the outermost domain that hit the surface of Io are assumed to stick; they are removed from the simulation and recorded as deposition.

The near-vent flow simulation is computationally intensive, but since the inflow boundary condition is steady at the vent, the near-vent regions will also become steady (in the time-explicit approach used here) much earlier than flow farther away. Because the gas is expanding supersonically into a vacuum, flow down-stream (higher in altitude) does not influence flow upstream (closer to the vent), and the plume simulation can be split into multiple stages where inner regions are one-way coupled with outer regions. This allows simulation of the expensive inner regions to be halted while the outer regions are still developing. The DSMC source pictured in Fig. 3.1c is separated into seven distinct regions (Fig. 3.2a), each of which is simulated independently for the first 1-2 km above the surface using 64 processors each for the three large regions on the left (Sources E, C, and A1) and one processor each for the four small circular regions on the right edge (A2, A3, A6, and B1). After this, the flow is simulated using  $\sim 1000$  processors in three stages; one stage from 2 to 20 km altitude, one from 20 to 60 km, and a final stage for the rest of the plume. Time step size, grid resolution, and particle weights are adjusted across domains so as to resolve the high-density flow near the vent while simulating the entire span of altitudes efficiently.

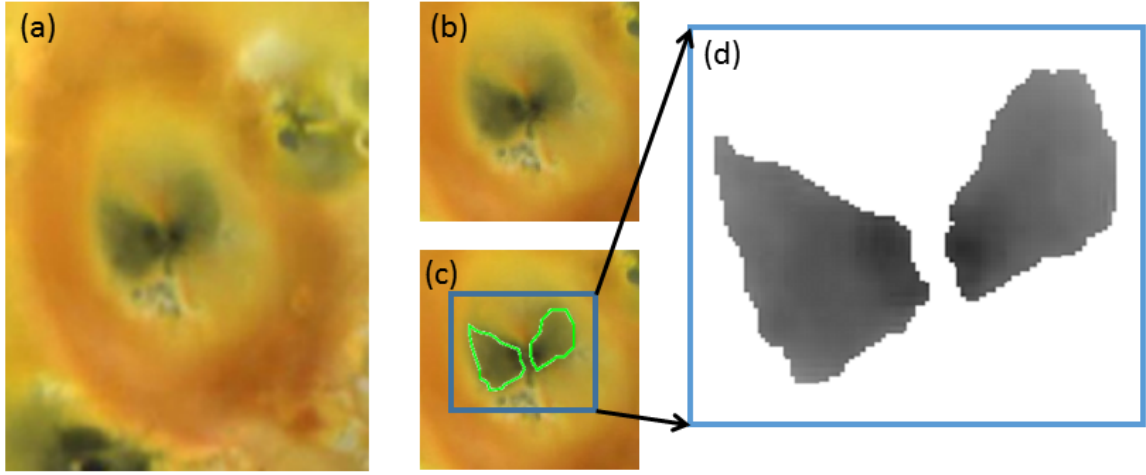


Fig. 3.3: (a) Galileo image of Pele’s multicolored deposition pattern on Io’s surface. (b) A region around the plume source where I believe coloration of the surface is strongly influenced by plume activity and from which target regions for comparison will be chosen. (c) The primary target region used to compare dust deposition to simulations is colored black. (d) Close-up of the grayscale surface inside the two fans of the target only; I fit my dust deposition model to each of the 3,194 gray pixels shown.

### 3.2.2 Gas and Dust Deposition Comparisons

Several kinds of output can be obtained from the plume simulations. In particular, simulated deposition patterns of gas and dust can be directly compared to Galileo observations. However, performing this comparison presents several challenges. As will be shown,  $\text{SO}_2$  gas in the simulated plume falls to the surface in a ring that closely resembles the large red ring observed at Pele. For the real plume, the ring is likely produced by species such as  $\text{S}_3$  or  $\text{S}_4$ , and the plume flow near the surface and far from the vent can be influenced by the presence of a sublimation atmosphere during the day (Zhang et al., 2003) or by interaction with plasma in the canopy. The actual red coloration of the surface is likely to be a complex function of the relative concentrations of different materials falling to the surface, the tendency

of each material to undergo chemical reactions while on the surface, and the optical properties of the resulting composite surface. Here, I only say that the long time scale of observed changes to Io's surface due to Pele – Geissler (2004) describes Pillan being covered over by Pele over the course of many months – indicates that the surface is not changing drastically over the course of a single day/night cycle. I further suggest that the effect of Pele on Io's surface is dominated by the night-side plume, which is not mediated by a sublimation atmosphere, which Zhang et al. (2003) showed can cause a gas-dynamic bounce and a much more diffuse primary ring. Then, if the red coloring is the result of other species (short-chain sulfur in the gas at the vent or  $S_2$  which reacts after depositing on the surface, for example) that track the gas flow, the mass flux of  $SO_2$  into the surface on the night-side can be taken to be a reasonable proxy for the redness of the surface in observations. This suggestion is supported by the remarkable qualitative similarity between the simulated gas ring and the observed red ring (shown later in Fig. 4.10).

The black fans to either side of Pele's vent (Fig. 3.3) are likely the result of a similarly complicated process. When Pillan erupted atop Pele's ring, a large amount of black silicate ash (Geissler et al., 1999) was laid down rapidly, which was then slowly covered by Pele over months. Pele's own black deposits do not appear to be associated with short eruption events; the black fans appear nearly constant in intensity relative to the large ring, despite the fact that there is surely other material (overlying the black ash) depositing in the same locations, even if not as much as at Pillan, which lies on Pele's red deposition ring. Simulations attempting to match Voyager observations of plume column density suggested the instantaneous presence of small numbers of particles of up to  $10\mu m$  in the flow (Zhang et al., 2004), and Hubble plume observations over long time periods lead to fairly uniform estimates of

mean particle sizes (Jessup and Spencer, 2012). For these reasons I treat the dust flow and eruption from Pele as a steady process.

Relatively small amounts of simulated plume gas are seen to hit the surface inside the large red ring (both in the present results and in Zhang et al., 2003), especially to the east and west of the vent (Fig. 4.10), and the rate at which existing deposits are overlaid by other (non-plume) material is assumed constant. I assume that only the (daytime) sublimation atmosphere acts to resurface the ground inside the ring, and that it coats the ground uniformly because there is very little plume gas above the surface in the regions of interest (see Chapter 7 for simulations of this interaction). This allows us to take the coloration of the surface in those regions to be a function only of the number and size of dust particles that strike the surface per unit time. A higher rate of particle deposition will darken the surface more because more dust will be present per unit depth in the surface frost deposited by the sublimation atmosphere, which is assumed to build up at a constant rate (over months, though there are day/night variations). Likewise, larger particles will darken the surface more than smaller particles on a per-particle basis because of their larger cross-sections. I assume a sparse coating of dust on the surface (so that depositing dust overlays only frost and not preexisting dust deposition) and that the surface darkness is proportional to the sum of the cross-sections of all dust particles that strike the surface per unit time. These assumptions are undoubtedly oversimplifications, but they enable us to determine dust size distributions that reproduce the observed deposition pattern and which are consistent with Zhang et al.'s results.

The particular Galileo observation chosen for the comparison is shown in Fig. 3.3a. Distortion due to the position of the spacecraft is ignored. I identify by hand

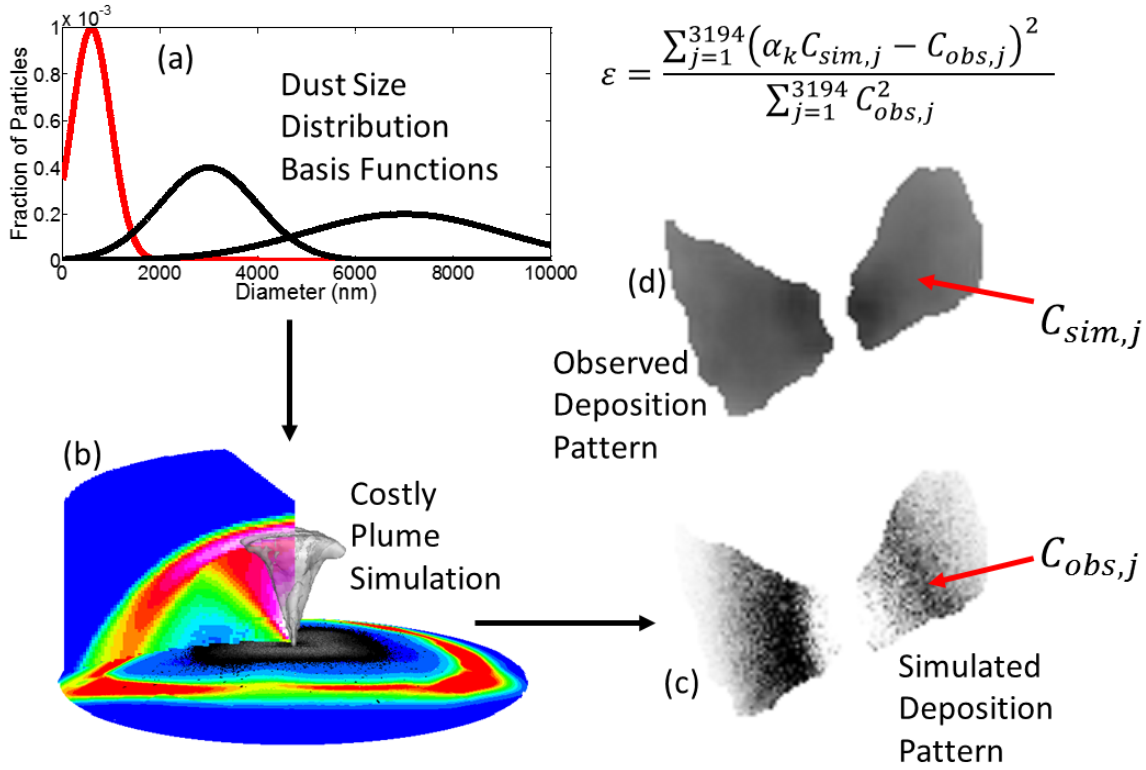


Fig. 3.4: (a) Sample overlapping basis functions which might be used to try to construct a best-fit size distribution are fed (b) one-by-one into the large plume simulation which yields (c) a simulated deposition pattern corresponding to each (the pattern shown corresponds to the red basis function in (a)). I then seek to find a fitting coefficient  $\alpha_k$  for this  $k$ th basis function which minimizes the sum-of-squares error on a pixel-by-pixel (for all  $j$ ) basis between the simulated pattern and the observed pattern (d).

regions of the deposition pattern that I feel provide the best basis for comparison (Fig. 3.3c). The regions of interest are the dark black fans to either side of the vent, away from the faint orange sprays to the north and south (which may overlay some dust). In these dark butterfly wing regions I suggest that the dust dominates the plume deposition (and it will be seen that gas deposition reaches a minimum while dust deposition reaches a maximum in these regions). Matlab is used to convert

the image to grayscale (0-255), and the surface darkness is measured as 255 minus the brightness of each of the pixels. Only the 3,194 pixels in the specified regions have these darkness values extracted and compared to the simulated deposition. The center of the observed image is excluded because surface coloration here is likely to be strongly influenced by unsimulated processes, such as the spewing of large slow particles or liquid lava with unpredictable velocities.

Simulated dust deposition data can be collected as described above for some hypothesized dust particle size distribution and I can determine how much of the observed deposition can be explained by that hypothesized distribution by following the process illustrated in Fig. 3.4. The center of the simulation is lined up with the center of the observation, and the simulation is rotated by about five degrees about its central axis to obtain a qualitatively better match of the gas rings by partially correcting for the perspective of the observation (but see the head-on comparison later in Fig. 4.10 where no rotation is needed). The simulated data (at a resolution of 0.3 km per pixel near the center of the domain to 3 km per pixel along the outer edges) are interpolated on to a grid of the same resolution as the observation (about 4 km per pixel) and pixels corresponding to the specified “butterfly wing” region (Fig. 3.3c, or a similarly-defined region) are extracted. These two vectors of data should be proportional to each other (i.e. one pixel in the simulation should be twice as dark as another pixel in the simulation if and only if the corresponding pixels in the observation also differ by a factor of two) if the simulation is accurate and if the model used to transform deposition densities and sizes to color is correct. Error in the model and Monte Carlo noise (clearly visible in Fig. 3.4c) prevent the two vectors from being exactly proportional, but I can perform a least-squares fit to find a best-fit proportionality constant  $\alpha_k$  which minimizes the sum-of-squares error. The simulated

size distribution of dust particles is deemed to correspond well with observation to the extent that the least squares residual is small (i.e. to the extent that the simulated data really are proportional to the observed data). However, it is infeasible to guess at an appropriate size distribution, simulate its deposition pattern, and check whether it can explain the observed deposition. I need a method that allows me to home in on a best-fit size distribution from a relatively small number of simulations. Because my model of simulated deposition implies that the deposition pattern of the sum of several sets of dust particles is just the sum of their individual deposition patterns, I can produce a best-fit size distribution from a linear combination of basis functions that are simulated separately.

We desire a best-fit dust size distribution that minimizes the error in the simulated dust deposition, calculated in a sum-of-squares sense by taking the absolute value of the pixel-by-pixel difference between the grayscale brightness of the observation and the model brightness of the simulated deposition pattern (Fig. 3.4). Ideally I would use a large number of delta functions for individual basis function distributions which would span the range of interesting grain sizes, but for a given signal-to-noise ratio the computational cost scales with the number of distributions to be simulated. Therefore I simulate a small number (9-15) of size distributions that span the size range between 20 nm and 10  $\mu\text{m}$ , where the upper limit is consistent with Zhang et al.'s (2004) findings that 10  $\mu\text{m}$  dust can explain features seen in Voyager column density observations. These dust size distribution basis functions are simulated separately, and the resulting deposition patterns are simultaneously least-squares fit to the target data, yielding a vector of fitting coefficients (one for each basis function). These coefficients are then applied to the basis functions to obtain a best-fit size distribution. The form of the basis functions, as well as their particular means, variances,

etc., are somewhat arbitrary, and this is further complicated by the non-orthogonality of these basis functions. (Even though one can choose non-overlapping basis functions in particle diameter space, the resulting deposition patterns overlap, and I am fitting using the computed deposition patterns.) I performed simulations for several choices of basis function sets and found that all produce similar results (see Section 5.5).

### 3.2.3 Time Integration of Dust Motion

Burt and Boyd (2004) describe a method for updating the velocities of dust particles on every time step. Their method was modified to increase the accuracy of time integration using a technique like the source term linearization described by Patankar (1980). Burt and Boyd compute the instantaneous drag on a dust particle as the sum of independent contributions from every gas molecule in the same DSMC cell. Unlike gas-gas collisions, this is entirely deterministic - the computed drag is just the expected value of the drag on the dust particle that would be obtained from doing a large number of stochastic collisions (statistical noise is not a desirable feature of this drag calculation because the dust particles are large and collide with gas molecules many times over a time step appropriate for gas-gas collisions). If gas that collides with the dust specularly reflects, the instantaneous drag force contributed by a simulated gas molecule is just proportional to the square of the magnitude of the relative velocity vector between the dust particle and the gas molecule (see Eqn 3.1).

An instantaneous drag force alone is not enough to move a dust particle appropriately in a discrete-time simulation. A time integration scheme is needed. Burt and Boyd simply apply the computed instantaneous drag force to a dust particle as if the particle experiences that drag force for the entire time step - they get a  $\Delta v$  by multiplying the computed drag by the time step size. This approach has a few



problems, especially for large time step sizes. First, for steady gas flow and in the absence of other forces, it overestimates the drag on dust. The effect of drag on dust is to bring it to a velocity where it experiences less drag; particles should experience less drag at the end of a time step than at the beginning. Second, there is always some dust velocity for which the method is unstable. The change in a particle's velocity is proportional to the square of the relative velocity, so for a sufficiently large relative velocity (depending on the time step size) the particle will overshoot the gas velocity, and for an even larger relative velocity the particle's new velocity will be even more extreme than its initial one (and its velocity will blow up over multiple iterations). This problem gets worse when other forces are added in. The equilibrium velocity of dust in a gravity field will be a terminal velocity, where drag balances gravity, rather than the gas velocity, as in Earth's atmosphere where a falling object will eventually stop accelerating when the upwards drag force exerted by the stationary atmosphere balances gravity accelerating the object downwards. This equilibrium terminal velocity will not be the same as the gas velocity, and so there will be some non-zero equilibrium relative velocity between the bulk gas and the dust. At such a non-zero equilibrium relative velocity, perturbations from the equilibrium velocity cause very large changes in the drag force because the drag force is roughly proportional to the square of the relative velocity. For an equilibrium relative velocity of 0 (arbitrary units), which would obtain for a system where drag is the only force acting on dust, a perturbation of 1 increases the drag force by an amount proportional to 1. For an equilibrium relative velocity of 100, however, a perturbation of 1 increases the drag force by an amount proportional to 201 ( $101^2 - 100^2$ ). For several of the simulations in the present work the dust reaches a terminal velocity which is hundreds of meters per second different from the gas velocity, and particles moving through a complex

gas flow can suddenly find themselves with large non-equilibrium relative velocities, so a much more accurate method is needed.

There are of course integration schemes which are more accurate than Euler and which are similarly agnostic as to the form of the function to be integrated, but these tend to be significantly more expensive. I take advantage of the expression for drag as a function of relative velocity to generate a cheap yet accurate time integration scheme. Here I reproduce Eqn. (1) from Burt and Boyd:

$$\mathbf{F}_p = \frac{\pi R_p^2 N_g}{V_c} (mc_r + \frac{\tau}{3} \sqrt{2\pi m k_B T_p}) \mathbf{u}_r \quad (3.1)$$

The vector drag force on a dust particle produced by a single simulated gas molecule  $\mathbf{F}_p$  is a function of the radius of the spherical particle  $R_p$ , the number of real gas molecules represented by the simulated molecule  $N_g$ , the volume of the DSMC cell  $V_c$ , the mass of a gas molecule  $m$ , the relative velocity vector between the dust and the gas  $\mathbf{u}_r$  and its magnitude  $c_r$ , the thermal accommodation coefficient for the dust  $\tau$ , the temperature of the particle  $T_p$ , and Boltmann's constant  $k_B$ . The total instantaneous force on a dust particle from all gas molecules in the cell is the sum of the contributions from all simulated gas molecules in the cell. Burt and Boyd's approach is to evaluate this sum and then apply the computed force over the entire time step. That is, they collapse this expression to a constant over a single time step, which is unsuitable for simulations in the present work because  $\mathbf{u}_r$  and  $c_r$  may change significantly over a time step. For example, when a dust particle crosses a shock it finds itself in a region where it is strongly interacting with gas at a very different velocity from that upstream of the shock.

My approach is to substitute  $\mathbf{u}_r = \mathbf{v}_g - \mathbf{v}_d$ , replacing relative velocities with

the difference between the gas and dust velocities. The basic idea is to allow the vector dust velocity to vary over the time step while holding everything else constant. I leave  $c_r$  as-is, and it will still be treated as constant over the time step. Combining several variables, this yields an equation of the form:  $\mathbf{F}_p = A\mathbf{v}_d + \mathbf{B}$ , which gives the drag contributed by a gas molecule as a linear function of the dust velocity, and where  $A$  and  $\mathbf{B}$  are functions of the gas velocity (and dust velocity, in the case of  $c_r$ ). The advantage of writing the equation in this way is that the sum of the contributions over all of the gas molecules in a cell will still have the same form – the sum of several linear expressions in a variable is itself linear in the variable. For  $C = \sum_{gas} A_i$  and  $\mathbf{D} = \sum_{gas} \mathbf{B}_i$ , I have now linearized the total force on the particle in the dust velocity. I substitute  $\sum \mathbf{F}_p = m_d \mathbf{a}_d$  to get acceleration as a function of dust velocity, yielding an equation of the form:  $m_d \mathbf{a}_d = C\mathbf{v}_d + \mathbf{D}$ . Acceleration being the time derivative of velocity, this can be directly integrated to get the velocity at the end of a time step as a function of the velocity at the beginning of the time step:

$$\mathbf{v}_{df} = \frac{1}{C}(e^{C\Delta t/m_d}(C\mathbf{v}_{di} + \mathbf{D}) - \mathbf{D}) \quad (3.2)$$

where:

$$C = - \sum_{gas} \frac{\pi R_p^2 m N_g}{V_c} (mc_r + \frac{\tau}{3} \sqrt{2\pi m k_B T_p}) \quad (3.3)$$

$$\mathbf{D} = \sum_{gas} \frac{\pi R_p^2 m N_g}{V_c} (mc_r + \frac{\tau}{3} \sqrt{2\pi m k_B T_p}) \mathbf{v}_g \quad (3.4)$$

Some special handling is required for the case where  $C = 0$ , but this only happens when all gas molecules in the cell have exactly the same velocity as the dust particle, and so the dust should experience no acceleration. Otherwise, this expression has several nice properties. For very short time steps, the dust velocity is unchanged. Unlike for Euler integration, for very long time steps the expression has

a limit at  $-D/C$  (note that  $C$  is always negative), which is a weighted average of the gas velocities. Because  $c_r$  was held constant, this is not the velocity where drag is 0. There can be some small overshoot of the equilibrium velocity, but the method will eventually converge on the equilibrium velocity over enough time steps and is guaranteed stable.

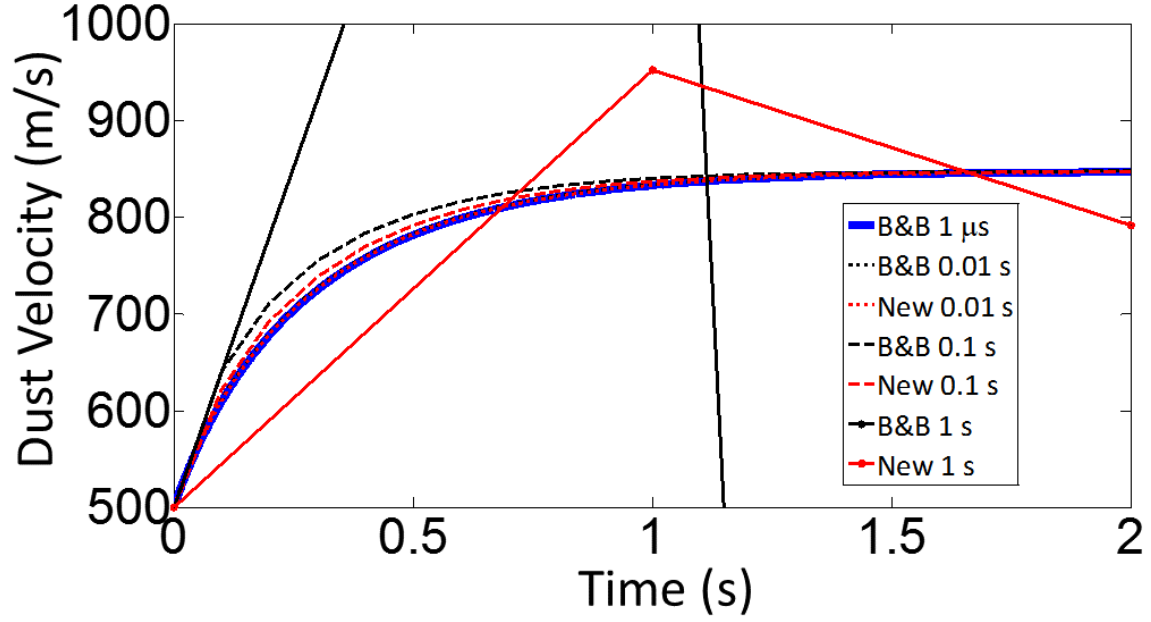


Fig. 3.5: Comparison of linearized drag calculation method (red lines) to the method of Burt and Boyd (2004) (black lines) for different time step sizes.

Fig. 3.5 compares the result of the new method to that of Burt and Boyd for the time-dependent velocity of a 10 nm diameter particle with a density of 1000 kg/m<sup>3</sup> moving through SO<sub>2</sub> gas at a number density of  $5 \times 10^{17} \text{ m}^{-3}$ , a bulk upwards velocity of 850 m/s, and a temperature of 500 K, while experiencing a gravitational acceleration of  $-1.796 \text{ m/s}^2$ . The dust particle begins with a vertical velocity of 500 m/s. The blue line uses Burt and Boyd's method with a time step of 1  $\mu\text{s}$ . Both

methods produce results which essentially lie on top of the blue line for time steps below 10 ms. For a time step of 100 ms, there is perceptible error in both methods, but the linearized calculation is much closer to the converged solution. For a time step of 1 s, both methods immediately overshoot, but the linearized calculation begins to converge on the gas velocity while Burt and Boyd’s method has gone unstable.

A similar issue can arise with Burt and Boyd’s expression for the temperature of dust particles for  $\tau > 0$ . Here the same overshooting/unstable behavior can yield negative temperatures. The same procedure – allowing one relative velocity term to vary instead of holding everything constant – yields a similar result for temperature at the end of a time step as a function of the temperature at the beginning of the time step.

In the simulations presented here, drag is never the only force acting on dust particles, and when calculating the motion of particles under gravity I use a predictor-corrector method. Rather than incorporate gravity into the above calculation, the delta-v found above is converted to an average acceleration over the time step and is applied as a constant acceleration during the predictor-corrector step. This will cause the simulations to find terminal velocities which are too far from the gas velocity. When a particle is at terminal velocity in a uniform gas it should experience the same drag force over the whole time step, because terminal velocity is an equilibrium velocity where drag balances gravity and so the particle’s velocity should not change. However, with this method the drag force is calculated assuming the particle’s velocity is approaching the gas velocity over the time step (and the drag force shrinks as the particle velocity approaches the gas velocity). The total drag force experienced by a particle at “true” terminal velocity will thus be lower than it should be, although this

effect is rarely significant in practice and amounts to an error of at most a few meters per second for the terminal velocities of even the heaviest grains in the lowest-density gas in the simulations here. It should be noted that Burt and Boyd's method does not have this problem, despite yielding too-high drag forces in most other circumstances.

### **3.2.4 Computational Grid and Load-Balancing**

The three-dimensional simulation of complex plumes, with such hugely varying length scales and mean free paths, presented some new computational challenges. Methods for automatically determining processor boundaries and the grid structure within processors were very important for setting up and performing the computations efficiently. The computational domain is a section of a spherical shell, bounded by surfaces of constant latitude, longitude, and altitude. Processor boundaries also lie along latitude and longitude lines, with each extending from the surface to the top of the domain. Each processor is typically allocated 40,000-60,000 cells. The grid of cells is uniform in latitude, longitude, and altitude within each processor. The distribution of this budget of cells to each spherical coordinate direction is automatically chosen so as to minimize the largest average cell size (in any dimension) anywhere in the processor. Because in DSMC particles collide only with partners in the same cell, this strategy approximately minimizes the distance between collision partners for a uniform grid. If this procedure results in a cell with less than a predefined minimum cell size, the cell allowance is reduced (rather than allotting 50,000 cells to the processor the next iteration will allot only 40,000, say) and the number of cells to allot to each spherical coordinate direction is recalculated. A uniform grid in latitude and longitude in each processor is suitable for this problem because the resolution is allowed to vary between processors such that processors which take up less volume

achieve finer resolutions, and the volume of a processor is tied to the local flow density, integrated in altitude (discussed below). This results in cell sizes which scale very nearly with mean free paths in each processor, in latitude and longitude. However, in simulations outside of Chapter 7 cell sizes do not vary with altitude (except across stages, which are simulated separately).

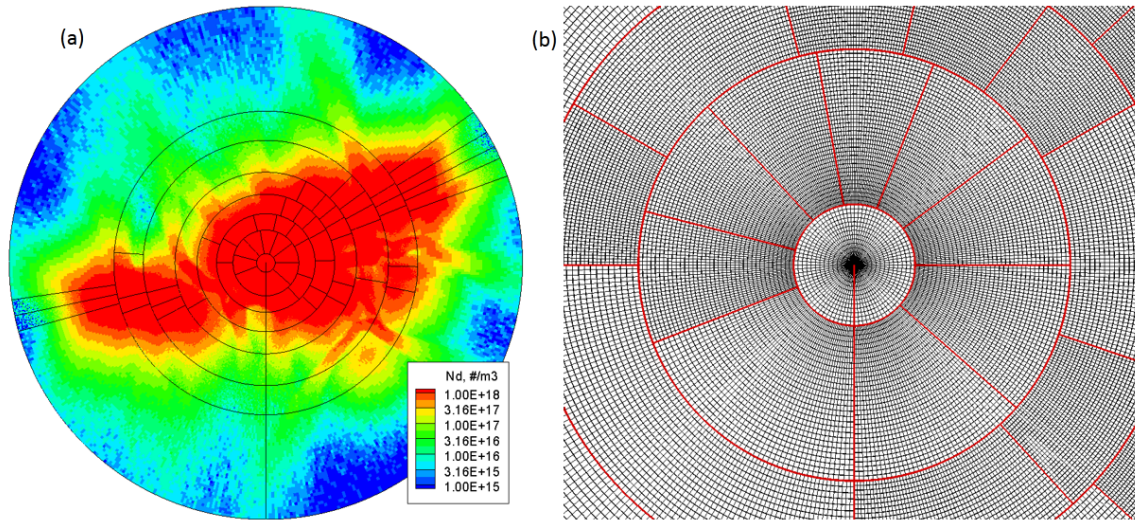


Fig. 3.6: (a) Number density contours for flow in a constant-altitude slice 1 km above Source A1, with black processor boundaries visible. (b) A close-up of the polar cap processor and the innermost ring. Processor boundaries are in red and cell boundaries are in black.

Figure 3.6a shows an example of the result of the adaptive domain decomposition. The simulation was performed on 64 processors – one polar cap and seven rings of nine processors each. Over the course of the simulation the processor boundaries adjusted so as to balance the number of particles in each processor, and here processors are seen to be concentrated near 2:00 and 9:00, following the shape of the red high-density region. Three processors in the outer ring simulate a large fraction of the total simulation domain, because density in the outer regions is generally very

low.

For the plume-only simulations in the present work, the source of the plume is located near the pole of the spherical domain. This has the advantage of placing a roughly radially symmetric flow in a roughly radially symmetric grid. Generally, we desire smaller cells nearer the central axis of the plume where densities are higher, but uniform decomposition in longitude produces a near-singularity in the grid at the axis. As the cell sizes shrink, it becomes difficult to keep enough simulated molecules in each cell to resolve collisions, and statistics-driven instabilities can occur (Zhang 2004). I mitigate this by using a non-uniform processor distribution that allows the placement of a single processor at the pole spanning 360 degrees in longitude and covering a very narrow range of latitudes. By allowing this polar cap processor a small number of cells, the cells remain acceptably large along the polar axis, but, because the processor does not extend out far in latitude, the cells do not grow unacceptably large along the processor’s outer edge. Figure 3.6b shows an example of the grid structure in latitude and longitude and the effect of the singularity at the axis is seen in the cells in the polar cap.

Load-balancing is an important consideration because the simulation can only proceed at the speed of the slowest processor. Most computer time is taken up by collisions between simulated gas molecules, the number of which tends to increase as the number of particles in a processor increases. A straightforward method of load-balancing that roughly approximates collision-based balancing is simple molecule balancing, i.e. balancing with the goal of placing an equal number of molecules in each processor (all of which have nearly identical numbers of cells).

While a precomputed set of processor boundaries is acceptable for many prob-



lems, it is not suitable for many unsteady flows. At the beginning of a plume simulation, all of the molecules are near the center of the domain. After the plume’s initial expansion, there are a large number of molecules around the periphery of the domain. Finally, after the canopy shock forms, most of the molecules are in an annulus around the center of the domain. With static load-balancing based on the steady plume, the early time steps would take just as long to compute as the later time steps, and the middle time steps would take longer than either. Dynamic load-balancing is used to compute the transient stages of the simulation quickly. At intervals, a crude (perhaps  $1,000 \times 1,000$ ) set of bins is used to map the molecules in latitude and longitude. This allows the domain to be split into a set number of rings in latitude, where each ring has roughly equal numbers of molecules. Then each ring is split up into a set number of processors in longitude, where each processor has a roughly equal share of the molecules in its ring. In this way a given number of processors can be moved around over the course of a simulation such that the number of molecules in a particular processor at any time is roughly equal to the total number of molecules divided by the number of processors.

### **3.3 Computational Method for Plume-on-Planet Simulations**

#### **3.3.1 Patching Plumes on to the Planet**

Modifying the technique described above (Section 3.2.1) for staging the Pele plume from seven source regions allows the patching of 3D or axisymmetric plumes into a full planet simulation where the interaction of the atmosphere and the plume or between several plumes can be investigated. The patching process is essentially identical to the method for combining the seven source regions for the Pele plume, only on a larger scale. Molecules leaving an inner domain have their positions and

velocities rotated around the planet to a specified latitude and longitude (with an initial rotation about the central axis of the inner domain so that the plume is oriented correctly at its new latitude and longitude) and are written to a file, which is read in by processors in the outer domain. For very large simulations using dynamic load balancing the constant re-reading of lengthy patch files can be expensive. Re-reading speed can be greatly increased by finding and storing the minimum and maximum latitudes and longitudes of any molecule in a particular patch file when the patch files are read in their entirety by every processor on the first time step. When re-reading, processors can skip files which contain only molecules outside of their current boundaries.

When investigating the plume/plasma or plume/atmosphere interactions, it is often unnecessary to simulate a complex, three-dimensional inner domain. A plume erupting from a round hole often suffices, and the near-source flow of such a plume is easily simulated axisymmetrically. However, an axisymmetric inner domain cannot simply be rotated to some point on the planet when patching into a three-dimensional atmospheric simulation. To link these simulations, before molecules in the axisymmetric simulation are written to a patch file they are rotated by a random amount around the axis of symmetry, yielding output which should be indistinguishable from a three-dimensional simulation of a round hole plume.

A concern when patching plumes on to the planet is that given a sublimation atmosphere the inner domains are no longer one-way coupled to the outer domains. The sublimation atmosphere itself should be two-way coupled through the side walls of the inner domain. The plume stem might influence the atmosphere and the atmosphere might influence the plume stem. Any effect that the falling plume has on

the sublimation atmosphere could also potentially find its way back into the inner domains, especially given the existence of directional winds away from the sub-solar point. I argue here that the effect of the plume stem on the atmosphere is unimportant, that the effect of the atmosphere on the plume stem is unimportant, and that by ignoring the effect of the plume stem on the sublimation atmosphere the entire sublimation atmosphere can be simulated consistently in the outer domain.

I use a simple surface model which assumes that the entire surface, except for the virtual vent, is covered in frost at 118 K. All  $\text{SO}_2$  that contacts the surface sticks with unit probability and the frost emits  $\text{SO}_2$  at a rate that preserves the equilibrium vapor pressure which is an exponential function of temperature taken from Wagman (1979). An axisymmetric plume erupts from an 8 km radius round hole at a density of  $6.426 \times 10^{-8} \text{ kg/m}^3$ , an upwards velocity of 850 m/s, and a temperature of 500 K (this is similar to a Pele-class plume from Zhang et al., 2003). Instead of simulating an entire plume, I simulate only the gas flow in the vicinity of the virtual vent – only the plume stem and the surrounding atmosphere. The domain extends only 60 km along Io’s surface and 45 km in altitude.

Fig. 3.7 shows how the plume and atmosphere are relatively independent except within about ten kilometers of the virtual vent. The plume is essentially the same in (b), without atmosphere, as in (a). With atmosphere there are perhaps slightly higher densities on the very fringes of the plume, representing particles with large velocities tangent to the surface, but virtually all of the plume mass is in the core of the stem. The plume does produce more rightward flow at the very top of the hydrostatic atmosphere, but this represents a relatively small amount of material. The atmospheric density in (a) quickly comes to resemble the undisturbed atmosphere

in (c), but, oddly, where it differs from the undisturbed atmosphere it appears to be *less* dense. The atmospheric density in (a) reaches a minimum right next to the virtual vent, then quickly grows to resemble the undisturbed case. The undisturbed atmosphere remains very dense over the region which in (a) contains the virtual vent, even though in (c) this region is a pure sink with no gas emission. The explanation is that the sticking surface in (c) is much less efficient at removing gas from the atmosphere than the fast-moving plume is. The plume stem entrains sublimated gas wherever they come into contact, creating an effective sink along the entire surface of the stem. This increases the mass in the plume, but apparently only slightly. The atmosphere in (a) and (c) also drops off slightly towards the edge of the domain on the right; this is because the right wall uses a vacuum boundary condition (this illustrates how vapor pressure equilibrium can reassert itself over very short distances). This boundary condition also explains the rightward flow in the atmosphere even in (c).

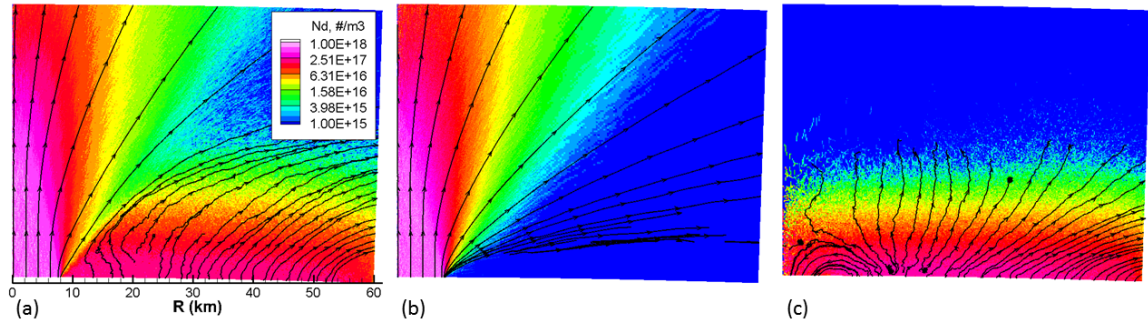


Fig. 3.7: Axisymmetric number density simulations for a Pele-type plume stem and 118 K sublimation atmosphere. (a) shows a plume stem with atmosphere. (b) shows a plume stem without atmosphere. (c) shows an atmosphere alone (with no sublimation where the plume vent was). Streamtraces show the motion of the gas.

Because the rising plume is essentially the same whether there is an atmosphere or not, and because the atmosphere over frost-covered regions depends only on the

surface properties except on very short length scales, I simulate plume stems without atmosphere. When patching the plume back on to the planet I simulate atmosphere in the outer domain, even over the region where the plume emerges, and this will be inaccurate only in the immediate vicinity of the vent. The actual model used for Pele’s vent has finer geometry and about 1/10 the total area as the round hole cases in Fig. 3.7. This smaller plume stem should affect the atmosphere even less. The plume may have relatively more exposed surface area, but the plume gas is also denser, and at least over the larger source regions the Pele model should be independent of a sublimation atmosphere. This is especially likely to be true because surface frost probably does not extend up to the edges of the lava lake at Pele.

### 3.3.2 Vertical Grid Structure

Ideally, DSMC cell sizes should be less than the local mean free path and gradient-based length scales. Often this is too difficult to achieve, and better results are obtained by using smaller cells in regions with higher densities and smaller length scales when resources are scarce. Load balancing (Section 3.2.4) efficiently distributes processors (and therefore cells) in latitude and longitude, but each processor extends from the bottom of the domain to the top in the radial direction. When there are large variations in density with altitude, a uniform grid structure is not appropriate (or at least is inefficient). Simulations using uniform grids were feasible for the simulations of the night-side Pele plume with dust, but the introduction of a sublimation atmosphere necessitated new gridding methods in altitude. Fine cells are needed to represent the atmosphere in a thin layer over Io’s surface (where the scale height is a few kilometers) and the plume canopy (which is tens of kilometers thick), but much coarser cells suffice between the atmosphere and canopy and especially above the canopy.

In older work with the UT DSMC code (such as Walker et al., 2010), an exponential grid was used. The goal of this scheme was to capture a hydrostatic atmosphere by increasing radial cell sizes exponentially such that the product of flow density at the bottom of each cell and cell size remained constant. This also caused cell sizes to be proportional to the mean free path at the bottom of each cell. A maximum cell size could also be specified which would eventually stop the exponential growth of cells and fill in the rest of the domain with a uniform grid. This method has several important drawbacks. No analytic function gives a cell index from a particle position, necessitating potentially expensive searches when indexing. Cells only get bigger with altitude, making it difficult to capture plume canopies without using a relatively small maximum cell size (and forgoing most of the benefits of the scheme in the first place). The method also interacted poorly with load balancing; it would fail when a processor had too many cells (the maximum cell size would be too large and the top of the domain would be reached before all allocated cells had been used) or too few cells (because a constraint on the ratio of cell size to mean free path for the bottom-most cell could not be satisfied). Because processors would have very different numbers of cells, the method would fail for many cases. In the course of this work I modified the exponential gridding scheme used in the DSMC code to automatically reduce the maximum cell size used in a processor with many cells or to resort to a uniform grid in a processor with too few cells. This modified method yields decent results, but care must be taken when setting the maximum cell size, which must still be small enough to capture flow features at altitude. While this approach was not used for the actual simulations presented here, the output grid onto which the simulation particles are resampled to display results uses this method.

Moore (2011) implemented a method where each column of cells is divided

into a number of segments, with each segment containing an approximately equal number of particles. Within each segment, cell sizes increase linearly. The method attempts to match cell sizes across segment boundaries and to choose cell sizes at the top and bottom of all segments which are proportional to the local mean free paths. This is a dynamic method, and the segment boundaries and cell sizes for the new linear segments grid are determined using the existing grid (which is initially uniform or exponential, but later is itself a linear segments grid), which is sampled over time. Segment boundaries can only be placed on cell boundaries of the old grid, and local mean free paths are taken to be an average of the mean free paths of those old cells overlapping with the new cells. The main advantages of this method for atmosphere-only simulations are faster searches during indexing and the grid's ability to adapt to changing length scales which are not a simple function of the surface temperature (as during eclipse). In principle this method allows for cells to become finer with altitude, but in practice it is unsuitable for thin, dense features like plume canopies and interacts very poorly with load balancing. However, extensive modifications to this method have made it suitable for combined plume and atmosphere simulation.

While the original linear segments method can place segment boundaries appropriately in a plume simulation, a plume canopy in the middle of a segment is effectively invisible to the method as it iterates to determine cell sizes within the segment. Only the mean free paths in the cells on the bottom and the top of each segment matter, and the method would often distribute cells away from the segment containing the plume canopy, leaving it with too-large cells. In a load-balanced simulation with different numbers of cells in each processor, the iterative method often fails outright or places too-fine cells at the surface (causing the DSMC simulation to miss collisions for lack of potential partners). If the old grid is too coarse and a very

large fraction of simulated particles are in only a few cells, the method can fail to find segment boundaries. Worst of all, in a dynamically load-balanced simulation, a new grid must be obtained immediately after load balancing. Re-initializing with a uniform or exponential grid which will be eventually replaced with a linear segments grid requires using the uniform or exponential grid for a substantial amount of time in the middle of a simulation and can significantly alter the result (if a uniform or exponential grid was good enough for the simulation then linear segments would be unnecessary). However, applying the linear segments method to an instantaneous snapshot of the density field produces terrible results due to the noise present in measurements of the local mean free paths. The method yields enormous changes in cell sizes between adjacent columns of cells, and this can produce feedback effects which trap particles in some columns while they pass freely through others, giving rise to unphysical density artifacts.

My implementation of linear segments, which was used for the combined plume/atmosphere simulations, is intended to produce relatively smooth grids which can capture both a sublimation atmosphere and a plume canopy, can be derived from noisy data immediately after load balancing, and can be determined automatically for a wide variety of processor shapes each having different numbers of cells in altitude. Given a number of cells in altitude and the number of simulated particles in each pre-existing cell, my implementation produces a new grid structure using a specified minimum cell size and number of linear segments. The total number of cells in altitude is divided up among the various segments as evenly as possible. The method starts at the bottom of the domain and moves up, attempting to place the segment boundaries such that the simulated molecules are apportioned equally, interpolating within the old cells. This allows a solution to be found even when all of the particles



in a column are in a single cell, as might happen for an initial uniform grid and a sublimation atmosphere. If a segment would be so small that at least one of its cells would have to be shorter than the minimum cell size, which again often happens with a tall domain and a sublimation atmosphere, its top boundary is moved up to allow every cell in the segment to take on the minimum cell size. If a segment would be so large that even if all later segments contained only minimum-sized cells they would exceed the remaining height of the entire domain, the current segment is shortened and the remaining segments are set to produce a uniform grid of minimum-sized cells. The bottom-most cell in the domain is set to the minimum cell size (if it has not already been fixed at this size due to the bottom-most segment being very short), and all other cell sizes are constrained to be a linear function of cell index and to match sizes across segment boundaries. This uniquely determines all cell sizes because all of the cells in each segment must add up to the segment's height. If smoothing between adjacent columns or within a processor is desired this can be done by performing the procedure twice, where during the second calculation the segment boundaries are set to an average of their initially-computed value and some average value.

The number of segments is somewhat arbitrary. Too few segments will do a poor job of tracking density changes in the gas. Too many segments will be expensive to search through during molecule indexing – one of the original goals of the method was to create a density-tracking grid that could nevertheless be quickly searched, since within each segment the cell in which a molecule is located can be determined analytically. Too many segments also risks having more segments than vertical cells in some processors, although this is easily avoided. I often aimed to have 5 to 10 cells per segment, but it is not important to be precise.

Choosing a minimum cell size is more difficult. Because the sublimation atmosphere decreases in density exponentially with altitude, a huge proportion of a column’s mass can be very close to the surface. A similar problem can occur with plume canopies, where virtually all of the mass in a column can be in a narrow canopy shock at some altitude. Simply allowing a processor to place almost all of its vertical cells over these small regions of high density can produce enormous errors. Without a very careful weighting scheme, many cells will lack sufficient molecules to perform accurate collisions. This can result in the densest parts of the simulation being effectively collision-less. On the other hand, a too-large minimum cell size can result in all of the usual problems of a too-coarse grid. I generally found it useful to set the minimum cell size according to a length scale that I wanted to resolve – usually about a tenth of a scale height. This could easily be made variable, based on surface temperature or similar, but because scale height does not change all that much over Io’s surface, and because the night-side lacks a significant atmosphere anyway, I usually used a constant value.

Fig. 3.8 shows an axisymmetric example calculation using this method. High resolution is maintained in the sublimation atmosphere and at the vent even as the grid is allowed to coarsen in regions of low gas density. In the rightmost image the canopy directly above the vent has much coarser cells than the canopy away from the vent, even though the canopy’s density peaks along the central axis. This illustrates the importance of choosing a sufficiently large cell budget and minimum cell size, or using a weighting scheme to place more processors over the center of the plume. In this case the simulation is intentionally too-coarse so that the grid structure is apparent in the figure (with a finer grid parts of the figure are just entirely black).

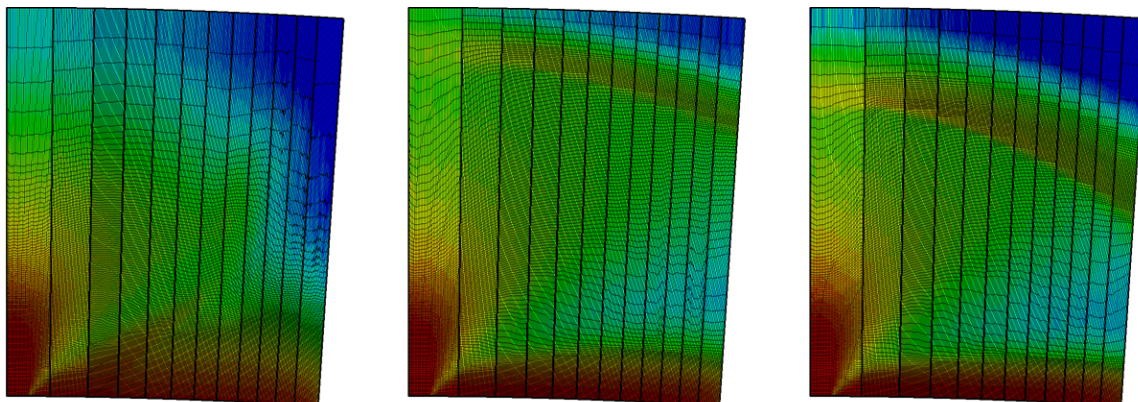


Fig. 3.8: Demonstration of dynamic load-balancing and adjustment of the vertical grid structure using the new linear segments implementation. An axisymmetric Prometheus-type plume with a sublimation atmosphere is simulated on 12 processors. Snapshots of number density are shown at 250 s, 750 s, and 1500 s, from left to right. Thick black lines are processor boundaries and thin black lines are cell boundaries.

### 3.3.3 Ion Weighting

In DSMC, two simulated particles which each represent the same number of real particles collide like real particles. That is, a single collision is simulated as if between two real particles and the results are assigned to all of the real particles that the simulated particles represent. With enough simulated particles, a statistically representative sample of the real gas evolves in time. However, it is sometimes desirable to allow simulated particles to represent different numbers of real particles. As long as all simulated particles have the same weight locally, as in a spatial weighting scheme like the one used here for the plume/atmosphere simulations, there are no implications for collisions, since molecules only collide locally. Molecules merely need to have their weights updated, and be cloned or destroyed accordingly, as they move from cell to cell. Plasma presents a special challenge for weighting because, while ions

carry a great deal of energy and momentum and have a large effect on the atmosphere and plumes, the number density of ions is very low compared to the number density of neutrals. For a local weight which is appropriate for neutrals, the average number of ions per cell is generally much smaller than 1. Simulated ions are very rare, but every cell with a simulated ion in it has a real ion density far higher than the average ion density. This yields extreme noise in the interaction between the ions and the neutrals. It is easy to see the wakes left by individual ions as they burrow through the sublimation atmosphere or plumes, leaving trails of daughter species behind. Each simulated ion can transfer an enormous amount of energy to the gas around it, causing unphysical expansions away from points of impact – rather than peppering the atmosphere with a large number of small impacts, simulated ions at the same weight as the neutral gas hit the atmosphere like bowling balls.

The obvious solution to the statistics issue presented by low-density ions is to weight them differently than the neutrals. This, however, requires a way to simulate the collisions of different-weight particles. The usual DSMC method for collisions between same-weight particles conserves momentum and energy, on average – real collisions conserve momentum and energy and DSMC just simulates a real collision and assigns the result to a pair of simulated particles which represent a very large number of identical pairs of particles. If each simulated  $\text{O}^+$  ion represents 1000 real  $\text{O}^+$  ions and each simulated  $\text{SO}_2$  molecule represents 1000 real  $\text{SO}_2$  molecules, the simulated collision between simulated  $\text{O}^+$  and  $\text{SO}_2$  particles represents 1000 identical collisions between real  $\text{O}^+$  and  $\text{SO}_2$  particles. For every real  $\text{O}^+$  ion that loses some amount of energy or momentum, there is a real  $\text{SO}_2$  molecule that gained that amount of energy and momentum. For particles with different weights this no longer works. If in a simulated collision one  $\text{O}^+$  ion transfers some energy to one  $\text{SO}_2$  molecule,

conserving energy, 100  $O^+$  ions all losing that same amount of energy while 1000  $SO_2$  molecules gain it means that 9 times as much energy as was transferred just appeared out of nowhere. For different-weight particles, it is no longer the case that each real particle represented by a simulated particle has a corresponding partner in the other simulated particle to collide with. This cannot be solved by simply scaling the amount of energy transferred from one simulated particle to the other – the post-collision state would no longer be representative of the real flow, since real particles represented by the simulation would not end up in the computed post-collision state. Instead, momentum and energy can be conserved on average in different-weight collisions by ignoring the effect of collisions on the higher-weight particle with some probability.

Consider an example collision between two real particles:  $N_i + I_i \rightarrow N_f + I_f$ . This is a possible result if we have a simulated neutral and a simulated ion in initial states  $N_i$  and  $I_i$ , each with weight  $W$ . The net effect of this collision on the state of the real flow being simulated is  $W \times [(N_f - N_i) + (I_f - I_i)]$ . The flow being simulated has lost  $W$  neutrals and ions in the initial states and has gained  $W$  neutrals and ions in the final states. Now suppose that ions are weighted by a factor of 10, so that each simulated ion represents  $W/10$  real ions while each simulated neutral still represents  $W$  real neutrals. Now, in order to simulate the same real flow we use ten times as many simulated ions, with each ion representing ten times fewer real ions. If before we expected to have one simulated collision between particles with states  $N_i$  and  $I_i$ , now we expect to have ten collisions. We seek a rule for doing these collisions that yields the same net effect on the flow as the normal collision procedure for the unweighted case. Just applying the unweighted rule yields a net effect of  $W \times [10(N_f - N_i) + (I_f - I_i)]$ . We get the right state change in the ions but too large of an effect on the neutrals, because the neutrals are being affected by ten times as

many collisions.

Instead we should use the stochastic rule:  $N_i + I_i \rightarrow 0.9N_i + 0.1N_f + I_f$ , where 90% of the time the neutral remains in its initial state. The expected state change per simulated collision is now  $W \times [0.1(N_f - N_i) + 0.1(I_f - I_i)]$ , because the W-weighted neutrals have only a 10% chance of changing state and the ions are W/10-weighted. Ten of these collisions have the same expected effect as a single simulated collision in the unweighted case.

The simulations presented here involve three kinds of ion-neutral collisions. Non-reactive collisions involve only the transfer of momentum and energy between the particles. Dissociation reactions involve the neutral partner breaking up into some number of neutral daughters. Resonant charge exchange reactions involve only the transfer of an electron from a neutral O or S atom to an ion, with no other change in state. Implementing this stochastic collision rule for the first two types of collisions is straightforward. For non-reactive collisions, the state of the neutral can be saved prior to computing the collision, and then it can be reverted with some probability afterwards. Likewise for dissociation reactions, although it is more convenient to skip the actual dissociation step instead of reverting it. It remains important to compute the ion's new velocities using the lower total collision energy obtained by subtracting off the dissociation energy of the neutral.

Implementing the stochastic collision rule for resonant charge exchange reactions is trickier. Perhaps the most intuitive approach is to convert the ion into a neutral every time while converting the neutral into an ion only a fraction of the time. This creates several practical difficulties. In this weighted simulation, simulated neutrals and ions represent different numbers of particles, so if for a neutral A

and an ion B we were to do  $A + B^+ \rightarrow 0.9A + 0.1A^+ + B$ , the net effect of ten such collisions would be an expected state change of  $W \times (0.1A^+ - A + 10B - B^+)$ . To make this work out the neutral would need to be cloned 9 times when it becomes an ion and the ion would need to be destroyed with probability 90% upon becoming a neutral. It is also quite hard to re-index in the middle of the DSMC collision routine, although one might just set aside all particles involved in charge exchange reactions for the rest of the time step.

Fortunately there is a more elegant solution. Rather than conceiving of the charge exchange reaction as a neutral and an ion exchanging an electron so that the neutral becomes an ion and the ion becomes a neutral, we should instead conceive of it as a neutral and an ion exchanging every property *except* charge. The choice of which post-collision particle corresponds to which pre-collision particle is fundamentally arbitrary. Instead of  $A + B^+ \rightarrow A^+ + B$ , we should think of the real collision as  $A + B^+ \rightarrow B + A^+$ . Then it looks almost exactly like a non-reactive collision – a neutral in some initial state becomes a neutral in some final state while an ion in some initial state becomes an ion in some final state. I obtain the stochastic rule  $A+B^+ \rightarrow (0.9A+0.1B)+A^+$ . While intuitively odd because the positions of particles can change as a result of a collision, it gives the right expected state change in the underlying neutral/ion flow being simulated.

### 3.3.4 Fast Plasma Simulation

Because the number of ions in a processor is typically much smaller than the number of cells in the processor, the usual DSMC algorithm is inefficient. Standard DSMC uses a small number of cells to keep track of a large number of particles. Loops over cells are preferred to loops over particles, and loops over cells are computationally

inexpensive. When sub-stepping plasma (by a factor of 100, here) using the standard DSMC algorithm, however, looping over cells was taking up the majority of computer time. Multiple loops over all cells occur during each substep when indexing particles to cells, and then another loop occurs when colliding particles.

Almost all of these loops can be replaced with loops over only those cells which contain ions, achieving significant speedup. On the first substep of each timestep, the regular indexing routine should be performed. A list of cells with ions in them should be created and stored, which will be used when colliding. After this, indexing should be done “on the fly” – the number of particles in a cell should be decremented when an ion moves. After particles move, a quick loop over ions instead of over cells determines which cells have ions in them and the number of ions in those cells.

### **3.3.5 Tracer Particles**

Visualizing unsteady 3D flows with small-scale features in large volumes is difficult. Snapshots of macroscopic flow properties on a grid can require a great deal of memory, can only easily display two-dimensional planes of data in a single image, and (for a statistical method) can be confusingly noisy when unsteadiness is important. It can be awkward to convey density and velocity at the same time, especially in three dimensions. For a particle-based method like DSMC, the mechanics of the simulation are obscured when visualizing the flow with macroscopic properties, and this can also obscure the underlying physics (or workings of the code, when debugging).

Tracer particles are an efficient means of intuitively visualizing these flows. By tagging some fraction of particles as tracers and writing the positions of all tracers to a file at regular intervals, a high time resolution movie of representative particles can



be created. Velocities are apparent as actual particle velocities, densities are apparent as actual particle densities, and three-dimensional structure can be seen relatively easily. Particles can be colored or sized by species, altitude, speed, or other property. For the plume simulations discussed here, informative tracer movies spanning half of an Io day only require about as much memory as an instantaneous snapshot of macroscopic properties (probably there are more efficient ways to output the macroscopic properties, but tracer particles very naturally only use lots of resources where there are lots of particles). Few of the results presented here will be images of tracer particles, since they are most useful for animations with hundreds of frames, but the technique was important for gaining insight into the physics of the plume/plasma and plume/atmosphere interactions.

Using tracer particles is very straightforward in a DSMC simulation with constant particle weight. For a simulation with varying particle weights, a naive tracer scheme will reflect the relative weights in the simulation - if in a constant-density flow there are twice as many simulated particles in one region as another because the regions' weights differ by a factor of 2, then there will be twice as many tracer particles too. Similarly, if proportionally more tracers are desired in regions where simulation weight is smaller, the tracer property can be handled like any other particle property for purposes of cloning and destruction. However, if it is valuable for tracer densities to be proportional to the simulated macroscopic density of the flow, some particles will need to gain or lose tracer status as they move across a weight gradient.

A procedure for conserving the number of tracer particles through a change in weights can be deduced by imagining a large collection of  $N$  physically identical particles with identical histories moving together, where  $T$  of them are tracers (so

the fraction of particles which are tracers is  $t = T/N$ ). The purpose of imagining a large number of particles is to allow us to treat random outcomes as taking on their expected value; the actual procedure determined here is to be applied on a per-particle basis. This collection of particles moves from a region with weight  $w_1$  to a region with weight  $w_2$  (let the weight ratio  $w = w_1/w_2$ ). After weighting is applied, the new number of particles is on average  $N' = Nw$ . The goal is to ensure that the number of tracer particles remains constant – that  $T'$  is equal to  $T$ .

For  $w > 1$ , each particle will be cloned  $\text{floor}(w - 1)$  times, with a uniformly distributed random number determining whether any fractional remainder produces a clone. Clones typically inherit all the properties of the original particle, but if tracer status is treated in this way the new number of tracers will be  $T' = Tw$ .  $T'$  can be forced to equal  $T$  simply by setting all clones to be non-tracers, since all of the original tracers are still present. The new tracer fraction is  $t' = T/N' = t/w$ .

For  $w < 1$ , each particle will be destroyed with probability  $1 - w$ . Some tracers will be destroyed, so some non-tracers need to be converted into tracers in order for  $T'$  to remain equal to  $T$ . The number of surviving tracers is  $Tw$  and the number of surviving non-tracers is  $(N - T)w$ , so to guarantee  $T' = T$  non-tracers must turn into tracers with probability  $p$  such that  $T = Tw + (N - T)wp$ . Solving for  $p$  yields  $p = (1 - w)/w \times T/(N - T) = (1 - w)/w \times t/(1 - t)$ . As before, the new tracer fraction is  $t' = t/w$ . This tracer fraction needs to be stored on a particle-by-particle basis, and updated whenever weights change even for non-tracers and even when cloning, in order to create the correct number of new tracers during destruction. The tracer fraction should be initialized with the probability that the newly-created particle was going to be a tracer. It is also important that  $t$  never be

allowed to reach 1, so therefore the probability that a newly-created particle is made a tracer should always be less than  $w_{local}/w_{max}$ . Note that this technique is indifferent to collisions, since those do not typically affect particle weights. If different species have different weights (or just different initial tracer fractions), then collisions which result in chemical reactions will need to also adjust the tracer fraction of the daughter particles.

## Chapter 4

### SO<sub>2</sub> in the Night-side Pele Plume

#### 4.1 Overview

Computational gas molecules are created in subsurface reservoirs in the source geometry described in Chapter 3.2.1 at virtual vent conditions of 500 K, 850 m/s, and  $5 \times 10^{18}$  molecules/m<sup>3</sup> and allowed to expand upwards into four staged domains. This uniform Mach 3 flow is substantially colder than the surface of the lava lake and is taken to be the result of complex low-altitude interactions (Section 4.2). The virtual vent altitude is taken to be negligible relative to the canopy height (and the lava lake could be in a depressed area as well). The source geometry causes complicated flow behavior at low altitudes. Flow features that arise near the vent propagate upwards, and sharp gradients can persist even after the flow has become nearly collisionless at higher altitudes below the canopy. During a transient start-up period (Zhang 2004), the simulated plume gas rises much higher than the observed plume canopy. Eventually, under the influence of gravity, the plume falls back on itself, and the canopy shock forms where the weight of the falling gas is supported by rising gas from below. Gas in the canopy is shunted off to the sides of the plume where it forms the large red deposition ring, and the canopy is constantly replenished by new gas rising from the surface such that it becomes a constant feature of the plume. This chapter begins by justifying the “virtual vent” model in detail before examining the gas plume at Pele in progressively larger domains and the plume’s giant deposition

pattern. Results here were previously published in McDoniel et al. (2015).

## 4.2 Below the Virtual Vent

The “virtual vent” model of (relatively) cold, uniform flow is a reasonable one for the Pele plume because complex flow very near (within meters of) the actual emission surface can give rise to nearly uniform-property flow at a higher velocity and lower temperature only a small distance (about 1 km) above the surface.

Radebaugh et al. (2004) discuss and summarize several lines of evidence suggesting that Pele is an active confined lava lake similar to, but much larger than, lava lakes on Earth. They reference the work of Burgi et al. (2002) on the Erta Ale lava lake in Ethiopia. Erta Ale has two sorts of activity – incandescent cracks and fountaining from larger holes in the crust (Fig. 4.1). At Erta Ale, both sorts of features are only a few meters across (although the cracks can be tens of meters long). Radebaugh et al. argue that fountaining explains the temporal variability of the thermal emission and the higher color temperatures which are observed when Pele is viewed at an angle. Davies (2007) also argues that temporal variation in thermal observations are a result of localized disruption of surface crust, on a small enough scale to leave the rest of the lake undisturbed.

I assume that, at Pele,  $\text{SO}_2$  escapes from the lava or is expelled from the lava from similar cracks or roughly circular fountaining regions. I assume that the gas emerges at the lava temperature and that it is nearly stationary just before it exits the lava. It will quickly (within  $\sim 1$  crack width or hole diameter) expand to Mach 1 due to the extremely low ambient pressure. If the gas is venting in this fashion, the crust will act as a gas dynamic throat, and under-expanded Mach 1 gas will rise from



Fig. 4.1: Erta Ale lava lake in Ethiopia, 80 m across and (right) Nyiragongo lava lake in the Democratic Republic of the Congo, several hundred meters across (varies). Both exhibit cracks and lava fountains. These lakes are much smaller than the lava lake at Pele, but I assume that the surface features are similar and have similar length scales.

the surface with a roughly vertical velocity.

The lava lake at Pele is orders of magnitude larger in area than terrestrial lava lakes, but small-scale features on its crust should not depend on the size of the lava lake but on material properties of magma and crust. Local regions of freshly exposed lava at Pele should be about as large as similar features seen on Earth. This is supported by the failure of observations to resolve such features, even at  $\sim 30$  m/pixel (although note that an October 1999 Galileo SSI image clearly indicates a long border region of the lava lake, but that McDoniel et al. (2011) show that gas emission from this elongated fissure cannot explain the observed deposition ring; this result is also described in Appendix A). Therefore, if Pele's crust is qualitatively similar to terrestrial lava lake crusts locally, it will be covered by an enormous number of features which are very small on the scale of the lake as a whole. For simplicity, I model the lava lake using uniformly spaced circular holes of gas-emitting liquid lava (Fig. 4.2), although similar results are obtained using a crosshatch pattern of uniform

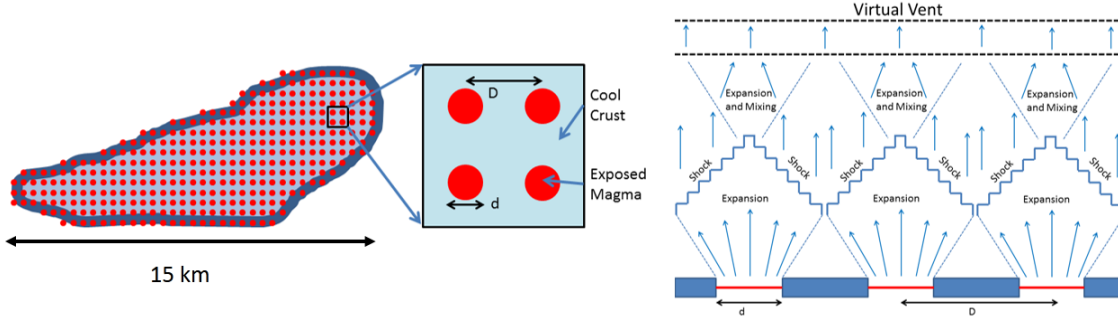


Fig. 4.2: (left) Drawing of large, irregular feature modeled after Source A1 from Fig. 3.2, covered with uniformly spaced circular sources (not to scale). The inset shows the two relevant lengths in the uniform circular source field model – the hole diameter and the hole spacing. The dark border of the lava lake is  $\sim 250$  m thick on this scale. (right) Schematic of flow emerging from an infinite plane of circular sources, seen from the side.

thickness cracks with uniform spacing. Because the hole diameter and spacing are so small on the scale of the lake and plume, gas emerging almost everywhere from the lava behaves as if it is expanding from an infinite array of round holes in an infinite plane of crust (this is demonstrated below). Therefore I ignore lake edge effects, and this allows me to take advantage of the symmetry of the problem; I simulate only one fourth of one square of crust around a circular vent, using specular boundary conditions on the side walls of the DSMC domain.

In these simulations (Fig. 4.3a, Fig. 4.4), gas expands out from the circular vents. The flow is expanding into a vacuum directly above the vents, but gas expanding laterally (parallel to the surface) encounters gas from other circular sources. Streamlines converge above the center of regions of non-emitting crust and the flow shocks. These shocks propagate out from the regions above the cool crust and meet above the holes, where expansion begins again. This strongly resembles the shock diamonds seen when supersonic jets exhaust into a background atmosphere (Fig. 4.3b,

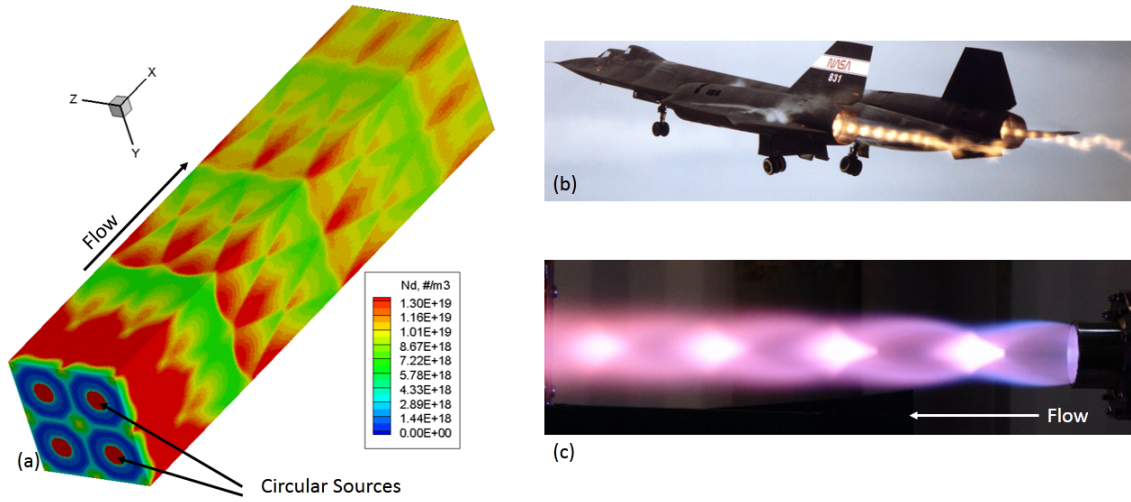


Fig. 4.3: (a) Density contours for  $\text{SO}_2$  gas emerging into a vacuum from an infinite plane of circular sources at Mach 1, expanding supersonically upwards. Four sources are pictured, with contours drawn on two of the domain's symmetry boundaries. Shocks and expansions in the gas flow strongly resemble shock diamonds typically seen in under-expanded supersonic jets in the atmosphere such as in (b) and (c). (b) Shock diamonds behind the engines of an SR-71B. (c) Shock diamonds in a jet at the Swiss Propulsion Laboratory.

c) and the physical explanation is similar except that the expansion waves are reflecting off a symmetry boundary rather than a contact surface. Rarefaction effects do not appear to be important in this near-surface region for reasonable gas densities (the Knudsen number, the ratio of the gas mean free path to a length scale, based on the hole diameter at the surface is  $6 \times 10^{-5}$ , and the Reynolds number, the ratio of inertial forces to viscous forces, is about 6700). The DSMC calculation is somewhat under-resolved, but the quantitative influence of the spatial resolution on observables is small. In the zero viscosity limit, this diamond pattern would persist indefinitely. With non-zero viscosity, and especially if the flow is turbulent, the shock diamonds dissipate and the flow will eventually become laterally uniform. For the virtual vent



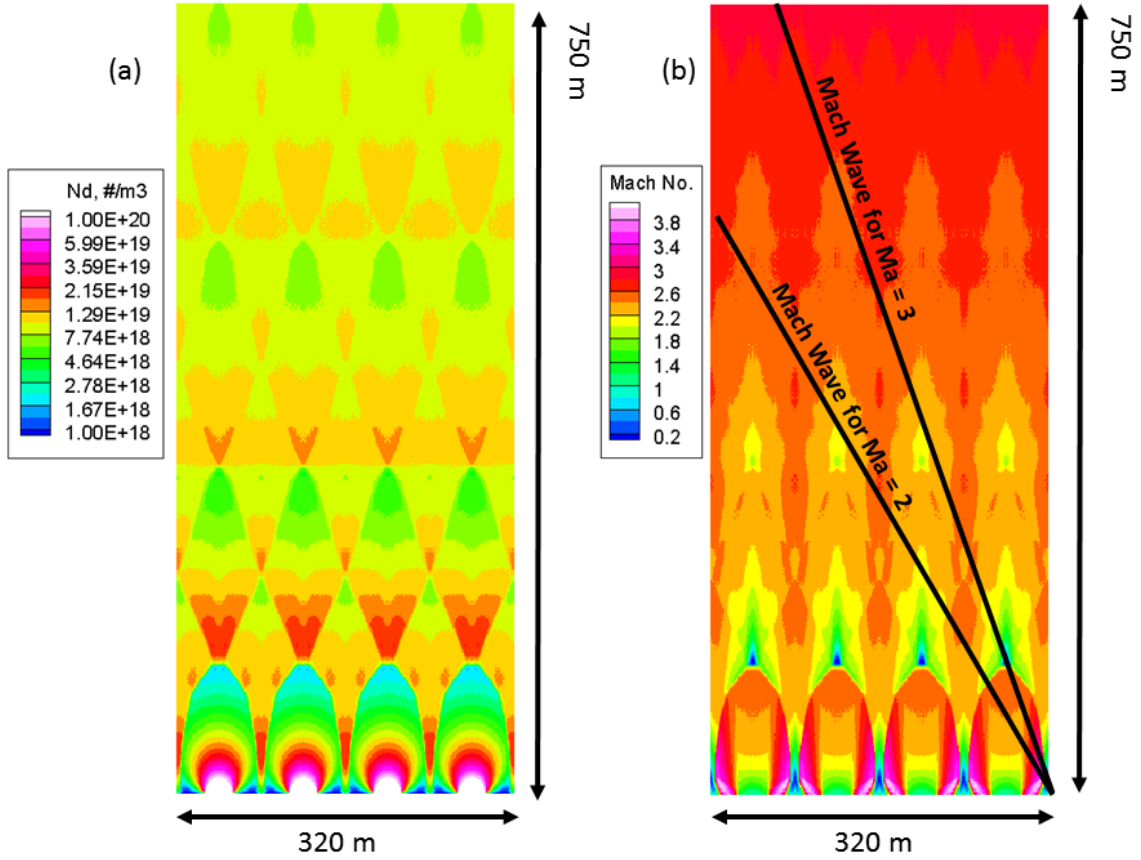


Fig. 4.4: (a) Number density contours for a uniform flow of  $\text{SO}_2$  rising from an infinite plane of circular sources at approximately Mach 1 ( $2.73 \times 10^{-5} \text{ kg/m}^3$ , 1333 K, 465 m/s), which quickly expands to around Mach 3. The shocks are initially strong, but viscosity has driven the flow nearly uniform by 750 m above the vent. (b) Mach number contours for the same flow. Mach waves for Mach 2 and 3 flow are drawn from one edge of the simulation to qualitatively show the possible influence of the edge of the lava lake on the actual flow below the virtual vent.

assumption to be valid, the flow must become uniform at a low enough altitude for the edge of the lava lake to be ignorable, and the flow must become uniform with properties consistent with the virtual vent used in my simulations. Ignoring radiative losses in the dense near-surface gas, the altitude at which the flow becomes roughly

uniform should depend only on a Reynolds number and a length scale. Calculating the Reynolds number (based on the hole diameter) requires a flow density and velocity at the holes. To obtain these, I refer back to the model of nearly stationary gas expanding to Mach 1 over a very short distance just above the lava. The flow velocity at Mach 1 is assumed to be consistent with isentropic expansion of  $\text{SO}_2$  from the lava temperature. For the simulation shown in Fig. 4.3, the gas velocity and temperature at Mach 1 are 465 m/s and 1333 K. This is reasonable if nearly-stationary gas just above the lava surface is in thermal equilibrium with lava at  $\sim 1500$  K, since this is the stagnation temperature of the Mach 1 gas (stationary  $\text{SO}_2$  gas at 1500 K which is allowed to adiabatically expand will reach the Mach 1 conditions given). Given this velocity, a hole diameter and spacing, and total lake area (from Fig. 3.1c), gas density is fixed by a desired mass flux.

Hole diameters can be estimated from terrestrial lava lakes, such as the Erta Ale lake (Fig. 4.1a). Here, diameters appear to range from meters to at most a few tens of meters. Hole spacing too can be very roughly estimated from Fig. 4.1a, but there are three other ways to constrain the spacing by constraining the area ratio (of gas-emitting surface area to total lava lake area). First, if the flow is to expand to approximately the virtual vent conditions by some low altitude, the area ratio must be large enough to prevent the flow from becoming uniform at a higher Mach number than the virtual vent Mach number of  $\sim 3$ . For uniformly spaced circular holes as in Fig. 4.3a, the area ratio is just  $\pi d^2/4D^2$ . The virtual vent Mach number is somewhat arbitrary, but it cannot be too high or the plume would look radically different. This consideration suggests that the area ratio must not be much less than about 0.1; an area ratio of 0.2 would allow Mach 1 flow to expand isentropically to Mach 3 (although the flow here is not really isentropic). Second, if hot cracks or fountains

dominate thermal emission from Pele, the total emitted power is determined by the area ratio and the size of the entire source region. For an average lava temperature at the gas stagnation temperature of 1500 K (the upper range of estimates from the literature, such as McEwen et al., 1998, Davies et al., 1999, and Zolotov and Fegley, 2000, cluster around 1450 K, so this is not very far off) and emissivity of 0.9, my 20 km<sup>2</sup> source region emits the 230 GW found by Davies et al. (2001) if there is an area ratio of 0.045. This area ratio yields a total hot surface area of 1.14 km<sup>2</sup>, which is right in the middle of the 0.4 to 1.6 km<sup>2</sup> range given by Davies (2007) for 1400 K emission. In a third approach, using the results of Zolotov and Fegley (2000) for the pressure of emitted gas (which they find to be between  $10^{-4.74}$  and  $10^{-5.42}$  bar), my assumed mass flow rate and vent temperature require area ratios of  $\sim 0.05 - 0.5$ .

These estimates for the area ratio ( $\pi d^2/4D^2$ ) all agree to within about an order of magnitude, and I chose an area ratio of 0.1 for some example simulations. This area ratio implies a vent gas density of about  $4 \times 10^{-5}$  kg/m<sup>3</sup> and a hole spacing of  $\sim 52$  m for holes  $\sim 28$  m diameter (I choose to err on the side of larger length scales). Example simulations using these parameters produce gas flows which are nearly uniform by 750 m altitude (Fig. 4.4), justifying the virtual vent assumption and my use of Mach 3 flow at the virtual vent. The bulk of the flow quickly expands to between Mach 2 and Mach 3, which justifies the assumption that the gas below the virtual vent behaves as if it is emerging from an infinite lava lake. This is due to the nature of supersonic expansion. Information (such as the location of the edge of the lava lake) only propagates through a flow at the speed of sound, so in supersonic flow the upstream gas (gas close to the surface, in this case) is uninfluenced by downstream conditions. The flow only “sees” the edge of the lava lake once it has reached the altitude at which it intersects a Mach wave drawn from the edge of the

lava lake, where the Mach angle is  $\mu = \arcsin(1/M)$  for some Mach number  $M$ . Some characteristic Mach waves are drawn in Fig. 4.4b to show that almost all of the flow below about 750 m altitude can be treated as emerging from an infinite lava lake. The flow is supersonic nearly everywhere and above Mach 2 above about 200 m altitude. This means that, below  $\sim 750$  m altitude, edge effects are only potentially important within about 320 m of the edge of the lava lake. This distance (and the altitude at which it becomes reasonable to speak of a virtual vent) will be smaller if the surface features at Pele are smaller than simulated here. Therefore treating the flow beneath the virtual vent as emerging from an infinite lava lake is justified.

### 4.3 Near-Vent Flow

The jets of  $\text{SO}_2$  rising from the seven source regions (Fig. 3.2a) exhibit complex three-dimensional structure. In the innermost simulation domains (below 2 km), below the altitude at which the seven sources interact with each other, the geometry of each source region controls the development of the flow in its vicinity. With sources as complex as the ones used here, the resulting flow fields are likewise complex and it can be difficult to predict the flow pattern based on physical intuition. Gas rising from a circular source expands out symmetrically in all directions and becomes less dense as it spreads out and speeds up. With a complex source gas streamlines (lines that follow the bulk velocity of the flow) can converge away from the surface (on the plane between two identical circular sources, for example), and this high pressure region will exhibit higher densities and temperatures. Secondary expansions will occur from these interaction regions. I have previously illustrated this effect of vent geometry on the structure of the flow at higher altitudes using simpler vent geometries such as a long, curved line (McDoniel et al., 2011, or see Appendix A). An elongated vent

will cause flow far from the vent to expand preferentially perpendicular to the major axis of the vent. A curved source will direct flow preferentially in the direction of its center of curvature.

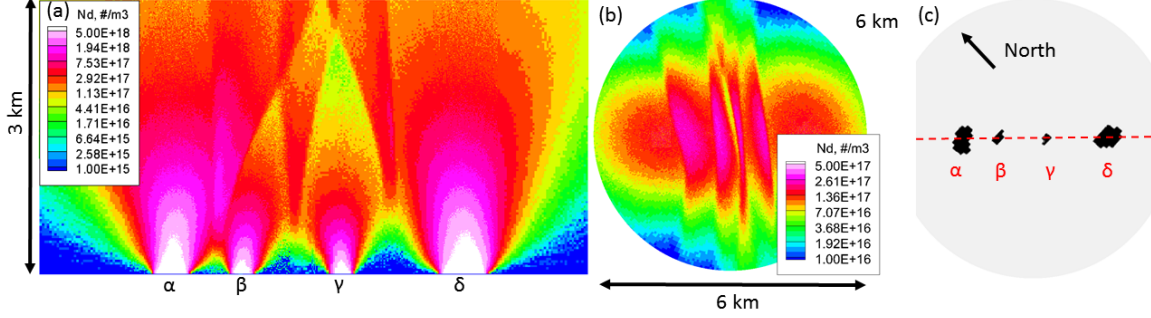


Fig. 4.5: Number density contours for  $\text{SO}_2$  in the immediate vicinity of Source E. (a) A slice of the plume flow seen from the side, along the dashed red line in (c), with gas rising from each of the four collinear vent regions (each is labeled to aid discussion). (b) A constant altitude slice at the top of the domain (3 km altitude). (c) The labeled vent regions, in black, on the same scale as in (b), with a dashed line indicating the orientation of (a).

Fig. 4.5 shows number density contours just above Source E from our simulated vent. The domain is a cylinder 6 km in diameter and 3 km tall. Interactions between the four source regions produce shocks, and at the top of this small domain the flow approximates flow out of a rectangular slot. Fig. 4.5a shows how the two smaller regions ( $\beta$  and  $\gamma$ ) in the middle emit less gas than the two outer regions, and gas density falls quickly as the flow rises from them. Interactions between the regions produce tall, narrow shocks of high-density gas as fast, low-density expanding gas from neighboring sources meets, slows, and turns. This is a process much like that seen between the circular sources in Section 4.2. The two large outside regions ( $\alpha$  and  $\delta$ ) also expand to either side, relatively unaffected by the smaller  $\beta$  and  $\gamma$  regions. Fig. 4.5b illustrates the preferential expansion of gas away from the major axis of the

sources. The two large outer sources are visible as nearly-circular spots on the left and right, and several thin shocks are visible between them. Even though the two smaller central sources are no longer discernible, their presence is partly responsible for the shock structure here. Gas in the shocked regions is expanding much more rapidly to the north and south than it is to the east and west, and this will carry over into later domains. Intuitively, this behavior arises because gas from each of the four sources is continuously flowing outwards in all directions. When the path of the gas is blocked by gas from another source, pressure increases, and the gas is forced to turn out at high speeds in a different direction. Similarly complex flow can be seen just above Sources C and A1 (not pictured). The other four source regions from Fig. 3.1c (A2, A3, A6, and B1) are simple circles, which produce axisymmetric flow before each interacts with other source regions. Source A1 is the largest, and dominates the later domains, but Source E exhibits many of the same types of flow interactions and is easier to visualize. These flows from different source regions are simulated independently of each other at low altitudes, as with the Source E simulation discussed here, and all seven flows are integrated into a larger domain (shown below) before they interact with each other.

The seven flows continue to develop in the next domain starting from an altitude of 2-3 km and begin to interact with each other. This domain is 84 km in diameter on the surface of Io and 20 km tall. The same kinds of phenomena seen between the source regions at E occur when flow from Source E meets flow from Source C (or when C meets A1, etc.), and this pattern of converging flow shocking and then expanding out in another direction (generally north and south, given the arrangement of sources) will continue on a larger scale. Fig. 4.6 illustrates the continued diverging expansion of jets forming from shock regions like those above

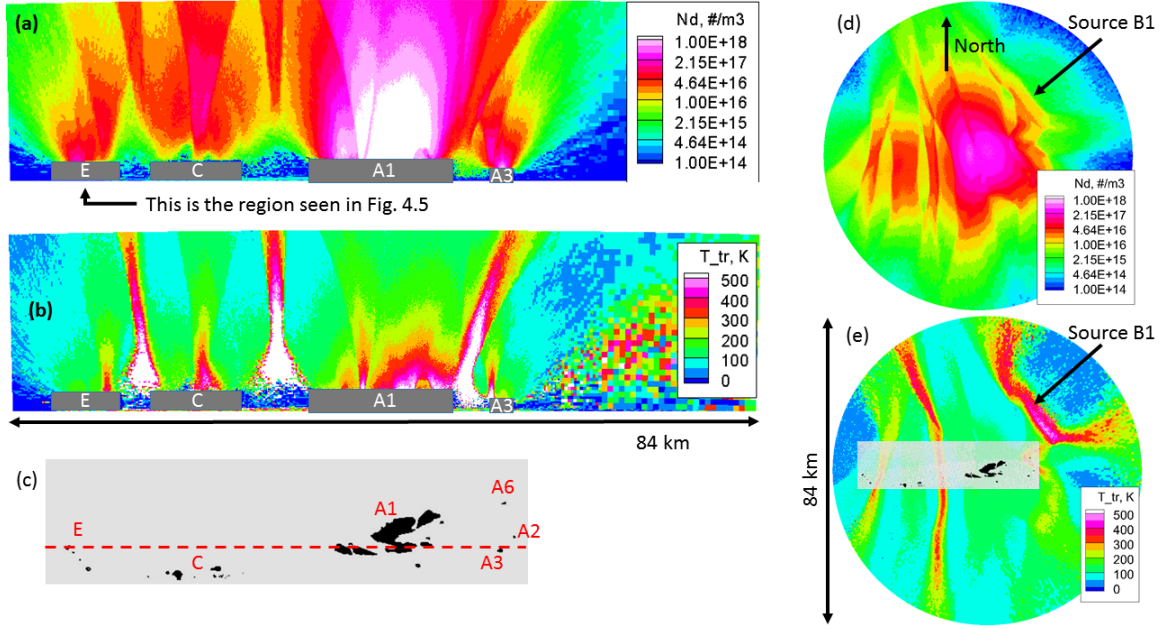


Fig. 4.6: Number density and translational temperature contours for the first large domain. (a) Number density contours on a slice through the middle of the plume, along the red dashed line shown in (c). (c) The source regions used as the virtual vent, in black, except for Source B1. (b) Temperature contours on the same slice as in (a). (d) Number density contours on a constant-altitude slice at the top of the domain (20 km). (e) Temperature contours on the same constant-altitude slice as in (d). The virtual vent is superimposed (Source B1 is not pictured but is labeled).

Source E. In Figs. 4.6a and b, gas emerges from the individual source domains at the boundaries of the labeled gray rectangles (sections of cylinders in 3D space). Shocks form between the source regions, in much the same way that shocks form between the smaller regions that make up Source E. These shocks interact with each other in complex ways, often merging to form a single, stronger shock extending out at a slightly different angle. High-density gas in shocked regions forms jets which expand outwards at high velocities; one jet emerging from Source A1 is of particular interest for the observable plume flow, and it will later be seen to continue moving to the west,

merging with the weaker flows from Sources E and C. The top-down view in Figs. 4.6d and e show how Source A1 is beginning to dominate the flow, as effects of Sources A2, A3, A6, and B1 are difficult to discern. A region of high density is apparent above Source C. Thin shocks with very high density gradients arise between Sources E and C and between Sources C and A1, as well as within the flow emanating from Source A1 alone. The flow has expanded out more strongly to the north and south than to the east and west, but the highest density is still mostly distributed along an east/west line. Temperature contours (Figs. 4.6b and e) are useful for visualizing the interactions of the vent regions. The flow is hottest where flows of gas with very different velocities have converged. Rarefaction matters here; the high-temperature area between Source B1 and the other sources is more diffuse than the other high-temperature areas because Source B1 is far away from the other sources relative to its size. The interaction region around it is of lower density than the others and a sharp shock feature cannot form.

In the penultimate simulation domain (Fig. 4.7), which is 200 km in diameter and 60 km tall, viscous effects and nearly free molecular expansion smear out some, but not all, of the complexity seen at lower altitudes. The asymmetry of the plume is apparent. In Fig. 4.7a, the gas continues to expand upwards while preserving many of the features that arose at lower altitudes, whereas in Fig. 4.7b the plume, viewed from a different angle, might almost seem to be emerging from a circular source (although note that these are thin slices and not line-of-sight integrated column densities). At the top of this 60 km high domain (Fig. 4.7c), the plume flow appears to contain two dominant features - a large diffuse flow of gas rising out of Source A1 and a sharp, elongated shock centered above Source C. However, this sharp jet is not primarily due to Sources E and C; it is formed when the strong oblique shock rising out of



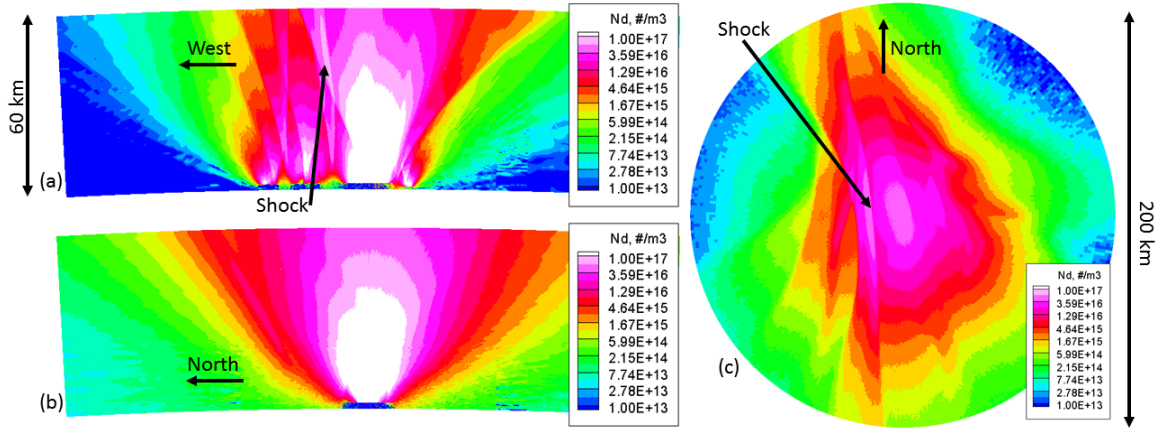


Fig. 4.7: SO<sub>2</sub> number density contours for the first and second large domains, 200 km in diameter and 60 km tall. (a) Contours for an east/west slice through the plume oriented in the same way as the slice in Fig. 4.6a. (b) Contours for a north/south slice oriented at 90 degrees to the slice in (a). (c) Contours on a constant-altitude slice at the top of the domain (60 km altitude).

Source A1 absorbs the flow from Sources E and C. In fact this feature persists even if Sources E and C emit no gas at all; the large-scale structure of the gas plume and the shape of the deposition ring are nearly the same in a simulation of gas emitting from Source A1 only (not presented). By the time gas reaches the top of this domain, there are few collisions occurring, and the residual asymmetry of the flow will persist into the final domain. It is important for the deposition patterns that an axis-switch has occurred; the major axis of the gas flow at this altitude is roughly north/south, whereas at lower altitudes, especially immediately above the virtual vent, the bulk of the gas is located near an east/west line. The gas will continue to expand out preferentially along this north/south axis, explaining the north/south elongation of Pele's red ring.

## 4.4 Gas Canopy and Column Density

Gas in the final domain, which is 1,600 km in diameter and 440 km tall, expands in a nearly free-molecular fashion until it reaches the canopy shock. Knudsen numbers based on the canopy height or on the length scale of density gradients remain small ( $O(10^{-3})$ ) on the plume's centerline just below the canopy, indicating that collisions are somewhat important, but the mean free path is hundreds of meters and temperatures are low. Note that the mean free path is measured in a reference frame moving with the bulk gas; just below the canopy, molecules only collide once for every 1-2 km they travel upwards, on average, because of the flow's large upwards bulk velocity. Gravity is by far the most important influence on the gas just below the canopy. Early in the simulations, before the canopy shock forms, the gas continues to an altitude of  $\sim 500$  km before falling back down. This falling gas collides with still-rising gas and causes the development of the canopy shock. Thereafter, rising gas sustains the canopy shock and replenishes gas above it as canopy gas flows around the sides of the plume to the ground, forming the deposition ring.

The plume flow in this final domain is notable for its continued asymmetry. Longitudinal slices of the plume taken at different angles are different from each other. Fig. 4.8c shows a north/south slice of the plume, nearly through the major axis of the deposition ring. At this angle, the plume appears regular and might be mistaken for the output of a large, round hole. The rising gas supports a round canopy that curves over the plume until it intersects the surface. However, in Fig. 4.8a, several irregular flow features are apparent. The oblique shock seen at lower altitudes continues merging with expanding jets from Sources E and C and gives rise to a high-density finger of gas which displaces the canopy shock by about 25 km.

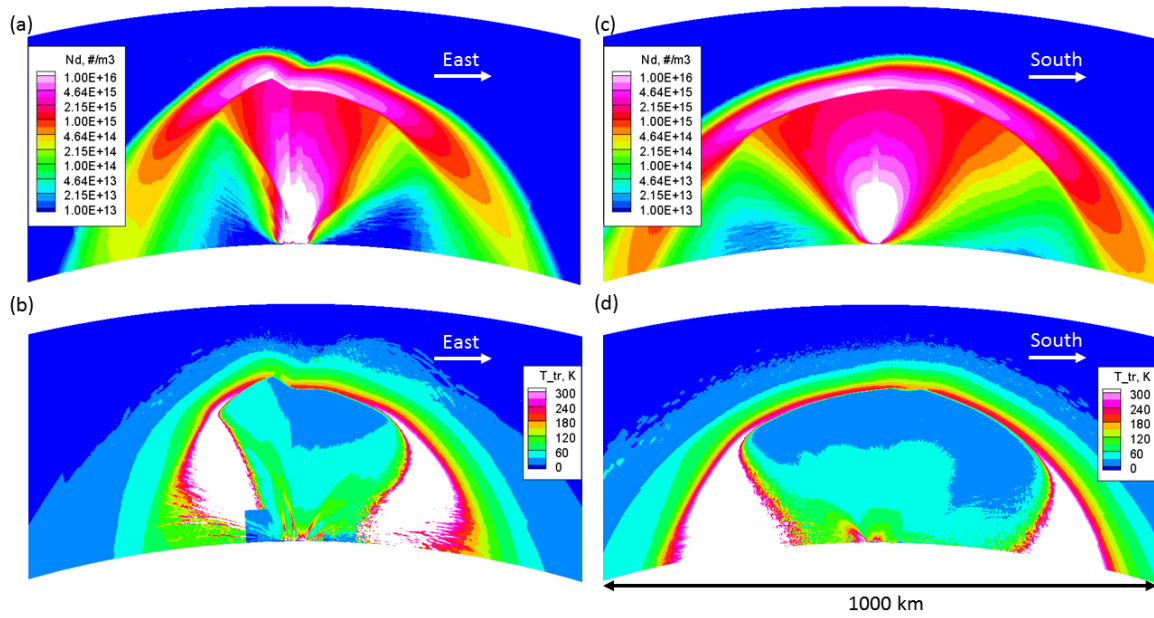


Fig. 4.8: SO<sub>2</sub> number density and temperature contours for all three large domains, 1,600 km in diameter along the surface of Io and 440 km tall. (a) Number density contours on an east/west slice showing the continued expansion of the smooth flow in Fig. 4.7. (b) Translational temperature contours for the slice in (a). (c) Number density contours on a north/south slice. (d) Translational temperature contours for the slice in (c).

The canopy is also much less developed at this angle and becomes less dense more quickly as the gas falls around the sides of the plume to the ground. This is due to the axis-switching behavior pointed out at lower altitudes (Section 4.3); less gas expands out along the east/west axis. The canopy intersects the ground closer to the plume's source as well, and this will be seen clearly in the simulated deposition pattern.

Number density along the plume's centerline falls to about  $1.6 \times 10^{15} \text{ m}^{-3}$ , which is lower than the density at the virtual vent by a factor of almost 4,000 (and lower than the density at the lava lake by a factor of about  $1.6 \times 10^5$ ), before shocking back up to about  $10^{16} \text{ m}^{-3}$ . This may appear to be a surprisingly weak expansion

(the flow is only about Mach 8 just below the canopy shock), but on this scale gravity plays a large role and removes a great deal of energy from the gas (roughly half of the kinetic energy in the gas at the vent has been lost by 350 km altitude). Peak centerline vertical velocity (of about 1,000 m/s) was actually reached at around 50 km altitude. Gravity outpaces continued expansion above this altitude. Figs. 4.8b and d show the gas cooling as it expands upwards before heating in the canopy after it shocks. High-temperature regions closer to the vent were used as markers for the interaction of source regions. Here, the extremely “hot” regions inside the canopy to either side of the vent indicate where the flow is highly non-equilibrium (Zhang et al., 2003). Because densities in these regions are so low and collisions are so rare, gas falling from the canopy passes through gas expanding outwards and upwards directly from the vent. The resulting velocity distribution is non-Maxwellian, effectively being two non-interacting streams of gas, and so the computed kinetic temperature (which is by definition the root mean square deviation of molecular velocities from the mean gas velocity) must be interpreted with caution. The cold artifact seen just to the left of the source in Fig. 4.8b illustrates the one-way coupling between the domains; this is the temperature of only the expanding gas in the penultimate domain, unaffected by gas falling from the canopy in the final domain.

Remote observations of plumes visualize line-of-sight columns of particles rather than slices, and one might suspect that integration in space would smear out much of the asymmetry described above. However, this is not the case, and simulated north/south column densities look quite different than simulated east/west column densities (Fig. 4.9). The strong oblique shock feature is less visible (though still apparent in Fig. 4.9a) in an integrated image, but the three-dimensional nature of the canopy shock is clearly evident, and the kink in the canopy seen in Fig. 4.8a is

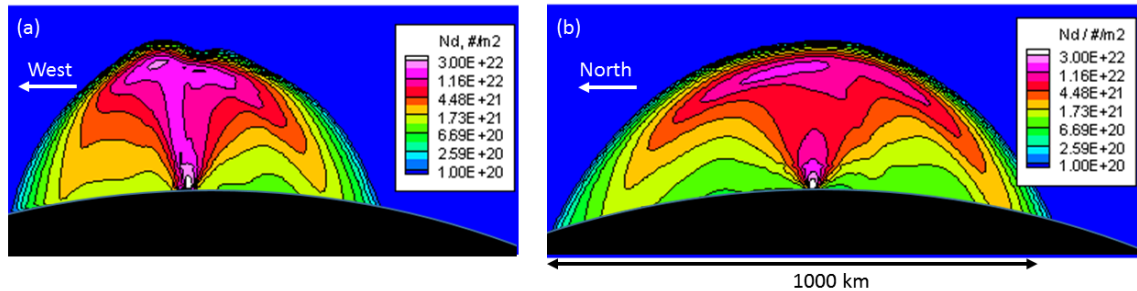


Fig. 4.9: SO<sub>2</sub> line-of-sight integrated column densities. (a) Column density seen from due south. (b) Column density seen from due west.

still visible. Unsurprisingly, the regular slice of Fig. 4.8c predicts the regular column density of Fig. 4.9b; here the plume appears similar to axisymmetric plume simulations (Zhang et al., 2003), with smooth expansion to a relatively uniform canopy. That such asymmetry is possible suggests that it will be difficult to draw conclusions about the structure of plumes from observations taken from only one viewing angle. Very fine particles in the plume which remain fully entrained in the gas flow will exhibit similar line-of-sight column densities. Condensate, which may preferentially form/grow in the canopy, should exhibit these asymmetries. Heavier dust, however, will decouple from the gas flow and may behave differently, so further simulations are required to explain observations of large particles (Chapter 5.6).

## 4.5 Gas Deposition

In my simulations, gas from the canopy falls to the ground in a narrow band, creating a ring of intense gas deposition. As discussed earlier, if we assume that the observed red ring is the result of deposition of S<sub>2</sub> or other molecules or particles that track the gas, then the simulated gas deposition can be directly compared to the observed red ring, at least in a qualitative sense. Simulated deposition images are

also a useful way of visualizing the three-dimensional canopy, since the ring appears where the canopy intersects the surface and the simulated deposition rate (mass flux to the surface) is roughly proportional to the canopy density at the surface (it varies somewhat depending on the downward velocity in the canopy at the surface, but this is nearly constant all around the ring). Simulated deposition patterns are obtained by recording all particles that impact the surface over a period of 1,000 seconds once the plume has reached a steady state (i.e. with a stable canopy shock and instantaneous deposition rates that only vary with statistical noise).

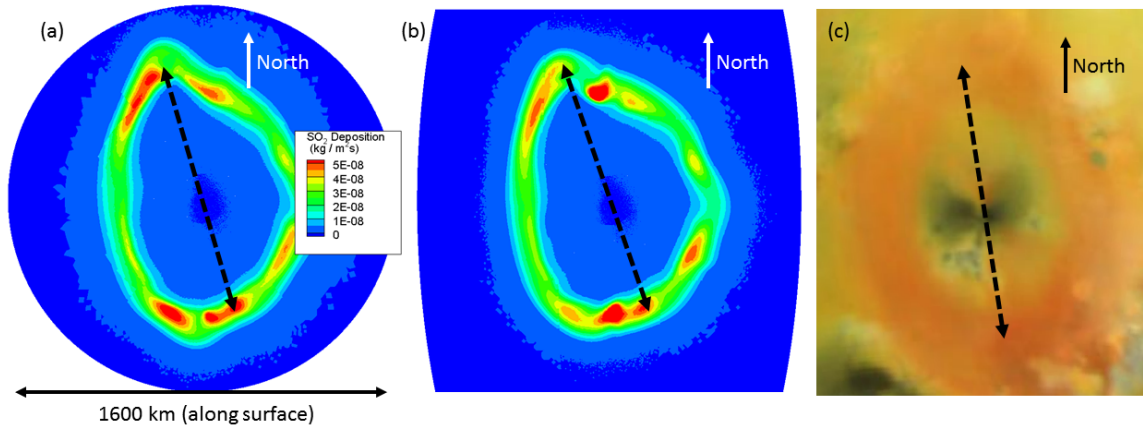


Fig. 4.10: Gas deposition patterns. (a) Contours of the deposition rate of SO<sub>2</sub> on the surface (in kg / m<sup>2</sup>s) for the plume simulations. (b) Contours of the deposition rate of SO<sub>2</sub> when fictitious forces are implemented to account for the non-inertial reference frame. The plume shown here was simulated at the equator of Io. (c) Pele's ring on Io's surface, as seen from the same head-on perspective used for the simulations, drawn from Williams et al. (2011). Lines of maximum diameter are drawn on all images.

The simulated deposition ring (Figs. 4.10a and b) is egg-shaped, with a larger diameter, higher deposition rate, and increased ring thickness to the north and south of the vent than to the east and west, as suggested by the slices shown earlier. It is sharper in the north and south, with particularly intense deposition at these ends.

The peak deposition rate is roughly  $7.5 \times 10^{-8}$  kg/m<sup>2</sup>s, and in every direction from the vent there is some area where deposition is more intense than  $2 \times 10^{-8}$  kg/m<sup>2</sup>s. The effect of Io's rotation and revolution about Jupiter causes a change in the ring's orientation, albeit a small one of just a few degrees. Fig. 4.10a shows the plume in a domain 1,600 km across centered at the north pole, while Fig. 4.10b shows the same plume centered at a point on the equator, with fictitious forces included to account for Io's rotation and revolution about Jupiter.

The shape and orientation of the simulated ring are in good qualitative agreement with observation. Direct comparisons are difficult to make because, on this scale, the curvature of Io is important. Lacking an observation from directly overhead, a simulated image from directly overhead can be compared to a composite of observations such as the global map of Williams et al. (2011), as in Fig. 4.10c. This image was obtained by wrapping the Williams et al. map around a sphere and orienting it such that Pele's source is the closest point to the viewer and a vertical line down the center of the image corresponds to a line of constant longitude - it is an azimuthal orthographic projection centered on Pele. Quantitative comparisons can also be made by referencing exact latitude and longitude values from the Williams et al. map. This allows comparisons of the simulated (a) and observed (c) deposition patterns, although this comparison will still be inexact due to the diffuse nature of the plume's deposition pattern. I choose points in the ring due north, south, east, and west of the source, as well as at the ends of the longest diameter. The simulated ring is  $\sim 8\%$  wider than the observation from east to west. It is  $\sim 4\%$  too long north to south. It is  $\sim 3\%$  too long along its maximum diameter, which is  $\sim 1,000$  km (this is a projected distance that does not account for the curvature of the moon). I can also compare the angle between due north and the maximum diameter. In the observation

I find that this angle is  $\sim 15$  degrees; in my simulation this angle is  $\sim 14$  degrees. The orientation of the simulated ring is almost exact, and several measures of ring size are very close.

These simulations do not include a background atmosphere, planetary winds, or interaction with Jupiter's plasma torus. The excellent agreement between the simulations presented here and observations suggests that these excluded phenomena are unimportant to the deposition process. This might be because deposition occurs mostly at night when the background atmosphere is negligible, while plasma is absorbed in the canopy, inflating an upper layer but not strongly affecting the bulk of the gas flow to the ground. These issues will be addressed in Chapters 6 and 7.

## 4.6 Explaining Other Observations

The remarkable agreement between the simulated and observed gas deposition ring strongly suggests that the plume model which produces that simulated ring is essentially correct. However, there are two features of observations of the gas at Pele that have not been explained.

First, fans of orange/red deposition are visible to the north and south of the vent in observations. While there is some deposition in similar locations in the simulations, and more than there is to the east and west of the vent, it is not nearly as intense as the ring deposition. This difference could be due to several factors. The observed ring deposition may be saturated, edge-of-the-lava-lake effects below the virtual vent may be important for explaining gas depositing near the vent (see Section 4.2), or the canopy may shield the inside of the ring from overlaying deposition by atmospheric gas. Further, the simulations contain suggestive features which



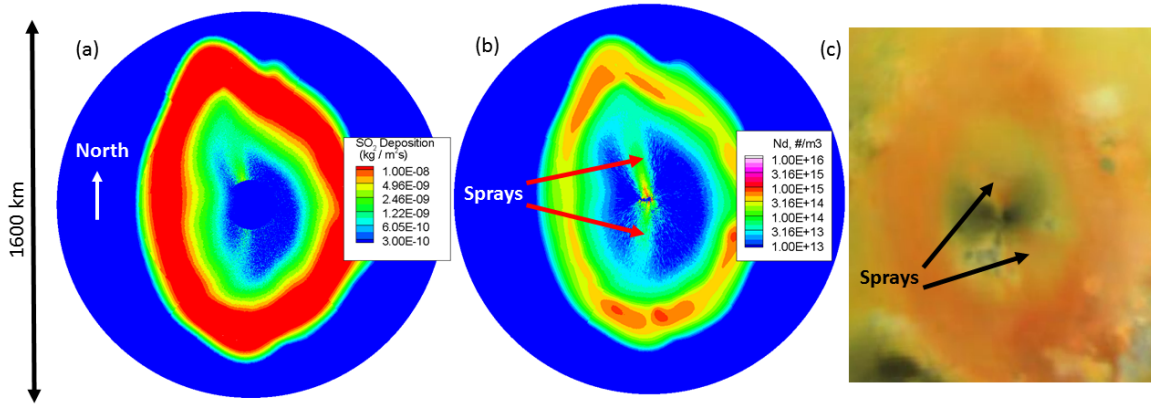


Fig. 4.11: (a) Recolored gas deposition pattern from Fig. 4.10a. (b) Number density contours for a constant-altitude slice of the plume  $\sim 500$  m above the surface. (c) Galileo image of Pele.

might explain these red sprays with the addition of some plausible assumptions. Fig. 4.11 presents gas flow near the surface in a slightly different way than the earlier Fig. 4.10. Fig. 4.11a is simply a rescaled Fig. 4.10a, with an exponential color bar instead of a linear one and with saturated gas deposition in the ring. This reveals low-density sprays to the north and south of the lava lake, where deposition exists even if it occurs at a rate an order of magnitude smaller than deposition in the ring. If the observed ring is in fact saturated with  $\text{SO}_2$ , such that the much lower deposition rate in the sprays can produce nearly as intense of a red coloring on the surface, then my current simulations suffice to explain the observation. Fig. 4.11b is a constant-altitude slice of gas density in the plume, as in Figs. 4.6d or 4.7c, so it is not directly comparable to mass deposition rate (which is the product of near-surface gas density and downward velocity). The densities shown are averages of the gas density in the first  $\sim 1$  km above the surface. Here, the jets are much more apparent and are nearly as dense as gas in the canopy where the canopy intersects the surface (at the ring).

The difference between Figs. 4.11a and b is due to the difference in gas velocity in the sprays and in the ring. Gas in the large ring is falling down through the canopy, whereas gas in the sprays is flying outwards from the lava lake nearly parallel to the surface of Io. However, because the gas is this dense at such low altitudes, a small increase in ground elevation over the 500 km between the lava lake and the large red ring would enhance deposition from these gas sprays. If the lava lake is just 2 km lower in elevation than the ring, every gas molecule in the spray near the surface in Fig. 4.11b would deposit inside of the large ring. The sprays can also be seen in Fig. 4.8c where gas on either side of the vent is much closer to the surface than the gas in Fig. 4.8a.

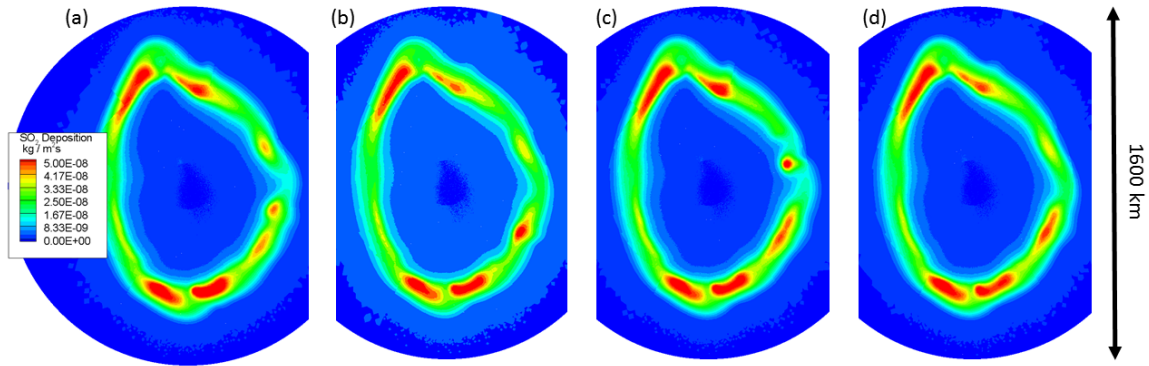


Fig. 4.12: Gas deposition rates for four nominally identical plume simulations. All plumes are run in the largest domain for 6,000 seconds before sampling the deposition rate over 500 seconds.

Pele's deposition ring is also not constant over time (Geissler et al., 2004), and my simulations cannot capture this long-term variability, although some simulations (Fig. 4.12) suggest that unsteadiness due to instability in the flow is possible even with a steady source. Some preliminary results (not presented) even suggest that small fluctuations at the vent or in the canopy can cause a transient buckling inward of the

southern edge of the ring as seen in the survey of surface changes by Geissler et al., but this requires further study. I can also suggest an explanation for the observation that the gas ring at Pele sometimes buckles inwards (Geissler et al., 2004). The work presented here has attempted to simulate a steady plume with constant conditions at the lava lake. In some preliminary simulations (not presented) I have seen that small changes to the vent conditions and geometry can produce small changes in the gas deposition. However, even in the simulations presented here the ring is seen to wiggle over time; the gas flow is never quite steady. This is reasonable for a Monte Carlo simulation of a supersonic jet with a high Reynolds number. Small changes in simulation parameters can produce subtle changes in the ring, even for nominally identical gas plumes sampled at the same times (Fig. 4.12). In simulating the various dust size distribution basis functions used in Chapter 5.1, nominally identical gas plumes were simulated (to determine the drag on the dust particles). These gas simulations differed only in random number generation and some subtle differences in the structure of the computational grid (due to automatic load-balancing; see Chapter 3.2.4). The various rings in Fig. 4.12 are all nearly identical in shape and orientation, but red regions of particularly intense deposition differ slightly between simulations. The eastern edge of the ring undergoes the most noticeable change from simulation to simulation, exhibiting sharp buckling in Figs. 4.12a and c with a region of particularly intense deposition in Fig. 4.12c at around 3 o'clock. This suggests that some of the unsteadiness in the observations, particularly the buckling seen at the southern edge of the ring, might be explained by occasional slight changes at the lava lake. This also suggests that some of the differences seen between Figs. 4.10a and 4.10b may not be entirely attributable to corrections for the non-inertial reference frame.

## Chapter 5

### Dust Grains in the Night-side Pele Plume

#### 5.1 Overview

Dust particles of sizes between 20 nm and 10  $\mu\text{m}$  are created in the flow at the virtual vent with velocities chosen according to the function determined in Section 5.2. Their real number density is assumed to be arbitrarily small so that they do not affect the gas flow. Dust particles have a density of 800 kg/m<sup>3</sup>, which is a little on the low side, but which is intended to partially account for the difference between real grain geometries and the simulated spherical particles. Irregularly-shaped real grains will have larger aerodynamic cross-sections than spherical particles of the same mass. Results here were previously published in McDoniel et al. (2015).

#### 5.2 Dust Inflow Conditions

The model of the flow just above the lava lake from Chapter 4.2 can also be used to inform the input conditions for dust at the virtual vent. For simulating dust in the giant plume, I need a boundary condition at the virtual vent that gives the dust velocity distribution (perhaps as a function of particle size). Here, I argue that models based only on gas conditions at the virtual vent tend to overestimate the velocities of large particles. A consideration of the flow of dust below the virtual vent, especially for large particles which can decouple from the gas, is necessary to constrain the vertical and (especially) tangential velocities of dust particles as they

enter the giant plume simulation domain.

Fig. 5.1a compares the vertical velocity of dust particles at the virtual vent as a function of particle diameter for three different “equilibrium” models of dust velocity. By assuming that all dust is entrained at the gas velocity at the virtual vent (850 m/s), we are likely to greatly overestimate the speed of heavier dust particles, since all particles come from the lava lake and drag from the expanding gas is insufficient to entrain heavy dust. Assuming that grains are at terminal velocity in the gas at the virtual vent, with drag and gravity balanced so that the dust is not accelerating, is also likely to produce errors (this still yields an upwards velocity because the gas velocity is so high) because the system is not actually in equilibrium in this sense. The heavy dust does not have time to reach terminal velocity as it rises because the gas is accelerating so quickly. Instead, I directly simulate the flow of dust below the virtual vent. I use a steady gas flow-field (Fig 4.3a, 4.4) and seed dust in the circular vents shown in Chapter 4.2, allowing it to travel up to the virtual vent altitude while experiencing drag from the gas. Dust that escapes the top of the 750 m domain is sampled, and from these samples I infer a velocity distribution function for dust at the virtual vent, which varies with particle diameter. I then sample from this velocity distribution when creating dust particles at the virtual vent for the giant plume simulations. The mean of this “Circle Model” distribution as a function of particle size is also shown in Fig. 5.1a. For almost all particle sizes, these mean velocities are lower than the velocities obtained from either of the models which used only information at the virtual vent (dust at the gas speed or dust at terminal velocity in the gas). Dust velocities overshoot the virtual vent velocity slightly at small particle sizes, mostly because the “Circle Model” expands slightly too much and is not fully uniform at 750 m, but this is unimportant because these small particles are still

coupled with the gas at the virtual vent and quickly decelerate in the large plume simulations.

As mentioned above, I initially chose to model the dust as fully coupled with the gas at the circular vents. Dust was created at the bulk gas vertical velocity of 450 m/s with zero tangential velocity. As seen in Fig. 5.1a, this model led to significant slip ( $\sim 350$  m/s) between the vertical velocities of the bulk gas flow and heavier dust particles at the virtual vent. Decoupling of the vertical velocities suggests that decoupling of velocity tangent to the surface is possible as well. I also find that the simulated line-of-sight integrated column densities for heavier dust are pencil-thin and do not compare well with the Voyager observation (Fig. 5.8a) when particles are introduced at the virtual vent with no tangential velocity. While the gas flow above the virtual vent is dense enough to strongly influence small particles, large particles can be almost entirely decoupled from the gas flow at the virtual vent such that they rise and fall almost ballistically in the plume simulation, so that if they begin at the virtual vent with no tangential velocity they rise straight up before falling back down on top of the lava lake. Large particles must therefore have some tangential velocity at the virtual vent, which the model of flow just above the lava lake must account for.

In any case it is unrealistic to assume that large particles have zero tangential velocity as they leave the surface of the lava lake. I imagine the surface bubbling like a pot of boiling oatmeal. Bubbles burst, releasing hot gas and spattering material in all directions. Some (primarily sulfurous) particles may condense out of vapor in the gas at low altitudes, coupled to the gas, or fine silicate particles may emerge from thin filaments of lava, and these particles will begin their trajectories at the gas velocity

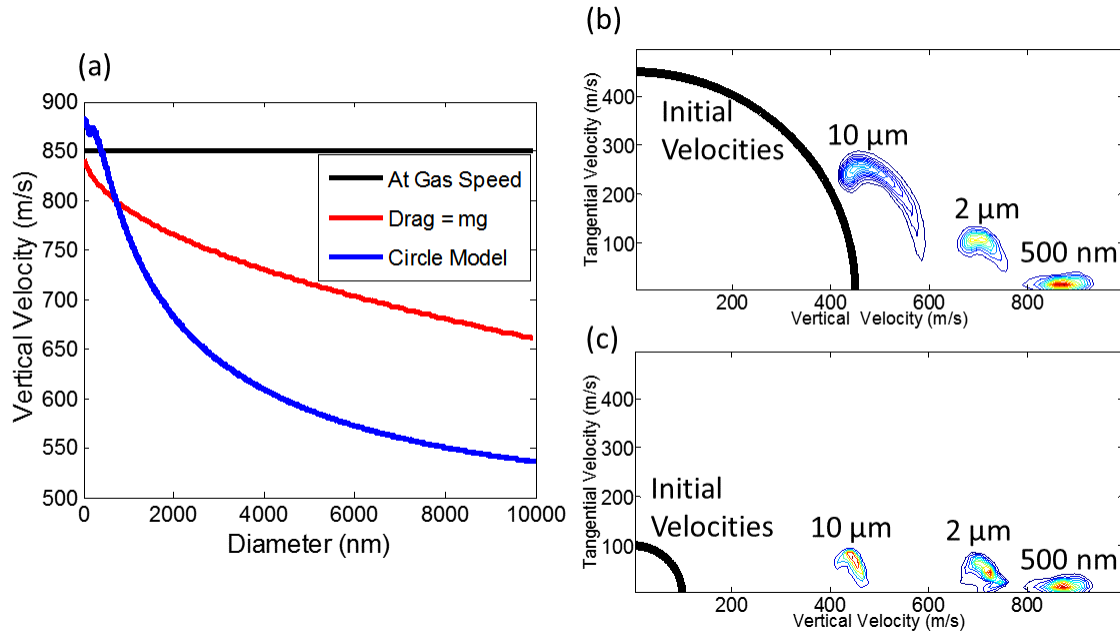


Fig. 5.1: Dust velocity as a function of particle size at the virtual vent for a variety of possible models. (a) Comparison of vertical velocity at the virtual vent for three “equilibrium” models. The black line shows the gas velocity of 850 m/s at the virtual vent. The red line shows the terminal velocity of dust in the gas at the virtual vent (calculated using an expression for the drag coefficient from Bird, 1994). The blue line shows the average vertical velocity at the virtual vent altitude dust when particles are created at the lava lake surface with 450 m/s vertical velocity and allowed to rise. (b) The 2D velocity distributions at the virtual vent altitude for three sizes of dust when dust is created at 450 m/s oriented in a random direction. The initial velocities of all dust particles lie along the solid black line. (c) The 2D velocity distributions for three sizes of dust when dust is created at 100 m/s oriented in a random direction.

or will quickly accelerate to the gas velocity. However, larger particles will only be introduced in the flow via the spattering mechanism, or perhaps will detach from crust at the edge of a hole, and will often appear with significant tangential velocity (and with some slip in vertical velocity too, relative to the bulk gas).

It is difficult to determine the velocity distribution of dust particles at the

lava surface; little is known about particle velocity distributions even for terrestrial volcanoes. Therefore, I examine the sensitivity of the dust velocities at the virtual vent to how they are input at the circular vents on the surface by simulating two cases in which dust particles are initialized with some velocity tangent to Io's surface (Figs. 5.1b and c). Dust particles enter the domain with a constant speed and a random direction (the velocity vector is uniformly distributed over the surface of a hemisphere), as appears reasonable for particles being ejected from the surface by bursting bubbles or sprays of lava. This produces large slip velocities between much of the dust and the bulk gas flow in each DSMC cell even very near the surface. Gas flow below the virtual vent remains dense enough to significantly deflect even the largest  $10\text{ }\mu\text{m}$  particles used in my simulations, and it will tend to accelerate all dust normal to the surface. However, the bulk gas flow hardly expands laterally below the virtual vent, and at the virtual vent the bulk gas flow is nearly uniformly vertical, so drag will tend to reduce the tangential/horizontal velocity of dust in the flow from the surface up to the virtual vent.

Comparing Figs. 5.1b and c we see that the velocities of small ( $< 2\text{ }\mu\text{m}$ ) dust particles at the virtual vent are not very sensitive to the choice of input conditions. Whether they are created at an initial speed of  $450\text{ m/s}$  (Fig. 5.1b) or  $100\text{ m/s}$  (Fig. 5.1c),  $500\text{ nm}$  particles reach the virtual vent with vertical velocities just over  $850\text{ m/s}$ , just as in the zero tangential velocity model in (Fig. 5.1a), and with a mean tangential velocity of less than  $50\text{ m/s}$ . It is clear that such small particles are coupled to the gas at the virtual vent. The vertical velocities of even  $10\text{ }\mu\text{m}$  particles are also quite insensitive to the choice of input conditions, and so the large particles will rise ballistically to a characteristic altitude in the plume regardless of their initial speed at the surface. The tangential velocity of large particles is very



sensitive to the choice of input condition, however, and tangential velocity affects their deposition patterns, which are discussed in Section 5.4, and their line-of-sight integrated column densities (Section 5.6). Column density observations allow us to constrain the tangential velocity of large particles at the virtual vent to some extent, but this remains a significant source of uncertainty. For the large plume simulations below, I chose to model the dust as emerging from the circular vents at 450 m/s with a random direction (the case shown in Fig. 5.1b). These velocity distributions were sampled in order to initialize dust at the virtual vent.

### 5.3 Dust Flow by Size

Even though dust particles in the real plume will exhibit a wide distribution of diameters (and shapes and compositions) spanning the entire range from 20 nm to 10  $\mu\text{m}$ , simulations of a set of narrow distributions are useful for understanding how the particle diameter affects its motion through the plume. All distributions shown in this subsection are uniform, taking on all integer nanometer values in their range (e.g. for a 20-24 nm distribution, 20% of the particles will be 20 nm, 20% of the particles will be 21 nm, etc.).

While very small dust particles ( $\sim 1$  nm diameter) should track the gas flow, larger particles tend to exhibit trajectories characterized by largely ballistic motion subject to a small drag force from the bulk gas flow which acts to nudge the dust in the direction of the gas flow. Dust of up to about 1  $\mu\text{m}$  is strongly coupled to the gas at the virtual vent and sizes up to several microns are weakly coupled (Section 5.2), and all simulated sizes decouple from the gas flow to some extent as altitude increases (and gas density falls). This results in dust particles encoding information from the

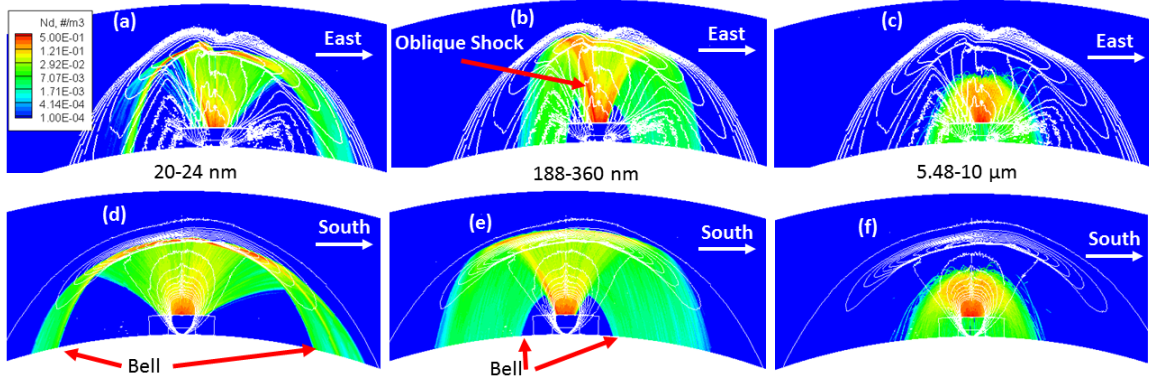


Fig. 5.2: Number density contours for several narrow size distributions of dust grains, with superimposed line contours of the gas slices from Fig. 4.8. (a), (b), and (c) show slices for three distributions seen looking north, while (d), (e), and (f) show slices for the same size distributions seen looking east. Only flow in the final simulation domain is shown and the absolute value of the number density is arbitrary due to my low mass loading assumption, but relative magnitudes are valid.

gas flow at low altitudes, preserving low-altitude features of the gas flow better than the gas itself does, with the degree of preservation depending on particle size.

Fig. 5.2 shows plume slices for some sample particle size distributions. Asymmetry is obvious for the two smaller size distributions, but not for the largest. Particles from the smaller distributions reach a maximum altitude at approximately the canopy height, whereas particles from the largest distribution, having decoupled near the virtual vent, travel ballistically to a much lower maximum altitude. Smaller particles, which remain coupled to the gas flow, are dragged upwards by expanding gas, attaining higher maximum altitudes. However, the maximum altitude of the dust in (b) and (e) is actually slightly higher than that for the lighter dust in (a) and (d). The smallest particles adjust to the gas quickly, and stop rising soon after encountering stationary gas in the canopy. Somewhat larger particles, while still partially coupled to the gas, rise through the stationary canopy for some time before drag and gravity

bring them to a halt. The largest particles (Figs. 5.2c and 5.2f) do not even reach the canopy before beginning to fall back to the surface.

The small particles in Figs. 5.2a and 5.2d are nearly fully-entrained in the gas flow. Flow features in the dust correspond well to those in the gas, even tracking the canopy all the way down to the surface. The larger particles in Figs. 5.2b and 5.2e have decoupled to some extent before reaching the canopy. The oblique shock feature seen in Fig. 4.8a is much more apparent in Fig. 5.2b, because the partially decoupled dust preserves this sharp feature from lower domains (Fig. 4.7a) better than the gas does. These particles are also too large to be entrained in the canopy, and they fall out of the canopy close to the central axis of the plume, impacting the surface much closer to the lava lake than does the gas. However, particles do not move ballistically as they travel back down through the plume. As seen in Fig. 5.2e, a bell forms around the source of the plume where dust does not reach the surface (this phenomenon in axisymmetric plumes was reported in Zhang et al., 2004). This is due to falling dust being deflected to the sides by rising gas. This deflection is also visible in Fig. 5.2d, but in Fig. 5.2f the particles are so large that the gas does not prevent them from falling straight down into the inner domains (the influence of rising gas in the inner domains on this dust is not simulated). The largest particles (Figs. 5.2c and 5.2f) also decouple from the gas flow before asymmetry develops on a large scale and so they preserve information from below the virtual vent. The trajectories of these particles are therefore most sensitive to the choice of dust input condition from Section 5.2 and are almost totally insensitive to developments in the gas flow above the virtual vent.

## 5.4 Dust Deposition by Size

An important result of the tendency of dust to preserve gas flow features from low altitudes is that dust does not exhibit axis-switching behavior to the same extent as the gas, except for the smallest particles. Relatively more (large) dust is directed to the east and west of the lava lake, and this can produce deposition patterns that look nothing like the deposition ring left by the gas. These deposition patterns, like the dust density contours from Section 5.3, are strong functions of particle size; we see a transformation from patterns that resemble the gas ring for very small particles, through stripes to the east and west of the lava lake for medium sizes, and finally to roughly axially-symmetric bullseyes on the surface for the largest particles.

Fig. 5.3 shows the deposition patterns produced by five different size distributions of dust particles which are uniformly distributed in the gas flow at the virtual vent. The smallest particles (Fig. 5.3b) reach the surface in a thin ring with features corresponding to those of the gas ring. This supports the conclusion from Section 5.3 that these small particles remain coupled to the gas flow throughout the entire plume.

As particle sizes increase, dust deposits more densely in a smaller area. The slightly larger dust in Fig. 5.3c still falls to the surface in a ring which resembles the gas ring, but many particles are falling out of the canopy before reaching the surface. However, there is still no dust deposition at all in some region surrounding the lava lake (for all but the largest size distribution). These “donut holes” correspond to the bell shapes seen in the dust flow in Fig. 5.2; falling dust that was initially entrained in the gas flow at the virtual vent cannot impact the surface in these donut hole regions because of deflection by rising gas.

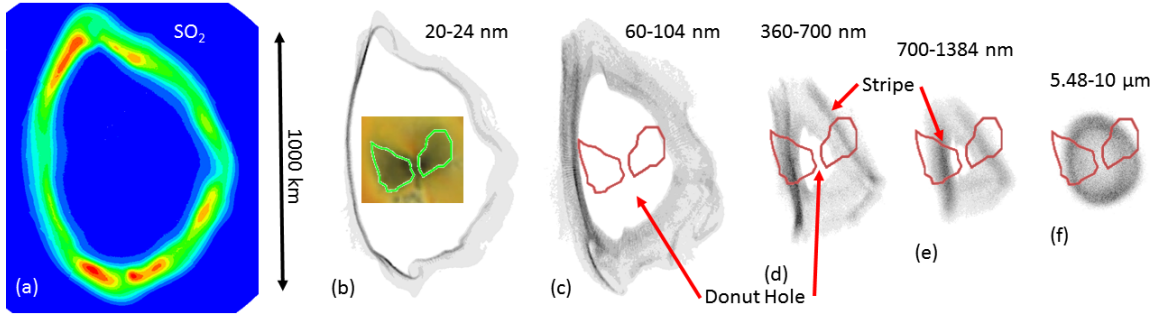


Fig. 5.3: Simulated deposition patterns for various sizes of dust grains, with the gas deposition ring for scale in (a). Pixel darkness is proportional to deposition rate and is normalized by the total number of simulated particles of each diameter. The target region and observation are shown on (b) and the target region is outlined on the other simulated dust deposition patterns.

In Fig. 5.3d, the particles deposit in a much smaller pattern than seen in Figs. 5.3b and c. Rather than forming a clear ring shape, these particles primarily fall in two long stripes to the east and west of the lava lake, with light deposition between them (except for in the “donut hole”). The stripes form because these particles decouple at low altitudes in the plume such that they preserve low-altitude gas features (Section 5.3). These medium-size particles are initially swept along by the gas into the shock structures seen in Chapter 4.1, but then decouple and are not dispersed along with the gas as the gas continues to expand. These concentrated sheets of dust particles continue on nearly ballistic trajectories until they form stripes on the surface. This feature is seen in the dust flow in Fig. 5.2b. As particle size continues to increase, as in Fig. 5.3e, this distinctive deposition pattern continues to shrink in size.

The largest particles (Fig. 5.3f) fall to the ground in a roughly symmetric spot or bullseye pattern. This is due to the early decoupling of large particles, which are not swept into the gas shocks in the first place, and corresponds to the nearly

symmetric dust trajectories in Figs. 5.2c and f. Deposition is somewhat more intense in a ring around the outside of the spot. This ring is largely an artifact of the initial velocity distribution chosen for the particles (Section 5.2). It is possible that a distinct donut hole would be seen even for the largest dust particles if deflection from rising gas in the inner domains (through which these large particles fall) were simulated.

## 5.5 Best-Fit Dust Size Distribution

As described in Chapter 3.2.2, I can obtain a best-fit size distribution by simulating a series of dust size distributions like those in Sections 5.3 and 5.4 and finding the linear combination of their deposition patterns which best matches the observed region (from Fig. 3.3). Recall that I intend to compare to a target region consisting of the “butterfly wing” regions to the east and west of the lava lake (Fig. 3.3d), excluding the immediate vicinity of the lake (so potential error due to a lack of a “donut hole” for the largest size distributions is irrelevant). With the results from Fig. 5.3 in hand, we observe that my fitting method will be unable to constrain the relative amount of the smallest particles in the plume, because these particles fall to the surface directly on top of the gas deposition ring (which is outside of my chosen target region, and in which red sulfur deposition would overlay the dust). Last, I note that the stripes seen in Figs. 5.3d and e are promising; they produce the most intense deposition in the “butterfly wings” and relatively little deposition in the excluded regions. Because the stripes move closer to the lava lake as particle size increases, one can imagine how a wide range of particle sizes might produce black fans to the east and west (the superposition of several stripes) with relatively little deposition elsewhere.

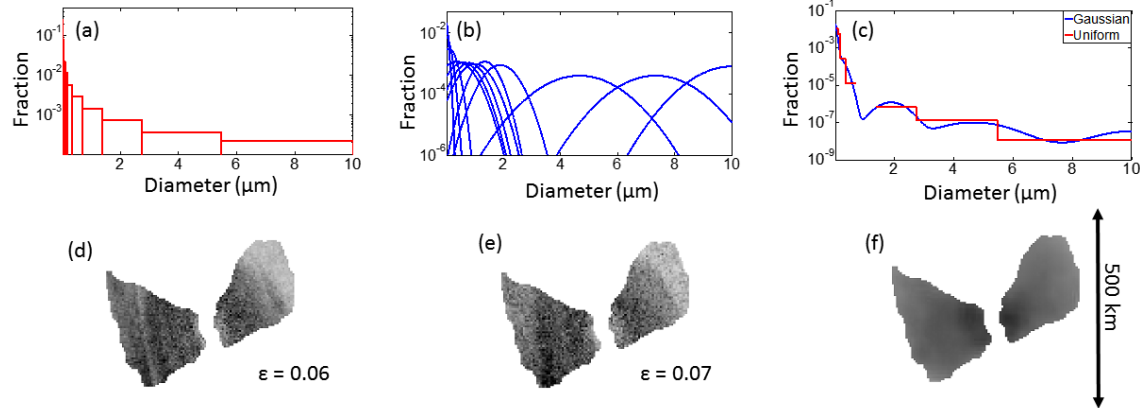


Fig. 5.4: (a) Set of uniform basis function size distributions. (b) Set of Gaussian basis function size distributions. Basis functions are normalized such that the sum of the values a basis function takes at all integer nanometer diameters between 20 nm and  $10\mu\text{m}$  is 1. (c) Best-fit size distributions obtained using the basis functions in (a) and (b). (d) Best-fit deposition pattern in target region obtained from the basis functions in (a), which is produced by the best-fit distribution in red in (c). (e) Best-fit deposition pattern in target region obtained from the basis functions in (b), which is produced by the best-fit distribution in blue in (c). (f) Target region from observation. Note the log scales on (a), (b), and (c), and in all cases “Fraction” represents the number fraction of particles in a distribution at each integer nanometer diameter.

The choice of what form to use for the simulated size distribution basis functions, how many of them to simulate, and what parameters to use for the individual distributions, is somewhat arbitrary. I performed simulations for about 30 basis functions, some uniform (like those presented above) and some Gaussian, as I explored various ways of spanning the space of grain sizes from 20 nm to  $10\mu\text{m}$ . I chose to use narrower distributions at smaller mean particle sizes because instantaneous acceleration due to drag is inversely proportional to particle size, because a particle’s contribution to deposition is proportional to the square of particle size, and because I wanted to be able to represent an approximately log-normal best-fit distribution.

As seen in Fig. 5.3, size distributions which broaden as particle diameter increases produce deposition patterns with features of roughly uniform width. I typically used 9-12 basis functions when producing a best-fit size distribution.

Fig. 5.4 shows the best-fit deposition patterns and size distributions produced by two different sets of basis functions. Fig. 5.4a shows a set of 12 non-overlapping uniform (“top hat”) basis functions, which produce the best-fit deposition pattern in Fig. 5.4d within the target region. Fig. 5.4b shows a set of 12 Gaussian basis functions, often with significant overlap, which produce the best-fit deposition pattern in Fig. 5.4e. Errors in the fit are small; the sum of squared residuals divided by the sum of the squared target data is about 7% for both. The best-fit size distributions obtained by applying the least squares coefficients to the basis functions directly are shown in Fig. 5.4c. The two best-fit distributions are close, suggesting that the form of the basis functions and their degree of overlap are unimportant. Both drop significantly around  $1\text{ }\mu\text{m}$ , with the uniform basis functions yielding no particles at all between 700 and 1,384 nm (this is the basis function whose deposition is shown in Fig. 5.3e). The Gaussian basis functions also yield no contribution from size distributions with means in that range, but I find particles at  $1\text{ }\mu\text{m}$  anyway due to the long tails on these functions. This drop at around  $1\text{ }\mu\text{m}$  persists in the best-fit size distributions for many other sets of basis functions, including sets that contain several very narrow distributions centered at  $1\text{ }\mu\text{m}$ .

The best-fit size distributions I obtain decrease by about six orders of magnitude as particle size increases. Surface darkness varies by less than an order of magnitude over the target region, and in my model particles darken the surface in proportion to their number fraction, so the fitting process is relatively insensitive to



exactly how dark the surface is. If regions close to the lava lake where only large particles fall were ten times darker, there would only be about ten times as many large particles in the best-fit size distribution, so that the best-fit size distribution would decrease by about five orders of magnitude from 20 nm to 10  $\mu$ m. Likewise, fitting to a uniformly dark surface inside the butterfly wings produces a result much like the one obtained here. The steady decrease in the best-fit distribution with particle size is due mostly to my darkness model (Chapter 3.2.2) and to the importance of particle size for explaining how far from the lava lake particles travel before they deposit (Fig. 5.3). In my model, particles darken the surface in proportion to their cross-sectional area, so even if 10  $\mu$ m particles are responsible for as much surface darkening as 100 nm particles, there will still be fewer of them by a factor of  $10^4$ . As seen in Section 5.4, as particle size increases from 20 nm, the distance from the vent at which particles deposit shrinks, rapidly at first, then more slowly. Larger particles (which fall closer to the vent) will tend to deposit with higher number densities than smaller particles just because they are falling in a smaller area. We also observed earlier (Fig. 5.3) that increasing the width of basis functions as particle sizes increase produces deposition patterns with roughly uniformly wide features. This effect tends to yield more small particles in the best-fit distribution; because particles from 700-1,384 nm fall to the ground in an area about as wide as the area in which 60-104 nm particles fall, fewer particles at each diameter between 700-1,384 nm are necessary to coat the surface with some density of particles. That is, the deposition patterns become more “tightly packed” as particle size increases, and this decreases the number of particles of any particular diameter which are necessary to explain a given surface coloration. It should also be noted that there are other ways to represent the best-fit particle distribution, for example as a distribution of the fraction of particles

with some cross-sectional area, or as a fraction of the total mass of the dust at each diameter. The cross-sectional area or the mass distributions can be obtained from my result by biasing the fraction by  $d^2$  or  $d^3$ , and so they are much flatter.

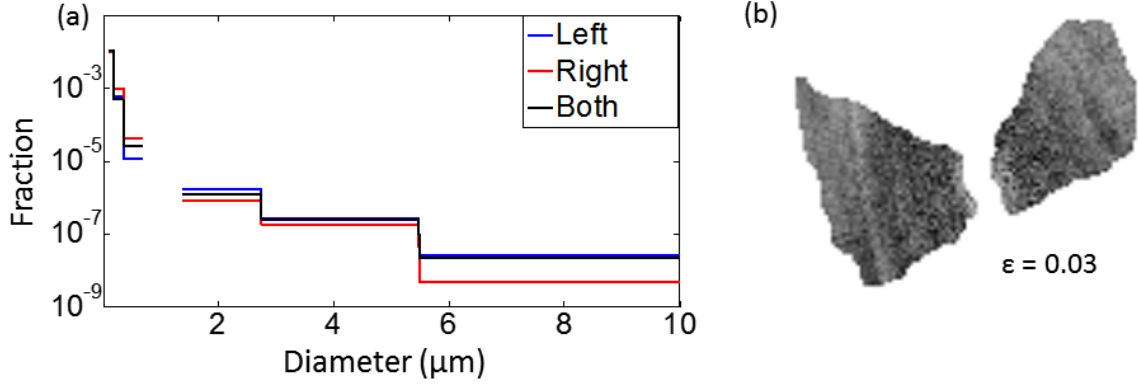


Fig. 5.5: (a) Comparison of the best-fit size distribution obtained earlier (Both) to those obtained when each butterfly wing is fit independently (Left and Right). (b) The composite best-fit deposition pattern produced when fitting each wing independently. The uniform basis functions from Fig. 5.4a were used.

An important source of fitting error is that my best-fit deposition patterns are consistently too dark in the western butterfly wing and too light in the eastern wing compared to the observation. The two wings can be fit separately, yielding two new best-fit size distributions (one for each wing). The composite best-fit deposition pattern (Fig. 5.5b) is a closer match to the observation. It is darker on the eastern edge of the east wing, and error has fallen to 3%. This is unsurprising, since this approach allows more degrees of freedom when fitting. However, Fig. 5.5a compares the best-fit size distributions obtained by fitting just the left wing, just the right wing, and both simultaneously, and all are remarkably similar. All of the distributions are within a factor of 3 everywhere except in the range of the largest basis function, where they differ by a factor of  $\sim 10$ . However, the eastern wing is relatively uninfluenced

by this basis function's deposition, so this is not an important distinction. Note that the eastern wing must play almost no role in determining the fitting coefficient for this basis function when both wings are fit simultaneously, since the other two best-fit distributions are right on top of each other in this range. The important source of error in the simultaneous fit is in the basis functions between 188-360 nm and between 360-700 nm. In fact, the deposition patterns for individual basis functions in Fig. 5.3 show a tendency to produce more intense deposition to the west of the lava lake than to the east, and this tendency is strongest for smaller particles. The possibility that this error is due to a failure to account for differences in the characteristics of the simulated source regions is discussed in Section 5.7.

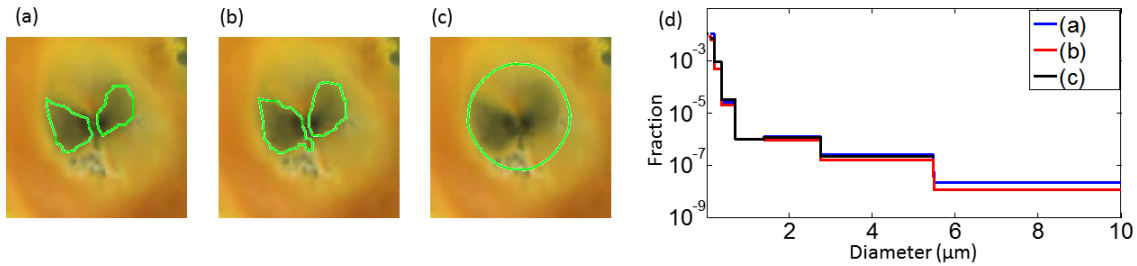


Fig. 5.6: (a) The target region used earlier. (b) A more generous target region which tries to capture nearly everything that could plausibly be due almost solely to dust deposition. (c) A circular target region extending out to the inner edge of Pele's red ring. (d) A comparison of best-fit size distributions obtained for different choices of target region.

The choice of target region has some effect on the best-fit size distribution, but only a small one. The target region was chosen so as to include only areas where the coloration of Io's surface seemed likely to be dominated by the rate at which dust deposited on the surface (e.g. not part of the large red ring and not north and south of the vent where gas deposition is important) and where the simulation is thought

to be reliable (e.g. not in the immediate vicinity of the vent, in part due to the error discussed above in the deposition of the heaviest dust falling back into the inner domains). Performing the same calculation with a variety of different target regions produces very similar best-fit size distributions (Fig. 5.6), although the large circular region of Fig. 5.6c yields a contribution from elusive  $1\text{ }\mu\text{m}$  dust. The fitting error increases significantly, but this is to be expected if my initial assumption that dust deposition alone cannot explain the surface coloration outside of the target region is a good one. The error increases because the simulated dust deposition cannot explain coloration due to the deposition of other materials which fall to the ground in qualitatively different patterns outside of the original target region.

## 5.6 Dust Column Densities

Line-of-sight integrated column densities of dust particles in the plume provide another opportunity to compare simulation and observation. It is difficult to make as direct a comparison as in the previous section because observations are more limited and because observations do not distinguish between ash particles and condensate. Nonetheless, there is insight to be gained.

Fig. 5.7 compares line-of-sight integrated column density for several kinds of particles. In Fig. 5.7a, the lightest particles produce column densities like the  $\text{SO}_2$  column density in Fig. 4.9b. As particle size increases, column densities in the core of the plume increase and the visible canopy shock becomes limited to the central axis of the plume before eventually disappearing, in line with what was seen for slices of particles in the plume in Fig. 5.2. Figs. 5.7d and e compare two different input conditions for dust at the virtual vent. Fig. 5.7d shows the heavy dust used

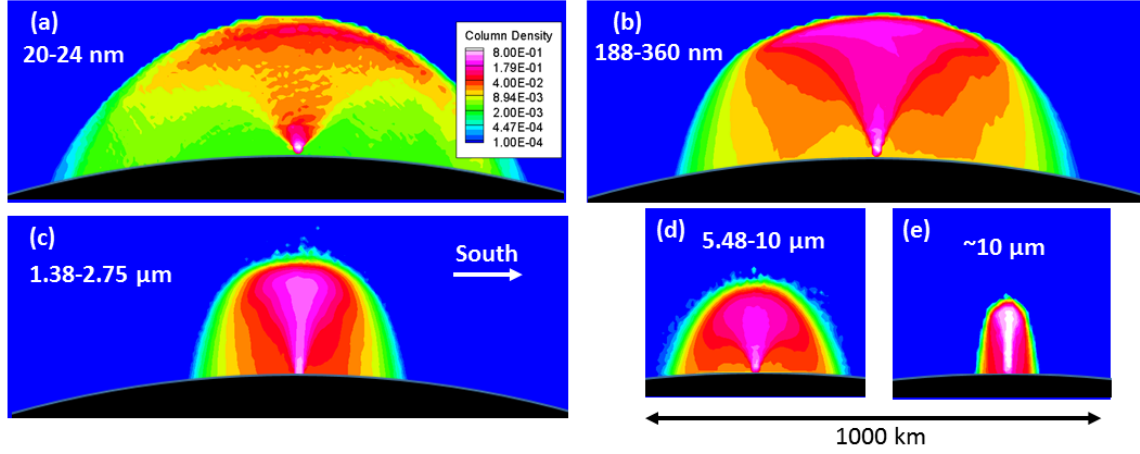


Fig. 5.7: Normalized line-of-sight integrated column densities for several size distributions of dust. (a), (b), (c), and (d) are uniform size distributions similar to those used in previous figures. (e) shows column density for the largest Gaussian basis function from Fig. 5.4b, where the dust is created at the virtual vent with a velocity of 450 m/s directly upwards, and no velocity parallel to Io's surface. All images are shown looking east, are drawn to the same length scale, and utilize the same color bar.

in results elsewhere in the present work, with a velocity distribution obtained from the sub-virtual vent model where the particles are given initial velocities of 450 m/s oriented in a random direction. Fig. 5.7e shows pencil-beam column densities which are produced by heavy dust initialized at the virtual vent with no velocity parallel to Io's surface. Even if there are relatively few large particles in the plume, the column density of large particles (created with no tangential velocity, as in Fig. 5.7e) at 150 km altitude remains nearly as high as it is at the virtual vent, because these particles remain in a tight column instead of spreading out. In spatially-resolved observations, this feature should be visible far out of proportion to the number of large particles in the plume as a whole if large particles are actually entrained in the gas at the virtual vent altitude. However, no such thin column feature is observed (Fig. 5.8).

Because the three-dimensional Pele plume looks so regular from this angle,

these results can be compared directly to column densities for particles simulated by Zhang et al. (2004). The results here are rather similar, except that the 20-24 nm particles correspond well with the 1 nm particles in Zhang et al., and likewise the 188-360 nm particles here most closely resemble the 10 nm particles in Zhang et al. The difference is largely due to vent geometry. Even though the plumes simulated in both works have the same mass flow rate, the vent used here is about an order of magnitude smaller in total area than the one used by Zhang et al. (who used a circular hole 8 km in radius). Gas densities just above my virtual vent are therefore an order of magnitude higher and particles are more strongly influenced by the gas as it initially expands upwards. This imparts higher velocities to particles before they decouple from the gas.

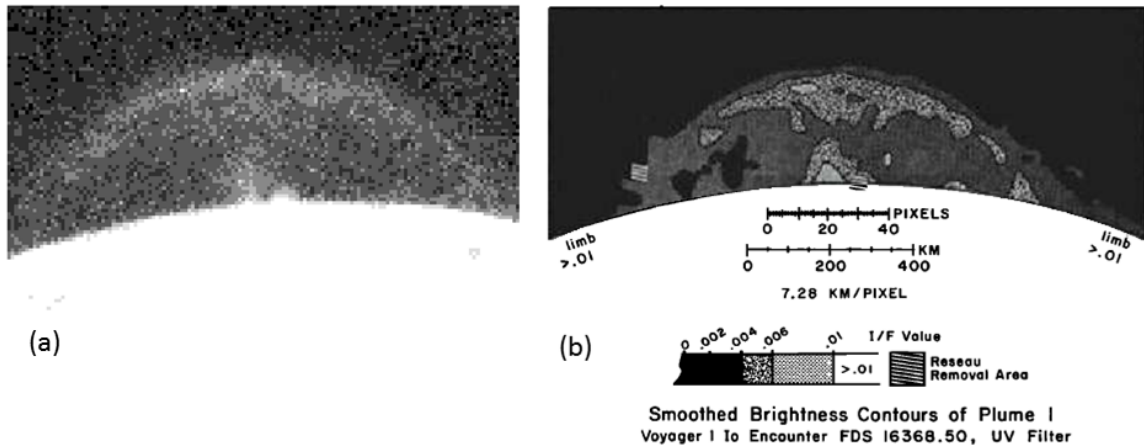


Fig. 5.8: (a) Voyager 1 observation of Pele through its UV filter. Image from PDS C1636850, stretched and saturated to better show the plume. (b) Contour levels for the observation in (a) from Strom et al., 1981.

We can also compare these results to a Voyager 1 observation of Pele in the UV (Fig. 5.8). While it is possible to construct a “best-fit column density” from my

best-fit size distributions by using the fitting coefficients determined in Section 5.5 and weighting the contributions of each particle size by its coefficient  $\alpha_k$  and by a scattering cross-section, heavier particles dominate and the result does not resemble observation (keeping in mind that the fitting method used could not constrain the smallest particle sizes due to their deposition patterns overlaying the gas ring). The column densities for 20-24 nm particles shown in Fig. 5.7a is the closest match to the observation and contours in Fig. 5.8. The column density of the smallest dust particles features a distinct canopy as well as a high-density region close to the surface, corresponding well with these features in Fig. 5.8b. Small particles in these simulations more closely resemble the observation than did the small particles in Zhang et al., 2004, which formed a pencil-beam structure near the surface (due to the larger vent area and slower expansion). This led Zhang et al. to suggest that large particles would be necessary to fit the near-surface feature in the observation, but that does not appear to be the case with my simulations. Further, the number of small ( $< \sim 60$  nm) particles in the plume is unconstrained by my simulations, both because small particle deposition was coincident with the gas ring and because my simulations do not include  $\text{SO}_2$  condensate, so it is possible that very large numbers of such particles are present. Very large particles are also unconstrained by my simulations due to the choice of target region on the surface, if they are slow enough at the virtual vent to remain in the lava lake's immediate vicinity. Such particles would also not rise very high and so would be unconstrained by observed column densities.

## 5.7 Non-Uniform Vent Conditions

In light of the results in Section 5.5, where a significant source of error in the best-fit deposition pattern was that my method produced too-dark deposition patterns in the left butterfly wing and too-light patterns in the right butterfly wing, I will now discuss the possibility that non-uniformity in the injection of dust into the plume simulation can explain this imbalance. The different source regions are potentially different in character, with Source A1 being a large lava lake while Sources E and C are smaller, isolated vents, so it is plausible that the mass flux of gas or dust out of the surface is different for each source.

The dust deposition patterns for various size distributions in Fig. 5.3 show that smaller particles (Figs. 5.3a-e) preferentially deposit to the west of the lava lake while the largest particles (Fig. 5.3f) deposit in a nearly symmetric ring. Because smaller particles remain coupled to the gas as plumes rising from each source region begin to interact, the deposition patterns of small particles are sensitive to where those particles are injected into the plume simulation. The gas flow is dominated by emission from Source A1, so light dust injected into the flow to the west of Source A1 will tend to fall to the west of the vent (light dust will have difficulty passing through the oblique shock seen in Fig. 4.7a and Fig. 4.8a.). This suggests that almost all small particles injected into the flow at Sources E and C will fall to the west of the vent. If in fact there is very little dust injected into the flow at these sources, my results will overestimate deposition to the west of the vent, which is what was seen in the best-fit deposition patterns.

Let us suppose that half of the dust injected into the plume at Source A1 falls to the west and half to the east, and that all dust (below some size, perhaps) injected



into the plume at Sources E and C falls to the west of the vent. Because we inject dust uniformly over the area of my simulated vent regions, I can approximate the effect of turning off dust injection at Sources E and C by weighting dust deposition in the western wing by a ratio of the areas of active regions. Rather than the full areas of Sources E and C and half of the area of Source A1 contributing to dust deposition in the western wing, only half of the area of Source A1 will contribute. This yields a scaling factor of between 0.7 and 0.8 (depending on how I account for the four small, scattered sources to the east of Source A1 which would likely deposit dust to the east of the vent). When simulated dust deposition in the western wing is weighted by this scaling factor before the fitting procedure is performed, the imbalance vanishes on the outer edges of the wings (Fig. 5.9b) and the fitting error is slightly lower. However, now the eastern wing is noticeably darker than the western wing closer to the vent.

Because the vent is small on the scale of the deposition patterns and because large particles decouple from the gas at low altitudes, the deposition patterns of large particles are only sensitive to the number of particles which are injected into the plume simulation, regardless of their distribution among the source regions. This is why the large particles do not exhibit the same imbalance as the small particles in Fig. 5.3 - the large particles are created at the virtual vent with an axisymmetric velocity distribution and are already largely uncoupled from the gas, so they rise and fall nearly ballistically, falling evenly all around the vent. This suggests that I ought not to scale the large dust deposition. In Fig. 5.9c, I scale only dust smaller than 1,384 nm in diameter, and we see further improvement along with a best-fit deposition pattern with no noticeable east/west anomalies which more closely resembles the pattern obtained by fitting the east and west wings independently (from Fig. 5.5b). Sum-of-squares error modestly improves with each step, though it does not fall to

the  $\epsilon = 0.03$  obtained when fitting each wing independently. This analysis suggests that Sources E and C are different in character from Source A1, and that much of the error in my best-fit deposition patterns is due to the uniformity of vent conditions in my model. Sources E and C should not be modeled as injecting as much dust (per surface area) into the plume as Source A1.

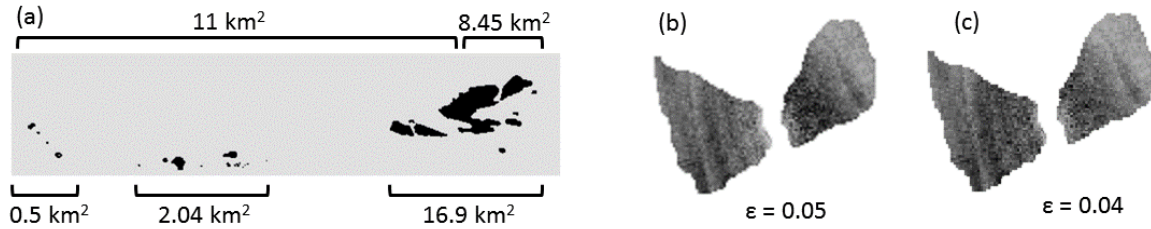


Fig. 5.9: (a) Sources E, C, and A1, with their individual areas labeled below. Above are the areas assumed to be contributing to dust deposition in the west (11 km²) and in the east (8.45 km²). (b) The best-fit deposition pattern obtained after scaling western dust deposition by 0.7. (c) The best-fit deposition pattern obtained after scaling the western deposition of only dust smaller than 1,384 nm in diameter.

## 5.8 Overlaying of Dust by Gas

While my simulations of dust deposition can produce good fits to the dark coloration of the surface inside of the selected target region (Section 5.5), the lack of observed dust deposition (black coloration) outside of the target region needs to be explained, since small dust particles do fall to the surface outside of the target region (Fig. 5.3). The target region was originally chosen so as to minimize the impact of plume gas deposition on the result, because it is reasonable to assume that significant plume gas deposition would overlay and hide the dust deposition in the ring and in the red sprays north and south of the lava lake. This is supported by the observation of red coloration in these regions, and my simulations (Chapters 4.5 and 4.6) show

how SO<sub>2</sub> might preferentially deposit where the surface appears red.

The mechanism by which dust is concealed by gas deposition may be complicated. With a steady plume, resurfacing is an ongoing process. Dust particles that produce the black coloration on the surface will have a lower albedo than other surface materials on Io like SO<sub>2</sub> frost, and likely lower thermal inertia as well (supported by modeling in Walker et al., 2012). Until black dust particles are covered by an optically thick layer of frost, they will absorb sunlight during the day and heat up to a greater extent than will the white, yellow, or red materials that cover the surface of Io near Pele. Walker et al. (2012) find that “non-frost” surfaces overlaid by only a thin layer of condensed gas (SO<sub>2</sub>, mostly) heat up rapidly at sunrise, causing the release of the trapped gas in a puff (the “dawn atmospheric enhancement”). This presents a puzzle about the overlaying of black dust at Pele by red/yellow plume material. Why is Pele not black everywhere that dust deposits, since SO<sub>2</sub> has difficulty sticking to warm dust? When Pillan erupted, leaving a black spot in the eastern part of Pele’s ring, how did the red ring re-establish itself?

One possibility is that the gas plume deposits so much material over a single night that an optically thick layer of frost can form on top of a dark dust deposit. However, the plume would have to be much denser than the one simulated here in order to produce an optically thick layer of frost overnight. The inner diameter of the large red ring is about 700 km while its outer diameter is about 1000 km. SO<sub>2</sub> ice has a density of about 1900 kg/m<sup>3</sup> (this depends on morphology and may be closer to 1500 kg/m<sup>3</sup>), and Nash et al. (1980) give 0.25 mm as the thickness at which a layer of fine-grained SO<sub>2</sub> frost becomes optically thick in experiments. The plume simulated here has a gas mass flow rate of 10,700 kg/s. If, as in my simulations, this is 100%

SO<sub>2</sub>, it would take the plume 0.6 years to deposit an optically thick layer of frost in the ring. Very little SO<sub>2</sub> frost will deposit during any particular night, and so SO<sub>2</sub> deposition consistent with observed column densities does not seem to be capable of overlaying dust.

However, because Pele is believed to contain as much as 30% S<sub>2</sub> by molar fraction (Spencer et al., 2000), overlaying of black ash by S<sub>2</sub> and products of S<sub>2</sub> may be possible, and products of S<sub>2</sub> could account for the red coloration anyway (McEwen and Soderblom, 1983). This can occur even if the deposition rate is slow since species other than SO<sub>2</sub> frost have much lower vapor pressures at dayside temperatures (this is why SO<sub>2</sub> dominates the sublimation atmosphere). S<sub>2</sub> has the same molecular weight as SO<sub>2</sub>, and so generally tracks the simulated SO<sub>2</sub> plume (Zhang, 2004). If the density and optical properties of sulfur on the surface are similar to those used above for SO<sub>2</sub> frost (an assumption I make for lack of good constraints on these properties), it should take around 1.9 years to deposit an optically thick layer of sulfur if Pele is 30% S<sub>2</sub> and is continuously erupting. This will take longer if there is less S<sub>2</sub> in the plume or if there are periods of reduced or no activity. Once the red sulfur layer becomes sufficiently thick, the higher thermal inertia and albedo of the solid material relative to loosely-packed dust grains may allow SO<sub>2</sub> frost to build up as well, since frost-covered surfaces will not reach the high temperatures of dusty surfaces during the day.

The predicted 1.9 years to overlay dust may be tested by comparison to Galileo observations of the eruption of Pillan. This eruption occurred over a short time and deposited black material which overlaid Pele's red ring. This black spot was then seen fading slowly over the course of subsequent observations, which supports my earlier

conclusion that Pele could not be laying down sufficient  $\text{SO}_2$  to produce an optically thick layer upon the dust in a single night. Geissler (2004) discusses changes in Pele and Pillan over time, and the observations used show Pillan’s black spot appearing in late 1997. By the end of 1999, the spot had faded considerably, and was no longer visible by the end of 2000. This overlaying took between two and three years, which is consistent with overlaying of dust by only  $\text{S}_2$  from a mostly continuously-active Pele which contains 20-30%  $\text{S}_2$ . Jessup et al. (2007) mostly find lower  $\text{S}_2/\text{SO}_2$  ratios, from 0.02 to 0.1, but there appears to be significant variation over time. They estimate a range between 0.08 and 0.3 for a 1999 observation (during the time when Pillan’s deposition was being covered over by Pele) and then a range from 0.2 to 0.31 for a 2004 observation.

## 5.9 Multiple Types of Particles

In Section 5.5, I found best-fit dust size distributions in terms of linear combinations of basis functions spanning 20 nm to 10  $\mu\text{m}$  (and I was only able to fit from about 60 nm to 10  $\mu\text{m}$  because smaller particles were overlaid by the gas ring). The best-fit size distribution derived from the uniform basis functions in Fig. 5.4c has a mean of 125 nm, weighted by number. This compares well with the observations of Jessup and Spencer (2012), who used the Hubble Space Telescope to find mean particle sizes of between about 50 and 100 nm in the Pele plume. My mean is larger, but this can be explained by the necessary exclusion from consideration of smaller particles. By fitting an analytic function to my distribution, I can extend it to smaller particles and obtain a measure of mean particle size which can be directly compared to the Jessup and Spencer observation. The log-normal distributions shown in Fig. 5.10 were obtained using Matlab’s non-linear least squares fitting function with a very

low tolerance and from a wide variety of starting guesses. Log-normal distributions have the form  $f = \frac{1}{d\sigma\sqrt{2\pi}}e^{-\frac{(\ln d - \mu)^2}{2\sigma^2}}$ , where  $d$  is the particle diameter in nanometers and  $\mu$  and  $\sigma$  are fitting parameters (note that these are not the mean and standard deviation of the distribution). Distributions shown here are scaled such that when summed at every integer nanometer between 20 nm and 10  $\mu\text{m}$  the result is 1.

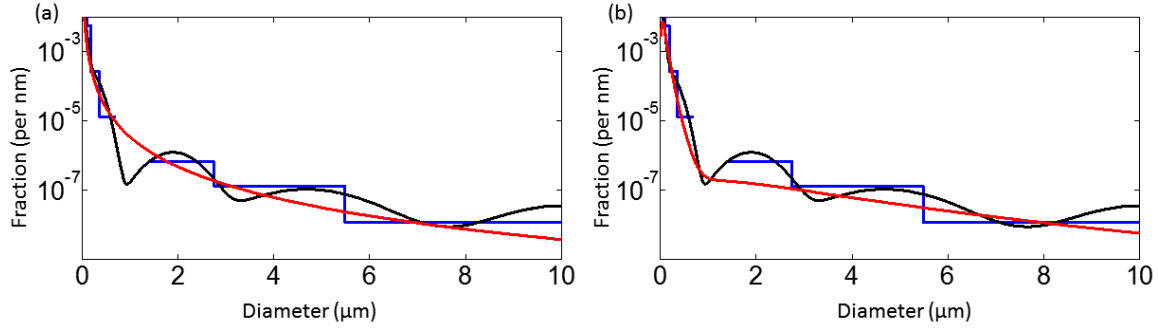


Fig. 5.10: (a) Comparison of best-fit size distributions to a single log-normal distribution, where  $\mu$  is -7.51 and  $\sigma$  is 2.81. (b) Comparison of best-fit size distributions to the weighted sum of two log-normal distributions. As with earlier plots of size distributions, 'Fraction' represents the fraction of particles with each integer nanometer diameter.

No single normal or log-normal distribution does a good job of capturing the behavior of the best-fit distributions in Fig. 5.4c due to the gap or drop at 1  $\mu\text{m}$ . Ignoring the gap, reasonably good agreement is found between my best-fit size distributions and a log-normal distribution with a  $\mu$  parameter of -7.51 and a  $\sigma$  parameter of 2.81 (Fig. 5.10a). This distribution has an extremely small mean (less than 1 nm) because it becomes very large near 0.

I get a more plausible result when I fit my combination of basis functions with the weighted sum of two log-normal distributions. One distribution with a  $\mu$  parameter of 4.25 and a  $\sigma$  parameter of 0.623 and another with a  $\mu$  parameter of

7.75 and a  $\sigma$  parameter of 0.797 can be combined (weighting the first by a factor of 0.6422 and the second by a factor of  $5.939 \times 10^{-4}$ ) to obtain the function shown in Fig. 5.10b. This function has a mean of about 88 nm, which is much closer to the finding of Jessup and Spencer, and also better captures the drop at  $\sim 1 \mu\text{m}$ .

This suggests that the true size distribution of dust particles in the plume is likewise the sum of two distributions, which indicates that there may be two different mechanisms of particle creation. Earlier (Section 5.2) I discussed a boiling oatmeal analogy to explain why large particles might have significant tangential velocity at the lava lake, while smaller particles might have a different creation mechanism involving small filaments of lava rather than large-scale spattering. These two different mechanisms would naturally result in two different particle size distributions.

I also note here that a coincidence is seen for particles in the plume at a particular diameter. As discussed just above, my best-fit size distributions yield a gap or trough at  $\sim 1 \mu\text{m}$ . The deposition patterns produced by dust distributions also cease contracting towards the vent at  $\sim 1 \mu\text{m}$ ; the radius of the deposition pattern in Fig. 5.3e is almost the same as that in Fig. 5.3f. It is plausible that these effects are related, but the nature of the connection is unclear.

## Chapter 6

### Night-side Plumes on Io

#### 6.1 Overview

The previous two chapters have investigated the Pele plume by itself, without interference from other sources of gas on Io or the Jovian magnetosphere. In this chapter I extend the plume model developed earlier to study plume/plasma and plume/plume interactions. I investigate the plume/plasma interaction at Pele and with simple plumes elsewhere on Io to see how plasma affects Pele's deposition and how the plasma interaction depends on plume location. I add a simple model of the Pillan plume to the Pele model of Chapter 4 to show how plumes of different strengths can interact and to show how plume/plume interactions can alter deposition patterns. These simulations do not include photochemistry, photo-ionization, or a sublimation atmosphere (for sublimation see Chapter 7). Particles which impact the surface, including ions, simply disappear (this is realistic for a night-side plume and neutral SO<sub>2</sub> but ignores sputtering induced by the plasma). Chemical reactions between neutral-neutral pairs and ion-neutral pairs are modeled as described in Moore (2011), but all reactions are charge-preserving and there is no mechanism for the net creation of ions.



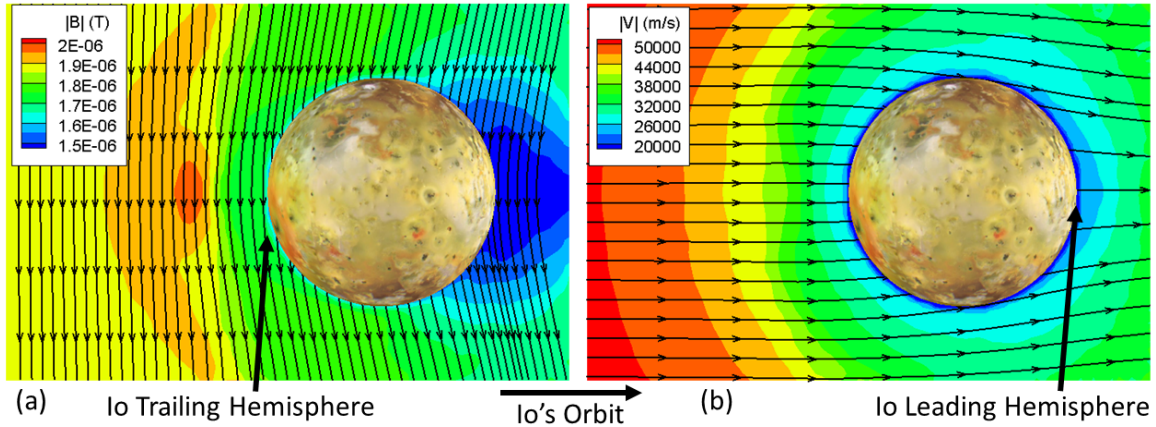


Fig. 6.1: Illustration of Io's plasma environment in the simulation. (a) Contours of magnetic field strength with field lines drawn. (b) Contours of bulk plasma speed with streamtraces drawn. The velocity is due to the combined effect of the B field and an E field which is due to the motion of the Io-fixed reference frame relative to Jupiter's magnetic field. The viewer is above Io's equator looking towards Jupiter. Io and the plasma torus orbit to the right, with the faster moving plasma overtaking Io in its orbit. Magnetic field and bulk plasma velocity are from Combi et al. (1998).

## 6.2 Plume/Plasma Physics

Jupiter's magnetic field rotates faster than Io revolves around the planet, so in an Io-fixed frame of reference the north-to-south magnetic field lines are overtaking Io in its orbit. In this reference frame which is moving with respect to the magnetic field, there is an electric field pointing away from Jupiter. The UT DSMC code models  $S^+$  and  $O^+$  ions moving under the effect of these static electric and magnetic fields in the Io-fixed frame of reference (Fig. 6.1). A magnetic field exerts a force on a charged particle perpendicular to the field and to the particle's velocity. An electric field accelerates a positively charged particle in the direction of the field. The combined effect of E and B fields, in the absence of other interactions, is that both positive and negative ions (and electrons) will take on an on-average velocity of  $\frac{\vec{E} \times \vec{B}}{|\vec{B}|^2}$  in the  $\vec{E} \times$

B direction while gyrating about B field lines (with thermal energy determining the gyroradius in the plane perpendicular to the B field and the particle's velocity in the B direction).

Fig. 6.2 shows example trajectories for an ion in velocity and physical space moving through uniform E and B fields. In Fig. 6.2a, an ion's velocity circles around a 57 km/s  $E \times B$  drift velocity, which is its average velocity over a gyration. Fig. 6.2b shows the corresponding trajectory in physical space. The ion's velocity in the Y direction is always negative (but not constant), so it always moves down while oscillating left and right. If there were significantly more energy in the ion's gyration, it would move upwards during some part of a gyration. In any case, its average trajectory is downward in the  $E \times B$  direction. Ion movement in the third coordinate direction, parallel to the B field, is unconstrained by the fields.

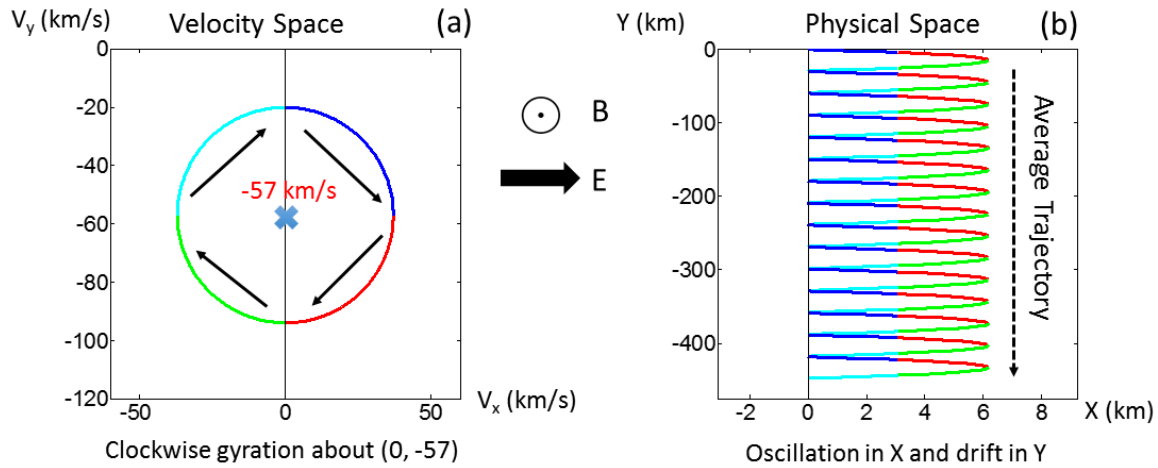


Fig. 6.2: Plots of an example ion's trajectory in 2D (a) velocity and (b) physical space. The trajectories are colored such that each part of the trajectory in velocity space corresponds to the same-colored regions of the physical trajectory.

Taking as input E and B fields from Combi et al. (1998) and upstream values in

Saur et al. (2004 book), ions are created far from Io (1000-2000 km) at a temperature of 1,160,500 K (100 eV), an upstream number density of  $3.6 \times 10^9 \text{ m}^{-3}$ , and an  $\mathbf{E} \times \mathbf{B}$  drift velocity of about 57 km/s, which falls to 12-20 km/s close to Io's surface. The bulk motion of the ions is in the  $\mathbf{E} \times \mathbf{B}$  direction, but there is substantial thermal drift along the B lines (ion velocities along B lines are initialized with a Maxwell-Boltzmann distribution at the ion temperature). In the absence of an atmosphere, many ions will strike the surface, leaving a shadow in the torus behind Io which is filled in from above and below due to thermal motion along B lines. The effect of plasma bombardment is therefore non-uniform over Io's surface. The trailing hemisphere (where Pele is located) encounters ions raining down from above. The poles and the sub- and anti-Jovian points experience ions sweeping past parallel to the surface, and the poles also experience a rain of high-energy ions from above (those moving along B lines). The leading hemisphere experiences relatively little plasma bombardment. The density, velocity, and energy of the local plasma flow determine the energy and momentum transfer to the gas.

In addition to this Io-scale asymmetry, ion/neutral interactions exhibit asymmetry on the scale of the ion gyroradius. Ions only drift in the  $\mathbf{E} \times \mathbf{B}$  direction because the  $\mathbf{E} \times \mathbf{B}$  velocity is their average velocity over a gyration and their motion is well-approximated as a series of complete gyrations between collisions. When interacting with a dense neutral gas, collisions frequently interrupt an ion's gyromotion and will tend to bring the ion to the neutral velocity. The ion will continue gyrating around the  $\mathbf{E} \times \mathbf{B}$  velocity, but if the neutral gas is sufficiently dense these constant interruptions can yield an average velocity which is different from the  $\mathbf{E} \times \mathbf{B}$  velocity (this is called ion slip and is explained in more detail in Mitchner and Kruger, 1973). For  $\text{O}^+$  ions in a 2000 nT field, the ion gyrofrequency  $\Omega_i$  is about  $12 \text{ s}^{-1}$ . The ion-

neutral collision frequency  $\nu$  depends on the ion velocity, the neutral density, and the collision cross-section.  $\text{SO}_2\text{-O}^+$  collision cross-sections used in the DSMC code vary with velocity but are often in the neighborhood of  $30 \text{ \AA}^2$ . The ion Hall parameter is the ratio of the gyrofrequency to the collision frequency ( $\beta_i = \frac{\Omega_i}{\nu}$ ) and will be unity at an  $\text{SO}_2$  number density of about  $5 \times 10^{14} \text{ m}^{-3}$  (depending somewhat on the choice of ion velocity in computing this parameter), which is achieved in many flows on Io. Pele's canopy and Io's atmosphere near the surface can reach number densities in excess of  $10^{16} \text{ m}^{-3}$ , for example. For such high collision frequencies, ion motion is not well-described as a series of completed gyrations, and the average ion velocity will differ from the  $\mathbf{E} \times \mathbf{B}$  velocity. Ions traveling through high-density neutral gas will acquire some average velocity in the  $\mathbf{E}$  field direction and will slow down in the  $\mathbf{E} \times \mathbf{B}$  direction. The  $\mathbf{E}$  field in the Io frame of reference points away from Jupiter, and so this effect breaks the symmetry of the ion/neutral interaction even at the sub-plasma point.

Fig. 6.3 shows axisymmetric simulations of plume/plasma interactions illustrating conditions that can be found in plumes on Io. A plume at the sub-plasma point will experience a rain of ions from above as in Fig. 6.3a. In Fig. 6.3b, ions encountering dense plume gas deflect in the direction of the  $\mathbf{E}$  field, away from the plume's central axis. As the canopy becomes less dense to the sides of the plume, ions collide less often and so are deflected less, eventually penetrating the canopy and resuming their on-average motion in the  $\mathbf{E} \times \mathbf{B}$  direction until they impact the surface. A plume at  $0^\circ$  or  $180^\circ$  longitude will experience a stream of ions tangent to Io's surface as in Fig. 6.3c. The simulation here is for a plume at the anti-Jupiter point; elsewhere the direction of the  $\mathbf{E}$  field would be different. Again, ions encountering dense plume gas deflect in the direction of the  $\mathbf{E}$  field (Fig. 6.3d), which this time

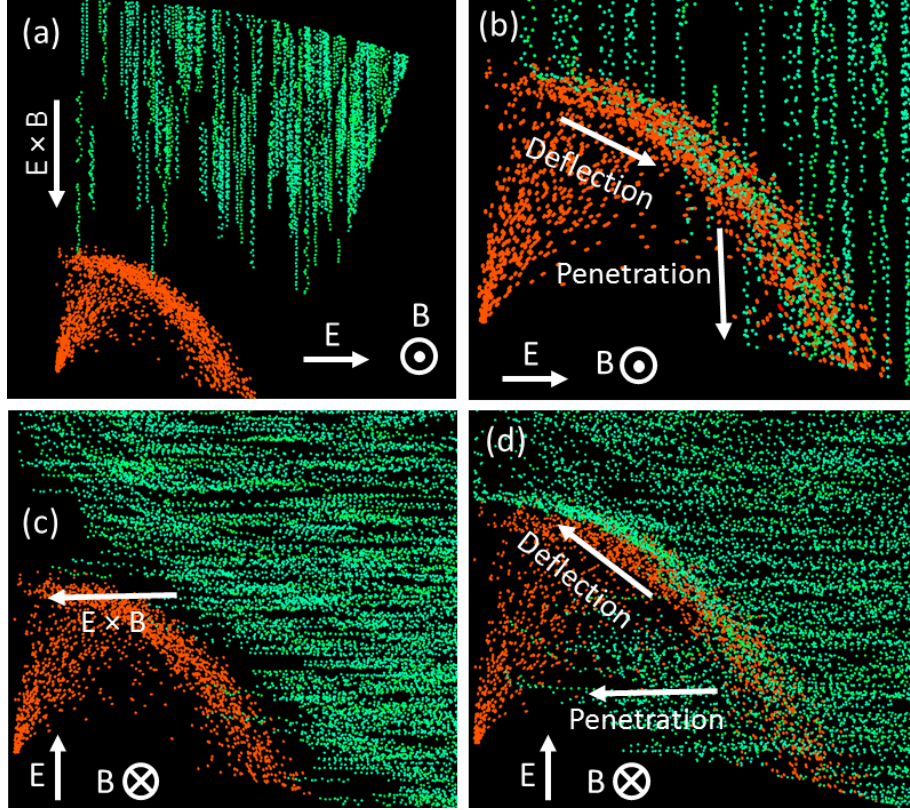


Fig. 6.3: Example axisymmetric simulations of plasma interacting with a plume. Tracer particles are shown for  $\text{SO}_2$  (orange) plumes with  $\text{O}^+$  and  $\text{S}^+$  ions (teal). The central axis of the plume is an axis of symmetry. (a) Ions rain down from above on to a plume, as would happen at the sub-plasma point on Io. (b) When ions collide with dense gas in the plume canopy, they deflect in the direction of the  $E$  field. (c) Ions stream in from the side towards a plume, as would happen at the anti-Jupiter point on Io. (d) Ions that encounter the plume's dense upper canopy are deflected in the direction of the  $E$  field, away from Io's surface. Because these simulations are axisymmetric the fields behave oddly close to the axis, but away from the axis the plume/plasma interaction is nearly the same as it would be for truly uniform fields.

points away from Io's surface. Ions that encounter the less-dense lower canopy can penetrate through; those that encounter the plume stem may still be deflected later. This deflection occurring in plume canopies can mean that plume canopies shield underlying gas from the plasma. However, on the other side of the plume in Fig. 6.3b or

for a plume on the other side of Io for the plume in Fig. 6.3d, deflection in the E field direction through the canopy will send ions *into* the rising plume stem. For a plume at the sub-plasma point, one side of the plume will resemble the case in Fig. 6.3b, with deflecting ions remaining in the canopy for long periods of time. On the other side of the plume, deflecting ions will take a direct route through the canopy, quickly penetrating to the rising gas below. Because ions reaccelerate between collisions, this causes the energy transfer to plume canopies to be asymmetric.

### 6.3 Location-Dependent Plasma Interaction

To illustrate the plume/plasma interaction and its location-dependence, I simulated two simple Pele-class plumes emerging from round holes (comparable to the plumes in Zhang et al., 2003) subject to plasma bombardment. First an axisymmetric plume was simulated emerging from an 8 km radius virtual vent at a number density of  $6 \times 10^{17} \text{ m}^{-3}$ , a temperature of 500 K, and a vertical velocity of 850 m/s. The axisymmetric domain extended for 100 km along Io's surface and 60 km in altitude, and particles leaving the axisymmetric domain in steady-state were patched on to a 3D planet-scale simulation in which ions were also simulated. The plume/plasma system was allowed to evolve for about 167 minutes and was then time-averaged over 200 time steps (150 s). The 3D simulations were performed on 992 load-balanced processors with about 120,000 particles per processor and 40,000 cells per processor on a uniform grid within each processor (so many of the cells were empty except for occasional ions passing through). Ions were weighted by a factor of 10 relative to the neutrals to improve the statistics of ion-neutral interactions.

### 6.3.1 Sub-Plasma Plume

A plume simulated at  $90^\circ$  east longitude on the equator (the center of Io's trailing hemisphere) is directly under the incoming plasma, which sweeps past Io in its orbit. Note that for a real plume, the sub-plasma point will move north and south over time as the torus tilts relative to Io ( $\pm 10^\circ$ ), but in simulations here the sub-plasma point is fixed at Io's equator. Pele, at about  $105^\circ$  east longitude and  $19^\circ$  south latitude, is close to this nominal sub-plasma point. For this sub-plasma plume, ions rain down from directly overhead. In addition to ions moving with the  $\mathbf{E} \times \mathbf{B}$  drift velocity, ions gyrate about magnetic field lines, parallel to Io's equatorial plane, and drift along the field lines (roughly) to the north and south.

Fig. 6.4 compares a plume at the sub-plasma point with a plume not experiencing any plasma interaction. Plasma inflates and heats the plume canopy, producing a taller plume with a more diffuse top. Density immediately above the canopy shock is lower and the entire canopy is significantly hotter as a result of ion impacts. The canopy remains highly collisional (Fig. 6.4g) just above the canopy shock, and the mean free path is less than 10 km well above the shock in the inflated canopy (compare to Fig. 6.4h), so the flow remains in equilibrium in the canopy and rotational temperatures are close to translational temperatures except at high altitudes. The effect of plasma is largely limited to the canopy, however. Fig. 6.4b shows somewhat higher temperatures inside the plume to the east and Fig. 6.4b and d show slightly higher (by up to about 200 K) temperatures just below the canopy relative to the no-plasma case in Fig. 6.4f. However, number densities inside the plume are nearly the same as for the case without plasma (Fig. 6.4e) and temperatures at lower altitudes are unchanged relative to the no-plasma case. The canopy shock is almost 10

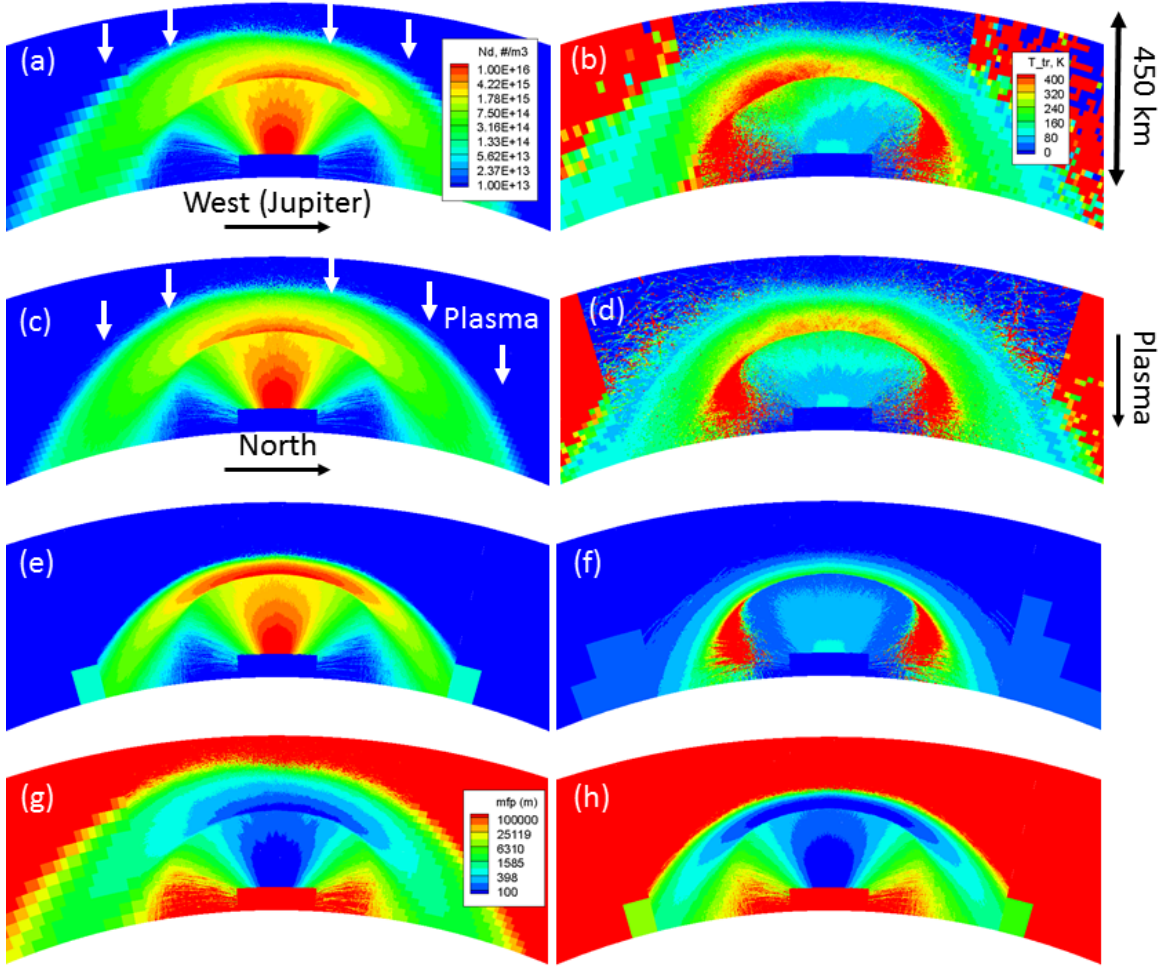


Fig. 6.4: (a-f) Number density (left) and temperature (right) contours for slices through a plume at the sub-plasma point. (a) and (b) are viewed from the north, with Jupiter to the right. (c) and (d) are viewed from the east, looking towards Jupiter. (e) and (f) are of an axisymmetric plume without plasma. (g) and (h) show mean free path contours for the slices in (a) and (e) respectively, computed as  $(\sqrt{2}n\sigma_{SO_2})^{-1}$ , where  $n$  is  $SO_2$  number density and  $\sigma_{SO_2} = 1.61 \times 10^{-18} \text{ m}^2$  is the collision cross-section for  $SO_2$ - $SO_2$  collisions.

km lower with plasma than without, which is perhaps a result of momentum transfer into the plume. Some “spikiness” in the number density contours inside the plume in Fig. 6.4a and c indicate where a few ions have penetrated and disturbed the gas



(this disturbance shows up due to statistical issues).

A striking feature of the plume/plasma simulation is the east/west asymmetry that develops in the plume. This is due to the Hall effect discussed earlier. Ions raining down from above hit the plume in Fig. 6.4a and deflect in the direction of the  $E$  field (which points away from Jupiter) in the Io-fixed frame, to the left. This angled trajectory decreases the time ions spend in the canopy on the western (right hand) side of the plume and increases time spent in the canopy on the eastern (left hand) side of the plume. Because the ions are constantly being reenergized by the fields as they collide with dense gas in the canopy, the plasma transfers more energy to the eastern side of the plume. Inflation and heating of the eastern side is thus more pronounced, as is apparent in Fig. 6.4a and b. As expected, no such asymmetry is apparent in Fig. 6.4c and d. For these slices, magnetic field lines run roughly right to left and ions are never accelerated along them by the fields.

It should also be noted that the total mass of plume material above Io's surface is nearly unchanged by plasma bombardment. While it might appear that the inflated plume would contain significantly more material (because particle flight times are on-average longer), the total neutral mass in a simulation with plasma is less than 2% greater than for a plume without plasma.

### 6.3.2 Polar Plume

A very different plasma environment is found at Io's poles. Now ions primarily stream into the plume from one side, although high-energy particles moving along field lines can still hit the plume from above. This case is also similar but not identical to that of a plume at the sub- or anti-Jovian point. The plume in Fig. 6.5 was simulated

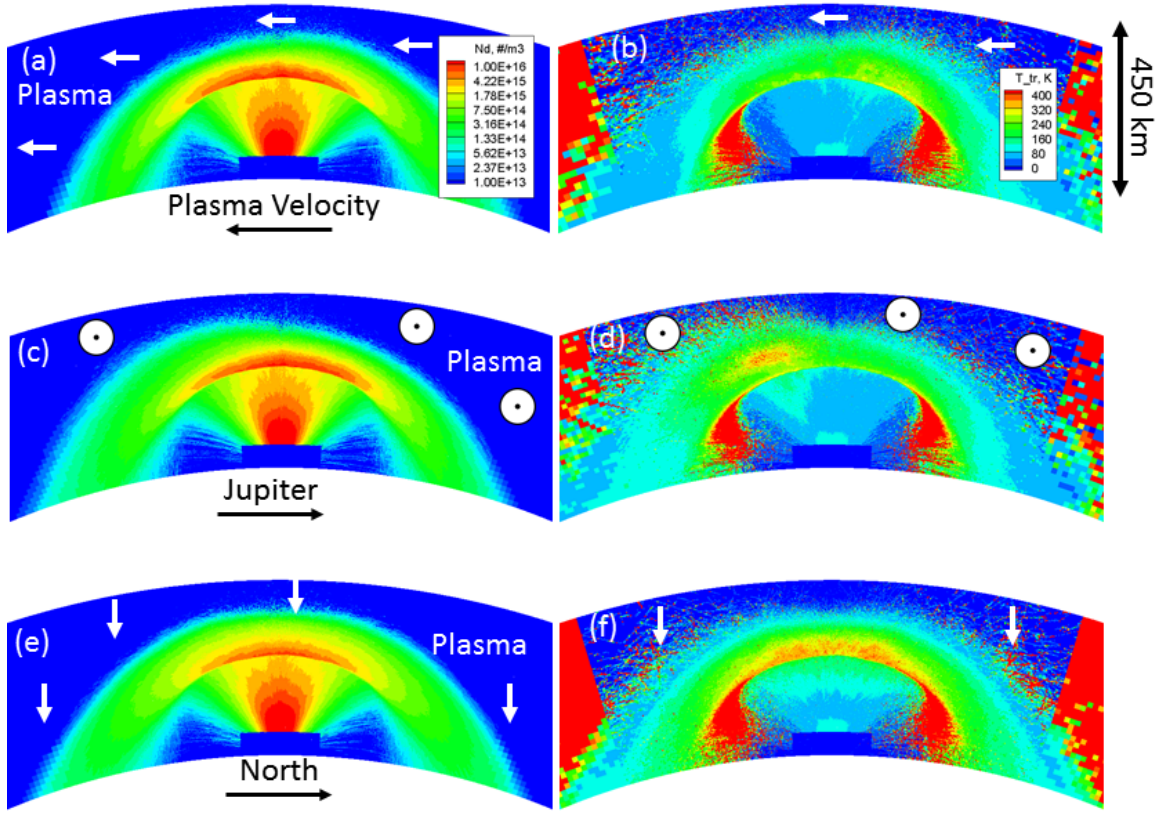


Fig. 6.5: (a-d) Number density (left) and temperature (right) contours for slices through a plume at the north pole. (a) and (b) are viewed with plasma streaming in from the right, with Jupiter behind the viewer. (c) and (d) are viewed with plasma streaming out of the page and Jupiter to the right. (e) and (f) repeat the two equatorial plume slices in Fig. 6.4c and d for ease of comparison.

at the north pole, and may be a rough analogue for Tvashtar (which is at about  $63^\circ$  north latitude). While a plume at Io's pole will never see a significant sublimation atmosphere, the lack of photochemistry in these simulations is somewhat unrealistic since gas hundreds of kilometers above Io's poles will almost always be in sunlight (except in eclipse)

Fig. 6.5 compares a plume at the north pole to the equatorial plume from Fig.

6.4. The same basic dynamics are apparent – the primary effect of plasma is to inflate and warm the canopy – but there are important differences due to the changed plasma environment. Asymmetry in the polar plume is apparent from all perspectives. The Hall effect is still apparent in Fig. 6.5c and d in the higher density and temperature in the plume canopy on the side of the plume facing away from Jupiter, and the side of the polar plume bombarded by plasma is preferentially heated (Fig. 6.5a and b). The side of the plume facing away from the plasma is shielded, with less heating of the canopy on that side (Fig. 6.5b), and there is less heating in general relative to the sub-plasma case (Fig. 6.5e and f). The interior of the plume is also less affected by the plasma, with little apparent heating even relative to the no-plasma case at the equator repeated in Fig. 6.4f. The canopy shock in the polar plume with plasma is only about 5 km lower than for a plume without plasma and 5 km higher than for the sub-plasma plume, supporting the idea that momentum transfer from the plasma pushes the canopy down. At the sub-plasma point plasma is driven into the plume by the fields while at the poles a smaller number of high-energy ions enter the plume from above while moving along B lines.

## 6.4 Chemistry and Column Density

Ion impacts occasionally cause chemical reactions directly and more commonly energize neutrals sufficiently to allow chemical reactions to occur during subsequent neutral-neutral collisions (remember that the bulk ion velocity drops to about 20 km/s close to Io’s surface, and at this relative velocity the non-reactive collision cross-section is larger than the reactive cross-sections from Parsons et al., 2012). Ions can also undergo resonant charge exchange with neutral S and O, producing very high-energy neutrals which are no longer constrained to gyrate around Jupiter’s magnetic

field lines. The generation of daughter species can show where plasma is depositing energy in plumes. Daughter species are often less condensable than  $\text{SO}_2$  and, once created, can bounce across the night-side of Io.

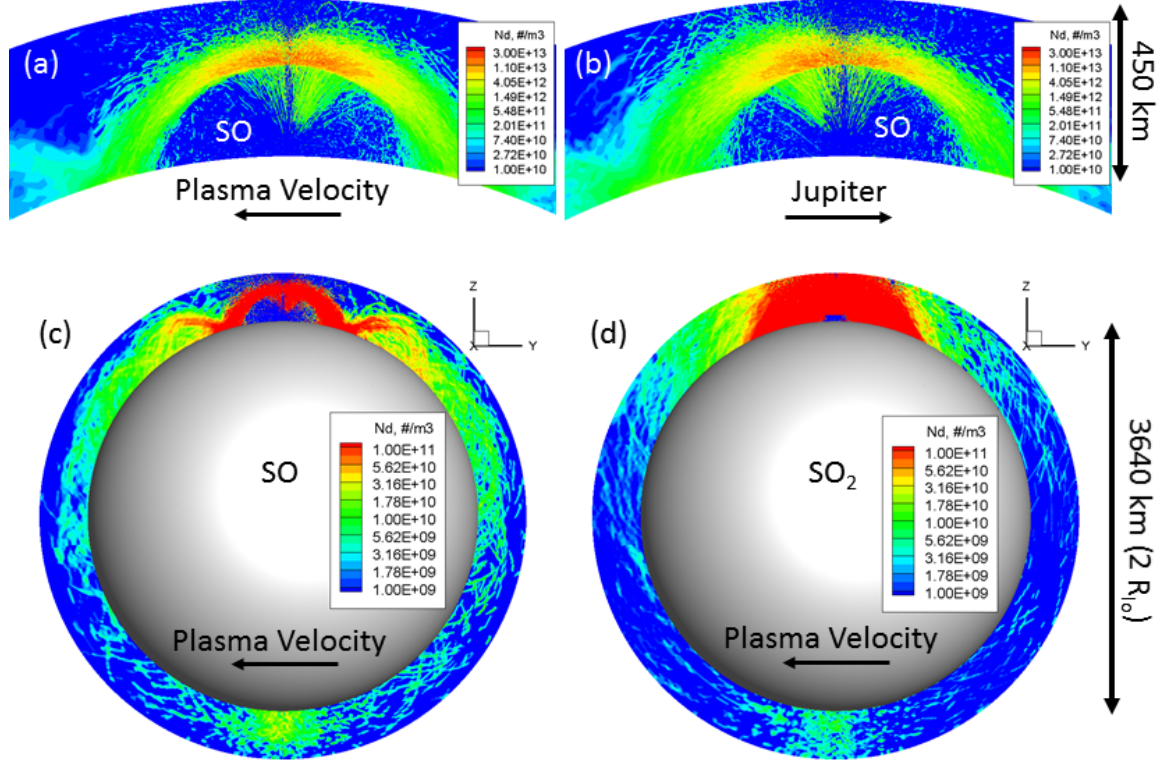


Fig. 6.6: Number density contours on slices for SO and  $\text{SO}_2$  in the polar plume model with plasma. (a) and (b) show SO slices from the same perspectives as Fig. 6.5a and c. (c) is the same slice as (a), zoomed out and rescaled to show SO over all of Io. (d) is the same as (c) except it shows  $\text{SO}_2$ . Slices here were time-averaged over 1000 time steps.

Fig. 6.6 shows SO number density contours for the polar plume from the previous section. SO is the most numerous daughter species, but even though its density peaks in the plume canopy the canopy is still dominated by  $\text{SO}_2$ . The appearance of SO in the simulation is a marker for plasma interaction, and Fig. 6.6a and b show

expected features in the canopy which correspond to the  $\text{SO}_2$  temperatures from Fig. 6.5. In Fig. 6.6a there is slightly more SO on the side of the plume facing the incoming plasma, while in Fig. 6.6b the SO is denser on the anti-Jupiter side of the plume. SO is preferentially created in the lower canopy where the  $\text{SO}_2$  flow is densest (denser flow provides more targets for ions), and energized neutrals, including daughter species, are unlikely to escape the plume before colliding with many other neutrals (see mean free paths for the sub-plasma case in Fig. 6.4g). Inside the plume, SO appears starting at about 100 km altitude, with relatively low density. This supports the earlier conclusion that plasma does not typically penetrate far into the polar plume.

Whereas without plasma virtually all erupted particles fall to the ground in a large ring, ions energize the top of the plume sufficiently to create a diffuse cloud above and around it (the inflated canopy seen earlier, where density decreases much more slowly with altitude than for the no-plasma case). The mean free path high above the canopy is very large and ion-neutral collisions in this diffuse cloud tend to send high-velocity neutrals flying away from the plume. SO is also only partially condensible in the UT model, and sticks to Io's surface on contact with probability 0.5 (the other half of the time it bounces diffusely on the surface). Significant amounts of SO are ejected from the polar plume, either from the upper canopy or after bouncing off the surface, and eventually find their way to the antipode where converging streams produce higher densities (Fig. 6.6c). Non-condensibility does not wholly explain the presence of SO far from the plume. Similar amounts of  $\text{SO}_2$  are also found thousands of kilometers from the plume source (Fig. 6.6d), and  $\text{SO}_2$  sticks to any surface it encounters in this model (although remember that there is a lot more  $\text{SO}_2$  than SO in the plume canopy).  $\text{SO}_2$ , unlike SO, is more prevalent on Io's leading hemisphere (Fig. 6.6d), suggesting that momentum transfer from plasma is important. Plasma

bombards the side of the plume on Io's trailing hemisphere, and  $\text{SO}_2$  tends to escape the plume towards Io's leading hemisphere, in the direction of the plasma flow. Many particles are actually being ejected from the plume with orbital velocities (many are elliptical orbits – the pictured domain is 450 km tall but the collisionless buffer cell is unpictured and extends another 1000 km). The ejected material is not creating anything resembling a hydrostatic atmosphere, and even if there were a sublimation atmosphere in these simulations most of the ejected material would fly over it. High-velocity particles ejected from plumes in this way are prime candidates for pick-up regardless of where the plume is located on the planet. These particles find their way all over Io and remain at high altitudes for long periods of time, so they can potentially be ionized by sunlight or by further interaction with plasma, supplying the plasma torus. Neutral densities over the plume's hemisphere can be several times the upstream plasma density of  $3.6 \times 10^9 \text{ m}^{-3}$  and the diffuse neutral cloud extends at least hundreds of kilometers from Io's surface even for night-side plumes like these.

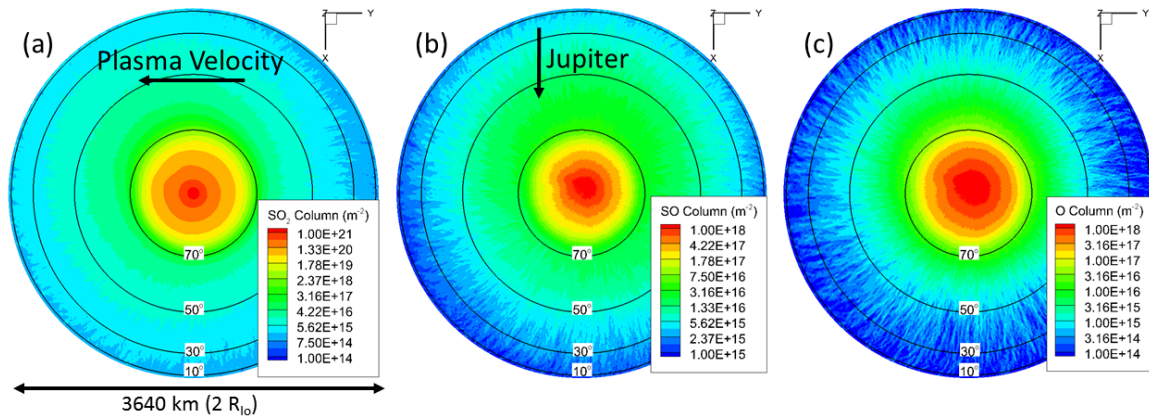


Fig. 6.7: Column densities for (a)  $\text{SO}_2$ , (b)  $\text{SO}$ , and (c)  $\text{O}$  on Io's northern hemisphere around a polar plume with plasma, looking down at the north pole. Plasma streams in from the +Y direction and Jupiter is in the +X direction.

Column densities looking down at Io's surface can more clearly show how ejected material is moving around Io and the asymmetry of the plasma interaction (Fig. 6.7). The SO<sub>2</sub> column around the polar plume (Fig. 6.7a) is biased in the direction of the plasma flow, which like the SO<sub>2</sub> density contours from Fig. 6.6d suggests that momentum transfer from the incoming ions (with their continual reacceleration by the fields) plays a role in ejecting the SO<sub>2</sub>. SO column density, however, is biased against the plasma direction and away from Jupiter (Fig. 6.7b), corresponding to where the plasma was reacting most strongly with the SO<sub>2</sub> plume (Fig. 6.5) and where most of the SO was generated. Neutral O (Fig. 6.7c) is similar, but sprays out preferentially away from Jupiter. While SO<sub>2</sub> dominates the total column density over the plume itself, it is overtaken by SO around 1000 km from the plume source where total column is about  $5 \times 10^{16}$ . There is approximately as much O as SO in the simulation ( $\sim 4 \times 10^{29}$  molecules), but the O is more concentrated over the plume. It is produced both when SO<sub>2</sub> dissociates into SO and O and when SO dissociates into S and O. The O density falls off quickly with distance from the plume because of resonant charge exchange reactions with O<sup>+</sup> ions. This large cloud of neutral O (and S) presents an extended target for incoming ions. Charge exchange reactions leave behind a neutral with escape velocity and a new ion which is quickly accelerated by the fields.

## 6.5 Shielding and Deposition

Although these plumes were not simulated alongside a sublimation atmosphere, the simulations can determine whether plumes can shield an underlying atmosphere or Io's surface from the plasma. This is again a location-dependent interaction, as seen in Fig. 6.8. A plume at the pole (Fig. 6.8a) shields the surface almost com-

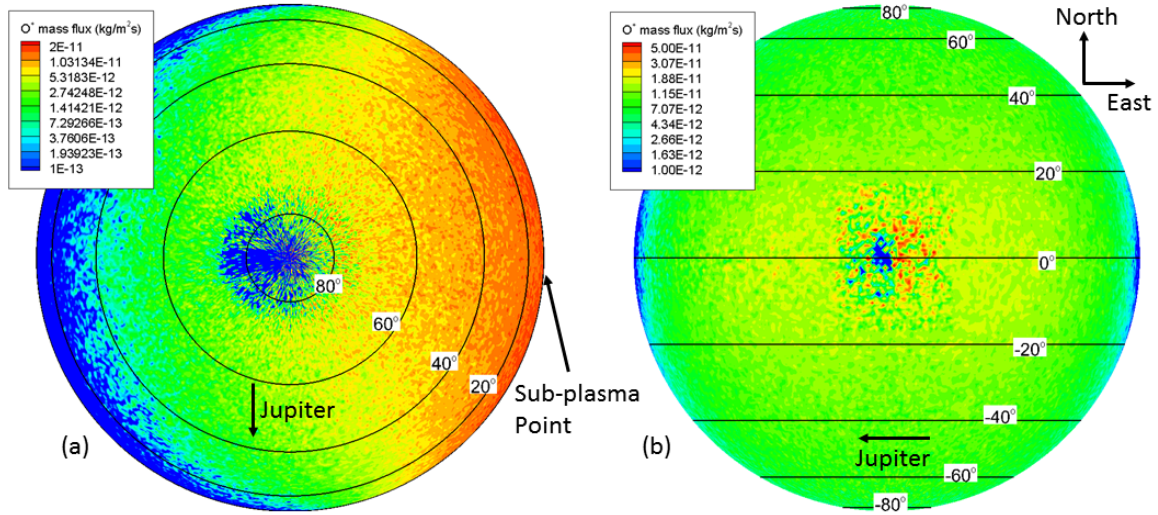


Fig. 6.8: Mass flux of  $O^+$  into hemispheres on Io's surface for (a) a polar plume and (b) a plume at the sub-plasma point. Plasma streams in from the  $+Y$  direction (streams into the page in (b)), Jupiter is in the  $+X$  direction, and the  $Z$  axis aligns with Io's polar axis.

pletely, with very few  $O^+$  ions penetrating the plume. However, at the sub-plasma point (Fig. 6.8b), the plume only shields a small region around its source and extending to the west, towards Jupiter. The rate of ion impacts immediately to the east of the plume source is actually increased by the plume. The equatorial plume is worse at shielding the surface because at the sub-plasma point the  $E \times B$  velocity is into the surface; ions are accelerated into Io's surface if they find themselves in low-density neutral gas (where ion slip is unimportant). At the poles, ion impacts into Io's surface are caused not by  $E \times B$  drift but by thermal motion along  $B$  lines. A single collision can disrupt this motion and prevent a surface impact. Significant column density at the poles can therefore prevent ion impacts almost entirely, which likely has implications for sputtering. The equatorial plume's enhancement of ion deposition to the east is once again due to the Hall effect; ions that would otherwise



have impacted the shielded region are not deflected away from Io entirely but instead just angle slightly away from Jupiter as they penetrate the plume. The lower flux of ions to the surface under the western side of the plume is balanced by a higher flux under the eastern side of the plume; the equatorial plume only redirects incoming ions slightly.

The effect of plasma on  $\text{SO}_2$  deposition is of major interest, especially in light of the results for Pele in Chapter 4.5. Fig. 6.9 compares  $\text{SO}_2$  deposition for the polar plume of the previous sections with and without plasma. Fig. 6.9a and b illustrate how plasma produces an extended, diffuse deposition ring reaching far from the source or the regions of peak deposition. Small amounts of deposition are apparent over the entire hemisphere when plasma is included in the simulation. Without plasma, the deposition is confined to a much sharper ring. By changing the color bar, Fig. 6.9c and d show that the plasma has produced an asymmetry in the  $\text{SO}_2$  deposition, with increased deposition away from the incoming plasma and generally towards Jupiter. The plume material which eventually deposits here is the least affected by plasma, which bombards the plume from the +Y direction and is deflected in the -X direction and preferentially inflates the canopy on those sides. The deposition ring is more diffuse all around when plasma is simulated, though, corresponding to the inflated canopy of Figs. 6.4 and 6.5. Peak deposition intensity has dropped by a factor of about 2 with plasma, comparing Fig. 6.9c and d. Plasma bombardment has produced a slightly larger ring with lower peak deposition in a wider band.

While both the sub-plasma and polar plume exhibited canopy inflation under plasma bombardment, plumes at other locations on Io should be shielded from the plasma. A plume at the anti-plasma point, for example, should see almost no plasma

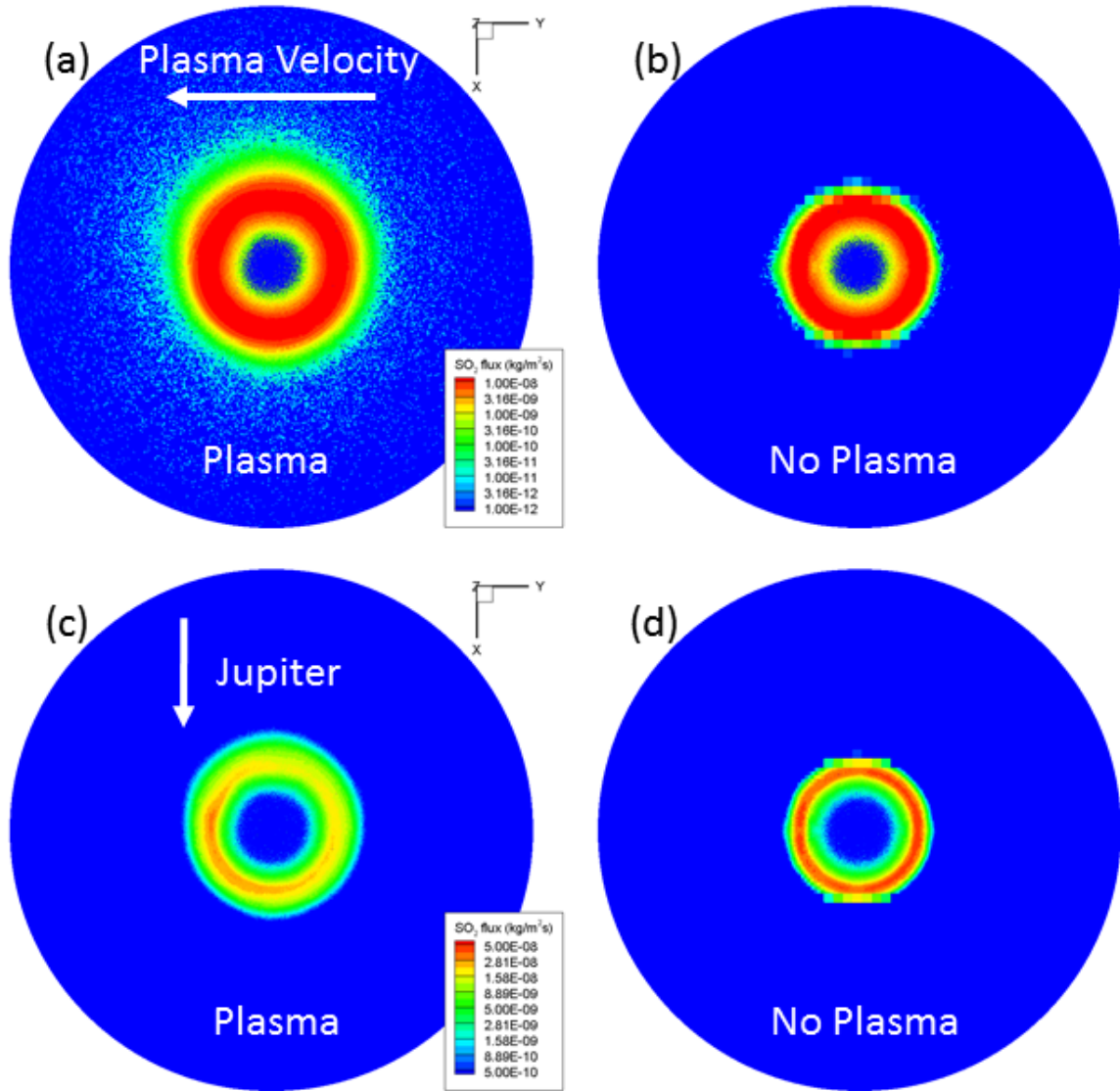


Fig. 6.9: Mass flux of  $\text{SO}_2$  into hemispheres on Io's surface for a polar round hole plume. (a) and (c) have plasma while (b) and (d) do not. (a) and (c) differ from each other only in the choice of contour levels. Likewise (b) and (d).

in its vicinity. If the canopy of an anti-plasma plume does not inflate, its deposition ring should be sharper, as in the simulations without plasma in Fig. 6.9b and d. In general, plume deposition patterns should be more diffuse for plumes which interact

more strongly with the plasma.

## 6.6 Plasma at Pele

Having explored the physics of the plume/plasma interaction for round-hole plumes, I return to the earlier model of Pele erupting from a lava lake used in Chapters 4 and 5. Plasma is not going to strongly influence the gas dynamics at low altitudes; the canopy shields the rising plume (Section 6.3). Plasma will inflate the canopy and produce a diffuse cloud of neutrals around the plume, but the major findings of those earlier chapters had to do with the deposition of gas and dust on Io's surface. Here, I patch the penultimate Pele domain on to Io at  $18.7^\circ$  south latitude  $104.7^\circ$  east longitude and perform a simulation like those for the polar and equatorial plumes earlier in this chapter.

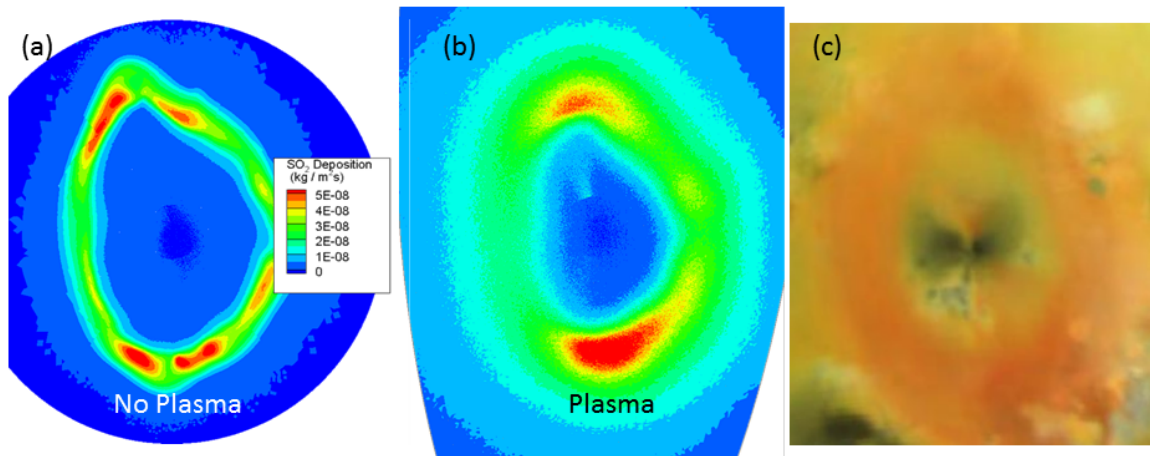


Fig. 6.10: (a) Deposition rate of the Pele plume from Chapter 4. (b) Deposition rate of the earlier Pele plume model simulated at  $18.7^\circ$  south latitude  $104.7^\circ$  east longitude, with plasma. (c) Galileo image of Pele on Io for comparison. Note that the color bar here is linear unlike for other presentations of gas deposition in this work.

As illustrated above with Fig. 6.9, plasma renders Pele’s SO<sub>2</sub> deposition more diffuse (Fig. 6.10). However, the overall shape (Fig. 6.10b) still compares well with the Galileo observation (Fig. 6.10c), and is perhaps an even better fit with a wider ring of more uniform deposition. If Io’s surface is red more-or-less in proportion to the amount of SO<sub>2</sub> from Pele that falls on it (not because of the SO<sub>2</sub> but because of other species carried with it), plasma may help explain the width of Pele’s ring. The simulated deposition ring unsurprisingly remains more intense to the north and south, although the distinct, discrete high-density regions of Fig. 6.10a have merged.

I did not perform simulations of dust in the Pele plume with plasma. Instead I argue that since all but the smallest dust particles have decoupled from the gas plume at high altitudes (Chapter 5), there is no mechanism in the present DSMC model by which plasma could substantially alter the trajectories of dust particles since plasma primarily affects gas in plume canopies. I believe that the results for dust in the Pele plume would be essentially unchanged with an updated gas flow-field, though very small dust particles should continue to track the gas flow even as the canopy inflates. However, it is possible that in reality plasma might directly interact with dust in some way, in which case this would need to be modeled, and if condensation occurs primarily in plume canopies plasma will likely be important for a model of condensation in plumes.

## 6.7 Pele and Pillan

In 1997, Pele’s red deposition ring was radically altered when Pillan explosively erupted from its eastern edge (Geissler et al., 2004). A large black spot, ringed in white, interrupted Pele’s ring. Additional yellow material encroached on Pele’s

deposition to the north and south, and even to some extent to the west. The  $SO_2$  content in the plume at Pillan was variable and apparently related to the amount of frost covering the erupting region (Jessup and Spencer, 2012). The mechanisms producing the Pillan plume and the plume’s composition are therefore likely to be different than for Pele in ways that my model does not capture. However, the case provides an opportunity to investigate the interaction between two separate plumes, close enough together that their canopies intersect but far enough apart that they do not resemble a single large plume as with the multiple source regions at Pele (Chapter 4.3).

I chose to model Pillan as a smaller plume, somewhat larger than Prometheus simulations from Zhang et al. (2003), centered at  $12.34^\circ$  south latitude  $116.75^\circ$  east longitude, although note that the actual eruption mechanism for Pillan appears to be different than the mechanism for Prometheus. The plume erupts from an 8 km radius round hole (this is a virtual vent) with a temperature of 350 K, a bulk upwards velocity of 550 m/s, and a density of  $6.426 \times 10^{-9}$  kg/m<sup>3</sup>. This is fairly arbitrary, although a much hotter or faster plume would be too big and the plume/plume interaction would be uninteresting if one were much more dense than the other. These conditions yield a total mass flux which is about half that from Pele and a plume about half Pele’s size, so densities are comparable in the plumes’ canopies. Pillan is modeled as consisting entirely of  $SO_2$ , like Pele, but the simulation records the origin of each molecule and so the plumes are separable in output. As with Pele, Pillan is staged, but only to an altitude of 30 km, and the inner domain is axisymmetric. Steady inflow from both plumes into the outermost domain was maintained until the system reached a steady state. Dust grains in Pillan were not modeled; presumably the dust flow is dominated by sufficiently heavy dust to lay down a symmetric round spot despite

interference from Pele. Plasma was not included in these plume/plume simulations. Other simulation parameters were identical to those for the 992 processor simulations of Chapters 4 and 5.

### 6.7.1 Canopy Interaction

When two plume sources are sufficiently far apart that they form separate canopies, but close enough together that their deposition rings would overlap, interaction between the plumes occurs between their canopies rather than between rising jets as was seen in Chapter 4.3. Fig. 6.11 illustrates the unsteady process by which two erupting plumes settle into an equilibrium. Each plume independently forms a canopy, with the smaller Pillan plume developing sooner (because the time to form a canopy is related to the ballistic time of particles in the plume). Pele’s canopy sweeps over the developed Pillan as Pele approaches its own steady-state, and this substantially deforms Pillan (Fig. 6.11d). But Pillan quickly reestablishes its canopy after Pele’s canopy has swept past. In steady-state the two canopies press against each other with little interpenetration – viewed from above (Fig. 6.11f) the interaction region is a sharp line even in column.

Fig. 6.12 shows contours for a slice through the plume system. Pillan’s canopy increases in density towards the interaction region. Pele compresses Pillan’s canopy on this side and supplies additional material. However, as the streamlines in Fig. 6.12a and the top-down view from Fig. 6.11f show, gas from Pele is turned aside before penetrating Pillan’s canopy. The temperature contours in Fig. 6.12b show the extent of the interaction region between the plumes. At low altitudes high temperatures are due to shocks that turn the gas from Pele and Pillan away from each other and into the ground. At high altitudes high temperatures are due to nonequilibrium low-

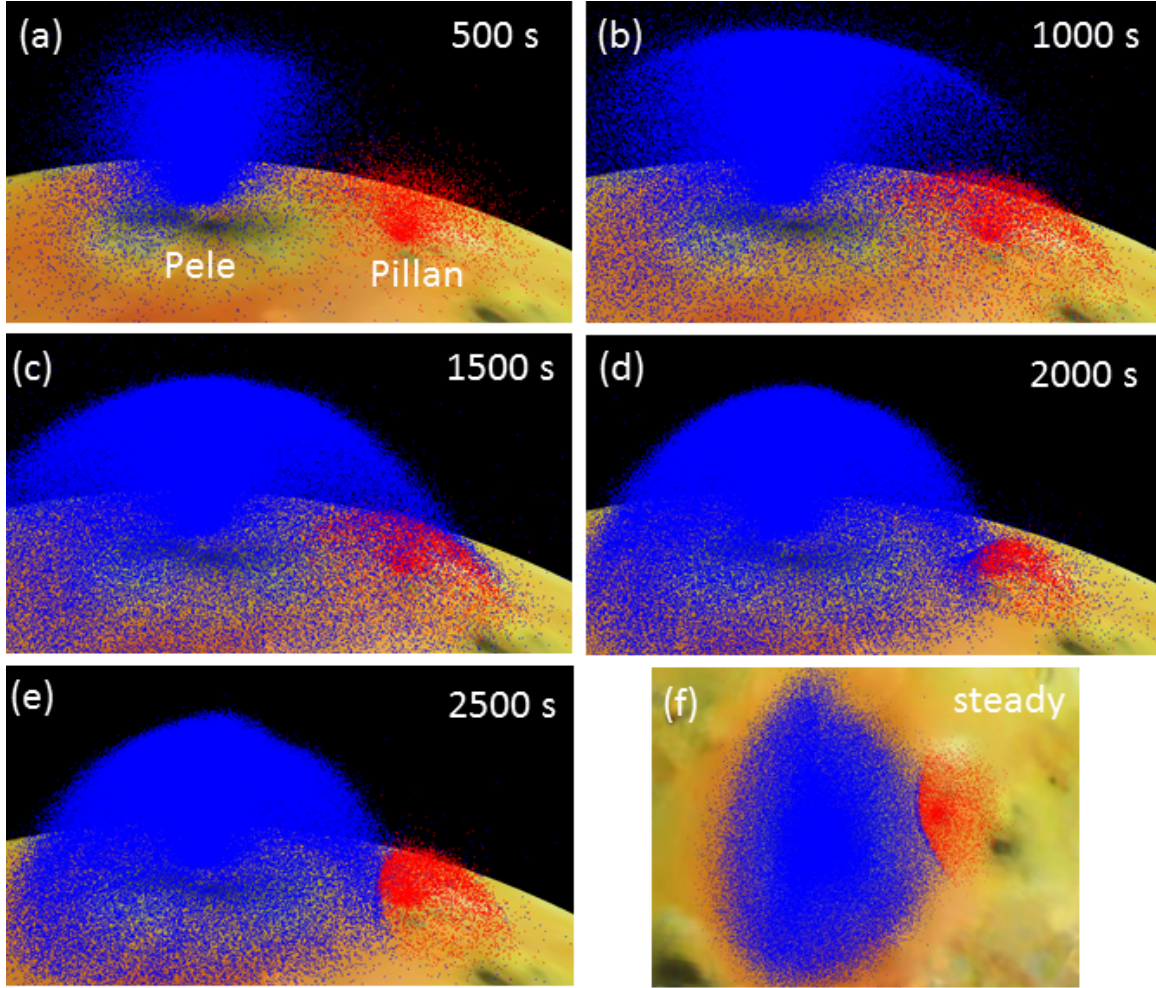


Fig. 6.11: Tracer particles for the Pele and Pillan at various times in the plume/plume system's development. Both plumes erupt in (a). The smaller Pillan plume forms a canopy first in (b). Pele's canopy begins to form in (c) and sweeps over Pillan, deforming it on the way. The plumes begin to go steady in (d), although the interaction region between the two is still sorting itself out. In (e) the system is essentially steady. (f) is a view from overhead at steady-state where the interaction region is clearly visible in column.

density streams of falling  $\text{SO}_2$  from Pele and Pillan's diffuse upper canopy. This can be verified from the mean free path contours in Fig. 6.12c, which quickly rise above 10 km over Pillan's canopy.

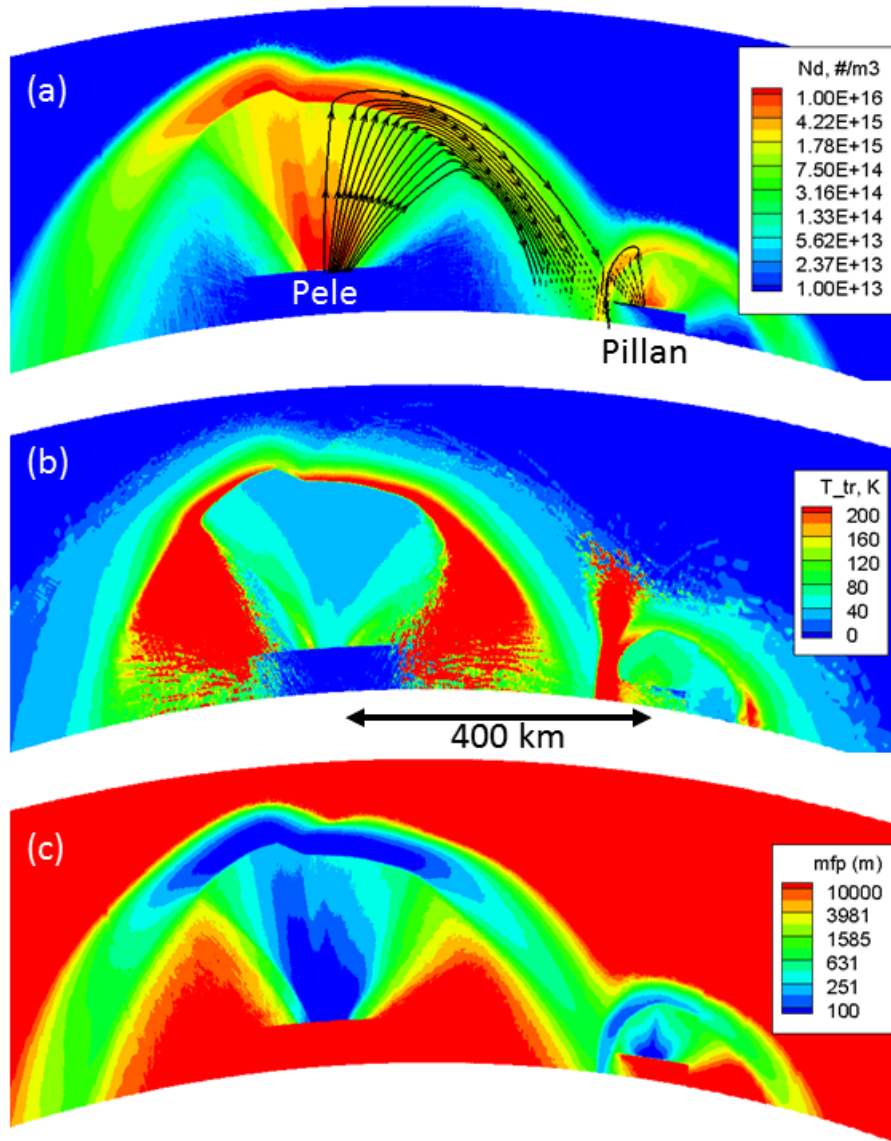


Fig. 6.12: (a) Number density with streamlines, (b) temperature contours, and (c) mean free path contours for a slice through the Pele/Pillan system. The slice cuts through the centers of both plumes. The sharp spike at the center of the rising Pillan plume is a grid artifact. The low-density region under Pillan corresponds to where the separately-simulated inner domain is patched in, as with previous plume simulations.



### 6.7.2 Gas Deposition

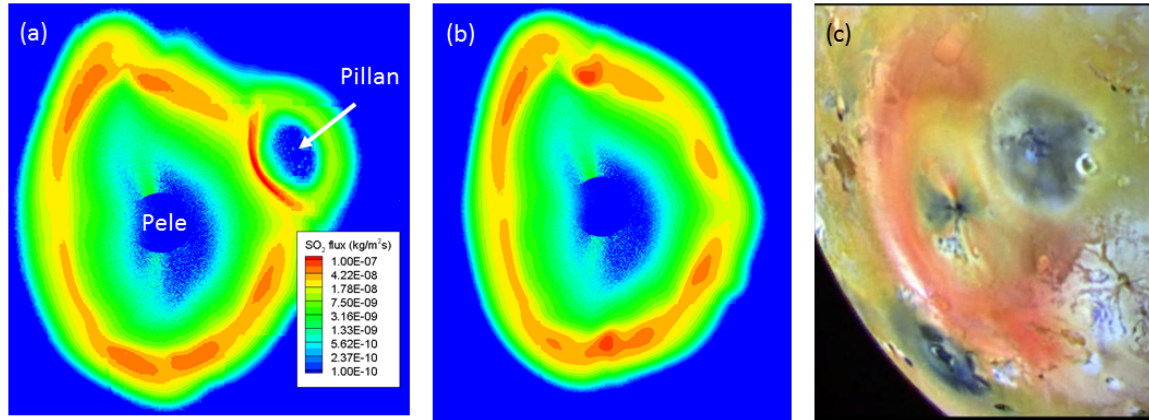


Fig. 6.13: (a) SO<sub>2</sub> deposition for the Pele/Pillan system. (b) Deposition for Pele in the absence of Pillan for comparison. (c) Galileo image of Pele on Io's surface some time after Pillan's eruption.

Fig. 6.13 compares the simulated deposition of the Pele/Pillan system to simulated deposition of Pele alone and to an observation of Pillan's black spot on Pele's red ring. The sharp interaction region seen in Figs. 6.11 and 6.12 produces a region of heightened deposition intensity between Pele and Pillan. Beyond a short distance from Pillan's ring, however, Pele is essentially undisturbed; differences elsewhere in Pele's ring are due to unsteadiness of the sort seen in Fig. 4.12. That is, the differences in Pele's ring appear to be due to natural oscillations or wobble in the high Reynolds number flow in Pele's canopy rather than to any influence from Pillan. It is notable that this simulated Pillan produces relatively little deposition away from Pele's ring while producing a concave structure on top of Pele's ring – perhaps an eruption to Pele's south explains the inward buckling of Pele's ring seen in some observations (such as the I24 image in Fig. 2.1).

Comparing the simulated Pele/Pillan system to the observation, it may be

that the simulated Pillan is too small. The white fringe around the observed Pillan is more strongly present on the Pele-facing side of the black spot and may result from the intense deposition seen below the interaction region in simulations. The orange and yellow material even closer to Pele's source is likely due to material from Pele if both plumes were active simultaneously; a slightly larger Pillan could push Pele's canopy further towards Pele's source than seen in the simulation.

## Chapter 7

### Plumes and Io’s Atmosphere

#### 7.1 Overview

Understanding the interaction between Io’s plumes and sublimation atmosphere is vital for making sense of observations of SO<sub>2</sub> on Io. In this chapter I illustrate principles of the plume/atmosphere interaction using axisymmetric models which build on the work of Zhang et al. (2003), and I use these simulations to develop a simple model for total column density. Three-dimensional simulations of round hole plumes with a simple surface model (entirely frost-covered, low thermal inertia,  $\cos^{1/4}$  temperature distribution) show how the plume/atmosphere interaction depends on plume latitude and capture the three-dimensional and time-varying nature of more realistic atmospheres.

#### 7.2 Axisymmetric Plume/Atmosphere Models

Many aspects of plume/atmosphere interactions can be seen with simple axisymmetric simulations. Zhang et al. (2003) simulated an axisymmetric Pele-type plume for surface temperatures between 105 K and 115 K and showed how the plume material condenses into the surface at low temperatures but is buffered from the surface by the sublimation atmosphere at higher temperatures. The plume gas “bounces” off the sublimation atmosphere, entraining some of it and actually lowering the pressure of the sublimation atmosphere around where the plume canopy impacts it. This

was seen to produce a net flow of  $\text{SO}_2$  away from the surface under the edges of the plume canopy, removing surface frost. Zhang et al. also examined column density and saw lower column densities at the edges of plume canopies than for the undisturbed sublimation atmosphere.

I performed similar simulations for surface frost temperatures from 110 K to 116 K and obtained similar results (Fig. 7.1), despite the many improvements made to the code since 2003. I simulated a medium-sized plume (about 130 km tall and about 400 km across) emerging from an 8 km radius round hole at 500 m/s and 300 K. The gas density at the virtual vent was typically  $3.426 \times 10^{-8} \text{ kg/m}^3$ , yielding about 1/3 of the total mass flux of Pele (landing in a ring of about 1/3 the circumference of Pele's ring). The simulations were performed without staging on 12 processors, and the surface model is the same as in Chapter 3.3.1. Varying the density of the plume in these simulations shows that the interaction between the falling plume gas and the sublimation atmosphere appears to depend on the falling plume gas being sufficiently dense to overpower the sublimation atmosphere. For the low density plume case of Fig. 7.1d, the disturbance in the sublimation atmosphere is restricted to higher altitudes.

I now use this axisymmetric model to investigate the relationship between surface temperature and total column density integrated over a large area around a plume. Column densities obtained from the two simulations in Fig. 7.1a and c are shown in Fig. 7.2. These agree qualitatively with the work of Zhang et al. (2003). The relative resilience of the hotter sublimation atmosphere is apparent in the blue line for the 116 K case at 200 km radius, although the absolute magnitude of the drop in local column due to the plume is similar in both cases. Integrating these column densities

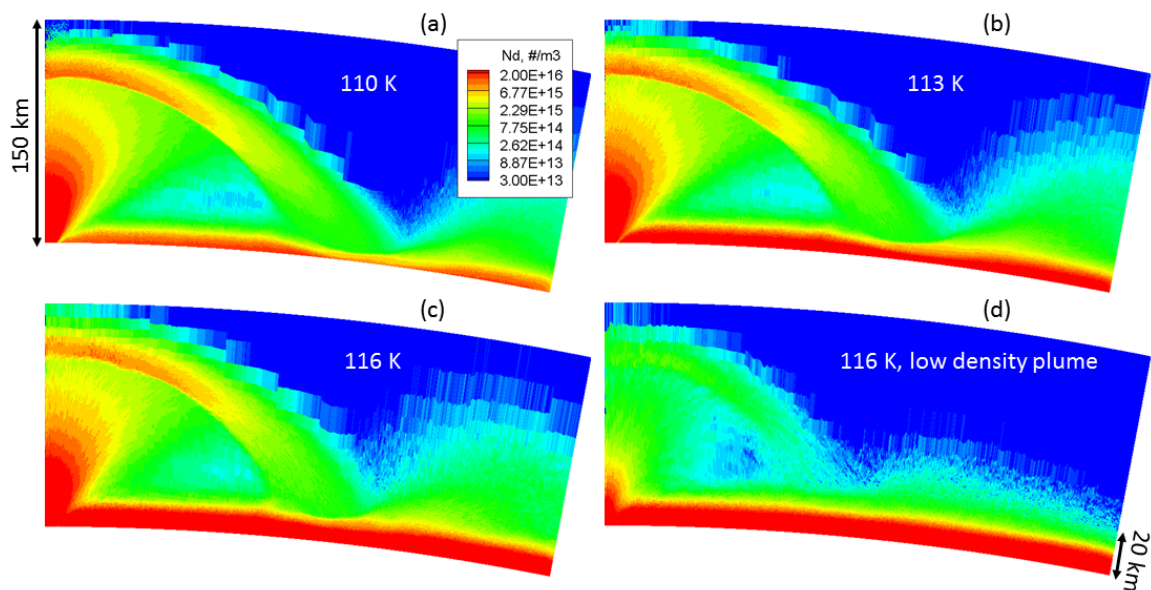


Fig. 7.1: Axisymmetric plumes simulated with a sublimation atmosphere produced by  $\text{SO}_2$  frost at several surface temperatures. Gas falling back to Io's surface in the plume canopy depresses the sublimation atmosphere locally. For higher surface temperatures there is a larger underlying atmosphere which is shielded from the plume by sublimated gas at higher altitudes. In (d), the 116 K case was simulated with a plume one tenth as dense as in the other simulations. This low density plume causes much less of a disturbance in the sublimation atmosphere. In all cases the plume gas “bounces” off the sublimation atmosphere to some extent, producing a region of enhanced density at high altitudes further to the right. In the low-density case (d), the falling plume has little effect on the atmosphere below about 20 km.

over a 350 km radius disc gives the total number of  $\text{SO}_2$  molecules above the surface for each case. When there is no sublimation atmosphere, the plume alone accounts for about  $2.22 \times 10^{31}$  molecules. The 110 K and 116 K atmospheres alone account for  $4.72 \times 10^{31}$  and  $3.87 \times 10^{32}$  molecules, respectively. The combined atmosphere/plume simulations at 110 K and 116 K produce  $6.12 \times 10^{31}$  and  $4.04 \times 10^{32}$  molecules, respectively. This means that the additional mass above Io's surface contributed by the plume is different in each case. In the 110 K case the plume contributes 63%

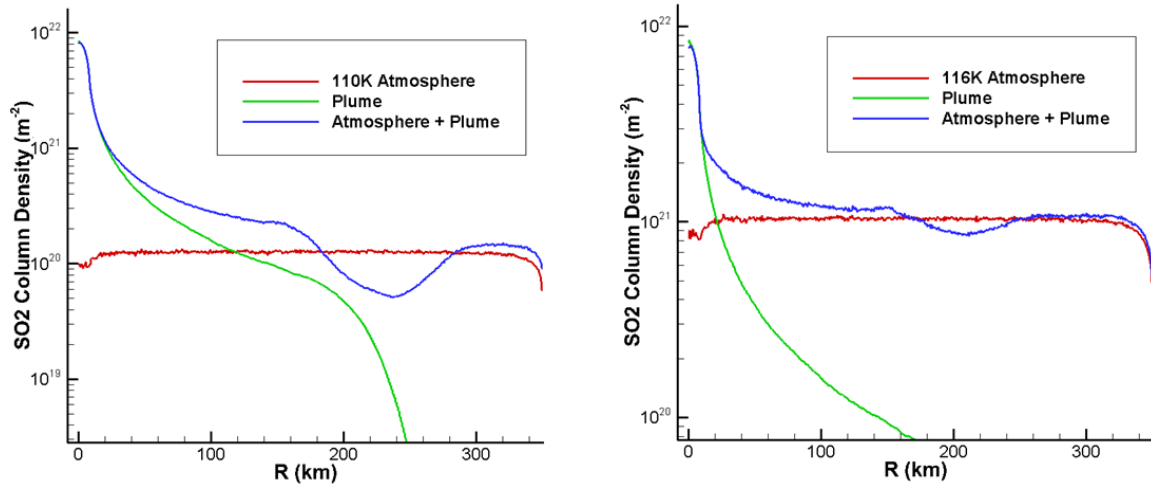


Fig. 7.2: Column densities as a function of radius from the symmetry axis of the domain for a variety of cases. Red lines are for a sublimation atmosphere with no plume. These dip slightly at the axis because of the sink where the plume would otherwise be and dip significantly at the right side because of the vacuum boundary condition there. Green lines are for plumes like those in Fig. 7.1 simulated without any sublimation atmosphere. Blue lines are for the 110 K and 116 K simulations from Fig. 7.1, with an interacting plume and atmosphere. Note that the Y-axis is different between the figures because the atmosphere changes by an order of magnitude – the green plume line is the same in both.

of the mass to the combined simulation that it would contribute in the absence of a sublimation atmosphere. In the 116 K case the plume contributes 75% of the mass to the combined simulation that it produces independently. This is presumably because the denser sublimation atmosphere in the 116 K case is better able to compensate for the impact of gas from the plume canopy. The finding is interesting because the additional mass contributed by the plume falls between surface temperatures of 0 K and 110 K and rises between 110 K and 116 K, but it must fall to 0 as surface temperature continues to increase (in the limit of very high surface pressure even the plume *stem* will fail to disturb the atmosphere).

This shows that the function relating plume mass flux and surface temperature to total column density at each point on Io's surface or just to total mass above Io's surface is not a simple one, despite often being assumed to be the sum of their independent contributions in other work (e.g. Tsang et al., 2012 or Walker et al., 2010). In the limiting case of a negligible sublimation atmosphere, a night-side plume like those shown in earlier chapters develops. This plume consists of some total mass of  $\text{SO}_2$  above Io's surface, obtained by integrating column density over the 350 km radius disc of the domain. As the surface temperature increases, the total amount of mass above Io's surface increases, but the net effect of the plume on the total mass drops because it displaces a weak sublimation atmosphere (illustrated by the 110 K case). At some point (below 116 K) the sublimation atmosphere begins to better resist the effect of the plume and the net effect of the plume on total mass rises again.

Physically, frost on the surface will tend to preserve vapor pressure equilibrium (VPE), acting as a local net sink if pressures rise above VPE and as a local net source if pressures fall below VPE. Plumes can produce a sustained non-VPE state, but the impact of plume material on the atmosphere will depend on the density of the falling plume material (and probably its velocity) and the surface pressure. In the limiting case of a very low-mass flux eruption, the rising plume material would fail to break through the atmosphere at all, and would be invisible from afar during the day because surrounding surface frost could maintain near-VPE conditions despite the plume's activity. At an intermediate mass flux, however, the rising plume might show up in column – recall from Chapter 3.3.1 that plume stems are so dense that it is difficult for the sublimation atmosphere to affect them – but the falling portion of the plume, which transports about as much material as the rising plume but which is spread over a much larger area, could be easily accommodated (that is, there

would be little effect on the local column) by a dense, collisional atmosphere. This is approximately the case for the low-density case in 7.1d.

### 7.3 A Simple Model for Total Column Density

Before continuing, it is important to clarify some terminology. Tsang et al. (2012) write about a “sublimation component” and a “volcanic component” of their atmosphere model. They determine each independently. The “sublimation component” is found analytically from VPE, hydrostatic balance, and a surface temperature while the “volcanic component” is assumed to be constant. These two are added together to find the total atmosphere. When we consider the plume/atmosphere interaction, however, the distinction between these components is difficult to define. We might speak of the “volcanic component” as material which has erupted directly from a volcanic vent, while the “sublimation component” is material which sublimated from surface frost. However, as will be seen later, volcanic molecules (in this sense) build up in a pre-existing sublimation atmosphere and continue to be supported from below by fresh sublimating gas. This is an important process, but it is strange to talk about gas which is thoroughly mixed with and indistinguishable from sublimating gas as part of the “volcanic component”. Instead, I define the “sublimation component” as the atmosphere that would be produced by sublimating gas alone, in the absence of any volcanism (this has the advantage of being the same as Tsang et al.’s definition). Then the “volcanic component” will be the *additional* atmosphere produced by volcanic activity, such that the sum of the two components is still the total atmosphere – thus my “volcanic component” is the additional mass due to the plume that was discussed in the previous section. The goal of a model for total column density is to determine the volcanic component given a sublimation component and a volcanic



mass flux (with perhaps some other parameters).

The large majority of the material in giant, dense plumes will always contribute to total column density, because for most of their height the sublimation atmosphere is negligible (their canopies are high above the exobase). As seen in the previous section, such plumes also exhibit a complex interaction with the sublimation atmosphere where their canopies approach the ground, often *reducing* total column density locally. However, this is not of great concern for explaining many observations, because the giant plumes have known locations and are relatively easily observed; observers of Io's sublimation atmosphere are typically careful to look in regions without known plumes. In a study like Tsang et al. (2012), the concern is not that their observations might be biased by giant plumes; they suppose instead that there is some dispersed, on-average volcanic component of the total atmosphere. As seen in simulations and as argued by Ingersoll (1989), the effect of such plumes on total column density is a local phenomenon. A “volcanic component” of the atmosphere, of the sort that might be mistaken for a sublimation atmosphere (i.e. it must be relatively uniform in space and not obviously just several discrete sources of material) must be the product of a large number of small plumes.

I suppose that these small plumes which produce a spatially-constant volcanic component resemble the low density case from Fig. 7.1d. If these plumes were very low density they would not affect the atmosphere significantly and would fail to rise above it, but if they were very high density we would see them clearly. The rising plume will contribute to column density independently of the sublimation atmosphere – a plume stem may displace some atmosphere, but its cross-sectional area is very

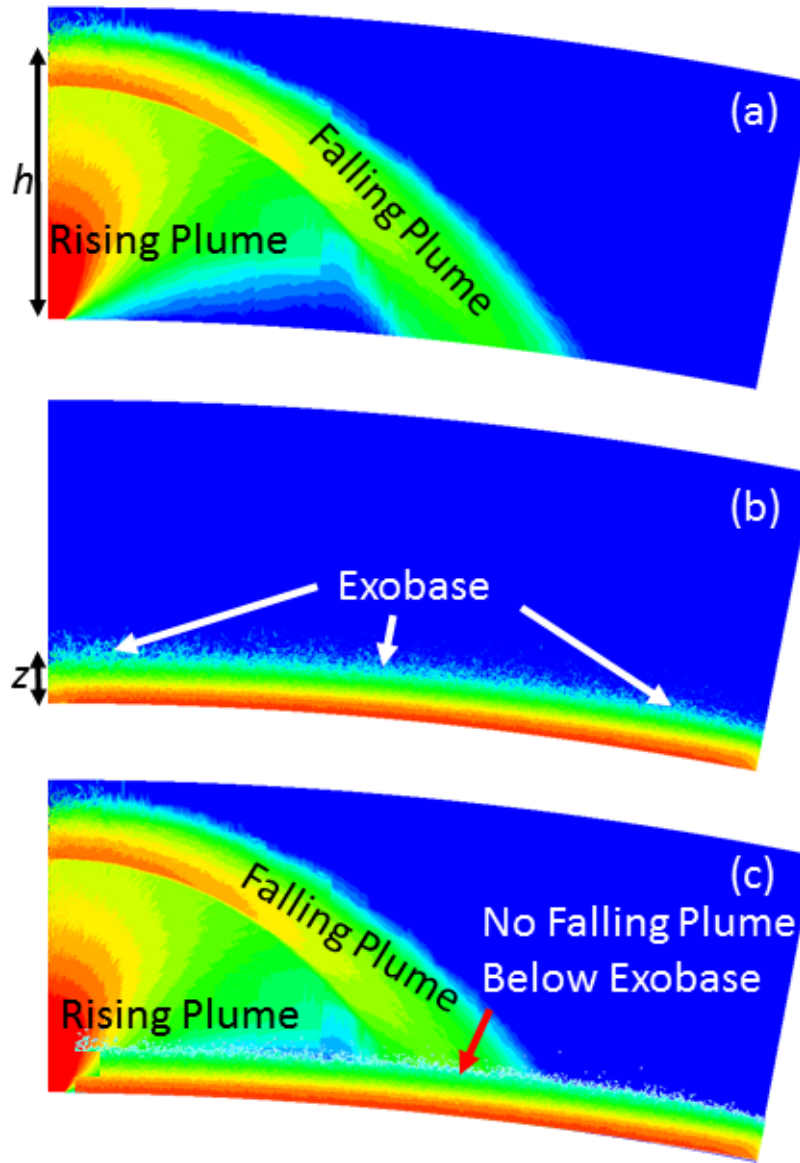


Fig. 7.3: Illustration of the model for total column density. (a) A plume of height  $h$  simulated with no sublimation atmosphere, consisting of a rising section and a falling section. (b) A sublimation atmosphere simulated with no plume, which is collisional up to its exobase at an altitude  $z$ . (c) The superposition of the rising plume, the sublimation atmosphere, and the falling plume above the exobase.

small<sup>1</sup> (see Chapter 3.3.1). Portions of the plume at high altitudes will contribute to column density because the sublimation atmosphere will be negligible. The falling plume will eventually cease to raise the local density (above what it would be in the absence of the plume) at low altitudes where the denser atmosphere can accommodate it, as seen in the previous section.

This model is illustrated in Fig. 7.3. The rising plume seen in Fig. 7.3a and the sublimation atmosphere (Fig. 7.3b) always contribute to the total atmosphere (Fig. 7.3c). On the assumption that these plumes are quite small, and less dense even than the low-density case from 7.1, it is reasonable to suppose that the falling plumes can be accommodated by the atmosphere upon reaching the exobase (or the exobase altitude of the sublimation-only case in Fig. 7.3b), where the mean free path in the undisturbed sublimation atmosphere is equal to a scale height (the exobase is typically at tens of kilometers altitude on Io). Below the exobase, the falling plume does not contribute to the total atmosphere, so Fig. 7.3c is a superposition of the rising plume, the sublimation atmosphere, and the falling plume above the exobase.

The exobase is approximately where the (still quite dense) low-density plume in 7.1d starts to significantly affect the sublimation atmosphere, although it is a little difficult to analytically determine where the exobase would be in the absence of the plume because the atmosphere cools rapidly with altitude. As the frost warms and the sublimation component grows, the exobase rises so that less of the falling plume remains above it. I also assume that observations are of large enough areas that both

---

<sup>1</sup>The plumes simulated in Fig. 7.1 erupt from 8 km radius holes, but this is probably unrealistically large for a small, hard-to-see plume, and the same mass flux could be produced from a much smaller hole at a much higher density, allowing even low mass flux plumes to punch through the sublimation atmosphere while rising.

plume stems and falling plume gas are seen at the same time.

For a very simple ballistic plume model, where particles constantly leave the surface going straight up with a velocity  $V = \sqrt{2gh}$ , which propels them to a height  $h$ , the fraction of airborne particles found below an altitude  $z$  is given by  $1 - \sqrt{1 - z/h}$ , as long as  $z < h$ . Half of the particles in the plume are rising and will contribute to total column density regardless, so I divide this by two to get the fraction of the ballistic plume material which is falling and which is below the exobase, then subtract it from one to get the fraction of material which is rising or which is falling but above the exobase altitude  $z$ :  $f = 0.5(1 + \sqrt{1 - z/h})$

This is the fraction of the night-side plume material (the “volcanic component” in the absence of any sublimation, or when the mean free path exceeds a scale height at 0 km altitude) that will contribute to total column density for some day-side exobase at  $z$ , and it is proportional to the volcanic component from plumes of height  $h$ . For  $z = 0$ , such as at night, all of the ballistic plume is above the exobase and will be observed. For  $z \geq h$  the entire plume is beneath the exobase; the rising plume will still contribute to total column density but the falling plume will not (the model likely breaks down at this extreme, since the rising plume would likely start to fade into the background sublimation atmosphere as well), so only half of the ballistic plume will contribute to column density. Between these extremes the fraction of contributing plume material will smoothly decrease as the collisional atmosphere covers up more of the falling plume. Exobase height  $z$  is a function of the surface temperature, with Io’s gravity and some properties of  $\text{SO}_2$ , which also determines the strength of the sublimation component. Thus for a volcanic component produced by plumes of height  $h$  which contributes some amount of total column density when the surface temperature is

$T_0$ , the volcanic component at some other temperature  $T_1$  can be obtained by scaling by the ratio  $f_1/f_0$ , calculating  $f$  at each temperature. This potentially produces a factor of two change in the volcanic component from these small, intermediate-density plumes as the surface temperature varies. This model is quite sensitive to the typical plume height  $h$  (although it could accommodate a distribution of several plume heights as a weighted average of their separate contributions). At most about 10% of a 350 km tall plume would be below a 70 km exobase, but a 60 km plume would be entirely submerged. However, the hard-to-see plumes which are of interest here are likely small.

To show why this variation in the volcanic component with surface temperature is important, I attempt to determine how this variation might affect the results of Tsang et al. (2012) (Fig. 7.4). Tsang et al. derived column densities from observations over a Jupiter year, showing seasonal variation. They fit these column densities with an atmosphere consisting of the sum of a sublimation component, which depended only on a sub-solar surface temperature, and a constant volcanic component. The sub-solar surface temperature over time was a function of a thermal inertia and an albedo. These two parameters, as well as the magnitude of the constant volcanic component, were what Tsang et al. attempted to constrain in their study.

I do not attempt to model Io's surface temperature over time. From Fig. 18 in Tsang et al. (2012), I determine that surface temperature ranges from about 110 K to about 116 K for the 300 MKS plot in their Fig. 17. I approximate their sub-solar temperature as a sinusoidal function of time, obtain surface pressures for those temperatures from VPE (using the same equation from Wagner, 1979, used by Tsang et al.), and then scale to a maximum sub-solar  $\text{SO}_2$  abundance of  $1.4 \times 10^{17} \text{ cm}^{-2}$ .

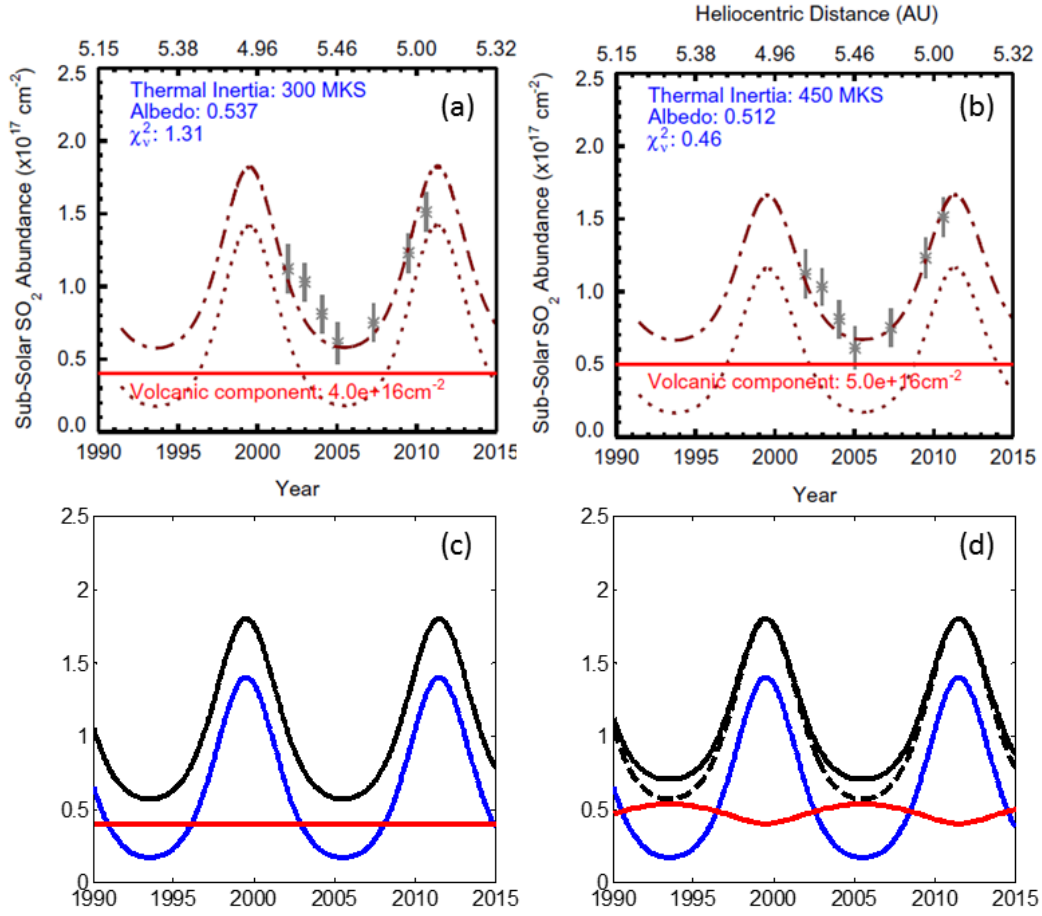


Fig. 7.4: Comparison of Tsang et al.'s (2012) model with and without a temperature-dependent volcanic component. (a) and (b) are from Fig. 17 in Tsang et al. For the indicated thermal inertias and albedos, their model produces a sublimation component shown by the dotted line. The solid red line is a constant volcanic component. The dashed line is the sum of these two components, taken to be the total atmosphere. The gray symbols are observational data to which they are attempting to fit. (c) is my attempt to reproduce (a), where the blue line is the sublimation component, the red line is the constant volcanic component, and the black line is the total atmosphere. (d) is the model in (c) with the substitution of a temperature-dependent volcanic component which is proportional to  $f$  and scaled to a minimum value of  $4 \times 10^{16} \text{ cm}^{-2}$ , where  $f = 0.5(1 + \sqrt{1 - z/h})$ ,  $z$  is the exobase altitude, and  $h = 50 \text{ km}$ . The dashed line is the total atmosphere from (c) for comparison.

This produces Fig. 7.4c, which compares well with Fig. 7.4a (Tsang et al.’s original plot).

I then determine an exobase altitude  $z$  by assuming the scale height of an isothermal hydrostatic atmosphere at 90 K (without plasma, the gas temperature drops rapidly with altitude, so this is chosen as an “average” temperature) with the surface pressure obtained from VPE with the frost at the frost temperature (between 110-116 K frost temperatures this ranges from 35-50 km). For a scale height  $H = \frac{RT_{90}}{g} = 6.5$  km, the number density where the mean free path is equal to a scale height is  $n = (\sqrt{2}H\sigma_{SO_2})^{-1} = 6.755 \times 10^{13} \text{ m}^{-3}$ . Then the exobase height for a hydrostatic atmosphere is  $z = -H \ln \frac{n}{n_0}$ , where  $n_0$  is the number density at the surface, obtained from VPE.

Where Tsang et al. use a constant volcanic component of  $4 \times 10^{16} \text{ cm}^{-2}$ , I compute  $f$  for every surface temperature and then set my volcanic component such that it is proportional to  $f$  and has a minimum value of  $4 \times 10^{16} \text{ cm}^{-2}$ . I chose 50 km for the typical plume height  $h$ . Using this model for the volcanic component produces Fig. 7.4d. The variation in the volcanic component tends to counteract the variation in the sublimation atmosphere (as the atmosphere gets denser it covers up more of the plume). The size of the effect (the difference between the solid and dashed black lines in Fig. 7.4d) is comparable to that of the effect Tsang et al. see by varying thermal inertia and albedo in their model (compare Fig. 7.4a to Fig. 7.4b).

Tsang et al. justify their use of a constant volcanic component over time by arguing that small plumes are long-lived and temporally stable and that the tidal interaction between Jupiter and Io, which is responsible for Io’s volcanism, is independent of heliocentric distance. They find best-fit thermal inertias ranging from 150

to over  $1000 \text{ Wm}^{-2}\text{s}^{-1/2}\text{K}^{-1}$ . They prefer the  $150 \text{ Wm}^{-2}\text{s}^{-1/2}\text{K}^{-1}$  value as higher values require albedos they deem too low. However, they can only obtain these lower values with large constant volcanic components – for  $150 \text{ Wm}^{-2}\text{s}^{-1/2}\text{K}^{-1}$  to be a good fit the constant volcanic component must be greater than the sublimation component for most of Jupiter’s year. This actually compares well with the  $200 \text{ Wm}^{-2}\text{s}^{-1/2}\text{K}^{-1}$  of Walker et al. (2012), who did not model plumes as contributing anything to the total atmosphere, but both are higher than the  $70 \text{ Wm}^{-2}\text{s}^{-1/2}\text{K}^{-1}$  of Rathbun et al. (2004), and far above other estimates discussed in Tsang et al. However, especially for small plumes, the results here show that the plume/atmosphere interaction can produce significant variation in the volcanic component over time. It may be that the high best-fit thermal inertia found by Tsang et al. is due to their fitting of the combined variation in both components with variation in only the sublimation component; they would likely obtain a lower best-fit thermal inertia with a time-varying volcanic component.

## 7.4 Equatorial Plume over an Io Day

The interaction between giant plumes and Io’s atmosphere can be further investigated with three-dimensional simulations that model surface temperature as a function of distance from the (moving) sub-solar point. An axisymmetric Pele-type plume is simulated emerging from an 8 km radius round hole (uniform vent conditions of 850 m/s vertical velocity, 500 K temperature,  $6.4 \times 10^{-8} \text{ m}^{-3}$  number density) up to an altitude of 60 km. Using the technique described in Chapter 3.3.1, this plume is patched into a three-dimensional planet-scale simulation. That is, plume particles are injected into the planetary simulation at 60 km altitude. Io’s surface is assumed to be entirely covered in  $\text{SO}_2$  frost with a surface temperature distribution on the day-



side given by  $T_s = (118 - 70) \cos^{1/4} \phi + 70$ , where  $\phi$  is the angle from the sub-solar point. The night-side surface temperature is set to 70 K. The sub-solar point moves around Io's equator at a rate of  $4.3633 \times 10^{-5}$  radians/s (a 40 hour day, though note that Io's day is actually closer to 42 hours long). At the beginning of the simulation, the plume is at the dawn terminator, which gives it enough time to develop before significant atmosphere develops beneath it. Simulations here were performed on 2002 processors. Particles far from the plume source were weighted by a factor of 100 relative to particles directly over the plume source in order to devote more processors to simulating the complex flow around the plume. All molecules are  $\text{SO}_2$ , but the simulations distinguish sublimated material from plume material so that each can be tracked.

Fig. 7.5 shows tracer particles for an equatorial plume simulation as the plume interacts with the atmosphere from dawn until dusk. Initially, the erupting plume behaves just like a night-side plume; a canopy forms and guides material down to the surface where it sticks. As an atmosphere develops beneath Pele to the east, plume material falling in the canopy fails to reach the surface and instead mixes with or bounces off sublimated material (starting at 50 min, continuing at 150 min). While this plume material diffuses down to the surface eventually, the sublimation atmosphere supports it as plume material spreads far from the plume itself (250 min). As a sublimation atmosphere develops to Pele's north and south, and eventually west, plume material begins to be supported all around Pele (250 min, 350 min). Close to noon, large amounts of plume material are suspended in the atmosphere all around the plume itself. As the plume proceeds to dusk, the local atmosphere collapses into the surface along with the plume material suspended in it (950 min, 1050 min). While this process is roughly symmetric about noon, an important asymmetry is that

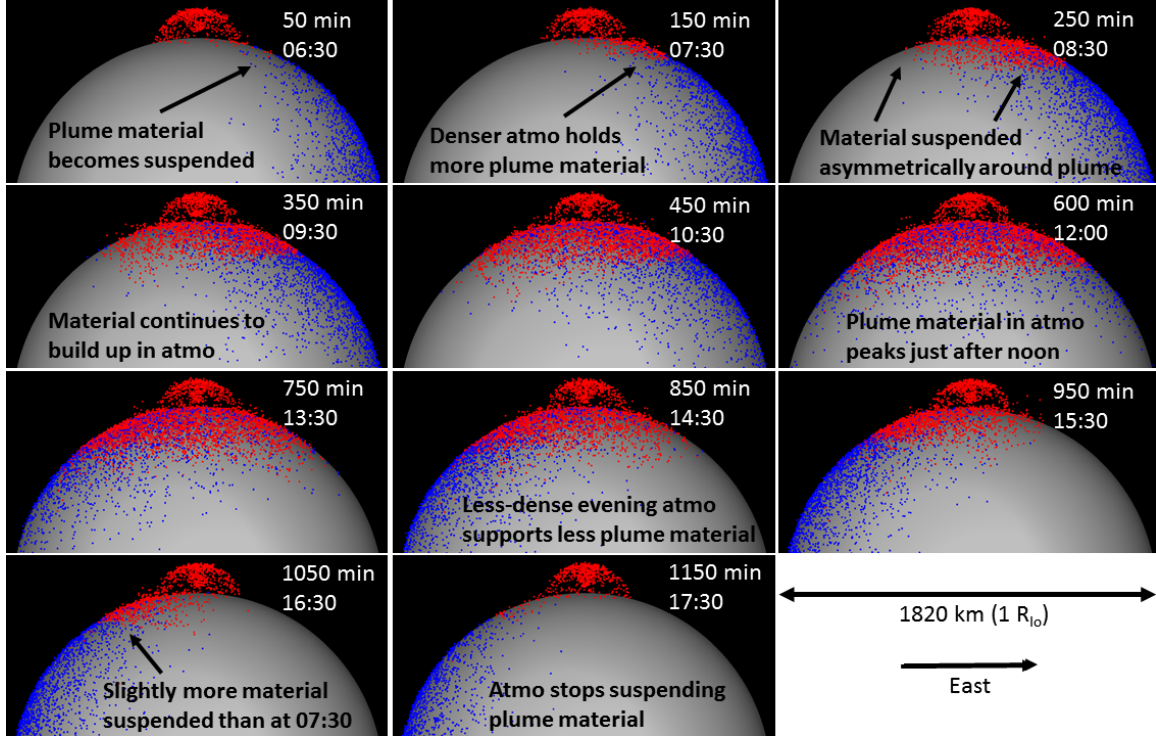


Fig. 7.5: Images of tracer particles for a simulation of an equatorial plume over half of a 40-hour day. Red particles are SO<sub>2</sub> from a patched plume and blue particles are sublimated SO<sub>2</sub>. Plume particle are over-represented by a factor of 25 relative to sublimated particles (to better visualize the plume). Time stamps give minutes since dawn (noon is 600 minutes after dawn) and local time at the plume source. The viewer is above the south pole.

plume material continues to build up in the atmosphere until after noon such that the amount of plume material above Io's surface peaks sometime between noon and 13:30, and slightly more plume material is present in the atmosphere near dusk relative to near dawn.

Fig. 7.6 provides a different perspective on the same simulation. As atmosphere advances under the plume during the morning, material flows out from the edge of the plume canopy into a semicircle (labeled A) which advances into the atmo-

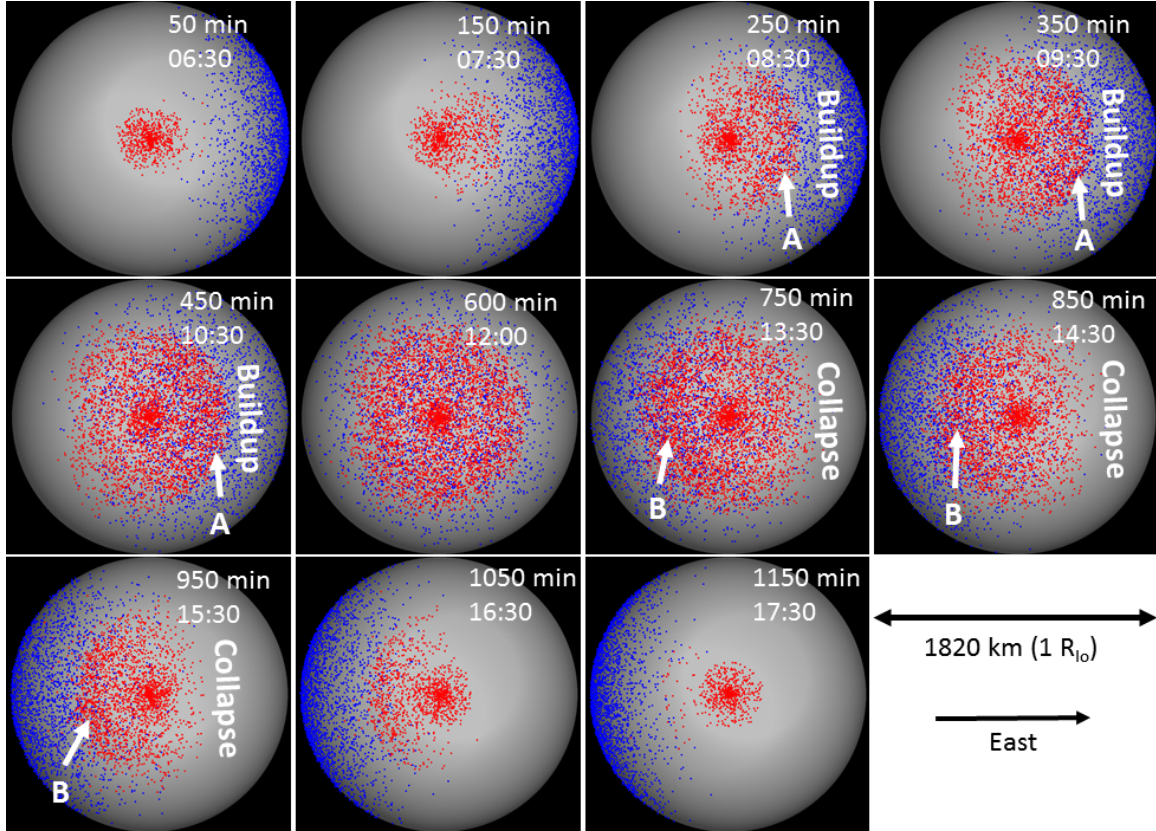


Fig. 7.6: Images of tracer particles for a simulation of an equatorial plume over half of a 40-hour day. Red particles are  $\text{SO}_2$  from a patched plume and blue particles are sublimated  $\text{SO}_2$ . Plume particle are over-represented by a factor of 25 relative to sublimated particles. Time stamps give minutes since dawn (noon is 600 minutes after dawn) and local time at the plume source. The viewer is directly above the plume.

sphere wherever the atmosphere is dense enough to support it. The creeping advance of plume material stops relatively early (it does not extend much farther east at noon than it did at 09:30). The density of plume material to the east of the plume continues to increase until noon, however. After noon, a similar circular feature appears to the west of the plume (labeled B). This feature does not form by slowly creeping out from the plume canopy, however. Instead, scattered material suspended in the

atmosphere to the plume's west at noon eventually finds its way to the surface, and newly-erupted material is confined to the circular feature. Meanwhile, plume material suspended in the atmosphere to the east of the plume collapses into the surface along with the sublimation atmosphere as local surface temperature drops. Near dusk (950 min, 1050 min), there is very little material to the plume's east and only scattered material to the west, mirroring the state of the system near dawn. Some asymmetry is apparent, however, with the circular feature (B) containing more material at 950 min than the eastern feature (A) contained at 250 min, and plume material is visible in a larger arc around the plume at 1050 min than at 150 min. This extra material is left over from earlier times, whereas in the morning plume material cannot become suspended until the atmosphere is sufficiently dense.

The interaction between the plume and the atmosphere is fundamentally similar to that seen just previously in Section 7.2 for axisymmetric plume/atmosphere systems. Axisymmetry is broken by the time- and space-varying surface temperature, but instantaneously and at each point where the plume canopy intersects the atmosphere, falling plume material is interacting with sublimated material coming off surface frost at some temperature. This is complicated somewhat by winds in the sublimation atmosphere produced by pressure differences, but these winds are generally slow. Depending on the density of the local sublimation atmosphere, plume material can drive it into the ground or bounce off it or mix with it (or some combination of these). Unless the plume can drive the sublimation atmosphere into the ground,  $\text{SO}_2$  from the plume will eventually settle into the atmosphere and mix with it, becoming indistinguishable from sublimated  $\text{SO}_2$ . It will slowly diffuse down to the surface and away from the plume, and will move with the bulk sublimation atmosphere where there is wind.

## 7.5 Equatorial Plume at Noon

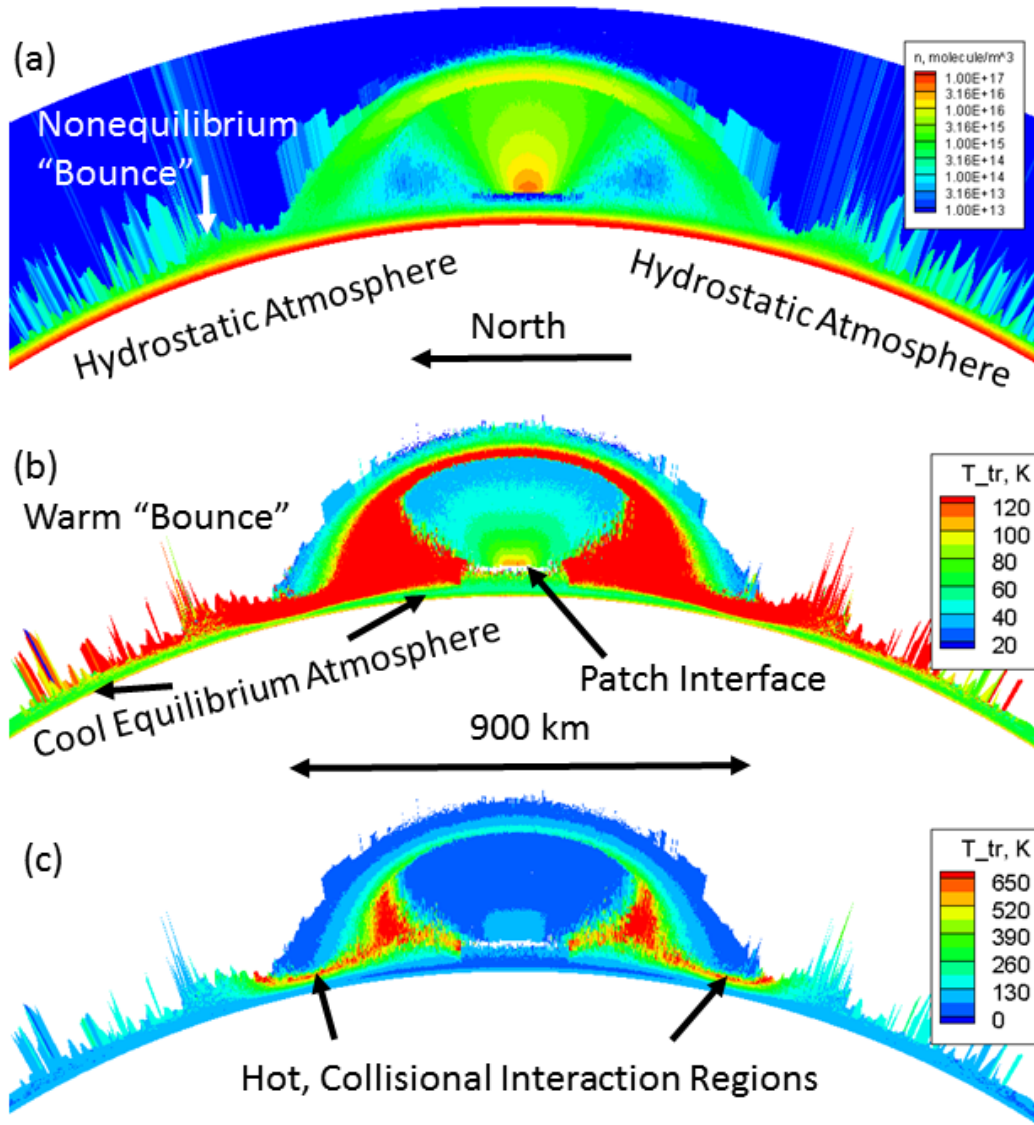


Fig. 7.7: Slices of an equatorial Pele-type plume at noon, where the peak day-side frost temperature is 118 K. (a) Number density contours of  $\text{SO}_2$ . (b) Temperature contours. (c) Temperature contours on an expanded color bar. For (b) and (c), regions with number density  $\leq 2 \times 10^{13} \text{ m}^{-3}$  and cells with vertical resolution coarser than 70 km are blanked.

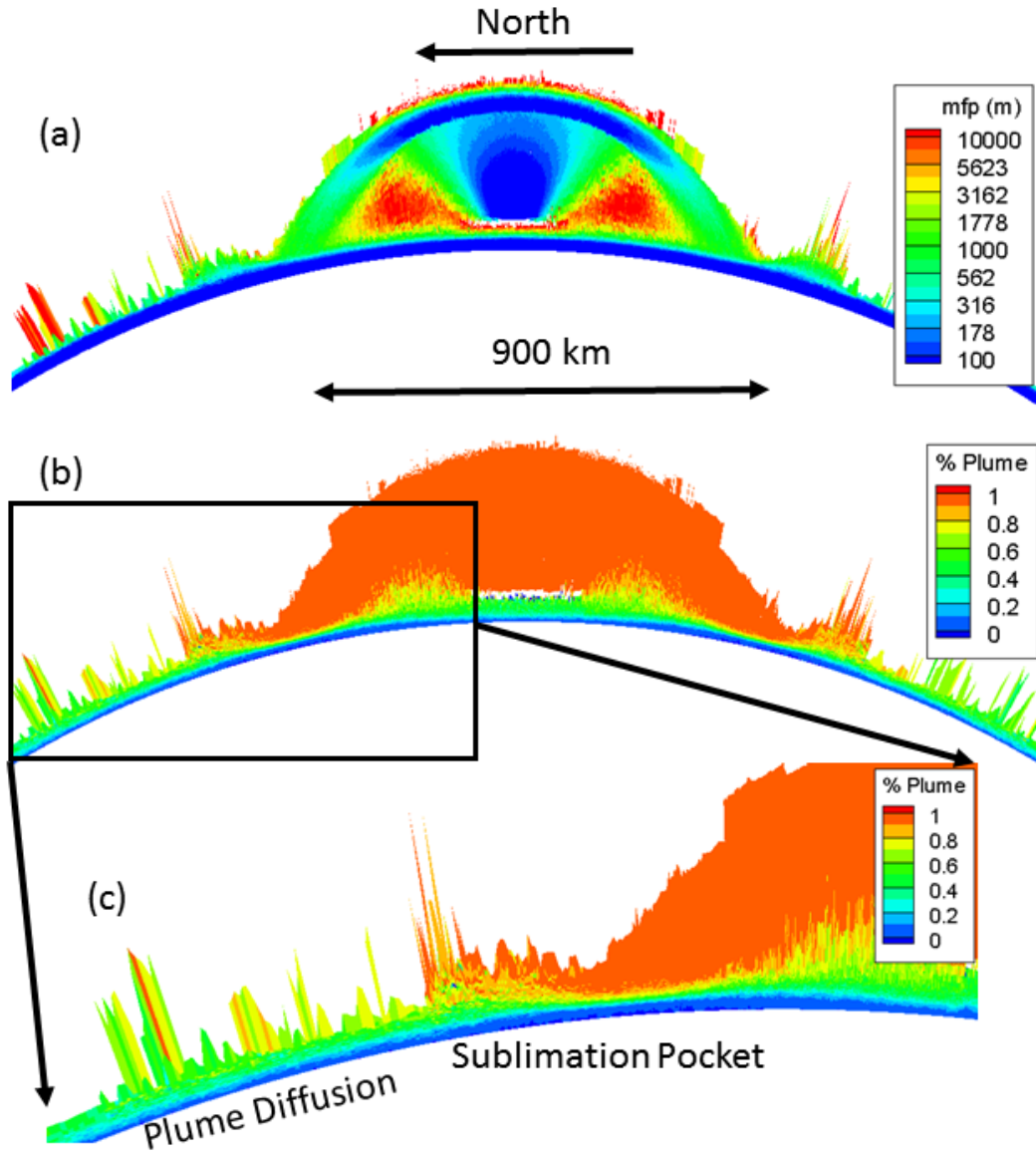


Fig. 7.8: Slices of an equatorial Pele-type plume at noon, where the peak day-side frost temperature is 118 K. (a) Contours of mean free path. (b) Contours of the fraction of particles which originated from the plume source. (c) blown-up view of (b) with an adjusted color bar. Regions with number density  $\leq 2 \times 10^{13} \text{ m}^{-3}$  and cells with vertical resolution coarser than 70 km are blanked.

Some of the features of the interaction can more clearly be seen in slices of the equatorial plume simulation time-averaged for a short duration around noon. The number density contours of Fig. 7.7a exhibit many of the same features as those for the smaller plumes at steady-state in Fig. 7.1. The plume develops independently of the atmosphere (in this case the plume is patched on to the planet at an altitude of 60 km) but gas falling back to the surface in the plume canopy eventually encounters the sublimation atmosphere. Some of this plume material bounces, creating regions of enhanced (but still low) density above the sublimation atmosphere at about 100 km from where the canopy intersects the surface of Io. However, mixing occurs very quickly, as seen in Fig. 7.8b and c. The plume canopy and the bouncing material are almost 100% plume material, but the top layer of the surrounding hydrostatic atmosphere is only  $\sim 50\%$  plume material. Mean free paths are kilometers or less in the falling plume canopy and in the hydrostatic atmosphere (Fig. 7.8a), so plume material is almost everywhere in thermal equilibrium with sublimated material where both are present. Plume material shocks when it encounters the hydrostatic atmosphere and increases the local pressure. Even sublimated material flows away from where the canopy intersects the atmosphere, creating a pocket of nearly-pure upwelling sublimated material directly under the interaction region. As the plume material is carried out away from the plume (or in towards the center of the plume), it diffuses down through the atmosphere, increasing the fraction of plume material at low altitudes. The atmosphere at very low altitudes is almost entirely composed of sublimated material everywhere because the surface is a sink for  $\text{SO}_2$  and all  $\text{SO}_2$  emitted by the surface is (by definition) sublimated. Plume material diffuses down from the (relatively) high-concentration upper atmosphere to the surface, where it deposits.



The temperature contours of Fig. 7.7b show how the falling plume equilibrates with the sublimation atmosphere. Away from interaction regions (far from the plume or directly over the plume source), the atmosphere is at 114-118 K just above the surface and cools rapidly with altitude (as expected without plasma). When falling plume gas hits the stationary sublimation atmosphere and shocks, it heats up and warms the sublimation atmosphere upon mixing with it, but the temperature profile of the hydrostatic atmosphere quickly recovers away from the plume canopy. The bouncing material appears to have a higher temperature, but the diffuse cloud of bouncing material is generally not collisional and is not in hydrostatic equilibrium with the underlying atmosphere. Adjusting the color bar to pick up regions of very high temperature only, as in Fig. 7.7c, one can see the very hot interface between the falling plume gas and the atmosphere generated by the shock in the plume gas when it hits the atmosphere. Fig. 7.7c also shows the extent of the warming in the atmosphere directly underneath the falling canopy.

Fig. 7.9a and b show the same contours as Figs. 7.7a and 7.8b, with more of the surrounding atmosphere visible and alongside plots of properties on Io's surface. In Fig. 7.9a, the bouncing material settles entirely into the atmosphere as it moves farther out, and the surface-level atmosphere becomes visibly less dense far from the sub-solar point (which is directly under the plume's patch interface). The total column density plotted on the surface reflects this, falling off towards the poles. While the peak total column density is at the sub-solar point, total column density has a local minimum in a ring where the plume canopy intersects the atmosphere (like those seen for the axisymmetric cases of Fig. 7.2). Fig. 7.9b shows the plume material continuing to spread away from the plume source while becoming less concentrated, both because it is expanding into a larger area and because some is lost into the surface on the way.



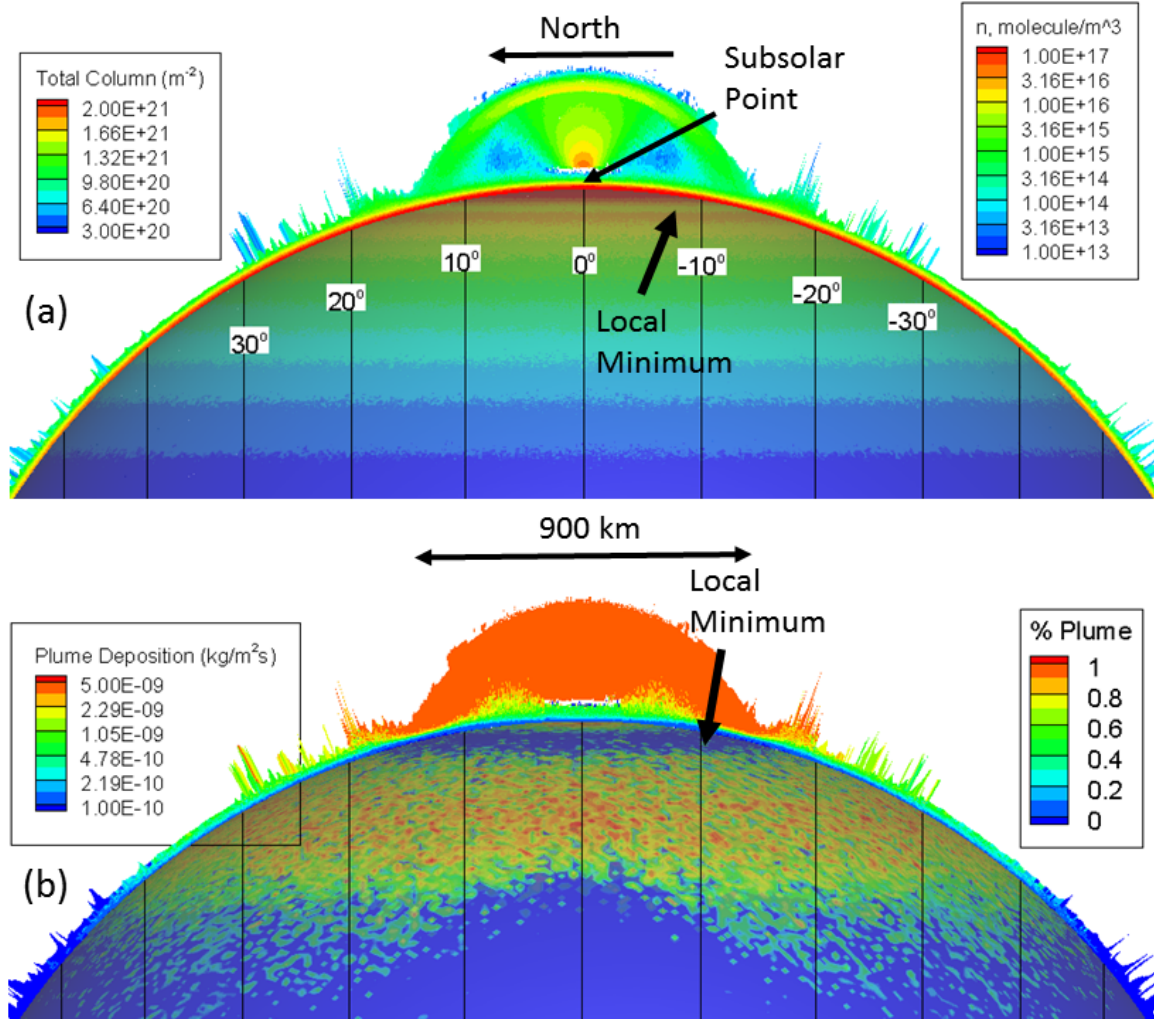


Fig. 7.9: Slices of an equatorial Pele-type plume at noon, where the peak day-side frost temperature is 118 K. (a) Number density contours of SO<sub>2</sub> with contours of total (combined plume and sublimation atmosphere) SO<sub>2</sub> column density over Io's surface. (b) Contours of the fraction of particles which originated from the plume source with contours of the deposition rate of plume material into Io's surface. Select lines of latitude are shown. Regions with number density  $\leq 2 \times 10^{13} \text{ m}^{-3}$  and cells with vertical resolution coarser than 70 km are blanked.

There is very little plume material in the atmosphere beyond  $\pm 40^\circ$  latitude. Plume material more easily reaches the surface as the surface temperature falls (away from

the subsolar point), since as the atmospheric column decreases the expected number of collisions experienced by a particle falling towards the surface decreases too. This combination of reduced density and faster diffusion produces fairly uniform deposition of plume material in a wide ring covering much of the day-side of Io. Plume material falls to the ground very differently than it did for night-side plumes (Chapter 4) – while the night-side Pele produced a ring where its canopy intersected the surface, the plume here deposits everywhere *except* where the canopy intersects the atmosphere. The peak day-side deposition rate is also an order of magnitude smaller than the peak night-side deposition rate.

Fig. 7.10 shows the equatorial plume at noon in column, and separates out the sublimated material from the plume material so that the column density of each can be viewed independently. The sublimated material (Fig. 7.10a) exhibits a relatively low-density ring around the peak sub-solar column density before rising again farther from the sub-solar point. This is where the plume canopy is falling into the atmosphere, creating high pressures which push material away. The plume material (Fig. 7.10b) achieves the greatest column densities over the region covered by its canopy (the red in the center is saturated – the peak column density along the plume centerline is about  $10^{22} \text{ m}^{-2}$ ) but produces fairly uniform column densities ( $\sim 2 \times 10^{20} \text{ m}^{-2}$ ) over a very large region on Io’s surface before eventually fading away. The green lobes to the northwest and southwest are likely a grid artifact; the grid is vertically coarser there and that inhibits the movement of plume material downwards through the atmosphere. The lobes represent only a small amount of material, though. Fig. 7.10c shows the fraction of the local column which is due to sublimated material. The plume dominates the area directly above its source (again, the blue is saturated) but quickly falls off to  $<50\%$  even within the region covered by the plume’s canopy. The

sublimated fraction achieves a local maximum around where the plume canopy first falls into the atmosphere and then falls again in the large surrounding region where plume material is suspended in the hydrostatic atmosphere.

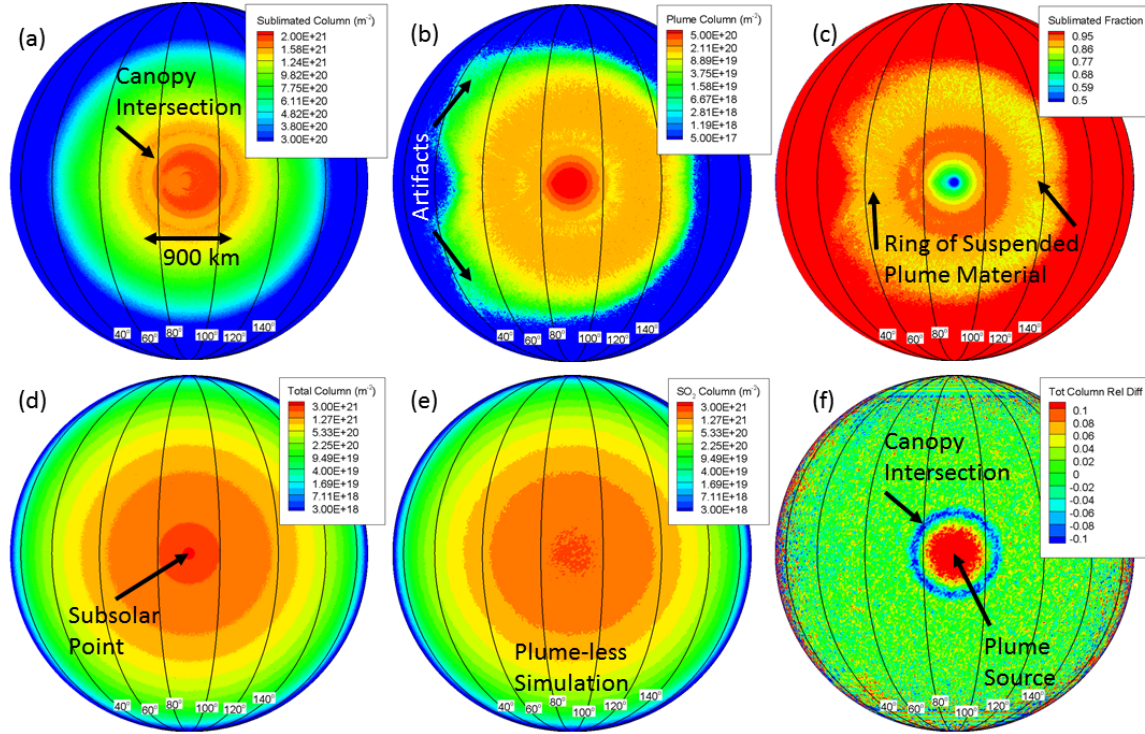


Fig. 7.10: Contours of column density and related properties for Io's day-side with an equatorial plume at noon, where the peak frost temperature is 118 K. (a) Column density for  $\text{SO}_2$  which sublimated directly from surface frost. (b) Column density for  $\text{SO}_2$  which erupted from the plume source. (c) Fraction of the local total column density due to sublimated material ((a) divided by (a) plus (b)). (d) Total column density. (e) Total or sublimated column density for a simulation of only the sublimation atmosphere, without a plume. (f) The relative difference in total column density between the plume/atmosphere simulation and the atmosphere-only simulation ((d) minus (e) divided by (e)), obtained by interpolating both onto a grid with half-degree resolution. These results do not include the plume inner domain below 60 km altitude, but this is almost entirely within regions where the figures are saturated already.

Except in the immediate vicinity of the plume source (at the subsolar point),

the total column density of the equatorial plume at noon simulation (Fig. 7.10d) is very similar to the column density produced by a sublimation atmosphere without a plume (Fig. 7.10e), as shown by the quantitative comparison in Fig. 7.10f. Over the region covered by the plume canopy, total column is significantly enhanced, and where the canopy intersects the atmosphere total column falls by about 10% relative to the plume-less case (similar to the steady, axisymmetric result in Fig. 7.2b). Outside of this ring of depressed column, the total column densities are nearly indistinguishable (although there is noise and some interpolation error in the figure). This supports the argument of Section 7.2 that the surface frost is very good at maintaining vapor pressure equilibrium; after plume material encounters the atmosphere and equilibrates with it, the total SO<sub>2</sub> atmosphere resembles the baseline plume-less case.

Including the plume’s inner domain, there are  $8.66 \times 10^{33}$  molecules of SO<sub>2</sub> in the equatorial plume simulation at noon. For the simulation of the sublimation atmosphere alone, there are  $8.56 \times 10^{33}$  molecules of SO<sub>2</sub>. The plume therefore only increases the total mass of the atmosphere by about 1.2%. These  $10^{32}$  molecules are the “volcanic component” of the system for an “atmospheric component” of  $8.56 \times 10^{33}$  molecules. The night-side plume, with no atmosphere, consists of about  $1.2 \times 10^{32}$  molecules of SO<sub>2</sub>. The plume produces a larger increase in the total mass of Io’s atmosphere when it is on the night-side, and contributes only about 84% of its night-side mass to total mass at noon. The model of Section 7.3 requires an exobase altitude of 190 km to get this result for a 350 km tall plume, which would require an extremely hot atmosphere (although note that Wong and Johnson, 2004, find an exobase altitude of 465 km with a temperature of 2800 K due to plasma). However, the model developed earlier did not consider the reduction of total column produced in a ring by a giant plume; for a weaker plume the interaction between its canopy and

the atmosphere would not be so significant and so it would contribute more additional mass to the atmosphere relative to the plume’s night-side mass. The Section 7.3 model was developed for smaller and weaker plumes than the one simulated here.

Even though the plume does not contribute much additional mass to the atmosphere beyond that which would have been produced by a sublimation atmosphere alone, plume material makes up a significant fraction of the atmosphere on most of the day-side (Fig. 7.10c). In fact there are  $8.33 \times 10^{32}$  molecules of plume  $\text{SO}_2$  in the equatorial plume at noon simulation, or 685% of the night-side plume. There are  $7.83 \times 10^{33}$  molecules of sublimated  $\text{SO}_2$  in the simulation, which is only 91% of the plume-less atmosphere case. The plume displaces almost 10% of the sublimation atmosphere at noon, and there is almost 7 times as much plume material above Io’s surface at noon than at night. If all material is  $\text{SO}_2$  as modeled here, this is perhaps only a bit of interesting trivia. However, the composition of plumes is characteristically different than the composition of Io’s sublimation atmosphere. Pele, for example, contains a significant amount of  $\text{S}_2$  (Spencer et al., 2000, and Jessup et al., 2007), which has the same mass as  $\text{SO}_2$  and so should move and diffuse similarly. These simulations predict that about 7 times as much  $\text{S}_2$  as is in the night-side Pele plume should be found above Io’s surface within about 1500 km of Pele at noon. If the Pele plume is about 15%  $\text{S}_2$  and if Pele is the only source of  $\text{S}_2$  then Io’s disk-integrated atmosphere should be about 1.5%  $\text{S}_2$  when Pele is at noon (assuming Pele can be approximated as an equatorial plume). Note that the plume modeled here produces about  $1.1 \times 10^4$  kg/s of  $\text{SO}_2$ . For different surface temperature models and different rates of  $\text{SO}_2$  eruption, these values will change, so that if Pele actually emits  $10^5$  kg/s of material it would displace much more sublimated material, would give rise to a higher concentration of  $\text{S}_2$  in the atmosphere, and so on. If multiple active

plumes are present on the day-side of Io, they will also indirectly interact with each other via the sublimation atmosphere. The composition of Io's atmosphere should disproportionately (relative to the volcanic mass flux) represent the composition of active plumes on the day-side even as the total mass of the atmosphere is largely determined by the temperature of sublimating surface frost.

Plume material is also found at the top of the hydrostatic atmosphere (Fig. 7.9b) almost everywhere, and so is preferentially exposed to plasma. For example, if plumes contain trace sodium, the process described here would result in relatively large amounts of sodium suspended in the upper day-side atmosphere of Io in large regions around plumes where it could be ejected from the atmosphere after interacting with high-energy plasma (assuming the atmosphere/plasma interaction is similar to the plume/plasma interaction of the previous chapter). The composition of the neutral cloud around Io should therefore also disproportionately reflect the composition of the plumes (even relative to the plumes' contribution to the sublimation atmosphere) and this mechanism could explain observations of elements like sodium (e.g. the sodium jet seen by Galileo, described in Burger et al., 1999).

## 7.6 Mid-Latitude Plume at Noon

Pele and many other plumes are not in fact on Io's equator, so to bracket many interesting cases I now turn to similar simulations for a plume at 30° north latitude (aside from some minor Coriolis effects these results will be applicable to a plume at 30° south latitude too). Fig. 7.11 shows density, temperature, and mixture fraction contours for the 30°N plume, comparable to Figs. 7.7 and 7.8 for the equatorial plume. The effect of surface temperature variation is much more apparent here, and

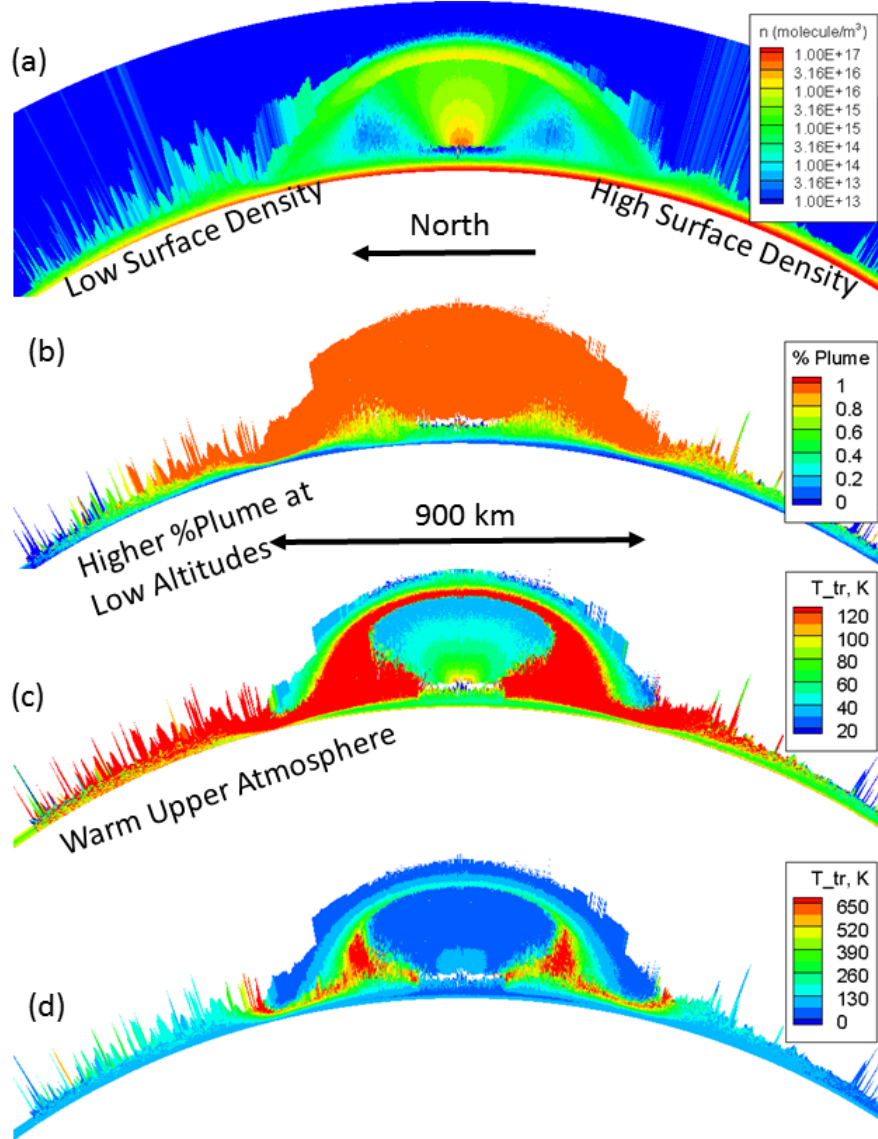


Fig. 7.11: Slices of a Pele-type plume at 30° north latitude, where the peak day-side frost temperature is 118 K. (a) Number density contours of  $\text{SO}_2$ . (b) Contours of the fraction of particles which originated from the plume source. (c) Temperature contours. (d) Temperature contours on an expanded color bar. For (b), (c), and (d), regions with number density  $\leq 2 \times 10^{13} \text{ m}^{-3}$  and cells with vertical resolution coarser than 70 km are blanked.

the north/south asymmetry of the 30°N simulation at noon can be seen in the surface atmospheric density in Fig. 7.11a. Plume material penetrates more deeply into the atmosphere to the north of the plume (Fig. 7.11b). The hydrostatic atmosphere to the north is much warmer than the atmosphere to the south (Fig. 7.11c and d) due to bouncing material falling back into the low-density atmosphere.

Fig. 7.12a shows the atmospheric density continuing to fall off to the north. The total column density likewise falls with distance from the subsolar point and plume source, which for the 30°N plume are in different locations. Where the plume canopy intersects the hydrostatic atmosphere there is a visible local decrease in the total column density. Fig. 7.12b shows that even though plume material makes up a high fraction of the total atmosphere just north of the plume, the plume fraction falls off rapidly with distance from the plume. To the south, the plume material suspended on top of the atmosphere spreads somewhat farther from the plume source. The low atmospheric density which enhances mixing to the north also allows plume material to diffuse down to the surface more quickly, while the dense equatorial atmosphere inhibits the flow of the plume material into the surface. However, the deposition rate of plume material into Io's surface in the north is similar to the rate in the south. A difference from the equatorial plume case of Fig. 7.9b is that some plume deposition is apparent below the interaction region of the falling canopy and atmosphere, but only to the north. The atmosphere there is not dense enough to completely shield the surface from plume material.

Column densities are particularly interesting for the 30°N plume because, unlike for the equatorial plume, the densest plume material (above the plume source) is not co-located with the densest sublimated material (above the sub-solar point).



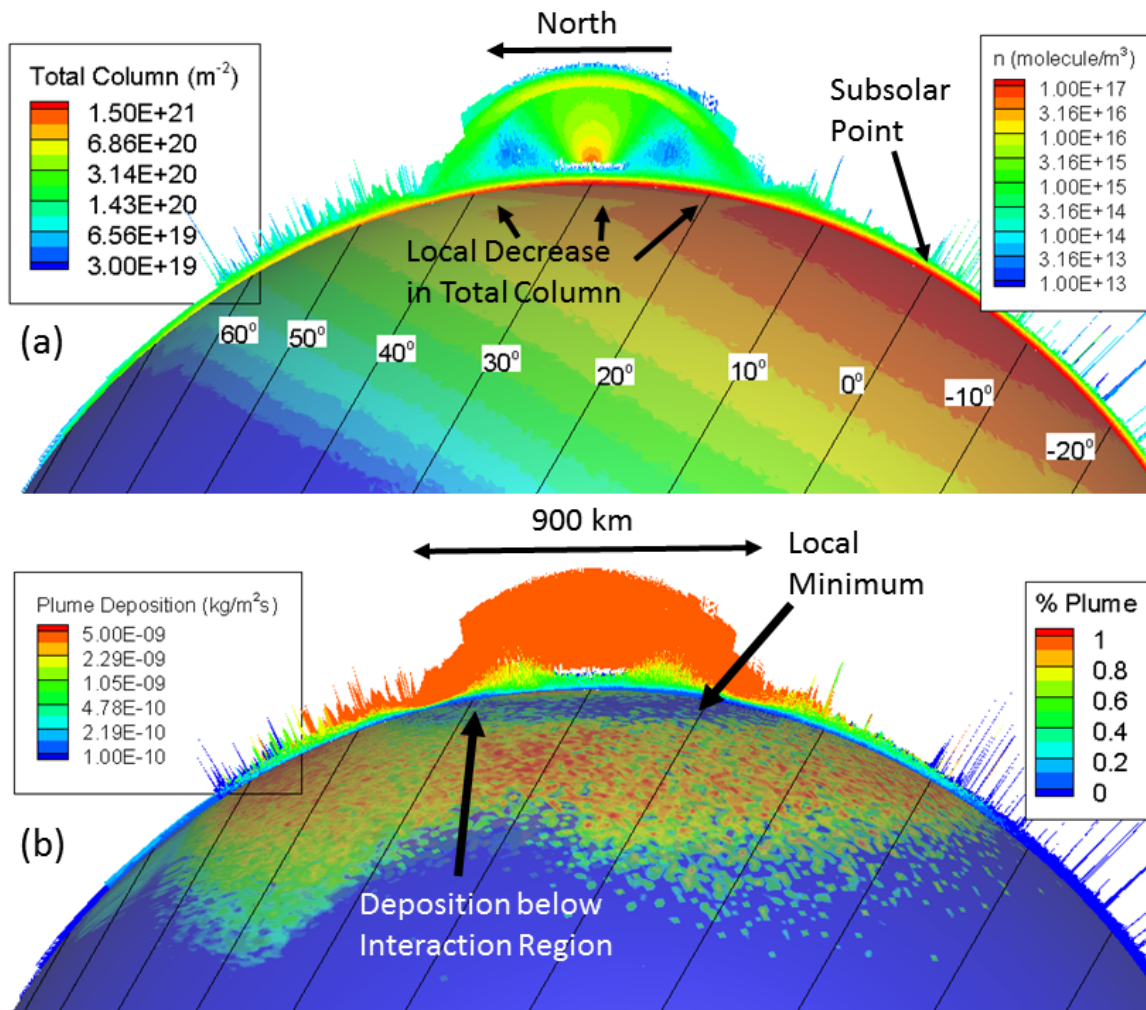


Fig. 7.12: Slices of a Pele-type plume at 30° north latitude, where the peak day-side frost temperature is 118 K. (a) Number density contours of SO<sub>2</sub> with contours of total (combined plume and sublimation atmosphere) SO<sub>2</sub> column density over Io's surface. (b) Contours of the fraction of particles which originated from the plume source with contours of the deposition rate of plume material into Io's surface. Regions with number density  $\leq 2 \times 10^{13} \text{ m}^{-3}$  and cells with vertical resolution coarser than 70 km are blanked.

The peak column density of the sublimated material (Fig. 7.13a) gets pushed just south of the equator. Sublimated column density remains depressed in a ring around

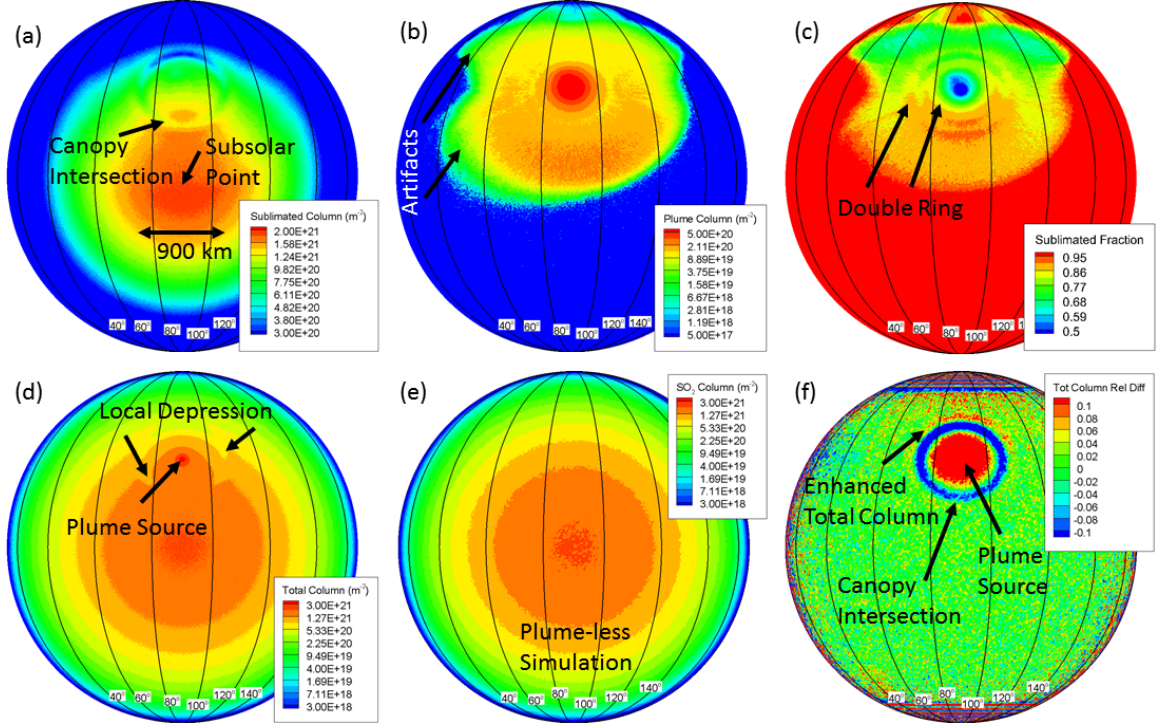


Fig. 7.13: Contours of column density and related properties for Io's day-side with a  $30^\circ$  north latitude plume at noon, where the peak frost temperature is 118 K. (a) Column density for  $\text{SO}_2$  which sublimated directly from surface frost. (b) Column density for  $\text{SO}_2$  which erupted from the plume source. (c) Fraction of the local total column density due to sublimated material ((a) divided by (a) plus (b)). (d) Total column density. (e) Total or sublimated column density for a simulation of only the sublimation atmosphere, without a plume. (f) The relative difference in total column density between the plume/atmosphere simulation and the atmosphere-only simulation ((d) minus (e) divided by (e)), obtained by interpolating both onto a grid with half-degree resolution. These results do not include the plume inner domain below 60 km altitude. As with Fig. 7.10, the lobe features far from the plume source and near the pole are likely artifacts.

the plume, as with the equatorial case, but is also visibly depressed in the entire northern hemisphere (this is why the peak sublimated column density is south of the equator). The column density of plume material (Fig. 7.13b) is significantly higher south of the plume than to the north. This is again due to the lower density of the

northern atmosphere allowing plume material to more quickly diffuse into the surface – the southern atmosphere can suspend more plume gas, and for longer. High column densities of plume material extend just past the equator. Even though there is more plume material to the south, Fig. 7.13c shows that plume material is a much more significant contributor to the total atmosphere to the plume’s north (as also seen in Fig. 7.11b). The total column density (Fig. 7.13d) could no longer be mistaken for a sublimation-only atmosphere, with the plume clearly increasing the local column above its source and depressing the local column in a ring. Performing the same sort of comparison as before, I obtain Fig. 7.13f, which resembles Fig. 7.10f with a ring of reduced column density where the canopy intersects the atmosphere and a disc of enhanced column density over the plume source. The 30°N plume also seems to produce a (red) semicircle of enhanced column density to the north of the low-density ring, corresponding to the double ring feature seen in contours of sublimated fraction (Fig. 7.13c). This red semicircle in Fig. 7.13f indicates a non-VPE atmosphere to the north of the ring, corresponding to the large amount of non-hydrostatic “bouncing” material relative to the mass of the local hydrostatic atmosphere there (Fig. 7.12a).

The 30°N plume/atmosphere simulation at noon contains  $8.65 \times 10^{33}$  total molecules of  $\text{SO}_2$ , almost the same as for the equatorial case – moving the plume had essentially no effect on the total mass of Io’s atmosphere. However, the atmosphere now contains  $8.03 \times 10^{33}$  molecules of sublimated  $\text{SO}_2$  and only  $6.24 \times 10^{32}$  molecules of plume  $\text{SO}_2$ , so the portion of the total atmosphere composed of plume material has dropped from 9.6% to 7.2%. This is likely due to the increased rate at which plume material moving to the north finds its way to the surface and sticks. However, the plume still contributes 5.1 times its night-side mass to the total atmosphere despite having very little effect on the total mass of the atmosphere; even for plumes at

mid-latitudes the surface frost can maintain VPE almost everywhere.

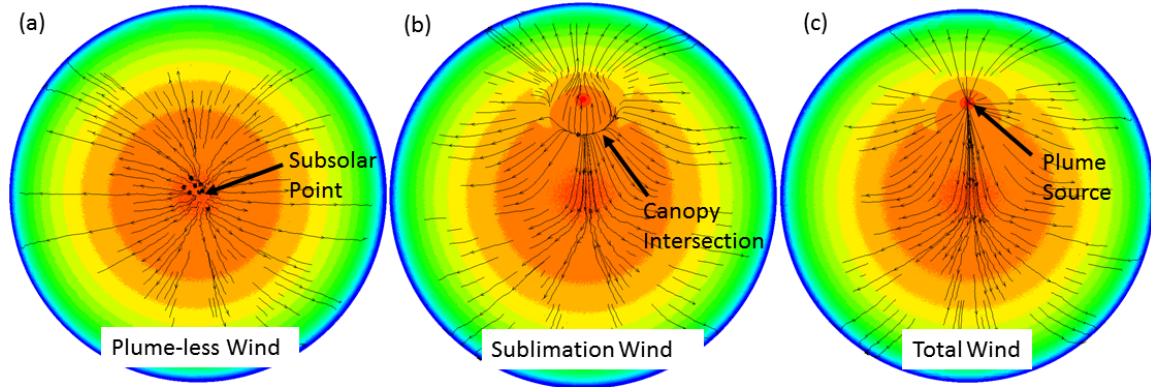


Fig. 7.14: Contours of total column density with streamtraces for (a) the atmosphere-only simulation and (b,c) the  $30^\circ$  north latitude plume with atmosphere simulation. Streamtraces in (b) represent the velocity of only the sublimated material, while in (c) they represent the velocity of both sublimated and plume material.

The mechanisms which maintain VPE are complex. As suggested by the spread of plume material out into the atmosphere around the plume, winds play a role in accommodating the large flux of plume material into the hydrostatic atmosphere. Fig. 7.14a shows streamtraces for the baseline plume-less case, obtained by averaging the velocities of all molecules in each column. Gas slowly flows away from the high pressure region above the sub-solar point and is accelerated to the night-side by pressure gradients (for more on simulations of winds in Io's sublimation atmosphere see Walker et al., 2011). Including a plume at  $30^\circ\text{N}$  completely changes the winds in the northern hemisphere. Fig. 7.14b shows streamtraces for only the sublimated material in the  $30^\circ\text{N}$  plume simulation. There is now flow southwards across the equator (although only moving at about 10 m/s). In the northern hemisphere the gas now mostly flows away from the plume instead of away from the sub-solar point. Where the plume canopy intersects the atmosphere to the south of the plume, the

wind switches directions; material flows north inside of this arc and south to the south of it. The plume canopy falling into the atmosphere creates a ring of high pressure (corresponding to the ring of high temperature and low column density seen earlier) which pushes material both outwards and inwards towards the plume source. Despite the depressed column density, material actually moves away from the interaction ring under the plume canopy (net flux out of the surface is positive from this ring, as described in Zhang et al., 2003). Streamtraces for the combined sublimated and plume flow (Fig. 7.14c) look similar to the streamtraces in Fig. 7.14b everywhere outside of the interaction ring, supporting the earlier conclusion that the plume material has become part of the hydrostatic atmosphere (displacing sublimated material), but inside of the interaction ring the total wind is dominated by erupting plume material moving away from the plume source.

Overall, the simulation of a plume at  $30^{\circ}\text{N}$  with a sublimation atmosphere displays many of the same features as the equatorial plume simulation from the previous section. With the possible exception of plumes near the poles (where the sublimation atmosphere will be thinner), plumes all over Io should have an out-sized effect on the composition of Io's atmosphere over the entire day-side and little effect on the total mass of the atmosphere outside of the region bounded by the night-side plume's canopy.

## Chapter 8

### Conclusions and Future Work

#### 8.1 Conclusions

Io's Pele plume and the interaction of giant plumes with Io's atmosphere and Jupiter's plasma torus were modeled using the direct simulation Monte Carlo (DSMC) method. An investigation of gas and dust flow from a plume source modeled after the lava lake at Pele provided an explanation for the shape and color of Pele's deposition pattern and constrained grain sizes in the plume. Simulation of the interaction of Io's sublimation atmosphere or Jupiter's plasma torus with Pele-type plumes at various locations on Io shed light on how Pele and other giant plumes interact with other aspects of Io's environment.

The most important conclusions are:

- Source geometry determines the shape of the gas deposition ring for giant plumes. Even though the source is small compared to the canopy height or ring diameter, the gas dynamics of the flow at low altitudes “encodes” features of the source geometry which propagate outwards as the flow expands. The lava lake source used here for Pele produces a deposition ring which closely matches observations.
- Complex source geometry gives rise to interactions between rising gas emerging from different parts of the source. An expanding jet from one source region

can encounter a jet from another and shock. This produces “axis-switching” behavior in the  $\text{SO}_2$ , and these near-vent interactions explain much of the far-field asymmetry of the plume. At Pele, such an interaction produces a kink in the plume canopy which is only visible from some angles; viewed from other angles the plume looks like an axisymmetric plume erupting from a round hole.

- The “virtual vent” model of plume sources, where uniform-property gas is created at high velocities and low temperatures (compared to gas just above the surface of a lava lake) is a reasonable approximation for the lava lake at Pele, where even complex gas flow produced by erupting fissures in the surface of a lava lake smooths out and becomes fairly uniform at low altitudes (1-2 km).
- The behavior of dust grains at Pele depends on the size of the grains and the motion of the gas. Very small grains ( $<100$  nm) remain entrained by the gas and follow its motion through the plume. Larger grains decouple as the gas density falls, and they preserve features of the gas flow-field below the decoupling altitude. Sufficiently large grains fan out to the east and west of Pele’s source even though the gas eventually expands preferentially north and south, creating the black “butterfly wings” seen in observations; large dust does not “axis-switch” with the gas. Even-larger grains decouple before source geometry becomes relevant and deposit in symmetric discs around the lava lake.
- The effect of plasma bombardment on plumes depends on where the plumes are located on Io. Asymmetry in the Io/plasma interaction yields more ion/neutral collisions on Io’s trailing hemisphere (which receives most of the plasma bombardment since the plasma overtakes Io in its orbit). Momentum transfer from the plasma is not very important to the bulk gas flow, but plasma warms and

inflates plume canopies while creating a large, diffuse cloud of neutral material above the plume. For plumes at sub- or anti- Jovian longitudes, these clouds are a large potential source of material for the plasma torus. At sub-plasma longitudes new ions are likely to be driven into the surface while at anti-plasma longitudes a plume would be shielded from plasma bombardment by Io. Plumes (or any other significant source of gas) effectively shield underlying atmosphere or surface from the plasma except near the sub-plasma point (where the ions are driven into the surface by the fields even if occasionally interrupted by collisions).

- Plume canopies are sufficiently dense to cause ion slip, with ions deflecting in the direction of the electric field rather than continuing in the  $E \times B$  direction around Jupiter. This can trap ions in plume canopies, producing a large and asymmetric energy flux into plumes as ions reaccelerate between collisions. Most chemical reactions also occur in the densest parts of plume canopies where ions deposit the most energy, and most daughter species remain confined within the plume and move with the  $SO_2$ .
- Plasma interaction causes plume deposition patterns to become more diffuse and more uniform. At Pele, this helps explain the thickness of the observed red ring on Io's surface.
- When the canopies of plumes intersect, as with Pele and Pillan, strong shocks form and they deflect falling material. Deposition underneath the interaction region is especially intense, and the larger plume's deposition ring may buckle inwards.



- The interaction between plumes and Io’s sublimation atmosphere is complex. When determining many quantities of interest it is a poor approximation to superpose a night-side plume and an independent sublimation atmosphere. In particular, the additional mass due to plume activity found above Io’s atmosphere at any given time depends not just on features of Io’s plumes, but on the local surface temperature around them. Only the largest plumes affect the total mass of Io’s atmosphere almost independently of surface conditions.
- Because the exobase altitude depends on surface temperature, small plumes increase the mass of Io’s atmosphere by larger amounts as surface temperature decreases. A dense sublimation atmosphere with a high exobase can hide the presence of small plumes by maintaining vapor pressure equilibrium in a hydrostatic atmosphere.
- Surface frost maintains vapor pressure equilibrium even when large plumes are active, and by doing so accommodates and supports plume material resting atop it while preserving the total mass (the combined mass of sublimated and plume material) of Io’s atmosphere. Massive amounts of plume material (many times the night-side mass of plumes) can become suspended in Io’s atmosphere during the day so that the composition of Io’s atmosphere may reflect the composition of all plumes currently in sunlight.

## 8.2 Future Work

The results presented here could be extended in several ways by performing different simulations using the same methods or by expanding upon the models used in this work.

- For the standalone Pele plume of Chapters 4 and 5, a model for condensation would allow for comparison to line-of-sight observations through the plume.
- Additional plume/plume simulations might be able to provide an explanation for the inward buckling of the southern portion of Pele’s ring seen in some observations.
- The cross-sections of ion/neutral collisions (except for resonant charge exchange reactions) are taken to be identical to cross-sections for neutral/neutral collisions. This is a bad assumption at low speeds, and should be addressed before an attempt is made to quantify escape from Io with the UT code.
- The modeled plasma includes no electrons, nor is there electron chemistry. Electrons may matter, especially where ions tend to move differently from electrons (such as in dense gas) under the influence of the background fields. Ambipolar diffusion could be included and in general the deformation of the electric and magnetic fields due to the simulated motion of the plasma could be considered.
- Simulations with plasma in a much larger, mostly-collisionless domain (large enough to cover Io’s entire orbit) could shed more light on how material from Io escapes or supplies the plasma torus.
- The plume and plasma models used here could be combined with the full surface models used by Walker et al. (2012) to investigate many features of Io’s environment simultaneously.

## Appendices

# Appendix A

## Effects of Source Geometry on Plumes

Before settling on the lava lake geometry used for the source of Pele described elsewhere in this work, I performed simulations of small, cold plumes erupting from a variety of source geometries. Understanding gained from these simulations helped me to select the final source geometry and inexplain how that source geometry produces the observed ring. Here I briefly review some early results. Unless otherwise noted, molecules are created with a temperature of 180 K and an upwards velocity of 200 m/s, producing plumes of about 50 km in height, and the simulations were run on 32 processors. For more detail see McDoniel et al. (2011).

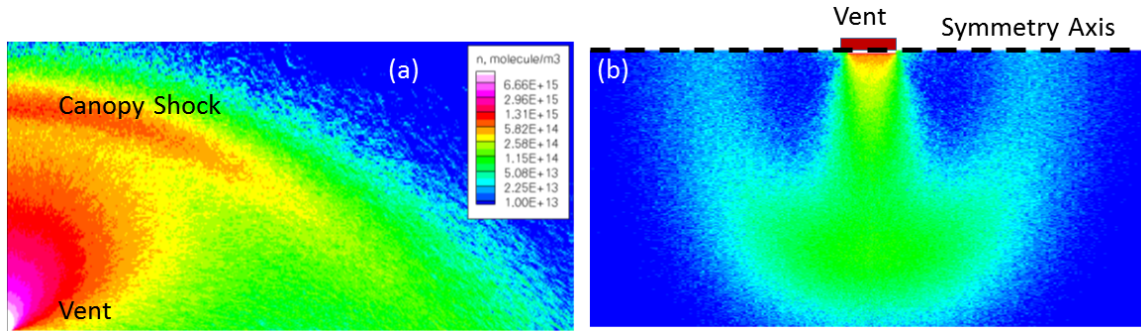


Fig. A.1: Number density contours for a plume erupting from a 20 km by 2 km rectangle. (a) A slice through the source's minor axis. (b) a constant-altitude slice at surface-level, where number density is a proxy for deposition intensity.

A very simple non-axisymmetric plume is one that erupts from a rectangular source. Fig. A.1 shows such a plume. Slices through this asymmetric plume resemble

slices from an axisymmetric plume (Fig. A.1a). However, asymmetry is apparent in the plume's deposition (Fig. A.1b, although note that the image is of number density contours at ground level rather than flux into the surface). Much more of the erupting material expands along the vent's minor axis than along the vent's major axis. This is somewhat peculiar at first glance, since initially the erupting material erupts uniformly from the vent (and so is mostly distributed along the vent's longer major axis). This axis switch is an important feature of near-field compressible plume flows – plume material tends to preferentially expand perpendicular to the major axis of the source.

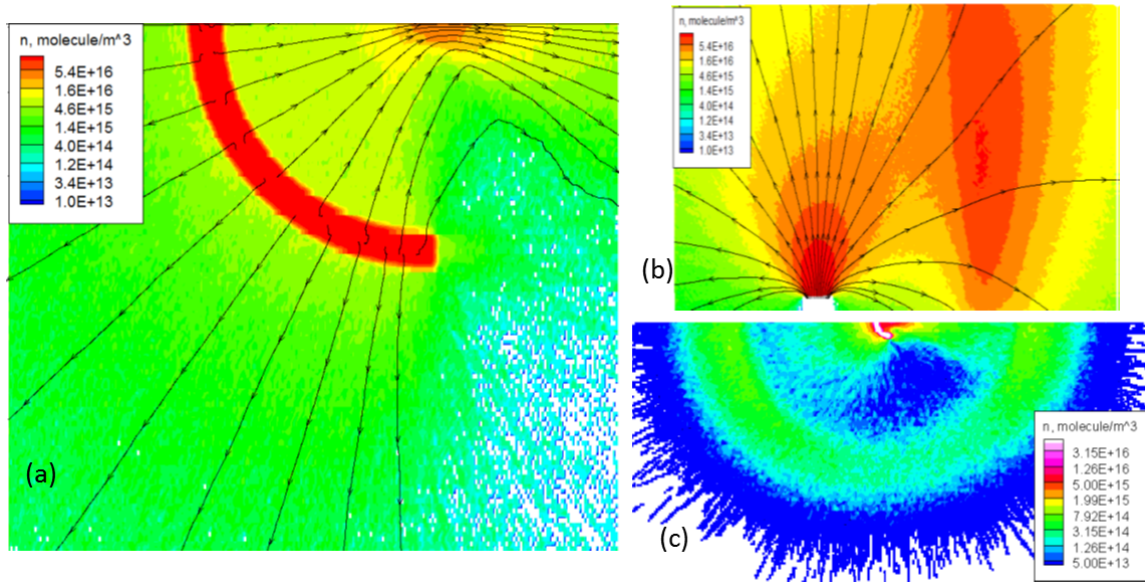


Fig. A.2: Number density contours for a plume erupting from a half-annulus 1 km wide with an inner radius of 7 km. (a) Ground-level contours with streamtraces in the immediate vicinity of the source (symmetry axis at the top). (b) A slice through the symmetry plane with streamtraces in the immediate vicinity of the source. (c) Surface-level contours for half of the entire plume.

Another simple geometry is a half-annulus. This case, shown in Fig. A.2,

illustrates the effects of curvature in the source geometry. In the immediate vicinity of the source (Fig. A.2a), flow expands towards and away from the center of curvature of the annulus. This is analogous to the earlier expansion along the minor axis of a rectangle – gas expands out from the long sides of the vent. However, because the source is curved in this case, the direction in which gas expands preferentially changes over the length of the source, and this produces diverging flow to the left and converging flow to the right. This generalizes to more complex geometries – flow converges where the source is concave. The converging flow meets at the center of curvature (top right of Fig. A.2a) and shocks, creating a large, dense region extending up through the plume to a higher altitude than the dense region directly above the source (Fig. A.2b). This is comparable to the strong jets that form between source regions at Pele. Finally, the half-annulus plume preferentially deposits material along the symmetry axis (Fig. A.2c). The most striking features are a deficit of material at 5:00 and very strong deposition at 3:00. The curvature of the vent has prevented flow from strongly expanding down and to the right, instead directing it to the right along the symmetry axis.

A first attempt at a realistic source modeled the virtual vent after a Galileo IR observation of Pele’s caldera (Fig. A.3a, inset). Fig. A.3a exhibits strong focusing of the gas everywhere that the source is concave. While the plume produced by this source had an egg-shaped deposition ring (Fig. A.3b), the orientation of the ring was off by around  $90^\circ$ . The overall curvature of the source can explain the shape of a deposition ring, but the orientation of the source also matters. From this I concluded that the true source must be concave to the northwest.

Finally, I modeled a virtual vent after a visible light image of the lava lake at

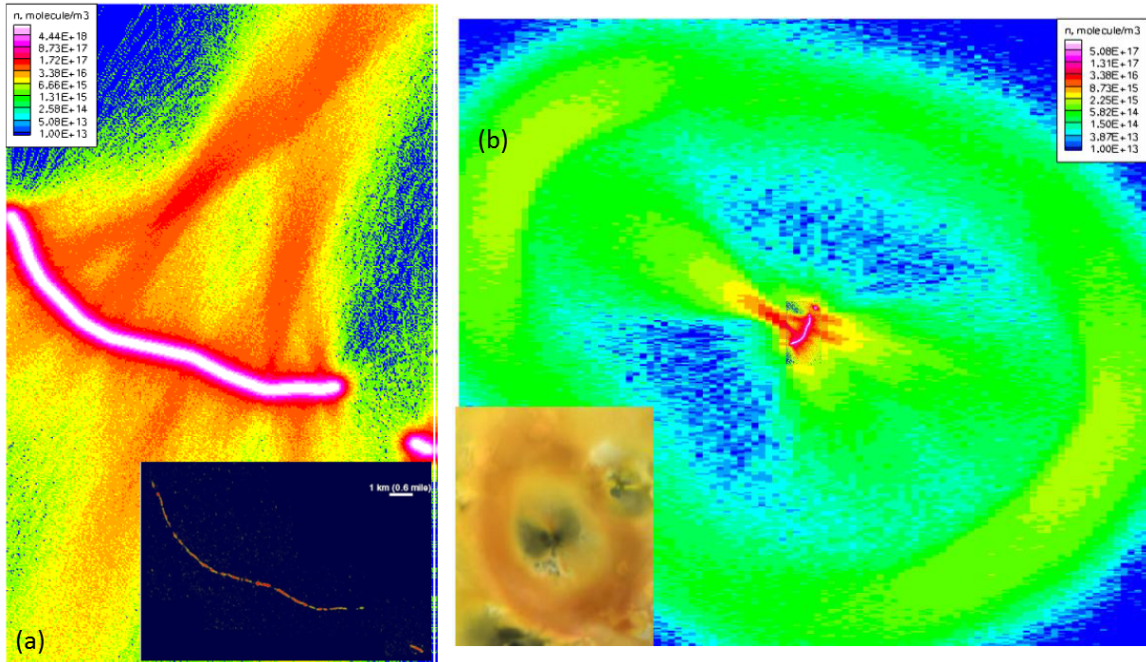


Fig. A.3: Number density contours for a plume erupting from a curved line source modeled after a 1999 Galileo SSI IR observation of Pele’s caldera. (a) Ground-level contours in the immediate vicinity of the source. Unlike other results in this chapter, this was simulated at Pele’s vent conditions on 64 processors. Galileo observation is inset. (b) Surface-level contours of the cold case for the entire plume, rotated by  $90^\circ$  to better compare with inset of Galileo observation of Pele.

Pele (Fig. A.4a, inset, image produced by the Planetary Image Research Laboratory at The University of Arizona from Galileo images). This produced the best deposition ring yet (Fig. A.4a). This source was slightly curved, but strongly resembled a rectangular source with a north/south minor axis. Even for this somewhat irregular source, slices through the plume (Fig. A.4b and c) resembled slices through axisymmetric plumes, but varied significantly with viewing angle. This eventually led to the choice of a heat map of the lava lake as the final source for Pele simulation. As seen earlier, this focuses gas in a way that reproduces the shape of Pele’s deposition ring.

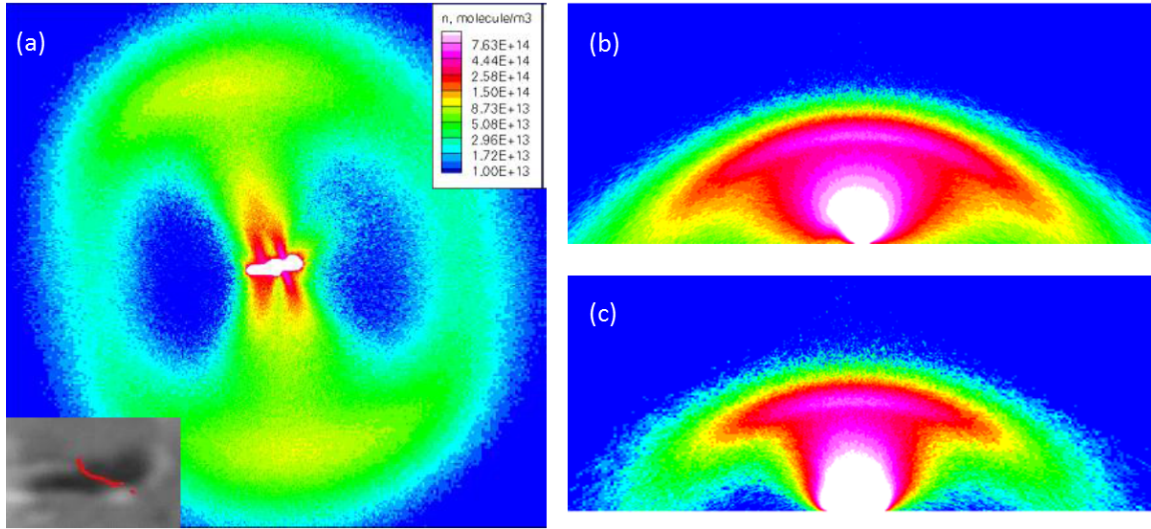


Fig. A.4: Number density contours for a plume erupting from a source modeled after the entire black lava lake seen by Galileo, shown in the inset in (a). (a) Near-surface contours for the whole plume, showing expansion along the vent's minor axis with two jets emerging from each side of the source, corresponding to highly concave parts of the source geometry. (b) A north/south slice roughly along the vent's minor axis, showing a full plume with a canopy that remains dense all the way to the ground. (c) An east/west slice roughly along the vent's major axis, showing a much more confined rising plume and a canopy which rapidly becomes less dense as it approaches the surface.



## Appendix B

### An Analytic Model for Plume Height

Even simple axisymmetric plumes must be simulated numerically because of the difficulty of an analytic treatment of a collisional gas rising and expanding, becoming nearly free-molecular, falling back on itself under gravity, and forming a canopy shock. Quantities of interest that can be obtained from simulations include the height at which the canopy shock stabilizes and the diameter of the deposition ring. Here I suggest a simple model for canopy height derived from conservation laws.

When a plume first erupts, there is no canopy shock. Once the expanding gas becomes collisionless, it rises to its ballistic height before falling back down. If the plume is dense enough, this falling material collides with fresh, rising material, producing a more-or-less stationary mass of gas high above the plume source. This mass is itself affected by gravity and falls. Fresh material continues to encounter it and is absorbed. The falling mass is arrested when rising gas carries sufficient momentum to support it against gravity. Now rising gas shocks to a halt upon encountering this stationary canopy of gas suspended over the plume. At steady-state the flow of mass into the canopy from below is balanced by flow down the sides of the plume and into the surface within the canopy. This flow within the canopy is hard to characterize.

Consider a simple model of a plume (Fig. B.1a) where gas erupts from a point source (labeled V) at some temperature  $T_v$  and upwards velocity  $V_v$ , yielding a stagnation temperature  $T_0 = T_v + \frac{V_v^2}{2C_p}$  for a gas with constant specific heats. This gas

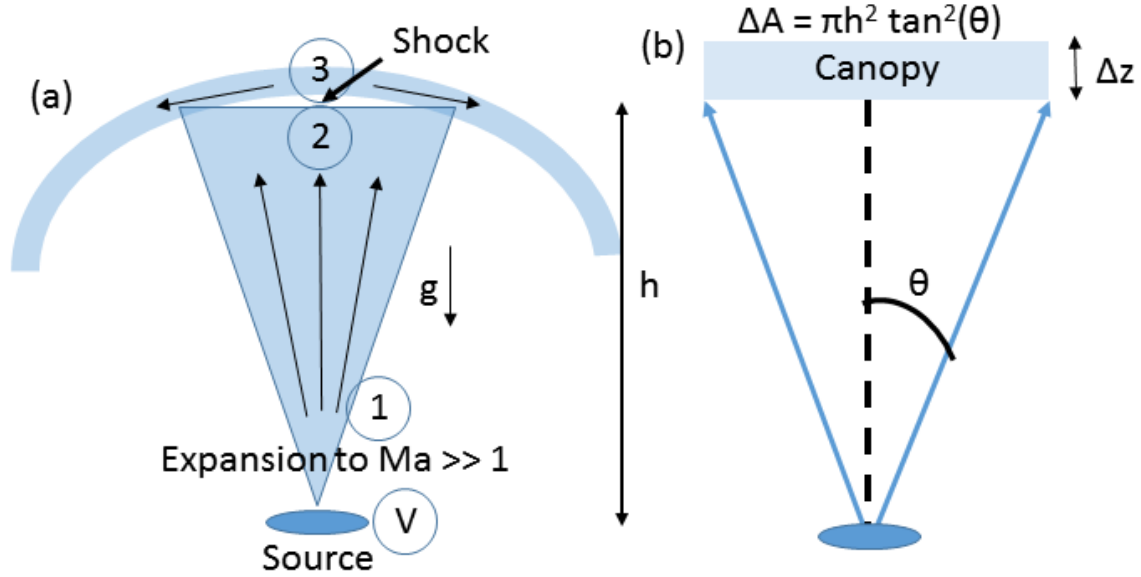


Fig. B.1: (a) Schematic of a plume erupting from a source at  $V$ , rapidly expanding to 1 at low altitude, then rising while decelerating due to gravity to conditions at 2. At a height  $h$  the rising gas shocks, forming a canopy at conditions 3. (b) Idealized model of a plume which expands in a cone with half-angle  $\theta$  from a point source. The rising gas produces a flat disc canopy with thickness  $\Delta z$  and diameter  $2h \tan \theta$ . Mass flux into the disc from below must equal mass flux out of the sides of the disc.

rapidly expands to  $T_1 \approx 0$ , converting all of its thermal energy to its ultimate velocity (label 1). Along the plume's centerline, this velocity  $V_1 = \sqrt{2C_p T_0}$  is directed straight up. As this fully-expanded gas rises along the plume's centerline to a height  $h$ , it loses energy to gravity in the amount  $gh$  per kilogram, reducing its velocity and stagnation temperature and yielding new conditions  $T_2 = T_1 \approx 0$  and  $V_2 = \sqrt{2(C_p T_0 - gh)}$  at some density  $\rho_2$  (label 2). Upon reaching the canopy at  $h$ , the gas shocks (label 3), becoming denser ( $\rho_3$ ), hotter ( $T_3$ ), and slower without losing energy (stagnation temperature). The stationary gas behind the shock quickly halts the newly-shocked gas ( $V_{z3} = 0$ ).

Simplifying the model further (Fig. B.1b), now suppose that the canopy over the plume source is a uniform-density slab of thickness  $\Delta z$  at the post-shock density  $\rho_3$ , where the area  $\Delta A$  is a disc of diameter  $D$  associated with a characteristic expansion angle of the plume and the plume height. The canopy is held up against gravity by momentum transfer from rising plume gas. Conservation of momentum yields  $\rho_3 g \Delta z \Delta A = \rho_2 V_2^2 \Delta A$ . This gives a result for the canopy thickness in terms of the pre- and post-shock conditions:

$$\Delta z = \frac{\rho_2}{\rho_3} \frac{V_2^2}{g} \quad (\text{B.1})$$

While the gas in the central canopy is stationary in  $z$ , constant supply of the canopy by erupting gas requires flow through the canopy out to the sides  $V_{x3} > 0$ . The gas must accelerate away from the plume's centerline if the canopy's density and thickness are to remain constant in  $x$ . Balancing the mass entering the canopy from below and leaving to the sides over some  $\Delta A$  with diameter  $D$ ,  $\rho_2 V_2 \frac{\pi D^2}{4} = \rho_3 V_{x3} \pi D \Delta z$ . Substituting the expression for  $\Delta z$  above and rearranging gives  $V_{x3} = \frac{Dg}{4V_2}$ . The kinetic energy lost out of the sides of the disc due to the bulk motion of a kilogram of gas is therefore:

$$\frac{V_{x3}^2}{2} = \frac{1}{2} \frac{D^2 g^2}{16 V_2^2} \quad (\text{B.2})$$

The temperature in the canopy could be obtained by applying adiabatic expansion and normal shock relations, but it will be low relative to the stagnation temperature at the vent and can be neglected. Stagnation temperature is conserved through the shock. An energy balance yields  $C_p T_2 + \frac{V_2^2}{2} = C_p T_3 + \frac{V_3^2}{2}$ . Or, neglecting  $T_3$  and recalling that  $T_2 \approx 0$ , gives  $V_2 = V_3$ . Substituting in Eq. B.2 gives

$$\frac{V_2^2}{2} = \frac{D^2 g^2}{32 V_2^2} \quad (\text{B.3})$$

Rearranging, I obtain  $V_2^2 = \frac{Dg}{4}$ . Using  $D = 2h \tan \theta$  and substituting into  $\frac{V_2^2}{2} = C_p T_0 - gh$  yields a relation for  $h$ :

$$h = \frac{C_p T_0}{\left(\frac{\tan \theta}{4} + 1\right)g} \quad (\text{B.4})$$

This relates the plume height  $h$  to the stagnation temperature of the plume, (constant) gravity, and a characteristic cone angle for the expanded  $Ma \gg 1$  plume. This cone angle will depend on the vent Mach number. If the Mach number at the vent is already very large, the plume will resemble a beam with  $\theta \approx 0$ . In this case the shock is predicted to be at the ballistic height  $\frac{C_p T_0}{g}$  of the erupting particles. The shock must actually be lower than this, but the result is not badly wrong – a simulation of a round-hole plume erupting on Io (with variable gravity, etc.) at 850 m/s and 0.01 K formed a shock at 215 km altitude rather than at the 225 km ballistic height. As the cone angle increases the shock is predicted to form at smaller fractions of the ballistic height.

A low Mach number plume will expand out in a wide cone, converting thermal energy into velocity in all directions as it expands. It is natural to choose  $\theta$  according to the Prandtl-Meyer function for the vent Mach number  $\nu(Ma_v)$ , where  $\nu_{max} - \nu(Ma_v)$  gives the maximum angle through which flow at  $Ma_v$  can turn isentropically as it expands. For  $\gamma = 1.333$ ,  $\nu$  ranges from  $0^\circ$  at  $Ma = 1$  to almost  $150^\circ$  for  $Ma \gg 1$ .  $\theta$  obviously cannot exceed  $90^\circ$  because of the surface of the planet. Taking  $\theta = \frac{\nu_{max} - \nu(Ma_v)}{2}$  for  $Ma_v > 1$  and  $\theta = \frac{\nu_{max}}{2}$  otherwise gives a maximum cone angle  $\theta_{max} \approx 75^\circ$  and provides a good fit to simulation results. Canopy heights range from about half of the ballistic height at low vent Mach numbers to the ballistic height at high vent Mach numbers.

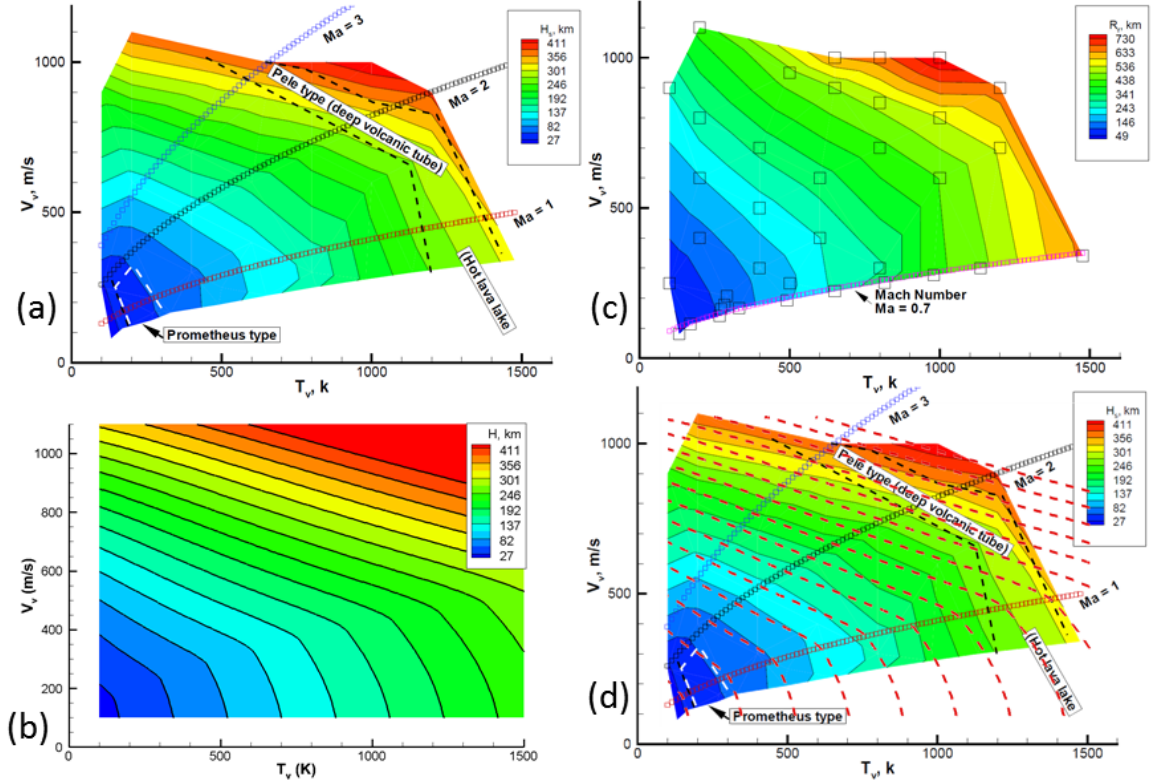


Fig. B.2: (a) Contours of constant canopy height for an axisymmetric plume erupting from an 8 km radius round hole as a function of vent velocity and vent temperature, from Zhang (2004). (b) Contours of constant plume height computed according to equation B.4 using half of the maximum turning angle for  $\theta$ ,  $C_p = 520$  J/K, and  $\gamma = 4/3$ . (c) Contours of constant ring diameter from Zhang (2004). Actual conditions simulated are marked with large squares; these were also the simulations used to construct (a). (d) Zhang's canopy height contours from (a) with the computed heights from (b) super-imposed as dashed red lines.

There are striking similarities between Zhang's (2004) contours of plume height (Fig. B.2a) and the results of equation B.4 (Fig. B.2b), as seen in Fig. B.2d. Equation B.4 captures the change in behavior of the contours around Mach 1 (note that Zhang's simulations do not provide excellent coverage of the  $Ma = 1$  line and that the exact position of the kink in the contours is uncertain for high  $T_v$ ). The slopes of the

contours are similar in both figures to either side of the  $Ma = 1$  line too. Flow below Mach 1 at the vent is highly under-expanded and its expansion into a vacuum may not be as simple as was assumed here. Quantitatively, agreement is excellent (often within 5%) at the conditions actually simulated by Zhang except at very low Mach numbers where Equation B.4 under-predicts canopy height.

Zhang's contours of ring radius (Fig. B.2c) are similar in shape to the contours of canopy height (and so are clearly related to stagnation temperature) except at low vent temperatures. For very high vent Mach numbers, the canopy shock is a small, flat disc on top of a narrow beam of erupting gas. Material is ejected from this shock at high speeds due to a large pressure gradient, increasing ring radius. At lower vent Mach numbers a curved canopy forms which can extend all the way to the surface, guiding material down.

This analysis assumed constant gravitational acceleration and specific heats, but it is probably reasonable to take  $\frac{C_p T_0}{g}$  as indicating the ballistic height of molecules for a vent at the given stagnation temperature even if the variations of specific heats and acceleration due to gravity are included. Radiation was also neglected, and this will tend to remove energy from hot gas near the vent, perhaps having an effect on canopy height that would offset the error due to assumption of constant gravity.

## Appendix C

### Comments on Simulating Complex Flows on Supercomputers

One of the biggest challenges in performing large-scale DSMC simulations on many processors is juggling concerns about the local grid structure and simulated molecule count with the need for load-balancing among processors while minimizing inter-processor communication. Grid resolution everywhere needs to be sufficiently high to capture flow features; coarse grids can produce results with large error by allowing collisions between molecules sampled from very different distributions. As the grid becomes finer, however, more simulated molecules are necessary in order to maintain reasonable statistics in each cell. Having too few molecules per cell gives rise to quasi-collisionless conditions; no matter the true density of the flow, the DSMC code cannot perform collisions in a cell with only one simulated molecule. Weighting schemes that take account of the flow density and the grid resolution are a natural response to this, but such schemes can be complex, and statistical issues can arise when weight gradients are large (multiplying particles only improves the statistics of the simulation when the clones can quickly become non-identical through collisions with other particles).

Load-balancing among processors should consider the time each processor requires between MPI barriers and is also constrained by the amount of memory available. Setting processor boundaries in a domain so as to divide the work involved

in computing collisions evenly across all processors may save time given unlimited memory, but if it results in one processor being responsible for almost all of the space within the domain, then gridding that space at an adequate resolution may require more memory than is available. Communication between processors also takes time and memory, and in DSMC is dominated by the sending of particles from one processor to another as they move across process boundaries in the domain. For very large simulations, communication consumes more time than any other task, and must be optimized. Furthermore, for unsteady flows, weighting, gridding, and load-balancing schemes need to be fast so that they can be performed multiple times per simulation. If processor boundaries move around as the result of a load balance (and they will), particles then need to be moved from processor to processor just as if they had crossed a processor boundary.

Gridding and load-balancing for the simulations in this work were explained in Chapter 3. Here I point out some common problems encountered before using these methods and while developing them. Then I briefly discuss weighting and communication. Finally, I comment on the benefits of GPU acceleration. This appendix is primarily intended for future graduate students seeking to expand on the results here using the UT DSMC code.

## **C.1 Common Problems with Gridding and Load-balancing**

A long-standing issue with plume simulations, especially with a grid defined in spherical coordinates, is that plume canopies may unexpectedly collapse. After an apparently steady-state plume develops, rising gas along the plume’s centerline somehow ceases to be sufficient to hold the canopy up against gravity, and the canopy



falls. This can severely deform the canopy everywhere until the canopy either attains a new steady-state (which is often an obviously unphysical inverted cone) or the mass falls to the surface and the plume simulation essentially resets to an eruption into a vacuum. While the proximate cause of this collapse is statistical noise – the canopy happens to become too dense for the rising gas to support – the error is self-correcting unless the grid along the plume centerline is too fine for the number of simulated particles present. Collisions are necessary both to hold up the canopy and for pressure gradients in the canopy to drive flow out to the sides of the plume. On spherical geometries the cell size in the azimuthal direction shrinks rapidly near the poles and the flow can be (inaccurately) nearly collisionless. An advantage of simulating plumes on the equator is that Cartesian grids (which spherical grids resemble on the equator) do not have these singularities. The polar cap described in Chapter 3.2.4 was designed to mitigate this problem. Otherwise, a weighting scheme can help to ensure adequate numbers of particles are in each cell along the plume centerline.

The method for gridding the domain vertically using linear segments, described in Chapter 3.3.2, occasionally produces very large cells. If in a column of atmosphere there are large stretches of very low density, the method will tend to use just one cell to cover each continuous stretch. The method is intended to allocate simulated particles evenly to all linear segments, and within segments the method comes close to allocating simulated particles evenly to cells. This means that at the edges of concentrations of material, cells will tend to extend far into the surrounding vacuum (until encountering more material or hitting a processor boundary). Problems can arise when large gradients exist in low-density flow in a column. The flow may locally be cold everywhere, but DSMC will compute collisions as if the gas at the top of a large cell is mixed with the gas at the bottom of the cell. Because of the

grid structure, the flow will seem much hotter than it actually is (even for ballistic particles because gravity will have done more work on high-altitude particles), and DSMC will compute collisions that should not occur between far-apart particles. A particular problem with plume and atmosphere simulations is that the plume material is "supported" by material tens of kilometers below it. Unphysically massive plumes can develop given enough time.

However, as with plume collapse, if the grid structure is too fine the opposite problem is often seen. This was the case with the northwest and southwest lobes in plume material column densities seen in Chapter 7. The grid was particularly fine at the plume source's latitude, and this allowed plume material to move down through atmosphere without colliding as much as it should have. A similar issue could arise in the atmosphere directly under the plumes where the grid is extremely fine because the processor domains are so small, with unphysically collisionless cells producing odd structure in the atmosphere flowing past. It is very important to choose good values for the number of cells per processor and for the various linear segments parameters.

When load-balancing (described in Chapter 3.2.4), an issue similar to that seen with the vertical grid structure can arise. If the domain contains large regions of vacuum, very few processors will be allocated to cover that volume. Often the vast majority of the simulated particles in such processors will be concentrated along one boundary. With a uniform grid in each processor (in latitude and longitude, and in altitude unless linear segments is active), the flow in these low-density regions will often be badly under-resolved. Recall that load-balancing divides the domain up into equal-particle latitude bands, then places processor boundaries within each latitude band to apportion particles equally among processors. For an equatorial

plume simulation on a domain covering the entire planet with no atmosphere, one such latitude band will be a very narrow slice on the equator. The first processor in the band will have a boundary at  $0^\circ$  longitude and the last will have a boundary at  $360^\circ$  longitude, but every other processor boundary will be within the plume (which only spans tens of degrees in longitude). The first and last processor in the band will tend to cover much more longitude than the other processors despite containing just as many particles, and the cells in these processors will be very coarse.

A simple solution at the expense of some speed is to artificially adjust the map of particle density from which the load-balanced processor boundaries are determined. Some fraction of the total number of particles in the simulation can be added to latitude/longitude bins of this map in order to force the load-balancing method to take some account of the volume simulated by each processor. In practice, the north and south polar cap processors provide good enough results in latitude without the need for further adjustment, but odd behavior can occur because of processors covering too much longitude. Fortunately, this adjusting of the particle map can also be done after the latitudinal boundaries are obtained but before the longitudinal boundaries are, and the amount added to each bin can be weighted by the latitudinal extent of the band. That is, processors in latitudinal bands with little total volume (such as a narrow slice on the equator, compared to most of the northern or southern hemisphere) can give more weight to volume in the particle map.

Different kinds of particles can also be weighted differently in the particle map. Because of sub-stepping, computing ion trajectories is much more expensive than computing neutral trajectories, so when load-balancing ions were counted several times each (on top of ions being weighted relative to neutrals in the actual simulation).

## C.2 Weighting

Spatially-dependent weighting is somewhat useful for plume-only simulations, although it was not used in this work except between stages – weights never differed within a single computational domain for neutral molecules, although ions were weighted differently from neutrals as described in Chapter 3.3.3. Weighting is vital for plume/atmosphere simulations, however. The simulation needs to resolve small features and high gradients inside plumes, and this requires small cells, many particles, and many processors. An appropriate weighting scheme which concentrates simulated particles in plumes causes load-balancing to allocate more processors to the area around the plume, and when more processors cover the same volume the grid within each processor is finer.

Weights should not change very rapidly – cloning several times between collisions should be avoided if possible, although destruction is acceptable because it does not amplify noise. In this work I used weighting schemes that varied with latitude and longitude only. I experimented with radial weighting in the atmosphere but was unable to obtain a good result. Typically I weighted particles by a factor of 100 in a 100 km radius cylinder around plume sources, decreasing exponentially to a factor of 1 at a distance of 600 km from the plume sources. The exponential fall-off in the weights ensured that a particle’s weight changes by a constant factor as it moves a given distance towards or away from a plume source.

## C.3 Communication

As more and more processors are used, communication between processors takes up a larger and larger share of total simulation time. Each processor stores a list

of particles contained in the volume for which it is responsible. When a particle finds itself in a region of space not assigned to its current processor then processors need to communicate in order to assign it to the appropriate processor. For large simulations it is therefore desirable to minimize the opportunity for particles to be in the wrong processor. Only particle movement or the movement of processor boundaries (when load-balancing) requires communication. However, parts of the UT DSMC code were written with smaller simulations in mind. Conceptually simple methods that rely on communication turn out to be costly. For example, every processor in a plume simulation with a virtual vent participates in the creation of particles in reservoir cells, even when the reservoir cell is entirely outside of the processor's boundaries. For small numbers of processors it is faster to distribute the creation of new particles and then send them to appropriate processors, but this is inefficient for large numbers of processors.

Originally, every processor communicated with every other processor twice per time step (or sub-step, with plasma) immediately after moving particles, once to determine how many particles needed to be sent between processors and again to actually send them. I obtained significant speedup by having processors only communicate with other processors to which it will be sending particles, or from which it will receive them during the second communication. It is possible to map processors so that they only ever communicate with neighboring processors (and maybe their neighbors' neighbors), and this would probably be necessary for 10k+ processor simulations in the future.

Load-balancing also presents a potential bottleneck for large simulations even as a method for load-balancing becomes more and more important as the number of

processors increases. The current load-balancing algorithm builds a map of particles in the entire simulation domain relatively quickly using binary reduction across all processors. However, when load-balancing produces new processor boundaries and these are applied, almost every molecule in the simulation could potentially find itself in the wrong processor. Perhaps the algorithm can be modified to attempt to minimize the number of particles traded between processors, or at least the rate at which processor boundaries move could be limited.

Another significant cost of load-balancing is that it requires the re-initialization of many arrays. In many ways load-balancing is like beginning a new simulation with a large number of pre-existing particles. A great deal of time can be saved by making re-initialization as quick as possible. For example, the patching method used to read particles from an inner domain into an outer domain relies on *each* processor reading a large list of molecules from *every* processor in the inner domain, only saving those that are inside of its boundaries. Naive re-initialization requires that this be repeated every time load-balancing occurs, but the positions of the most extreme molecules in each file can be saved when reading the files for the first time. Later, after load-balancing, an entire file can be skipped if the most extreme molecules in it are all outside of a processor's current boundaries.

## C.4 GPU/MIC Acceleration

The Stampede supercomputer at TACC has Xeon Phis attached to each node. These are essentially GPUs (Intel calls it a "Many Integrated Core" architecture), though easier to program, consisting of a large number of weak cores with relatively little memory per core. Code running on the primary cores can offload some work to

the Phi coprocessors, or the coprocessors can be addressed as if they were collections of primary cores. I experimented with both approaches, and found that the Phi cores were too slow to be used as primary cores – the serial parts of the UT code took them far too long. Modest speedup was obtained offloading some collisions to the Phis, but not much. The main obstacle encountered was that a Phi does not share memory with the primary cores on its node, and there is latency in beginning transfers as well as time spent actually transmitting data. My most successful approach was to send only part of the molecule list in each processor to the Phis, containing only those molecules in a selection of cells that I intended the Phis to compute collisions for. The results were not impressive; transfer times were still too long. Collisions take more time than anything else in the UT code (other than communication, sometimes), and no real speedup was evident when offloading the movement of particles (unfortunately the particles need to be moved back to the primary cores after moving in order to be indexed).

I think it might be possible to accelerate DSMC with the Phis (or with something similar like a GPU) by using them to compute single collisions. The usual DSMC collision routine is to loop over a large number of cells, test pairs of particles in each cell, and then perform collisions between certain pairs. The computation of a single collision is surprisingly expensive, with potentially many random number draws depending on the physics modeled. And a single collision only requires two particles' worth of data transfer. If each primary core spawns a large number of Open MP processes when looping over cells to compute collisions, some fraction of the processes could offload single collisions to the Phis. Because multiple processes would be active simultaneously, the primary cores would spend no time idle while waiting for data transfer to and from the Phis. GPU acceleration is *almost* a big deal for DSMC; if

future hardware implementations include shared memory or just faster transfer rates, it should be a priority.



## Bibliography

- Austin, J. and Goldstein, D. (1996). Direct numerical simulation of low-density atmospheric flow on Io. In *Molecular Physics and Hypersonic Flows*, pages 749–758. Springer.
- Austin, J. V. and Goldstein, D. B. (2000). Rarefied gas model of Io’s sublimation-driven atmosphere. *Icarus*, 148(2):370–383.
- Ballester, G. E., Strobel, D. F., and Moos, H. W. (1990). The atmospheric abundance of SO<sub>2</sub> on Io. *Icarus*, 88(1):1–23.
- Bellucci, G., D’Aversa, E., Formisano, V., Cruikshank, D., Nelson, R., Clark, R., Baines, K., Matson, D., Brown, R., McCord, T., et al. (2004). Cassini/VIMS observation of an Io post-eclipse brightening event. *Icarus*, 172(1):141–148.
- Bigg, E. (1964). Influence of the satellite Io on Jupiter’s decametric emission. *Nature*, 203:1008–1010.
- Bird, G. A. (1994). *Molecular gas dynamics and the direct simulation of gas flows*. Clarendon.
- Boyd, I. D. and Burt, J. M. (2004). Development of a two-way coupled model for two phase rarefied flows. 42nd AIAA Aerospace Sciences Meeting.
- Bridge, H., Belcher, J., Lazarus, A., Sullivan, J., McNutt, R., Bagenal, F., Scudder, J., Sittler, E., Siscoe, G., Vasyliunas, V., et al. (1979). Plasma observations near Jupiter: Initial results from Voyager 1. *Science*, 204(4396):987–991.

- Burger, M. H., Schneider, N. M., and Wilson, J. K. (1999). Galileo’s close-up view of the Io sodium jet. *Geophysical research letters*, 26(22):3333–3336.
- Burgi, P.-Y., Caillet, M., and Haefeli, S. (2002). Field temperature measurements at Erta’Ale lava lake, Ethiopia. *Bulletin of Volcanology*, 64(7):472–485.
- Combi, M., Kabin, K., Gombosi, T., DeZeeuw, D., and Powell, K. (1998). Io’s plasma environment during the Galileo flyby: Global three-dimensional MHD modeling with adaptive mesh refinement. *Journal of Geophysical Research: Space Physics* (1978–2012), 103(A5):9071–9081.
- Cruikshank, D. and Murphy, R. E. (1973). The post-eclipse brightening of Io. *Icarus*, 20(1):7–17.
- Davies, A. G. (2007). *Volcanism on Io*. Cambridge University Press.
- Davies, A. G., Keszthelyi, L. P., Williams, D. A., Phillips, C. B., McEwen, A. S., Lopes, R., Smythe, W. D., Kamp, L. W., Soderblom, L. A., and Carlson, R. W. (2001). Thermal signature, eruption style, and eruption evolution at Pele and Pillan on Io. *Journal of Geophysical Research: Planets* (1991–2012), 106(E12):33079–33103.
- Davies, A. G., Veeder, G. J., Matson, D. L., and Johnson, T. V. (2012). Charting thermal emission variability at Pele, Janus Patera and Kanehekili Fluctus with the Galileo NIMS Io Thermal Emission Database (NITED). *Icarus*, 221(1):466–470.

- Douté, S., Schmitt, B., Lopes-Gautier, R., Carlson, R., Soderblom, L., Shirley, J., Team, G. N., et al. (2001). Mapping SO<sub>2</sub> frost on Io by the modeling of NIMS hyperspectral images. *Icarus*, 149(1):107–132.
- Fanale, F. P., Brown, R. H., Cruikshank, D. P., and Clake, R. N. (1979). Significance of absorption features in Io’s IR reflectance spectrum. *Nature*, 280:761–763.
- Feaga, L. M., McGrath, M., and Feldman, P. D. (2009). Io’s dayside SO<sub>2</sub> atmosphere. *Icarus*, 201(2):570–584.
- Frank, L., Paterson, W., Ackerson, K., Vasyliunas, V., Coroniti, F., and Bolton, S. (1996). Plasma observations at Io with the Galileo spacecraft. *Science*, 274(5286):394–395.
- Geissler, P., McEwen, A., Keszthelyi, L., Lopes-Gautier, R., Granahan, J., and Simonelli, D. (1999). Global color variations on Io. *Icarus*, 140(2):265–282.
- Geissler, P., McEwen, A., Phillips, C., Keszthelyi, L., and Spencer, J. (2004). Surface changes on Io during the Galileo mission. *Icarus*, 169(1):29–64.
- Geissler, P. and McMillan, M. (2008). Galileo observations of volcanic plumes on Io. *Icarus*, 197(2):505–518.
- Geissler, P. E. and Goldstein, D. B. (2007). Plumes and their deposits. In *Io After Galileo*, pages 163–192. Springer.
- Howell, R. R. and Lopes, R. (2011). Morphology, temperature, and eruption dynamics at Pele. *Icarus*, 213(2):593–607.
- Ingersoll, A. P. (1989). Io meteorology: How atmospheric pressure is controlled locally by volcanos and surface frosts. *Icarus*, 81(2):298 – 313.

- Ingersoll, A. P., Summers, M. E., and Schlipf, S. G. (1985). Supersonic meteorology of Io: Sublimation-driven flow of SO<sub>2</sub>. *Icarus*, 64(3):375–390.
- Jessup, K. L., Spencer, J., and Yelle, R. (2007). Sulfur volcanism on Io. *Icarus*, 192(1):24–40.
- Jessup, K. L. and Spencer, J. R. (2012). Characterizing Ios Pele, Tvashtar and Pillan plumes: Lessons learned from Hubble. *Icarus*, 218(1):378–405.
- Jessup, K. L. and Spencer, J. R. (2015). Spatially resolved HST/STIS observations of Io’s dayside equatorial atmosphere. *Icarus*, 248:165–189.
- Jessup, K. L., Spencer, J. R., Ballester, G. E., Howell, R. R., Roesler, F., Vigel, M., and Yelle, R. (2004). The atmospheric signature of Io’s Prometheus plume and anti-Jovian hemisphere: Evidence for a sublimation atmosphere. *Icarus*, 169(1):197–215.
- Kabin, K., Combi, M., Gombosi, T., DeZeeuw, D., Hansen, K., and Powell, K. (2001). Io’s magnetospheric interaction: an MHD model with day-night asymmetry. *Planetary and Space Science*, 49(3):337–344.
- Kivelson, M., Khurana, K., Russell, C., and Walker, R. (2001). Magnetic signature of a polar pass over Io. In *AGU Fall Meeting Abstracts*, volume 1, page 01.
- Kliore, A., Fjeldbo, G., Seidel, B., Sweetnam, D., Sesplaukis, T., Woiceshyn, P., and Rasool, S. (1975). The atmosphere of Io from Pioneer 10 radio occultation measurements. *Icarus*, 24(4):407–410.

- Lellouch, E., Belton, M., De Pater, I., Paubert, G., Gulkis, S., and Encrenaz, T. (1992). The structure, stability, and global distribution of Io's atmosphere. *Icarus*, 98(2):271–295.
- Linker, J., Kivelson, M., and Walker, R. (1991). A three-dimensional MHD simulation of plasma flow past Io. *Journal of Geophysical Research: Space Physics* (1978–2012), 96(A12):21037–21053.
- Linker, J. A., Khurana, K. K., Kivelson, M. G., and Walker, R. J. (1998). MHD simulations of Io's interaction with the plasma torus. *Journal of Geophysical Research: Planets* (1991–2012), 103(E9):19867–19877.
- Linker, J. A., Kivelson, M. G., and Walker, R. J. (1988). An MHD simulation of plasma flow past Io: Alfvén and slow mode perturbations. *Geophysical research letters*, 15(11):1311–1314.
- Lipatov, A. S. and Combi, M. R. (2006). Effects of kinetic processes in shaping Io's global plasma environment: A 3D hybrid model. *Icarus*, 180(2):412–427.
- McDoniel, W., Goldstein, D., Varghese, P., Trafton, L., Buchta, D., Freund, J., Kieffer, S., Levin, D. A., Wysong, I. J., and Garcia, A. L. (2011). Simulating irregular source geometries for Ionian plumes. In *AIP Conference Proceedings-American Institute of Physics*, volume 1333, page 1157.
- McDoniel, W. J., Goldstein, D. B., Varghese, P. L., and Trafton, L. M. (2015). Three-dimensional simulation of gas and dust in Io's Pele plume. *Icarus*.

- McEwen, A. S., Keszthelyi, L., Geissler, P., Simonelli, D. P., Carr, M. H., Johnson, T. V., Klaasen, K. P., Breneman, H. H., Jones, T. J., Kaufman, J. M., et al. (1998). Active volcanism on Io as seen by Galileo SSI. *Icarus*, 135(1):181–219.
- McEwen, A. S. and Soderblom, L. A. (1983). Two classes of volcanic plumes on Io. *Icarus*, 55(2):191–217.
- Mitchner, M. and Kruger, C. H. (1973). *Partially ionized gases*. Wiley New York.
- Moore, C., Goldstein, D., Varghese, P., Trafton, L., and Stewart, B. (2009). 1-D DSMC simulation of Io’s atmospheric collapse and reformation during and after eclipse. *Icarus*, 201(2):585–597.
- Moore, C., Miki, K., Goldstein, D., Stapelfeldt, K., Varghese, P., Trafton, L., and Evans, R. (2010). Monte Carlo modeling of Io’s [OI] 6300Å and [SII] 6716Å auroral emission in eclipse. *Icarus*, 207(2):810–833.
- Moore, C. H. (2011). *Monte Carlo simulation of the Jovian plasma torus interaction with Io’s atmosphere and the resultant aurora during eclipse*. PhD thesis, the University of Texas at Austin.
- Moore, C. H., Walker, A. C., Goldstein, D. B., Varghese, P. L., Trafton, L. M., Parsons, N., and Levin, D. A. (2012). DSMC simulations of the plasma bombardment on Ios sublimated and sputtered atmosphere. In *50th AIAA Aerospace Sciences Meeting, Nashville, TN. Jan. 9th–12th. AIAA-2012-0560*.
- Moreno, M. A., Schubert, G., Baumgardner, J., Kivelson, M. G., and Paige, D. A. (1991). Io’s volcanic and sublimation atmospheres. *Icarus*, 93(1):63–81.

- Morris, A., Goldstein, D., Varghese, P., and Trafton, L. (2012). Modeling the interaction between a rocket plume, scoured regolith, and a plume deflection fence. In *Earth and Space 2012*, pages 189–198.
- Nash, D., Fanale, F., and Nelson, R. (1980). SO<sub>2</sub> frost: UV-visible reflectivity and Io surface coverage. *Geophysical Research Letters*, 7(9):665–668.
- Parsons, N., Levin, D., and van Duin, A. (2012). Development of a chemistry model for DSMC simulation of the atmosphere of Io. In *50th AIAA Aerospace Sciences Meeting including the New Horizons Forum and Aerospace Exposition*, page 227.
- Patankar, S. (1980). *Numerical heat transfer and fluid flow*. CRC Press.
- Pearl, J., Hanel, R., Kunde, V., Maguire, W., Fox, K., Gupta, S., Ponnamperna, C., and Raulin, F. (1979). Identification of gaseous SO<sub>2</sub> and new upper limits for other gases on Io. *Nature*, 280:755–758.
- Prem, P., Artemieva, N., Goldstein, D., Varghese, P., and Trafton, L. (2014). Transport of water in a transient impact-generated lunar atmosphere. *Icarus*.
- Radebaugh, J., McEwen, A. S., Milazzo, M. P., Keszthelyi, L. P., Davies, A. G., Turtle, E. P., and Dawson, D. D. (2004). Observations and temperatures of Io’s Pele Patera from Cassini and Galileo spacecraft images. *Icarus*, 169(1):65–79.
- Rathbun, J., Spencer, J., Tamppari, L., Martin, T., Barnard, L., and Travis, L. (2004). Mapping of Io’s thermal radiation by the Galileo photopolarimeter–radiometer (PPR) instrument. *Icarus*, 169(1):127–139.

- Saur, J., Neubauer, F. M., Connerney, J., Zarka, P., and Kivelson, M. G. (2004). Plasma interaction of Io with its plasma torus. *Jupiter: The Planet, Satellites and Magnetosphere*, pages 537–560.
- Saur, J., Neubauer, F. M., Strobel, D. F., and Summers, M. E. (1999). Three-dimensional plasma simulation of Io’s interaction with the Io plasma torus: Asymmetric plasma flow. *Journal of Geophysical Research: Space Physics (1978–2012)*, 104(A11):25105–25126.
- Saur, J., Neubauer, F. M., Strobel, D. F., and Summers, M. E. (2000). Io’s ultra-violet aurora: Remote sensing of Io’s interaction. *Geophysical research letters*, 27(18):2893–2896.
- Saur, J., Neubauer, F. M., Strobel, D. F., and Summers, M. E. (2002). Interpretation of Galileo’s Io plasma and field observations: I0, I24, and I27 flybys and close polar passes. *Journal of Geophysical Research: Space Physics (1978–2012)*, 107(A12):SMP–5.
- Saur, J. and Strobel, D. F. (2004). Relative contributions of sublimation and volcanoes to Io’s atmosphere inferred from its plasma interaction during solar eclipse. *Icarus*, 171(2):411–420.
- Smith, B. A., Soderblom, L. A., Johnson, T. V., Ingersoll, A. P., Collins, S. A., Shoemaker, E. M., Hunt, G., Masursky, H., Carr, M. H., Davies, M. E., et al. (1979). The Jupiter system through the eyes of Voyager 1. *Science*, 204(4396):951–972.
- Smyth, W. H. and Wong, M. (2004). Impact of electron chemistry on the structure and composition of Io’s atmosphere. *Icarus*, 171(1):171–182.



- Smythe, W. D., Nelson, R. M., and Nash, D. B. (1979). Spectral evidence for SO<sub>2</sub> frost or adsorbate on Io's surface. *Nature*, 280:766.
- Spencer, J. R., Jessup, K. L., McGrath, M. A., Ballester, G. E., and Yelle, R. (2000). Discovery of gaseous S<sub>2</sub> in Io's Pele plume. *Science*, 288(5469):1208–1210.
- Spencer, J. R., Lellouch, E., Richter, M. J., López-Valverde, M. A., Jessup, K. L., Greathouse, T. K., and Flaud, J.-M. (2005). Mid-infrared detection of large longitudinal asymmetries in Io's SO<sub>2</sub> atmosphere. *Icarus*, 176(2):283–304.
- Stewart, B. (2010). *Numerical simulations of the flow produced by a comet impact on the Moon and its effects on ice deposition in cold traps*. PhD thesis, the University of Texas at Austin.
- Stewart, B. D., Pierazzo, E., Goldstein, D. B., Varghese, P. L., Trafton, L. M., and Moore, C. H. (2009). Parallel 3D hybrid continuum/DSMC method for unsteady expansions into a vacuum. In *47th AIAA Aerospace Sciences Meeting, Orlando, Florida, AIAA*, volume 266.
- Strom, R. and Schneider, N. (1982). Volcanic eruption plumes on Io. In *Satellites of Jupiter*, volume 1, pages 598–633.
- Strom, R. G., Schneider, N. M., Terrile, R. J., Cook, A. F., and Hansen, C. (1981). Volcanic eruptions on Io. *Journal of Geophysical Research: Space Physics (1978–2012)*, 86(A10):8593–8620.
- Trafton, L., Caldwell, J., Barnet, C., and Cunningham, C. (1996). The gaseous sulfur dioxide abundance over Io's leading and trailing hemispheres: HST spectra of

Io's C 1B 2-X 1A 1 band of SO<sub>2</sub> near 2100 angstrom. *The Astrophysical Journal*, 456:384.

Tsang, C. C., Spencer, J. R., and Jessup, K. L. (2015). Non-detection of post-eclipse changes in Ios Jupiter-facing atmosphere: Evidence for volcanic support? *Icarus*, 248:243–253.

Tsang, C. C., Spencer, J. R., Lellouch, E., López-Valverde, M. A., Richter, M. J., and Greathouse, T. K. (2012). Io's atmosphere: Constraints on sublimation support from density variations on seasonal timescales using NASA IRTF/TEXES observations from 2001 to 2010. *Icarus*, 217(1):277–296.

Wagman, D. (1979). Sublimation pressure and enthalpy of SO<sub>2</sub>. *Chem. Thermodynamics Data Center Natl. Bureau Standards, Washington, DC*.

Walker, A. C. (2012). *A comprehensive numerical model of Io's chemically-reacting sublimation-driven atmosphere and its interaction with the Jovian plasma torus*. PhD thesis, the University of Texas at Austin.

Walker, A. C., Goldstein, D. B., Varghese, P. L., Trafton, L. M., Moore, C. H., Levin, D. A., Wysong, I. J., and Garcia, A. L. (2011). Loki-a lava lake in rarefied circumplanetary cross flow. In *AIP Conference Proceedings-American Institute of Physics*, volume 1333, page 1175.

Walker, A. C., Gratiy, S. L., Goldstein, D. B., Moore, C. H., Varghese, P. L., Trafton, L. M., Levin, D. A., and Stewart, B. (2010). A comprehensive numerical simulation of Io's sublimation-driven atmosphere. *Icarus*, 207(1):409–432.

- Walker, A. C., Moore, C. H., Goldstein, D. B., Varghese, P. L., and Trafton, L. M. (2012). A parametric study of Io’s thermophysical surface properties and subsequent numerical atmospheric simulations based on the best fit parameters. *Icarus*, 220(1):225–253.
- Williams, D. A., Keszthelyi, L. P., Crown, D. A., Yff, J. A., Jaeger, W. L., Schenk, P. M., Geissler, P. E., and Becker, T. L. (2011). Volcanism on Io: New insights from global geologic mapping. *Icarus*, 214(1):91–112.
- Wong, M. C. and Johnson, R. E. (1995). The effect of plasma heating on sublimation-driven flow in Io’s atmosphere. *Icarus*, 115(1):109–118.
- Wong, M. C. and Johnson, R. E. (1996). A three-dimensional azimuthally symmetric model atmosphere for Io: 1. photochemistry and the accumulation of a nightside atmosphere. *Journal of Geophysical Research: Planets (1991–2012)*, 101(E10):23243–23254.
- Wong, M. C. and Smyth, W. H. (2000). Model calculations for Io’s atmosphere at eastern and western elongations. *Icarus*, 146(1):60–74.
- Zhang, J. (2004). *Simulation of gas dynamics, radiation and particulates in volcanic plumes on Io*. PhD thesis, the University of Texas at Austin.
- Zhang, J., Goldstein, D., Varghese, P., Gimelshein, N., Gimelshein, S., and Levin, D. (2003). Simulation of gas dynamics and radiation in volcanic plumes on Io. *Icarus*, 163(1):182–197.

- Zhang, J., Goldstein, D., Varghese, P., Trafton, L., Moore, C., and Miki, K. (2004). Numerical modeling of Ionian volcanic plumes with entrained particulates. *Icarus*, 172(2):479–502.
- Zolotov, M. Y. and Fegley, B. (2000). Eruption conditions of Pele volcano on Io inferred from chemistry of its volcanic plume. *Geophysical research letters*, 27(17):2789–2792.
- Zolotov, M. Y. and Fegley Jr, B. (2001). Chemistry and vent pressure of very high-temperature gases emitted from Pele volcano on Io. In *Lunar and Planetary Institute Science Conference Abstracts*, volume 32, page 1474.